Eine Direkte Inversion Methode für die Zweidimenzionalen Modellung in der Geomagnetische Induktion Forschung

Zusammenfassung

Die elektlische Leitfähigkeit des Gesteines und Minerals ist eine der wesentlicheste Eigentum im Erdmaterial. Die Forschung der geomagnetische Induktion ziele nach die Vermutung auf die Verbreitung der elektrischen Leitfähigkeit im Untergrund. Weil die Leitfähigkeit des Gesteines und Minerals auf die Temperature, den Wasserinhalt, die chemische Zussamensetzung, der Umfang des partielles Schmerzen und so fort stark angewiesen ist. die Kenntnisse in seiner Verbreitung versehe die wichtigen Information an der Untersuchung auf den geophysichen Verfahren unter den Inselbogen System. In dieser Forschung hat die neue Methode für die Interpretation von geoelektromagnetische Beobachtungen entwickelt worden, und die Verbreitungen unter den nordöstlichen und zentralen Japan habe untergesucht worden.

Ein neue Verfaren wird entwickelt durch Anwendung des verallgemeinertes Nichtlinear-Kleinste-Quadrat auf den geomagnetische Induktion Problem, für einer ubergeugenden Modell von der zweidimenzionaler Untergrundstruktur der elektrischen Leitfähigkeit zu erwerben. Die zweidimenzionale Erde mit einer flachen Oberfläche wird im Anwesenden Modellieren angennommen, die in enier Anzahl von nichthomogener Blocken mit ständigen elektrischen Leitfähigkeiten zerfallen. Der geneuer Ausdruck hat verleicht gewesen zu abschätzen die Teilableitung von der theoretischer induktiver Antwortfunktionen für den Parameter in

bezug auf die Leitfähigkeit durch Formulierung der Induktion Gleitung mit der begrezt Element Methode (FEM).

In der Anwesenden Forschung wird die geomagnetische Übertragungsfunktion und der Logarithmus von der Magnetotellurischen Impedanz fur Input Daten gebraucht, weil der Logarithmus von der nichthomogenen Leitfähigkeit zu bestimmt durch die Inversion werden. Diese Forschung klärte, dass die Verbindung die geomagnetische Ubertragungsfunktion und das Impedanz viele Information an der Untergrundstruktur und darum der höcher Entschlossenheit im Verfahren dem Inversion bringen kann.

Einige Zahlenverzuchen hatte für etwas simpele Modellen und der entsprechende syntaktische Daten ausgefürt gewesen, vor den Anlegen von dieser Methode zum wirklichem Observationergebnis, was die folgenden Gesichtsbildungen um diesem Inversion Methode offenbärte.

1) Die räumliche Verbreitung der Teilableitung angebe deutlich der Unterschied zwischen Sensitivitäten dem Impedanz und der Übertragungsfunktion zu der Untergrundstruktur, der erste zum absolutem Wert von der untergrunden Leitfahigkeit aber der letztere zum seitlichem Gegensatz in der Leitfähigkeit sensitiv ist.

2) Dieser Schema ist genugent standfest für Modellen mit der lesser Grad von Freiheit, aber die Stabilität abnenmt sich naturlich mit der Vergrösserung Grad von Freiheit.

3) Die Amplitude der Teilableitung und die Mitveränderung (Covariance) sind gut Anzeigern für die Genauigkeit der Auflösung.

4) Die Vermessungen des elektromagnetisches Feldes ans Meeresboden sind besonders wesentlich für die Forschung der Unterseestruktur, weil die Beobachtungen auf Land und Seeoberflache manchmal einfach

nichtsensitiv zu der Struktur bekommen.
5) Diese Methode bringt im allgemeiner die höcheren Auflösung in der höcher Leitfähigkeit, und die lesser Auflossung in der lesseren leitfähigen Struktur der Induktion Wirkung schwach ist.

Die zweidimenzionale Verbreitungen der elektrischer Leitfähigkeit unterhalb der nordöstlichen und zentralen Teilen von Japan habe mit dieser Inversion Methode untergesucht worden, durch die Zerlegung des Ergebnis von der Beobachtungen der geomagnetischen und geoelektrischen Feld Veränderung auf den Land und ans Meersboden herum Japan. Im Anfang des Modellieren war die Verbreitung der Leitfähigkeit in der seichter Tiefe hinunter zu etwas Kilometern mit dem Ergebnis von Magnetotellurische Vermussung in der ELF und VLF Frequenzbereichen gegeben. Demnächst war die untergrund Modellen mit der Teilung die Schnillflahe des Erdes in der nichthomogenen Blocken. Der Anfangswert wurde zu jeder Nichthomogenität gegeben, die erwartungsvolle Wirkungen und die Erfolgen der eindimenzionalen Magnetotellurischen Inversion auf dem Land und ans Meeresboden in Betracht geziebt.

Fur den Inversion von nortostliche Japan (NEJ) wurde die Übertragungsfunktionen an 15 Stellen und die Impedanze an 4 Stellen als Data für 15, 30 60 und 120 Minuten Perioden angewenden. Fur zentrale Japan (CJ) wurde 26 und 5 Stellen beziehingsweise als Data Punkte gegebend die Übertragungsfunktionen und die Impedanzen ausgewählt. Die elektrischen Leitfähigkeiten widerstehend Strukturen und der Blocken, woauf keine Messung verfügbar ist, wurde bevor der Inversion gegeben, weil dieser den Inversion Verfahren unsicher machen. Damnächst war die direkten Inversionen fur 8 unbekannte

Parametern für die NEJ Modelle und 7 Parametern für die CJ Modellen ausgeführt. Das wiederfolend Verfahren hat nach 48 Mal Wiederholungen fur NEJ gekonvergiert, weil 32 Mal Wiederholungen fur die Annäherung der CJ Daten erforderlich gewesen hat. Der Abschluss kann als den Folgende gegeben werden.

1) Die beiden Modellen erwiesen sich eine gemeinsame Gesichtzug, die ein Stück des Erdkruste unter die Japanischen Insel uber einstellig leitfähiger als ander Teilen ist. Die östliche Grenz dieses Leiter übereinstimmt mit der Aseismischenfront für die NEJ Modelle. Dieses Ergebnis vorschlagt nachdrücklich, dass diese hoche Leitfähigkeit nicht von der Thermalursprung sondern von der möglichen Existenz des Wasser im tieferem Erdkruste.

2) Diese Forschung deutete die Existenz einer leitfähigen Schicht, die das Asthenosphere entsprecht, im Obererdmantel beide unter den Pazifik-Ozean und die Philippin-See an. Unter die Philippin-See gibt es 30 Kilometer tief hochleitfähigen Schicht, weil die Tiefe zu die leitfähigen Schicht als 140 Kilometer unter den Pazifik-Ozean abgeschätzen wird. Dieser Unterschied kann zu einer im Alter des Lithospheres schreiben.

3) Es gibt eine dunne leitfähigen Schicht an der Oberfläche der untergehende Platte in beider Modellen. Es ist nötig, dass die Totalleitfähigkeit ungefähr 10^3 S die geomagnetischen Veränderung zu erklären ist. Diese Schicht kann als die von dem Meeresboden Sediment und/oder dem Wassertragendem unterseeischem Basalt betrachtet werden.

4) Das NEJ Ergebnis anziegt, dass der Erdmantel Keil um ein Vielfaches leitfähiger als den untergehenden Pazifishen Lithosphere.

Dieser Unterschied möglich zuschreiben einer im Geotherms.
5) Der Obererdmantel unter den Philippin-Platte ist höcher leitfähig als diese unter die Honshu-Insel und die Japan-See, daraus ergibt sich dass die Platte Bewegung spielt eine wichtige Rolle in der Ursache der hochen Leitfähigkeit im Ozeanischem Asthenosphere.
6) Die Leitfähigkeit des Erdmantel Keiles beitragt möglich zu abnehmen gehend weiter nach dem Japan-Graben zu die Japan-See, aber die Richtung ist nicht vollständig festgestellen wegen den Mangel an Daten ans Meeresboden in der Japan-See. Dieser mag ergeben sich dass der Wasser Inhalt ebensogut wie die Thermalstruktur im Obererdmantel in der Bestimmung der elektrischen Leitfähigkeit beitragen.

Überall in der Forschung hat die Wichtigkeit des Wasser Inhaltes im tieferem Erdkruste und Obererdmantel aufmerksam gemacht worden. Die Wirkung des Wassers kann die hochen leitfähigen Schicht im tifer Erdkruste und die abnehmenden Richtung der Obererdmantelen Leitfähigkeit gut erklären. Es ist wahrscheinlich, dass der Oberplatte Leiter die Quelle des Wasser ist, die mit dem Wasser zum Erdmantel Keil und daher dem tiefer Erdkruste unter die Japanischen Inselbogen versorgt.

A DIRECT INVERSION METHOD FOR TWO-DIMENSIONAL MODELING IN THE GEOMAGNETIC INDUCTION PROBLEM

BY

Hisashi Utada

Earthquake Research Institute
The University of Tokyo

June,1987

ABSTRACT

The electrical conductivity of rocks and minerals is one of the fundamental physical properties of the earth's material. Geomagnetic induction study aims at determining the distribution of the electrical conductivity in the earth. Since the conductivity of rocks and minerals is strongly dependent on temperature, water content, chemical composition , degree of partial melting and so forth, the knowledge of its distribution provides important information on the investigation of the geophysical processes beneath the island arc system. In the present study, a new method has been developed for the interpretation of geoelectromagnetic observations, and the conductivity distributions beneath the northeast and central parts of the Japan have been investigated.

In order to determine a convincing model of the two-dimensional conductivity structure in the earth, a new technique was developed by applying the generalized non-linear least squares method to the geomagnetic induction problem. In the present modeling, the two-dimensional earth with a plain surface is assumed, which is divided into a number of inhomogeneous blocks with constant conductivities. By formulating the two-dimensional induction equation with finite element method (FEM), the exact expression has been put forward to evaluate the partial derivatives of the theoretical inductive response functions with respect to the parameter relating to the inhomogeneous conductivity.

In the present method, the geomagnetic transfer function and the logarithm of the magnetotelluric impedance tensor were used for input

data, while the logarithm of the inhomogeneous conductivity was adopted as the parameter to be determined by the inversion. The transfer function and the impedance were analyzed separately in most of the previous works. The present investigation clarified that the combined use of these two response functions provides much information on the subsurface structure and, therefore, the higher resolution in the inversion process is attained.

Prior to the application of the present method to the actual observations, several numerical experiments have been performed against some simple models and corresponding synthetic data sets. Following features about the present inversion method were revealed by the numerical experiments;

1) Spatial distribution of the partial derivatives definitely indicates the difference in the sensitivity of the impedance and the transfer function to the subsurface structure; i.e. the former is sensitive to the absolute value of the conductivity with a maximum amplitude of the partial derivative just above the inhomogeneity, while the derivative being maximum above the boundary between different materials shows that the latter is sensitive to the lateral contrast in conductivity.

2) The present scheme is sufficiently stable for models with the lower degrees of freedom, though the stability decreases with increasing degree of freedom as a common feature of the least squares.

3) The amplitude of the partial derivative, as well as the covariance matrix, works as a good indicator for the accuracy of the solution.

4) In the investigation of the submarine structure, seafloor measurements of the electromagnetic fields are particularly important, since the observations on land and on sea surface will sometimes become

quite insensitive to the structure.

5) The present method generally provides the higher resolution to the structure with the higher conductivity. The less conductive structure is weakly resolved since its induction effect is small.

By analyzing the the results of the observations of the geomagnetic and electric field variations on land and at seafloor around Japan, the two-dimensional electrical conductivity distributions beneath the northeast and the central parts of Japan have been investigated by use of the present inversion method. In the modeling, the conductivity distribution at the shallower depth down to several kilometers was estimated on the basis of the results of the magnetotelluric surveys at the higher frequencies of ELF and VLF ranges. Then, the subsurface models were constructed by dividing the cross section of the earth into inhomogeneous blocks by making reference to the other geophysical and geological evidences, as well as the electromagnetic ones. The initial value was applied to each inhomogeneity by taking into account the expected induction effects. Results of the one-dimensional inversion of the magnetotelluric soundings on land as well as on seafloor were found to be useful in construction of the initial model of the conductivity structure.

For the inversion of northeast Japan (NEJ) data, the transfer functions at 15 sites and the impedances at 4 sites were employed as data for the periods of 15, 30, 60 and 120 minutes. In case of central Japan (CJ), 26 sites and 5 sites were selected as the data points giving the transfer functions and the impedances, respectively, for the same discrete frequencies as those for NEJ. Conductivities of the resistive structures and the blocks where no observation is available on top were assigned before the inversion, because they make the inversion process unstable. Then, the direct inversions were performed for 8 unknown parameters for NEJ and 7 parameters for CJ. The iterative process has converged after 48 cycles of iteration for NEJ, while 32 cycles of iteration has been required for the convergence of the inversion of CJ data. Conclusions based on the final models are given as follows;

1) Both models show a common feature that a part of the lower crust beneath the Japanese island is conductive by more than one order of magnitude compared with other parts of the crust. The eastern boundary of the conductor coincides with the aseismic front for NEJ model. This result strongly suggests that this high conductivity is not of thermal origin but caused possibly by the existence of water in the lower crust.

2) The result of the present investigation infers the existence of a highly conductive layer, which corresponds to the asthenosphere, in the upper mantle both beneath the Pacific Ocean and the Philippine Sea. Beneath the Philippine Sea Plate, the highly conductive layer extends at the depth of 30-100 km. On the other hand, the depth to the conductive layer beneath the Pacific Plate was estimated as deep as about 140 km. This difference can be attributed to the difference in the age of the lithosphere.

3) A thin conductive layer exists at the top of the subducting slab in both models; i.e. the Pacific Plate and the Philippine Sea Plate. It was found that the total conductance (product of the conductivity and the thickness) of about 10^3 S is required in both models in order to explain the features of the electromagnetic variations in the vicinities of the Japan trench and the Nankai trough. This layer can

be regarded as the layer of seafloor sediments and/or water bearing submarine basalts, and as a water reservoir to supply water to the mantle wedge.

4) The NEJ result indicates that the mantle wedge is more conductive by several factors compared with the underlying Pacific lithosphere. This difference may be attribute to the difference in geotherms.

5) The upper mantle beneath the Philippine Sea Plate is highly conductive compared with those beneath the Honshu island and the Japan Sea. This implies that the plate motion plays an important role in causing the high conductivity of the asthenosphere.

6) The NEJ result shows the possible tendency that the conductivity of the wedge mantle decreases going farther from the Japan trench toward the Japan sea, although the tendency is not completely established because of the lacking in data on the seafloor of the Japan Sea. This may imply that the water content, as well as the thermal structure contributes in determining the conductivity of the material in the upper mantle.

Throughout this study, the significance of water content in the lower crust and the upper mantle has been pointed out. The highly conductive layer in the lower crust and the tendency of the decreasing conductivity toward the back arc side can be well explained by the effect of the water content. The slabtop conductor is likely to be the source of the water, which supplies water to the mantle wedge and to the lower crust beneath the island arc of Japan.

Acknowledgements

I am deeply grateful to Professor T. Yukutake for his continuous advise and encouragement throughout this investigation. Appreciation is also expressed to Professor Y. Hamano for critical reading of the manuscript and valuable comments.

I am greatly indebted to Mr. Y. Sasai and Professors J. Segawa and S. Uyeda for valuable discussions and kind advises. I also wish to express my sincere thanks to Mr. Y. Tanaka for his helpful advise on field technique, and to Professor N. Sumitomo for his kind encouragement.

I am very grateful to the members of Research Group for Crustal Structure, Japan for kindly providing me ULF data on land. I acknowledge the valuable discussions given by Drs. T. Kagiyama and I. Nakagawa. My thanks also go to Messrs. S. Koyama and T. Shimomura for their assistance in field works.

Discussions with Drs. J. H. Filloux and L. K. Law were highly helpful for the present study.

I appreciate the kindness given to me by all the staffs and students in the Division of Geomagnetism, Earthquake Research Institute.

Numerical calculation was performed on a HITAC M280H computer at the Earthquake Prediction Data Center of Earthquake Research Institute, the University of Tokyo.

CONTENTS

1. Introduction

Electrical conductivity of rocks depends on various physical states, i.e. temperature, pressure, water contents, oxygen fugacity, etc. Consequently, information on the conductivity distribution gives us fundamental data to infer the physical state within the earth.

So far, various kinds of techniques have been explored to reveal the conductivity structure of the earth. The most prevailing method is the electromagnetic induction method. Transient geomagnetic variation of external origin induces electric current in the earth's interior. The induced current is primarily dependent on the earth's conductivity structure. Hence, the detailed analyses of the geomagnetic and the geoelectric field variations enable us to make clear the electrical conductivity distribution in the earth.

The transient electromagnetic field penetrates into the deeper part of the earth as the period of the variation becomes longer. The variation field can be separated into the external and the internal ones. The ratio of the internal to the external field works as an electromagnetic response function which depends on the conductivity distribution with depth. Thus, assuming that the conductivity varies only radially in the earth, investigation of the nature of the electromagnetic variation for the wide range of frequency gives a model of conductivity distribution with depth. In classical studies, such approaches were for a spherical earth model. Chapman (1919) studied a uniform core model, in which the central sphere is conducting with a constant conductivity, and the spherical shell outside the conducting sphere is an insulator. On the basis of the result of the analyses of Sq (solar quiet daily variation) fields, he derived a uniform conductivity value of 3.6×10^{-13} e.m.u. (3.6×10^{-2} S/m) for the conducting sphere with radius of $0.96R_e$ (R_e: the earth's radius). Further detailed investigation was made by Rikitake (1950a), who used analyses of not only Sq but also Dst (main phase of geomagnetic storm), s.f.e (solar flare effect), geomagnetic bays etc., and pointed out that the uniform conductivity values obtained for the more gradual variations are consistently larger than those for the more rapid variations.

Lahiri and Price (1939) took the lead in the study of a non uniform earth model where they assumed an analytical form for the conductivity distribution. Takeuchi and Saito (1963) and Eckhardt (1963) formulated the response functions for an arbitrary distribution of the conductivity. After that, with the development of high speed computers, several models of conductivity distribution for spherically symmetric earth have been presented until Banks (1969,1972) obtained his optimum model. Fig.1.1 summarizes the results of the above mentioned works. These models have common features as follows:

(1) The shallowest part of the earth is rather resistive with a conductivity of 10^{-2} S/m, or less.

(2) Conductivity increases abruptly at the depth of 400 $\sim$ 600 km up to 10^{0} S/m.

(3) At the deeper part, conductivity increases gradually with depth.

Bailey (1970) proved that the radial distribution of the earth's conductivity can be uniquely determined under certain conditions if the electromagnetic response is known for all frequencies. Therefore, accumulation of much improved data set with high resolution and wide frequency range is desirable in this subject.

A geomagnetic variation of external origin would be regarded as considerably uniform within a certain area of local extent. However, it has often been noticed, since the early 1950's, that the vertical component of geomagnetic fluctuation with the periods shorter than several hours behaves quite differently from one site to another. Such a behavior cannot be accounted for either by spatial dependence of the external field itself or the internal field arising from the electromagnetic induction in a laterally uniform earth. Thus, the origin of the anomalous behavior of vertical geomagnetic field has been interpreted as indicating the lateral heterogeneity of subsurface conductivity distribution, which is denoted by the term, 'Conductivity Anomaly (CA)'.

Fig.1.2 shows an example of such an anomalous behavior of the vertical component. In contrast with the rather smooth distribution of H and D (horizontal intensity and declination) components, the irregular distribution is conspicuous in the vertical component. Rikitake (1950a,b,c,1951) and many successors pointed out the anomalous behavior of vertical component observed in the central part of Japan as shown in Fig.1.2. Rikitake (1969) interpreted the geomagnetic variation anomaly in Japan in terms of marked undulation of a conductive layer in the mantle (Fig.1.3). Similar geomagnetic variation anomalies were found in various regions (e.g. Rikitake, 1966).

Anomalous Z variation has generally a good correlation with the horizontal field variations, which can be expressed empirically:

$$\Delta Z = A\cdot\Delta H + B\cdot\Delta D \qquad (1-1)$$

where ΔZ, ΔH and ΔD are variations of downward, northward and eastward components, respectively. The coefficients, A and B, determine the characteristics of the geomagnetic induction. Eq.(1-1) can be interpreted as indicating that the geomagnetic variation is restricted in a plane determined by a vector (A,B). Such a plane is often called the Rikitake-Yokoyama plane (Rikitake and Yokoyama, 1955).

A representation method by an arrow, called the Parkinson vector, was put forward by Parkinson (1959). The Parkinson vector can be obtained by projecting a normal vector of the Rikitake-Yokoyama plane onto the earth's surface. Another representation is sometimes made by use of the Wiese vector, which is almost identical to the Parkinson vector except 180 degree's difference in direction (Wiese, 1962).

Recently, Eq.(1-1) has been treated in the frequency domain as:

$$Z(f) = A(f)\cdot H(f) + B(f)\cdot D(f) \qquad (1-2)$$

where Z(f), H(f) and D(f) are the Fourier transforms of the variations of vertical, horizontal components and declination, respectively. The complex coefficients A(f) and B(f) are dependent on frequency, and called geomagnetic transfer functions. Everett and Hyndman (1968) presented a method to derive the transfer functions from a set of geomagnetic variation data by means of the least squares. The transfer functions are often represented by an arrow in a similar way to the Parkinson vector. The arrow derived from the transfer functions are called the induction arrow or the induction vector.

Since the geomagnetic variation induces electric current in the earth, the induced electric field contains information on the subsurface conductivity structure. It is well-known that a relationship between the induced electric field and the horizontal magnetic field variations can be expressed in a way similar to Eq.(1-2):

$$E_x(f) = Z_{xx}(f)\cdot H(f) + Z_{xy}(f)\cdot D(f) \qquad (1\text{-}3a)$$

$$E_y(f) = Z_{yx}(f)\cdot H(f) + Z_{yy}(f)\cdot D(f) \qquad (1\text{-}3b)$$

where $E_x(f)$ and $E_y(f)$ are the Fourier transforms of the northward and the eastward components of the induced electric field. The coefficients $Z_{xx}(f)$, $Z_{xy}(f)$, $Z_{yx}(f)$ and $Z_{yy}(f)$ form 2x2 tensor. In case of electromagnetic wave propagation in a medium, electric to magnetic field ratio defines the characteristic of the medium and is called the impedance. Analogous to that, the tensor defined by Eqs.(1-3a) and (1-3b) is called the impedance tensor. The impedance tensor contains information on the conductivity distribution in the earth. The method of investigation of the earth's conductivity structure by use of the impedance tensor is called the magnetotelluric method (Cagniard, 1953), often denoted by MT. The magnetotelluric method is widely used in the investigation of local and regional conductivity distribution, as well as the magnetovariational method by use of the transfer functions.

Since the conductivity of sea water is as high as 3-4 S/m, depending on its salinity and temperature, geomagnetic variations are greatly affected by the distribution of oceans and seas. Several reports on the effect of sea water on geomagnetic variations have appeared reported in 1960's to 1970's. Clear understanding of the induction effects by the presence of sea is highly important because most tectonically active regions, such as spreading and subduction zones, are located in ocean areas.

A coast forms a distinct boundary separating a conductive ocean from a resistive land. Because of the large conductivity contrast, electric current induced in the sea tends to flow in parallel to the coast, which causes a large amplitude of the vertical magnetic field at the coastal area. Parkinson (1964) found the geomagnetic variation anomaly in the southern coast of Australia, and called the phenomenon the coast effect.

On a small island, one of the most typical sea water effect, called the island effect can be observed. Sometimes the polarity of the vertical component of geomagnetic variation becomes to opposite at two sites on an island. The island effect was first discovered on Oahu island, Hawaii by Mason (1962). Since then, many examples have been reported (Sasai, 1967, 1968; Honkura, 1971; Honkura et al., 1974, 1981; Klein, 1976; Klein and Larsen, 1978). The island effect can be regarded as the perturbation of induced electric current by an island; i.e. current flows in sea water avoiding the resistive island.

Extremely large amplitude of vertical component is often observed at the tip of a peninsula, which is called the peninsula effect (Sasai, 1969). The peninsula effect can be considered to be a special case of the coast effect with irregular coastline, and may be regarded as a combination of the coast and island effects. The induced electric current tends to flow in parallel to the coastline. If the shape of the coastline has an irregularity, such as a peninsula, the current flows round along the coastline. This flow pattern causes a large amplitude of the vertical magnetic field that sometimes exceeds that of the correlating horizontal components.

In a narrow sea passage such as a strait, concentration of induced current occurs, which produces anomalous Z variation in the surrounding area. The effect is called the channeling effect. The channeling effect is characterized by reversed variation of Z on the opposite side of the channel (Yamashita, 1976).

Above mentioned sea water effects can be regarded as results of electromagnetic induction in horizontally non uniform conductor. These effects can be caused also by sedimentary layers. A typical example of the channeling effect by sedimentary layer have been found in the southern Great Plains, U.S.A. (Porath and Dziewonski, 1971). The anomalous feature of the geomagnetic variation in north German was found to be principally caused by such a channeling effect (Untiedt,1970). Local concentration of the electric current sometimes causes enhancement in amplitude of horizontal geomagnetic variation (Nishida, 1976). Anyway, it should be noticed that the information on the shallower conductivity distribution is highly important even in the investigation of deeper structure, because existence of shallow conductive layer sometimes causes a significant induction anomaly at longer periods.

Existence of highly conductive seas essentially obscure the electromagnetic responses of the structure below, and hence makes the investigation of conductivity distribution beneath coastal area quite difficult. Honkura (1974) derived, by numerical modeling technique, two dimensional models of subterranean conductivity distribution beneath northeast and central Japan (Fig.1.4). In order to overcome the difficulty of the effects of the Pacific Ocean and the Japan sea, he made an attempt to account for the frequency dependence of the transfer functions. He showed that the sea water effects are dominant in spatial distribution of the geomagnetic variation in these areas, and concluded that seafloor measurements are indispensable to make clear the conductivity structure beneath the Japanese Island Arc in detail.

For the purpose of the measurement of the geomagnetic signals in the ocean, a new apparatus has been developed by Filloux (1967). He also developed the instrument for the electric field measurement, and have conducted magnetotelluric soundings in several areas in the Pacific Ocean (Filloux, 1967, 1977, 1980a,b, 1981). The results indicated the existence of conductive layer beneath the Pacific Ocean. The conductivity is found to be about 10^{-1} S/m, and does not vary very much from one area to another. However, it was found that the depth to the conductive layer increases with the age of the oceanic plate (Filloux, 1981).

Seafloor apparatus for measurement of the geomagnetic field variation, which is often called ocean bottom magnetometer (OBM), has also been developed by Poehls and von Herzen (1976) and Law and Greenhouse (1981). In Japan, Segawa, et al.(1982) succeeded in making a new type ocean bottom magnetometer. In 1981, extensive electromagnetic measurements were conducted in the Northwest Pacific, off northeast Japan (Yukutake, et al.,1983). Since then, seafloor measurements have been carried out once a year around Japan. Meanwhile, Hamano et al.(1984) developed a instrument for electric field measurement on seafloor (denoted by OBE), and succeeded in observation of electric field variations correlated to the geomagnetic field disturbances.

Technique of land observations has been much improved in recent years. Research Group for Crustal Resistivity Structure, Japan (1984), made detailed observations of electromagnetic field variations in northeast Japan in 1981 and in central Japan in 1982. In these field experiments, observations were made for wider frequency range compared to previous ones; i.e. at ULF micropulsation range, Schumann Resonance frequencies in ELF range and 17.4 kHz signal in VLF range, as well as ordinary period range of geomagnetic disturbances.

This thesis attempts to clarify the subterranean conductivity structure beneath the Japanese Island Arc on the basis of the above mentioned new datasets. New methods of analysis have been developed for that purpose. The whole process of the investigation can be summarized as follows:

(1) Determine the shallower structure of the electrical conductivity on the basis of magnetotelluric measurements at higher frequencies such as in ELF and VLF ranges, and sometimes at ULF micropulsation periods.

(2) Compile the results of land and seafloor measurement of the electromagnetic field variations.

(3) Give the first order approximation of the conductivity model by one-dimensional inversion of magnetotelluric data, as well as referring to other geophysical and geological evidences.

(4) Apply the direct inversion scheme to obtain an optimum two-dimensional model of the conductivity distribution which accounts for the spatial and period dependences of both the transfer functions and the magnetotelluric impedances.

In Chapter 2, previous results of laboratory measurements on the electrical properties of rocks and minerals will be reviewed. This review will be reffered to in the later discussions. The theory of interpretation will be presented in Chapter 3. The formulation of inversion schemes is made in this chapter. In Chapters 4 and 5, techniques of field measurements and data processing will be described for ELF and VLF, and ULF ranges, respectively. The application of the whole method will be made in Chapters 6 and 7 to derive two-dimensional models beneath northeast and central Japan, respectively. Geophysical implications of the models will be discussed in the last chapter.

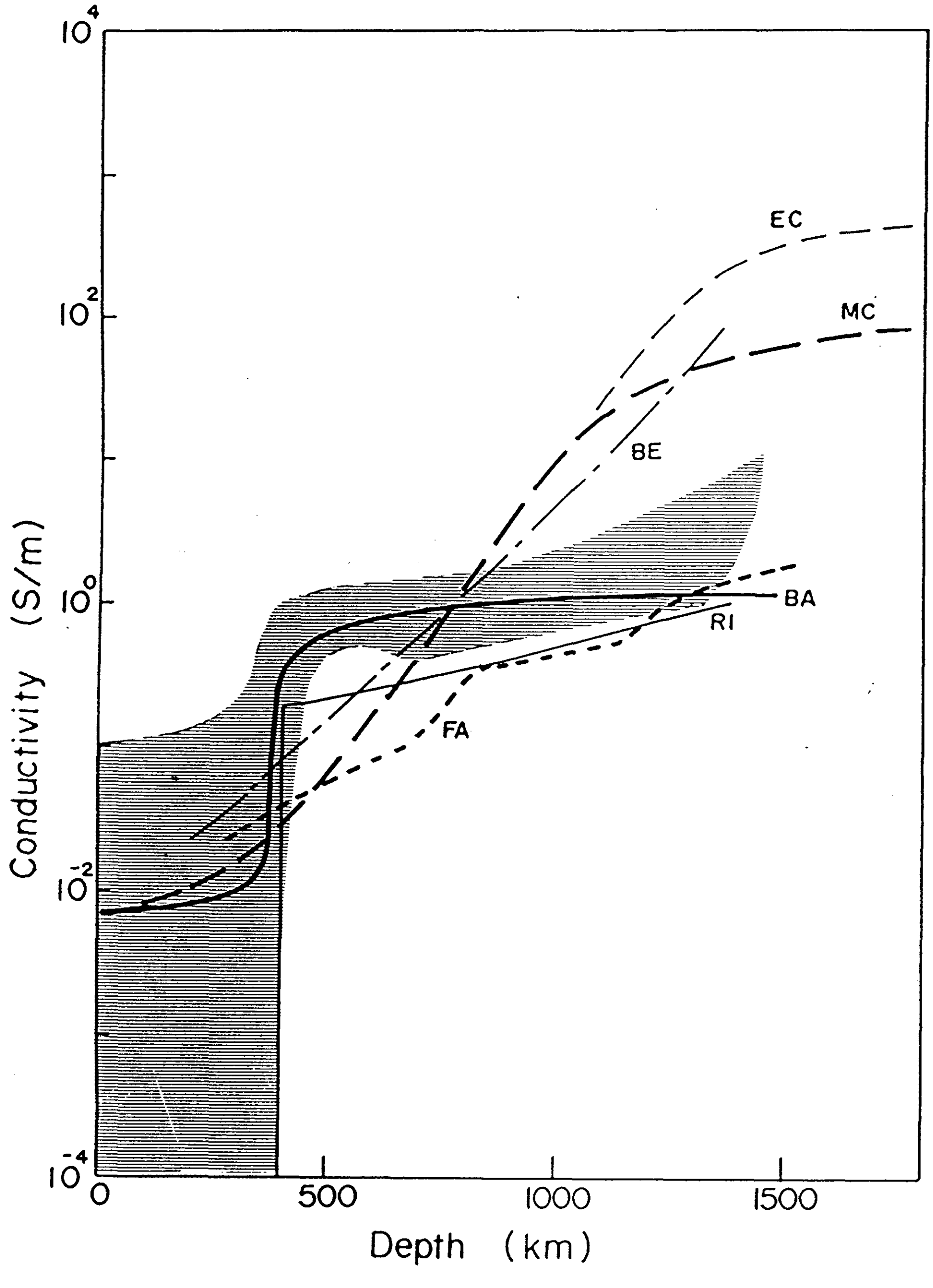

Fig.1.1 Global models of the mantle conductivity distribution.
EC: Eckhardt (1968)
MC: McDonald (1957)
BE: Berdichevsky et al.(1974)
FA: Fainberg and Rotanova (1974)
RI: Rikitake (1966)
BA: Banks (1969)
Shaded area denotes the acceptable range by Banks (1969).

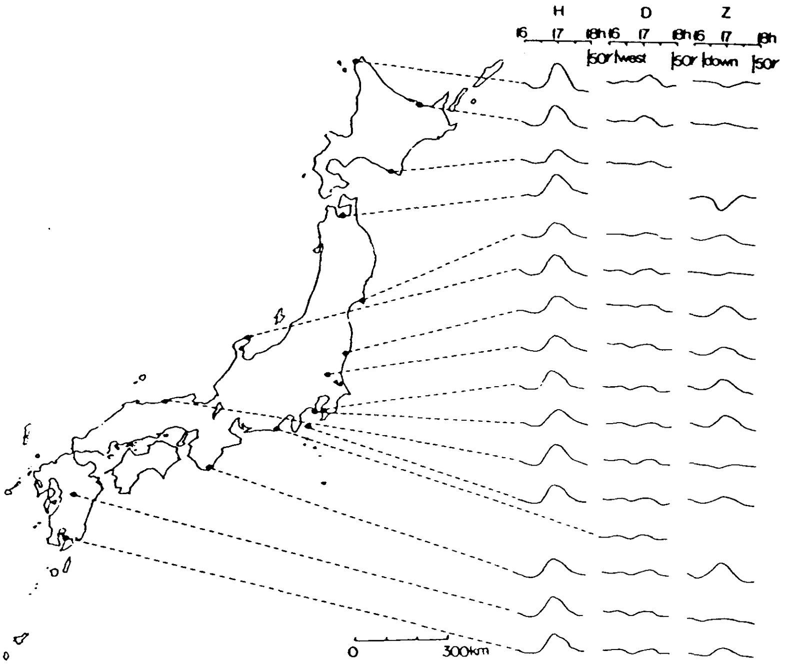

Fig.1.2 An example of simultaneous record of geomagnetic bay observed in Japan (after Rikitake, 1967).

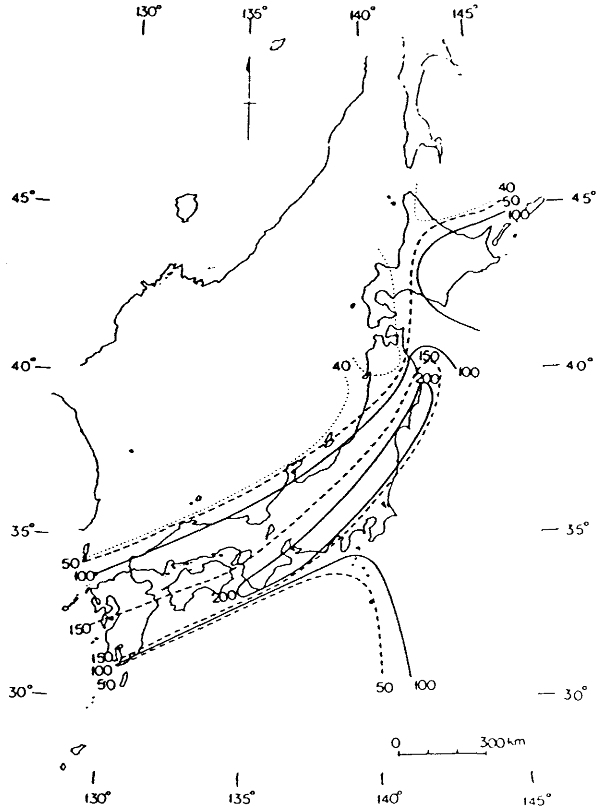

Fig.1.3 A model of conductivity structure beneath Japan proposed by Rikitake (1969). Contours indicate the depth to the top of highly conductive layer in kilometers.

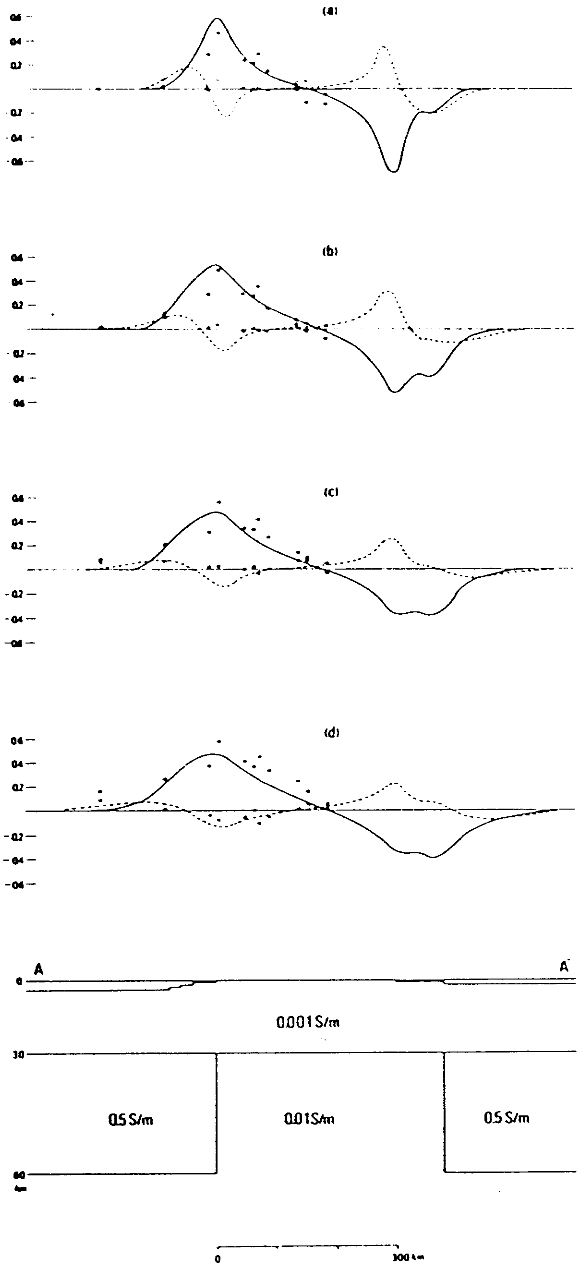

Fig.1.4 a model of conductivity structure beneath the central part of Japan proposed by Honkura (1974).

2. Electrical Conductivity of the Earth's Material

The electrical conductivity, σ, of silicate minerals is strongly dependent on temperature. When water exists in the pore space, the bulk conductivity is affected strongly by the water content. Melts and other fluids also affects the electrical conductivity. In the investigation of the conductivity distribution within the earth, highly conductive structure has often been found to correlate with geothermal environment, groundwater distribution, and so forth. Therefore, for the interpretation of the electrical conductivity structure in the earth, it is of great importance to review results of laboratory experiments on the electrical of conductivity of rocks and minerals, which consist of the earth's crust and mantle, in various physical states.

2.1 Temperature and pressure dependence of the electrical conductivity

Most of the rock forming minerals can be classified into either semiconductor or dielectrics. As a function of absolute temperature, T, the conductivity, σ, can be expressed as

$$\sigma = \sum_{i} \sigma_i \cdot \exp[-E_i/kT] \qquad (2\text{-}1\text{-}1)$$

where σ_i and E_i are the constant and the activation energy which depend on the i-th conduction mechanism, composition, grain size, etc., and k is the Boltzmann constant. The relative importance of the conduction mechanism also depends on temperature. At present, three kinds of electric conduction are considered in the earth according to the charge carriers, i.e. impurity, intrinsic electron and ion, respectively. For relatively low temperature as in the earth's crust, impurity conduction is dominant. At higher temperatures, the other two are supposed to be the dominant mechanisms, although it is not well-known which is actually dominant in the mantle (Duba, 1976).

Kariya and Shankland (1983) compiled the laboratory data of the electrical conductivity of dry rocks which are regarded as possible components of the lower crust. They investigated the compositional effect on the temperature dependence of the electrical conductivity by a statistical method, where they classified crustal rocks into three groups: granite, gabbro and basalt groups. They concluded that the conductivity increases from silicic to mafic composition; i.e. basaltic rocks are more conductive than granitic rocks by one or two orders of magnitude at the same temperature and pressure.

In the acidic rocks, the electrical conductivity varies depending on the quartz content (Parkhomenko, 1982); i.e. the conductivity increases from granites to diorites for the temperature range of 100-1200°C. Moreover, large variations in conductivity due to mineral composition have often been observed below 600°C, or so, while it is much less dominant at higher temperatures.

Fig.2.1 show the temperature dependence of the electrical conductivity for various kinds of rocks and minerals derived from laboratory experiments. Though the conductivity varies by many orders of magnitude with temperature and composition, it is obvious that the relation of Eq.(2-1-1) holds throughout the temperature range.

The change in conductivity of rocks with pressure can be attributed to the change in the effective mass, or to the change in the mobility of current carriers. For example, as interatomic distances decrease with increasing pressure, the amplitude of thermal oscillations of atoms will decrease. As a result, the thermal scattering of charge carriers decreases, and the mobility increases.

In general, semiconductive materials show a relatively large increase in conductivity with the increase of pressure. On the other hand, when there is a strongly metallic character in composition such as the sulfides of iron and nickel, which could be possible components of the earth, the absolute values of the conductivity become high, while the pressure dependence largely decreases (Parkhomenko, 1982). Although the pressure dependence of the conductivity of basic rocks such as gabbro and basalt is particularly higher than that of other rocks in the temperature range of 100 - 650°C, the conductivity increases only by several factors of magnitude with an increase in hydrostatic pressure up to 20 kbar. Therefore, in the investigation of the conductivity structure in the crust and the upper mantle, the pressure effect is less significant than the temperature effect on determination of the conductivity of rocks so long as dry state is concerned. In the presence of water, however, sometimes pressure effect becomes dominant as will be shown in a later section.

Since the electrical conductivity of rocks depends strongly on the temperature, high temperature is often considered as a cause of the high conductivity in the upper mantle. However, reliable experiments for olivine show that the temperature higher than 1500°C is required for high conductivity of 0.1 S/m (Fig. 2.1). At such a high temperature, partial melting of rocks will occur in the upper mantle

(Kushiro et al., 1968). Liquid phase of partially molten mantle material is considered to be basaltic. Therefore, we have to consider the bulk conductivity of mantle material with the inclusion of basalt melt.

Many laboratory experiments indicate that the conductivity of basalt melt is much higher than that of solid olivine, which is considered to be a major constituent in the upper mantle, at the same temperature (Watanabe, 1970; Presnall, et al, 1972; Rai and Manghnani, 1978). Therefore, partial melting can yield a high conductivity at relatively low temperatures. However, existence of molten magma does not necessarily mean high conductivity; the degree of interconnection of liquid phase is significant for the bulk conductivity (Waff, 1974). If the liquid phase is interconnected with each other through narrow passages (case(1)), the bulk conductivity , σ_1, can be expressed as

$$\sigma_1 = \sigma_m[3\sigma_s+2f(\sigma_m-\sigma_s)]/[3\sigma_m-f(\sigma_m-\sigma_s)] \qquad (2\text{-}1\text{-}2),$$

whereas in case (2) where magma exists in isolated pockets,

$$\sigma_2 = \sigma_s[\sigma_m+2\sigma_s+2f(\sigma_m-\sigma_s)]/[\sigma_m+2\sigma_s-f(\sigma_m-\sigma_s)] \qquad (2\text{-}1\text{-}3),$$

where σ_m and σ_s denote the conductivity of melt and solid phases, respectively, and f is the melt fraction (Waff, 1974). For an extreme case of $(\sigma_s/\sigma_m)<<f<<1$, bulk conductivity for cases (1) and (2) can be expressed as follows:

$$\sigma_1 = 2f\sigma_m/3 \qquad (2\text{-}1\text{-}4)$$

$$\sigma_2 = \sigma_s \qquad (2\text{-}1\text{-}5)$$

Eq.(2-1-5) indicates that the isolated partial melt barely increases the bulk conductivity. On the other hand, Eq.(2-1-4) tells us that the existence of the interconnected liquid phase increases bulk conductivity proportionally to the melt conductivity and the melt fraction.

Fig.2.2 summarizes the conductivity structure beneath major ocean revealed by the electromagnetic sounding in various regions. Each result can be characterized by the existence of a highly conductive layer below a resistive layer. However, Fig.2.2 shows that the thickness of the upper resistive layer varies from place to place. We compare the result of the magnetotelluric sounding conducted in the region close to the East Pacific Rise (Filloux, 1981) with one in the Northwest Pacific in the vicinity of the Japan Trench (Yukutake, et al., 1984). The conductive layer appears at the depth of about 20 km for the former result, while the resistive layer is as thick as about 150 km for the latter.

It is well-known that the partial melting reduces the seismic velocity. The low velocity zone is usually considered to the asthenosphere. Oldenburg (1981) made a one-dimensional inversion of seafloor magnetotelluric data from various regions of different plate age, and concluded that the highly conductive layer coincides well with the low velocity layer at the various regions. As Filloux (1980) suggested, therefore, the concept that the conductive layer indicates the asthenosphere seems reasonable.

Although the conductive layer roughly coincides with the low velocity layer, it has been pointed out (e.g. Rikitake and Honkura, 1985) that there are systematic differences between the depths to their top; i.e. the depth to the highly conductive layer is usually deeper than that to the low velocity layer. This fact also supports the proposition that the conductive layer corresponds to the asthenosphere on account of following reason. At least several percent of partial melting is required to increase the conductivity to the order of 10^{-1} S/m at about 1200°C, while seismic velocity reduces sufficiently with only a few percent of melt fraction (Shankland et al., 1981). The depth dependence of the degree of partial melting is a possible explanation for the above mentioned difference in the depth. At the shallower depth in the asthenosphere, the melt fraction would be so small that the electrical conductivity remain almost unchanged but the seismic velocity is significantly reduced. With increasing depth, partial melting will proceed to increase the interconnectivity of melt phase and to yield high conductivity.

In the present study, the electrical conductivity distribution will be investigated beneath the three oceanic regions around Japan: i.e. the Pacific Ocean, the Philippine Sea and the Japan Sea. Above discussions will be of great importance in the interpretation of the result.

2.2 Effect of water on the electrical conductivity

For shallower part of the earth's crust, electric conduction is electrolytic; i.e., the conducting medium is water distributed in the pore structure of the crustal rock. The electrical conductivity of water bearing rocks depends on the water content, the salinity of the water and the geometry of the pore structure.

The conduction of an electrolyte is determined by the mobility of the ion. In this case the mobility depends on both temperature and concentration. Increasing temperature of an electrolyte decreases the viscosity, resulting in a higher terminal velocity of an ion (higher mobility). If a solution contains high concentration of ions, the motion of each ion will be influenced by other ions close to it, which is to reduce the mobility (e.g. Keller and Frishknecht, 1966).

When an electric field is applied to an electrolytic solution, the amount of electric current can be calculated by multiplying the number of ions (concentration) by the velocity with which they move. The current flowing in the electrolyte per unit electric field intensity can be written as:

$$I = A \cdot F \cdot (c_1 v_1 + c_2 v_2 + \cdots + c_k v_k \cdots) \qquad (2\text{-}2\text{-}1)$$

where c_k and v_k represent the concentration and the mobility for each identical ion in the solution, and A and F denote the cross-sectional area through which current flows and Faraday's number, respectively. The conductivity of the solution can be determined by considering the current flow through a unit cross-sectional area at a unit electric field intensity as:

$$\sigma = F\cdot(c_1v_1 + c_2v_2 + \cdots + c_Kv_K\cdots) \tag{2-2-2}$$

Curves in Fig.2.3 show the relationship between the resistivity and the salinity of sodium chloride at various temperatures ranging from 0 to 140°C. Increasing the temperature decreases resistivity (increases conductivity), as has been previously explained. High concentration of ion decreases the mobility and thus has an effect of increasing the resistivity to some extent. However, high concentration means that the density of charge carrier increases at the same time. As a result, the resistivity of the solution decreases as increasing the salinity. However, the rate of decrease is reduced for higher concentration. The bulk conductivity of a water-saturated rock should behave in the same way.

When a rock is partially saturated with water, the bulk conductivity increases with the increase of the water content. In partial saturation, we have to consider the effect of desaturation on bulk conductivity. The texture of rock also has some contribution to the conductivity, as has been the case of the partial melting in the previous section.

Porosity of rocks can be classified into three general groups on the basis of their geometry. As for consolidated sedimentary rocks and volcanic ash bed, porosity is called as intergranular, which consists of the rock grains and the space left after the grains were compacted. In the second group, porosity is primarily formed as joints, which can be seen in most igneous rocks. The third group of porosity, common in limestones and in some volcanic rocks, is called as vugular, consisting of large, irregular cavities.

Pore spaces should be connected and filled with water in order to yield a high electrical conduction through the bulk rock. In all three types of porosity, pore volume consists of two parts; large cavities and narrow passages which are called the storage pores and the connecting pores. Most of the resistance to the electric current flow is caused by the connecting pores, because they have much smaller cross-sectional areas. Therefore, a rock with the higher ratio of connecting pores to storage pores will have the higher conductivity for the same porosity.

In general, the pore geometry is quite irregular so that the relationship between the conductivity and the pore volume should be determined empirically. A large number of of experiments have been done in correlating the conductivity and the water content. The result has led to the well-known Archie's law expressing the relation as:

$$\sigma = a\sigma_w\phi^m \qquad (2\text{-}2\text{-}3)$$

where σ and σ_w denote the bulk conductivity and the conductivity of pore water, respectively, ϕ is the porosity expressed as a fraction per unit volume, and a and m are the parameters which should be determined empirically.

The value for the parameter a varies from slightly less than 1 for rocks with intergranular porosity to slightly more than 1 for rocks with joint porosity. Meanwhile, the exponent m is known to take values around 2; which is a little larger than 2 for well-sorted granular rocks, and somewhat less than 2 for poorly sorted granular rocks.

Fig.2.4 shows the conductivity models in various continental areas, which were obtained by different investigators using a variety of techniques and represent results of both one-dimensional and two-dimensional modeling. In general, the electrical conductivity structure beneath a continental region can be divided into at least three parts: (1) a surface layer of high conductivity possibly associated with sediments and groundwater, (2) a low conductivity layer associated with crystalline basement, and (3) a deeper high conductivity layer. The deep conductive layer is often associated with the upper mantle or the lower crust beneath a tectonically active region and can be explained by partial melting. On the other hand, a highly conductive layer is sometimes found at relatively shallower depth even beneath the stable continental shield area. Some examples of conductive material used to explain crustal high conductivity include water (Hyndman and Hyndman, 1968; Dvorak, 1975; Olhoeft, 1981), hydrated minerals such as clays (Drury and Hyndman, 1979) and serpentine (Stesky and Brace, 1973), Magnetic oxides (Stesky and Brace, 1973), graphite (Alabi et al., 1975) and sulfur (Olhoeft, 1981).

Among these possible mechanisms to enhance electrical conduction of crustal rocks shown above, the presence of water are most frequently proposed. At shallower depth, the strong influence of water on the electrical conductivity of rocks has been shown previously. However, at the temperature and the pressure of lower crustal depth, water is considered to be in a super-critical state. Quist and Marshall (1968) showed that ionic fluids become insulating with increasing temperature at high pressure. This result may be negative to the proposal to ascribe the cause of high conductivity in the lower crust to the presence of water.

Olhoeft (1981a,b) showed that the presence of water effectively increases the conductivity of granite and basalt (Fig.2.5(a)). Some hydrated and magnetic oxide bearing rocks, especially serpentinites, do have appropriately high conductivity (Drury and Hyndman, 1979). However, Stesky and Brace (1973) noted that not all serpentinites have high conductivities but they resulted from the presence of free water. The above results indicate the difference in the effects on conductivity between the free and structural waters. Olhoeft (1981) measured a hornblende schist in vacuum and obtained essentially the same conductivity as that of dry granite (Fig.2.5(b)) so long as the hornblende was kept below the temperature where structural water was released or else the released water was removed by the vacuum pump.

Thus, the presence of a water-rich fluid seems one of the most probable explanation for the high conductivity in lower crust. But we have to consider the problem whether and how water exists in the lower crust.

Norton and Taylor (1979) inferred water penetrations to 6-10 km from oxygen isotope depletions. Gregory and Taylor (1981) also suggested that convective fluid flow in fractures can penetrates the oceanic crust into the mantle. These results support an open crust to movement of pore fluid; the water in the lower crust are essentially of meteoric origin.

On the viewpoint of the connection to the surface being poor, Fyfe et al.(1978) argued for the persistent fluids having water pressure almost equal to the lithostatic pressure, particularly in the metamorphic regions. This condition implies that the porosity would be kept open by the relatively high pore pressure under the lower crustal condition. In the island arc, this situation would be a conceivable one because of the possible dehydration of an underlying subducted slab (Takahashi, 1978; Tatsumi et al. 1983).

In order to explain the electrical conductivities, it is not necessary to insist either on an open fluid circulation or on trapped water model in the lower crust. What should be emphasized here is that the presence of free water is one of the most promising cause for a highly conductive layer at lower crustal depth.

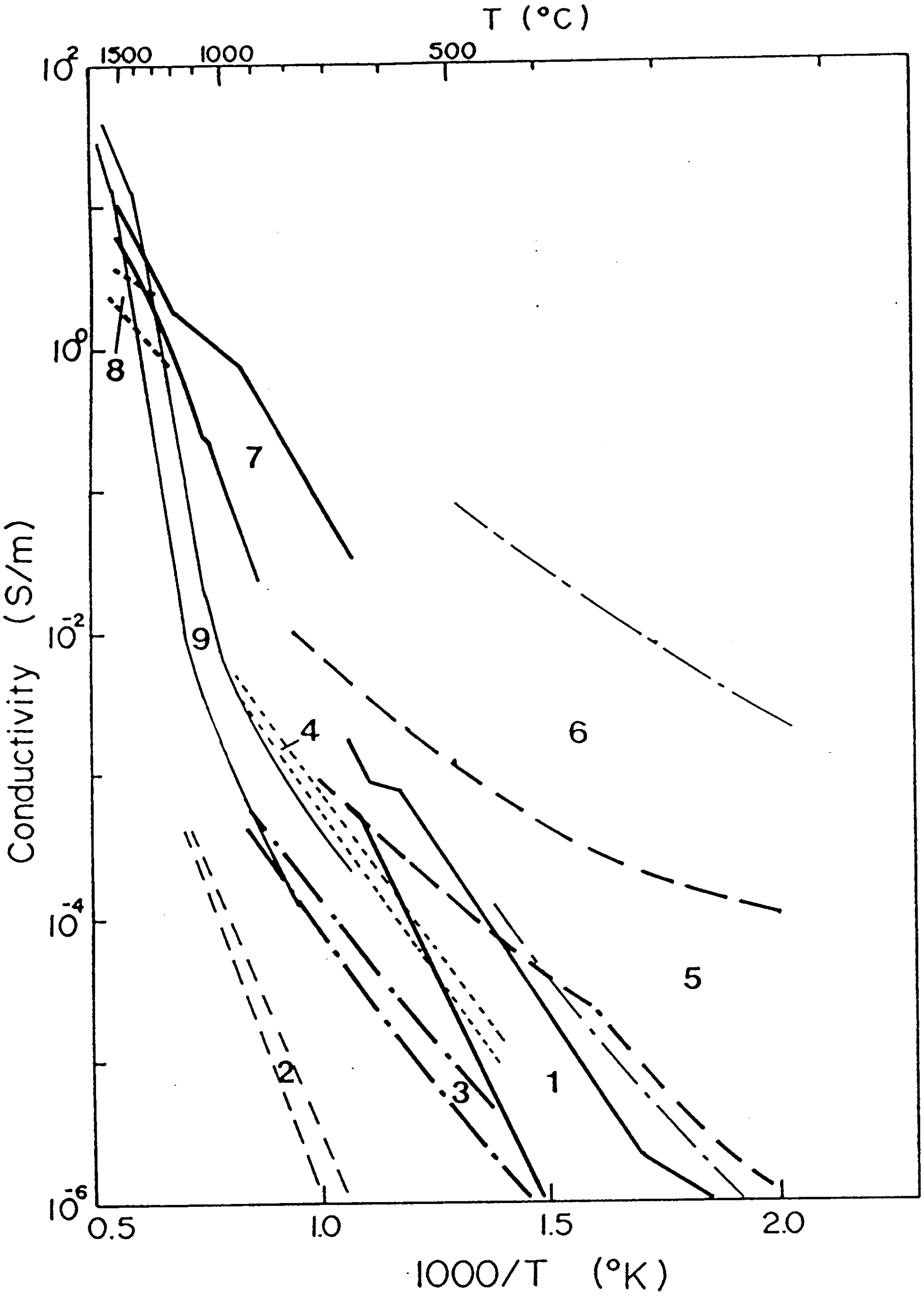

Fig.2.1 Temperature dependences of various rocks and minerals. 1) peridotite and olivinite (Dovorak, 1973); 2) pyroxine (Duba, et al, 1973); 3) Garnet (Kariya and Shankland, 1983); 4) granite (Olhoeft, 1981); 5) Indian basalt (Gupta and Sharma, 1978); 6) oceanic basalt (Drury and Hyndman, 1979); 7) olivine basalt (Watanabe, 1970); 8) andesite (Tyburczy and Waff, 1983); 9) Ultramafic rocks (Rai and Manghnani, 1978).

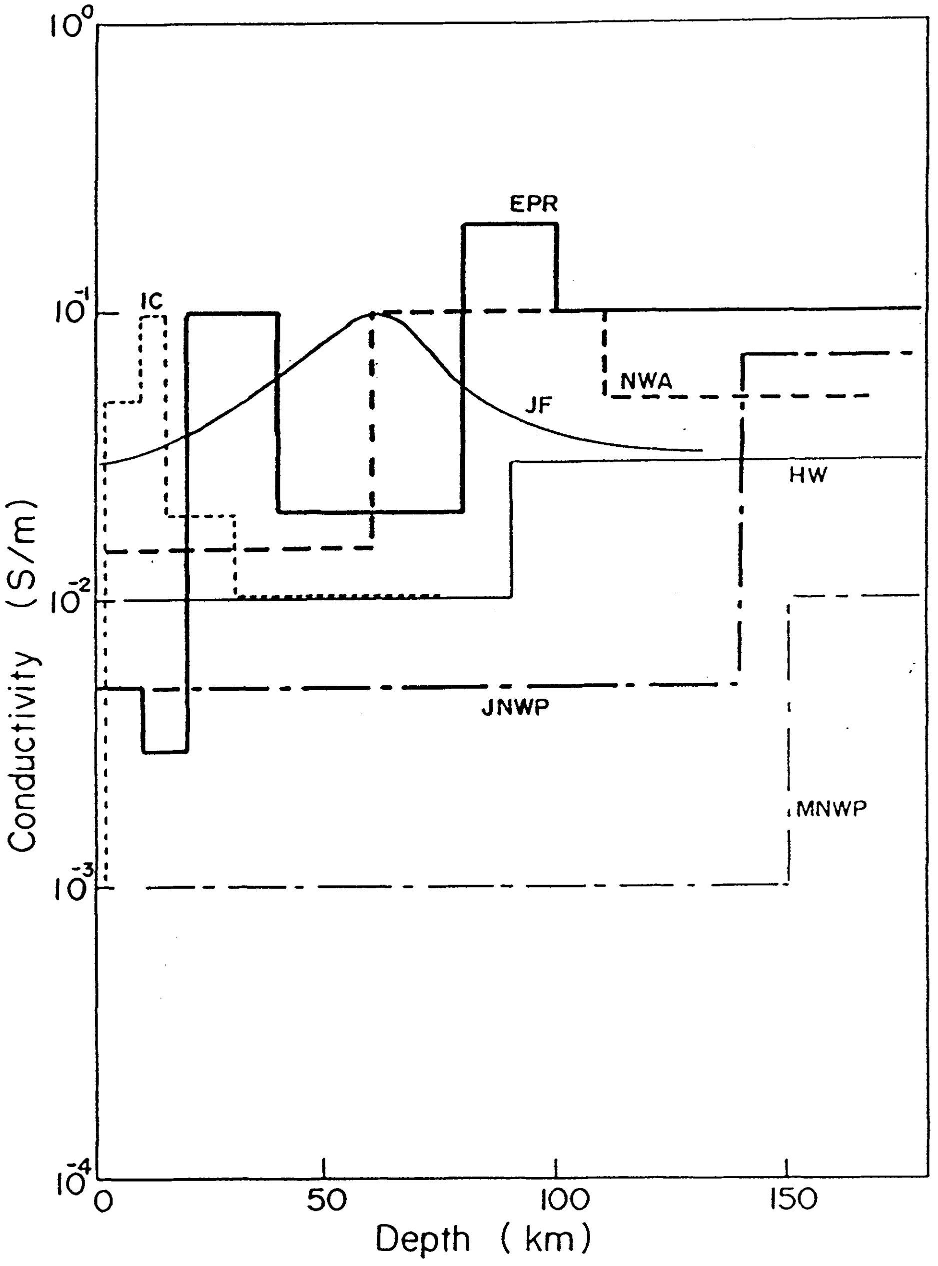

Fig.2.2 Conductivity structures beneath oceanic regions. See Table 2.1 for references.

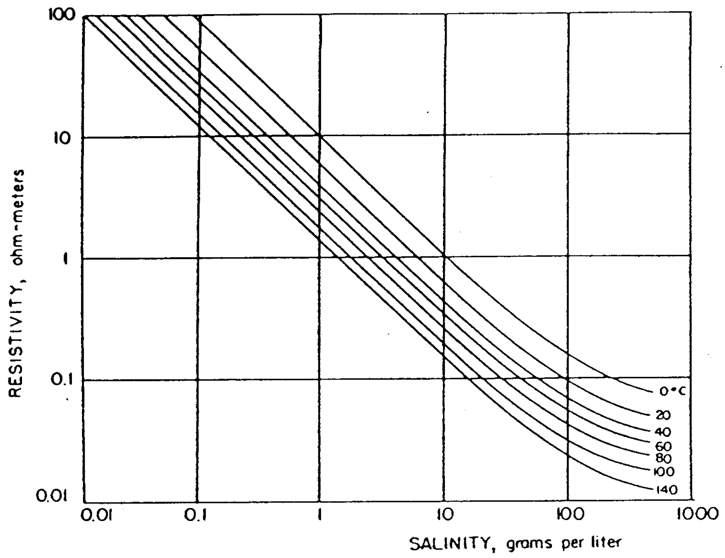

Fig.2.3 Relation between the resistivity of solution of sodium chloride and the salinity for various temperatures (After Keller and Frischknecht, 1966).

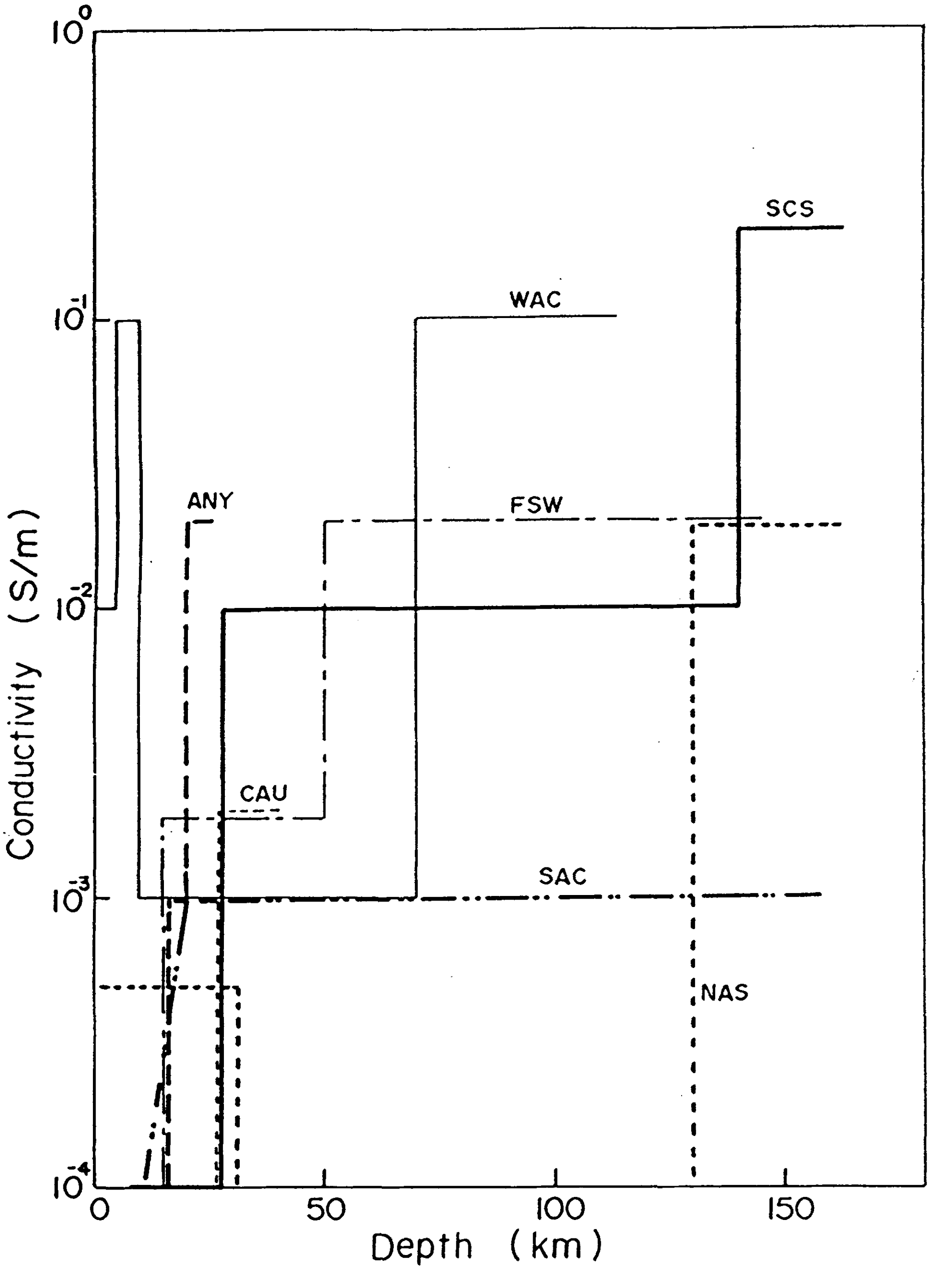

Fig.2.4 Conductivity structures beneath continental areas. See Table 2.2 for references.

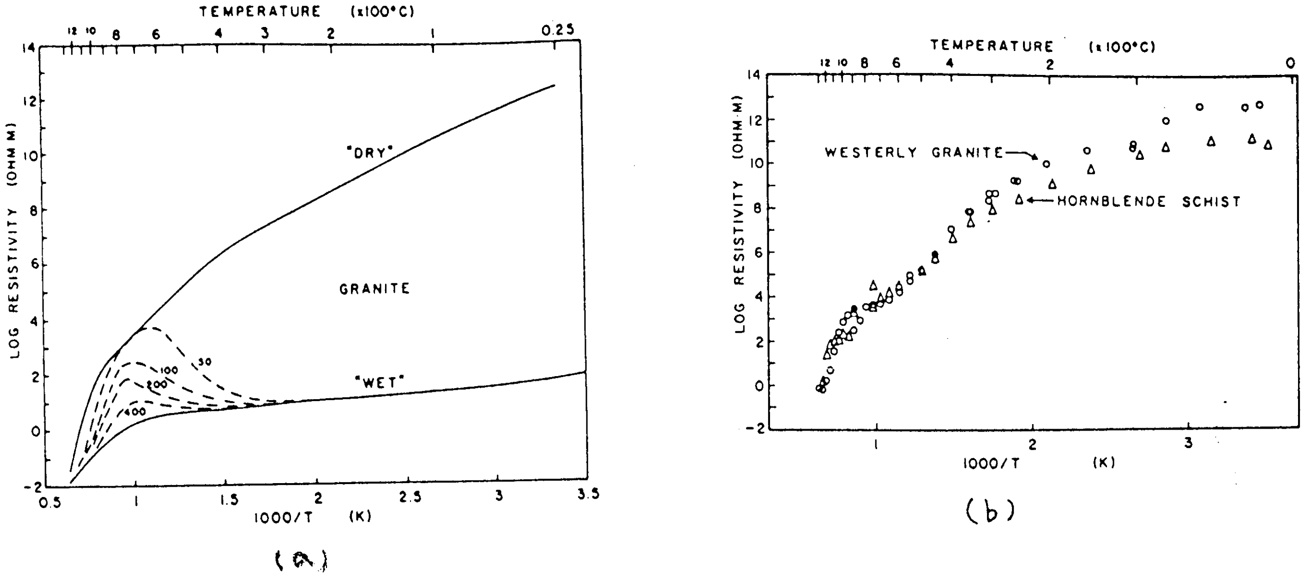

Fig.2.5 Temperature dependences of electrical resistivity for dry and wet granite (a), and for granite and hornblende schist in dry state (b) (after Olhoeft, 1981).

Table 2.1 Summary of the electromagnetic investigations in the oceanic areas in Fig.2.2.

Abb.	Locality	Method*	Reference
EPR	East Pacific Rise	MT	Filloux (1981)
JF	Juan de Fuca Ridge	GDS	Law and Greenhouse (1981)
HW	Hawaii	IE	Klein and Larsen (1980)
JNWP	Japan Trench, NW Pacific	MT	Yukutake, et al.(1983)
MNWP	Mariana Trough, NW Pacific	MT	Filloux (1981)
NEIC	Northeast Iceland	MT	Belbo and Bjorunsson (1980)
NWA	Northwest Atlantic	GDS	Poehls and von Herzen (1976)

*) MT: Magnetotellrics, GDS: Geomagnetic depth sounding, IE: Island effect.

Table 2.2 Summary of the electromagnetic investigations in continental areas given in Fig.2.4.

Abb.	Locality	Method*	Reference
WAC	West African Craton, Mali	MT	Ritz (1984)
NAS	Central African Shield, Niger	MT	Ritz (1983)
SAC	South African Craton	DC	Van Zjil, et al.(1975)
ANY	Adironduck, New York	CSEM	Nekut, et al.(1977)
SCS	Scandinavian Shield, Norway	HSG	Jones (1980)
FSW	Fennoscandia, Sweden	MT	Jones (1982)
CAU	Central Australian Shield	DC	Constable, et al.(1984)

*) MT: Magnetotellrics, DC: Direct current sounding, CSEM: Control source electromagnetic sounding, HSG: Horizontal spatial gradient method.

3. Theory of Interpretation

The ultimate aim of the present investigation is to obtain the two-dimensional structures of the earth from electromagnetic observations. The method consists of the following steps.

(1) Calculate one dimensional conductivity models by the magnetotelluric analysis for the available sites.

(2) By interpolating the obtained structure, construct a starting model for the further two-dimensional analysis.

(3) Evaluate theoretical responses from the starting model by using a FEM method.

(4) By calculating partial derivatives of the response functions for the model, refine the model iteratively.

For the investigation, one dimensional inversion of magnetotelluric data, calculation of two-dimensional inductive responses, and the direct inversion method for two-dimensional conductivity distribution are employed. These techniques are newly developed in the present study. Following, the fundamental theory of each step and the development made in the present investigation are explained in detail. The coordinate system used in this study is given in Fig.3.1.

3.1 Maxwell's equation and the induction equation

The basic equations in electromagnetic induction study of the Earth are Maxwell's equations which can be expressed as follows:

$$\nabla \times E = \partial B/\partial t \qquad (3\text{-}1\text{-}1)$$

$$\nabla \times H = J + \partial D/\partial t \qquad (3\text{-}1\text{-}2)$$

$$\nabla \cdot D = 0 \qquad (3\text{-}1\text{-}3)$$

$$\nabla \cdot B = 0 \qquad (3\text{-}1\text{-}4)$$

The magnetic induction B, the electric displacement D and the electric current J in the above equations can be obtained from the magnetic field H and electric field E:

$$B = \mu H \qquad (3\text{-}1\text{-}5)$$

$$D = \varepsilon E \qquad (3\text{-}1\text{-}6)$$

$$J = \sigma E \qquad (3\text{-}1\text{-}7)$$

where μ , ε and σ are the magnetic permeability, the dielectric constant and the electrical conductivity, respectively. Throughout the present study, μ and ε are assumed to be constant everywhere with values equal to those of the vacuum. We assume that the time variation of the electromagnetic fields are sinusoidal with an angular frequency ω . Then, time derivative, $\partial/\partial t$ in Maxwell's equations can be replaced with $-i\omega$. For the frequency range we concern, the displacement current can be neglected; i.e. $i\omega D = 0$. Eliminating B, D and J with the aid of Eqs. (3-1-5), (3-1-6) and (3-1-7), we can reduce Maxwell's equation (3-1-1)-(3-1-4) to

$$\nabla \times E = i\omega \mu H \qquad (3\text{-}1\text{-}1)'$$

$$\nabla \times H = \sigma E \qquad (3\text{-}1\text{-}2)'$$

$$\nabla \cdot H = 0 \qquad (3\text{-}1\text{-}3)'$$

$$\nabla \cdot E = 0 \qquad (3\text{-}1\text{-}4)'$$

Taking curl of Eqs. (3-1-1)' and (3-1-2)' we have,

$$\nabla \times \nabla \times E = i\omega \mu \nabla \times H \qquad (3\text{-}1\text{-}8)$$

$$\nabla \times [(1/\sigma)\nabla \times H] = \nabla \times E \qquad (3\text{-}1\text{-}9)$$

Substitution of Eq.(3-1-2)' into Eq.(3-1-1)' leads us to the following equations:

$$\nabla \times \nabla \times E = i\omega \mu \sigma E \qquad (3\text{-}1\text{-}8)'$$

$$\nabla \times [(1/\sigma)\nabla \times H] = i\omega \mu H \qquad (3\text{-}1\text{-}9)'.$$

Thus, the variables E and H can be separated with each other. These two independent equations are the basic equations for the electromagnetic induction studies and are called the induction equations. If either quantity E or H is obtained by solving the one of the induction equations, the other field variation can be derived by taking curl operation on the former as evident from eqs. (3-1-1) and (3-1-2).

3.2 Evaluation of one-dimensional magnetotelluric impedance

One-dimensional analysis is the most conventional and well-known technique in the magnetotelluric sounding method. Its basic concept was first founded by Cagniard (1953). In the one-dimensional modeling, we assume that the conductivity, σ , is horizontally uniform, and the electromagnetic wave is a plane wave traveling in Z direction whose electric field vector has only X-component E_x. Then the vector equation (3-1-8)' can be expressed by a scalar field component E_x as follows:

$$\partial^2 Ex/\partial z^2 = i\omega\mu\sigma \ Ex \qquad (3\text{-}2\text{-}1).$$

A typical solution of Eq.(3-2-1) has a form:

$$E_x = A \exp[\pm \gamma z] \qquad (3\text{-}2\text{-}2),$$

where A is an arbitrary constant and γ denotes the wave number, which can be written explicitly by using μ and σ , and the frequency, ω , as

$$\gamma = [\ i\omega\mu\sigma\ ]^{1/2} \qquad (3\text{-}2\text{-}3).$$

In general, the wave number consists of a real and a imaginary part and is expressed here as follows:

$$\gamma = (\ 1 + i\ )/\ \delta \qquad (3\text{-}2\text{-}4),$$

where

$$\delta = [\ \omega \mu \sigma / 2\ ]^{-1/2} \qquad (3\text{-}2\text{-}5).$$

This indicates that, when the electromagnetic wave is traveling in a conductive medium, the amplitude decays along the travel path. The amplitude of the wave is attenuated by a factor of 1/e in a travel distance δ , which is usually called the skin depth. The skin depth is an important and useful parameter in the electromagnetic sounding methods because it gives a guess of the field penetration depth into the earth, or the sounding depth. Eq.(3-2-5) shows that the skin depth is a function of frequency and conductivity. Fig.3.2 gives the relation of the skin depth to frequency and conductivity.

Since the positive and the negative value of γ can be a solution of Eq.(3-2-1), a general solution is expressed as

$$E_x = A \exp[+\gamma z] + B \exp[-\gamma z] \qquad (3\text{-}2\text{-}6)$$

The first and the second terms of the right-hand side of Eq.(3-2-6) corresponds to the upward and downward traveling waves, respectively. Here, we must evaluate the unknown constants A and B from the boundary conditions.

By using the relation between the electric and the magnetic fields in Eq.(3-1-1)', we have in this case:

$$\frac{\partial Ex}{\partial z} = -i\omega \mu\ Hy \qquad (3\text{-}2\text{-}7)$$

Using the expression for the electric field in Eq.(3-2-6), the magnetic field can be written as:

$$H_y = -\gamma\ (A \exp[\gamma z] - B \exp[-\gamma z])/i\omega\mu \qquad (3\text{-}2\text{-}8)$$

By combining Eq.(3-2-6) and (3-2-8), we can determine the ratio of electric to magnetic field strength of electromagnetic wave travailing in a medium: i.e. the impedance of the medium as follows:

$$Z = E_x / H_y = \frac{-i\omega\mu\ (A \exp[\gamma z] + B \exp[-\gamma z])}{\gamma\ (A \exp[\gamma z] - B \exp[-\gamma z])} \qquad (3\text{-}2\text{-}9)$$

When the medium is a homogeneous half space, there exists no upward traveling wave. Hence, the impedance at any depth can be simply written as:

$$Z = i\omega\mu / \gamma = (i\omega\mu / \sigma)^{1/2} \qquad (3\text{-}2\text{-}10)$$

From this equation, we can obtain a simple expression for the apparent resistivity for the magnetotelluric method (Cagniard, 1953):

$$\rho_a = | Z |^2 / \omega\mu \qquad (3\text{-}2\text{-}11)$$

Eq.(3-2-10) tells us that the phase difference between the electric and the magnetic field will be 45 degrees when the earth is homogeneous.

For a horizontally stratified earth model shown in Fig.3.3, both the upward and the downward traveling waves should be taken into account for each layer. Using hyperbolic cotangent, Eq.(3-2-9) can be rewritten as

$$Z = -\frac{i\omega\mu}{\gamma}\coth[\gamma z + \ln(C)] \qquad (3\text{-}2\text{-}12),$$

where,

$$C = (A/B)^{1/2} \qquad (3\text{-}2\text{-}13).$$

The constant C can be determined from boundary conditions. Eq.(3-2-12) can be expressed as

$$\ln(C) = \coth^{-1}[-\gamma Z(z_1)/i\omega\mu] - \gamma z_1 \qquad (3\text{-}2\text{-}14).$$

for $z=z_1$. Then the impedance at another depth z in the same layer can be evaluated from

$$Z(z) = i\omega\mu/\gamma \; [\gamma(z_1-z) + \coth^{-1}[\frac{\gamma Z(z_1)}{i\omega\mu}]] \qquad (3\text{-}2\text{-}15).$$

Therefore, the impedance at the surface, Z(0), can be expressed with the one at the interface between the top and the second layer, $Z(z_1)$, by using Eq.(3-2-15):

$$Z(0) = i\omega\mu/\gamma_1 \coth[\gamma_1 h_1 + \coth^{-1}[\frac{\gamma_1 Z(z_1)}{i\omega\mu}]] \qquad (3\text{-}2\text{-}16),$$

where h_1 is the thickness of the top layer. In the same manner, the impedance at the top of the k'th layer is written by

$$Z(z_{k-1}) = i\omega\mu/\gamma_k \coth[\gamma_k h_k + \coth^{-1}[\frac{\gamma_k Z(z_k)}{i\omega\mu}]] \qquad (3\text{-}2\text{-}17),$$

where h_k is the thickness of the k'th layer, $z_k - z_{k-1}$. At the top of the n'th layer which extends to infinite depth, $zn = \infty$, the impedance becomes simply:

$$Z(z_{n-1}) = \frac{i\omega\mu}{\gamma_n} = (\frac{i\omega\mu}{\sigma_n})^{1/2} \qquad (3\text{-}2\text{-}18).$$

Eqs. (3-2-16), (3-2-17) and (3-2-18) give the regression formulae to obtain the surface impedance for a multi-layered model.

Fig.3.4 shows theoretical sounding curves (apparent resistivity and phase at the surface vs. frequency) for a simple two-layer model. Frequency is normalized by the characteristic value which gives a skin depth equal to the thickness of the first layer. Here following features should be noted:

1) If the frequency is higher than the characteristic value, the apparent resistivity approximately gives the resistivity of the first layer.

2) At sufficiently low frequencies, on the other hand, the apparent resistivity gives the true resistivity of the second layer.

3) When the substratum is more conductive than the top layer, the phase is greater than 45°, otherwise it is less than 45°.

These features can be used for the first rough interpretation of the actual data.

3.3 One-dimensional inversion of magnetotelluric data

One dimensional inversion is now a popular technique for the interpretation of the magnetotelluric data. For the inversion, two different approaches have been taken. One is the layered earth model (e.g. Jones and Hutton, 1981), where the regression formula given in the previous section are utilized. In the other approach, continuous variation of the electrical conductivity with depth (Oldenburg, 1983) is assumed, in which numerical integration of the induction equation is required. In both methods, the observed impedances at various frequencies are utilized to determine the conductivity distribution as a function of depth. In the present study we apply a layered model approach, since the layered model is more appropriate as a starting model for the later two-dimensional numerical modeling. In this case, the conductivity and the thickness of each layer are the unknown parameters to be determined.

The present method includes two steps. First, an optimum model is determined by a modified Monte-Carlo method. Then, the confidence limit of the optimum parameter is derived from the variation of χ^2 against various values of the parameter. The scheme is explained in the following.

For the actual modeling, we assume complex impedances at m different frequencies have been obtained from the observation. Then, the conductivity and the thickness of each layer, are searched for so as to minimize

$$\chi^2 = \frac{1}{W} \sum_{i=1}^{m} \frac{1}{e(f_i)^2} \{\log[\, Z_{ob}(f_i)] - \log[\, Z_c(f_i)\}^2 \quad (3\text{-}3\text{-}1),$$

where $Z_c(f_i)$ and $Z_{ob}(f_i)$ are the calculated impedance and the observed impedance at the frequency of f_i, respectively. W is calculated from

$$W = \sum_{i=1}^{m} \frac{1}{e(f_i)^2} \qquad (3\text{-}3\text{-}2)$$

where $e(f_i)$ is the observation error. The weight is determined so that Data with a smaller error has a larger contribution in determination of the layer parameters. Since the impedance is a complex quantity with real and imaginary parts, χ^2 of Eq.(3-3-1) has a degree of freedom of 2m. (This is not always valid, for all the impedances are not independent. More precise discussion will be given later.) On the other hand, the degree of freedom of n-layer model is 2n-1 because each layer has two parameters:i.e. thickness and conductivity, while the bottom layer has an infinite thickness. Thus, the number of layers that can be determined by this data set will be at most m.

Many schemes have been applied to minimize χ^2 in Eq.(3-3-1). Here we used a method which determines the layer parameters by generating random numbers successively (Jones and Hutton, 1981). The advantage of using this method is that the parameters of the optimum model are independent on the starting model. On the other hand, this method requires a large number of calculations. So the time consumption for the numerical calculation may sometimes be a disadvantage. However, since the theoretical impedance is given by simple analytical forms (Eqs.(3-2-16),(3-2-17) and (3-2-18)) in the present case, the calculation is not so time consuming.

In this method, the conductivity and the thickness of the i'th layer for a new model are derived from:

$$\sigma'_i = \sigma_i \cdot x^{r_1} \qquad (3\text{-}2\text{-}3)$$

$$h'_i = h_i \cdot y^{r_2} \qquad (3\text{-}2\text{-}4)$$

where r_1 and r_2 are the independent Gaussian random numbers with zero means and unit variances. The dashed parameters refer to those of the new model. x and y give limits for conductivity and thickness. Usually we take 10 for y and 100 for x. This means that the layer thickness and the conductivity can vary within ranges of two and four orders of magnitude, respectively. The range is sufficiently wide to reduce the effect of the initial assumption. Thus, this method is almost independent of the initial values. The theoretical responses $Z'_c(f_i)$ $(i=1,\cdot\cdot,m)$ are calculated for the new model and compared with the observation. The value of χ'^2 is calculated from Eq.(3-2-3) and (3-2-4) by replacing $Z_c(f_i)$ with $Z'_c(f_i)$. If χ'^2 is smaller than χ^2 , then the previous parameters are replaced by the new values. If χ'^2 is greater than χ^2, no action is taken and continues to generate other random number. The whole process is terminated when the value of χ^2 becomes less than a presetted limit.

Each parameter (conductivity and thickness) is now very close to the value which gives the minimum value of χ^2 in the 2n-1 dimensional space. Next we examine the confidence interval for each parameter. Fig.3.5 shows an example of the χ^2-ρ_i and χ^2-h_i sections for a three layer model. The distribution of χ^2 against each layer parameter is approximated by the fourth order polynomial as follows,

$$\chi^2(d_i) = a_{0.i} + a_{1.i}d_i + a_{2.i}d_i^2 + a_{3.i}d_i^3 + a_{4.i}d_i^4 \quad (3\text{-}3\text{-}5)$$

where d_i denotes log of either the resistivity, ρ_i, or the thickness, h_i normalized by its optimum value, ρ^{op}_i or h^{op}_i; i.e.

$$d_i = \log[\rho_i / \rho^{op}_i] \text{ or } \log[h_i / h^{op}_i] \quad (3\text{-}3\text{-}6)$$

The curves in Fig.3.5 are the best fit curves obtained by the least squares sense. The steepness of the curve reflects the resolution of the determination of each parameter. Here we define the confidence interval of determination by the half width of the curve as is shown in Fig.3.5.

In this way, we can determine the layer parameters and their confidence limits for the n-layer model. According to the previous brief discussion about the degree of freedom, number of layers can be equal to the number of frequencies where impedances are obtained. However, not all the impedances at different frequencies are independent in many cases. Hence, we have to determine an optimum number of layers for the available data set.

The procedure is done by carrying out the inversions successively with increasing the number of layers, n. While the number of layers, n, is less than the optimum value; i.e. the degree of freedom of the data set, the χ^2 for the n layer model, $\chi^2(n)$, will decrease with increasing n. But it will be almost constant for n's greater than the optimum number n_{op}. Fig.3.7 shows examples of the determination of n_{op}. In this example, three-layer model are appropriate for most of the results, since χ^2 scarcely decreases for four or five layers. The minimum $\chi 2$ is different from site to site depending on the noise level and the number of data points for each site.

In the magnetotelluric sounding, it is often very interesting to know how deep the deepest layer (third layer in this case) continues. The sounding depth is given by the skin depth (Eq.(3-2-5)) at the lowest frequency, providing the structure is homogeneous. The maximum sounding depth for a multi-layered model should be defined analogous to the skin depth for a homogeneous medium. Assume we have an optimum n-layer model by using the above mentioned method. Then, a boundary is added below the deepest boundary of the optimum model, where the conductivity contrast at this boundary is one order of magnitude. If the assumed boundary is deep enough compared to the actual sounding depth, χ^2 calculated with the additional substratum little differs from the optimum value. However, χ^2 will be significantly larger than the optimum value when the additional boundary is too shallow. In this way we define the maximum sounding depth as the depth of the additional boundary by which the calculated χ^2 departs from the optimum value by 10%.

The validity of the above definition was examined by use of a homogeneous model. In this case, the maximum sounding depth should be coincide with the skin depth of the lowest frequency. Theoretical apparent resistivities and phases were obtained at five different frequencies, and several scatters were added to the data. Then, the maximum sounding depth was estimated by the above mentioned process. The results are shown in Fig.3.6. Level of scatter in each data set is denoted by 's' for each case in the figure (s=0.5 corresponds to the scatter of 50% of the true apparent resistivity). Curves denote calculated χ^2 for each data set by varying the depth of the additional boundary. Curves with dots and crosses correspond to the resistive and conductive basement case by one order of magnitude compared with the first layer, respectively. The estimated maximum sounding depths are shown by arrows. It is natural that the estimated depth is much shallower than the skin depth of the lowest frequency with large scatters in data, while they are comparable with little scatter of less than 10% or so (Fig.3.6).

By use of the result of the one-dimensional modeling, the starting model is constructed for the further two-dimensional modeling.

3.4 Two-dimensional modeling technique by a finite element method

If the electromagnetic field variations are independent of the x coordinate and the electrical conductivity is uniform in x direction, it is well known that the induction equations given by Eqs. (3-1-8)' and (3-1-9)' are decoupled into two modes. In an analogy of wave guide, these two modes are called E-polarization mode and H-polarization mode, respectively. In the former case, the electric field has only one component parallel to the strike of the structure (x-direction) , while two components of the magnetic field exist in the plane perpendicular to the strike. In the latter case, the magnetic field varies along x-direction and the electric field is confined in the y-z plane. In both cases, the vector induction equations (Eqs.(3-1-8)' and (3-1-9)') can be reduced to scalar differential equations with respect to x-components of electric (E-polarization) and magnetic (H-polarization) field variations, respectively.

By solving the induction equation under a given conductivity distribution, we can evaluate the theoretical inductive responses for the two-dimensional problem. Various methods have been adopted to numerical modeling of the two-dimensional conductivity structure. For example, Jones and Price have put forward a simple formulation by a finite difference method (FDM). Since then, progresses have been made by many authors (e.g.. Jones and Pascoe (1972), Brewit-tylor and Weaver (1978)). Swift(1971) and Madden and Swift (1969) made a different approach based on a network analogy of transmission lines. Other methods, such as a finite element method (Coggon, 1971; Rodi, 1976; Ogawa et al.,1986) and integral equation method (Hohman, 1975;

Lee, 1975) have been used for two-dimensional electromagnetic modelings, and have provided useful basis for a two-dimensional or even three-dimensional (Hohman, 1975; Weidelt, 1975) interpretations.

In this study, a finite element method was employed to solve the two-dimensional induction equation. This method is the most appropriate one to model the complicated structure. Basic concept of the FEM modeling scheme used in this study will be reviewed in the followings.

3.4.1 Formulation of Galerkin equation

Letting $\partial/\partial x = 0$, the induction equation for each mode can be expressed as

$$\left[\frac{\partial}{\partial y}\left(h \frac{\partial}{\partial y} \right) + \frac{\partial}{\partial z}\left(h \frac{\partial}{\partial z} \right) + \lambda \right] u = 0 \qquad (3\text{-}4\text{-}1)$$

where, for E-polarization mode,

$$u = E_x \qquad (3\text{-}4\text{-}2)$$

$$h = 1/(i\omega\mu) \qquad (3\text{-}4\text{-}3)$$

$$\lambda = \sigma \qquad (3\text{-}4\text{-}4)$$

and, for H-polarization mode,

$$u = H_x \qquad (3\text{-}4\text{-}5)$$

$$h = 1/\sigma \qquad (3\text{-}4\text{-}6)$$

$$\lambda = i\omega\mu \qquad (3\text{-}4\text{-}7)$$

Here, we call the scalar variable u as the electromagnetic potential, because the other field variables (y- and z-components of the magnetic and the electric fields for E- and H-polarization cases, respectively) can be obtained by taking spatial derivatives of u as follows:

$$H_y = -h\frac{\partial u}{\partial z} \qquad (3\text{-}4\text{-}8)$$

$$H_z = h\frac{\partial u}{\partial y} \qquad (3\text{-}4\text{-}9)$$

for E-polarization case, where h is given by Eq.(3-4-3). Similarly, for H-polarization case, we have:

$$E_y = -h\frac{\partial u}{\partial z} \qquad (3\text{-}4\text{-}10)$$

$$E_z = h\frac{\partial u}{\partial y} \qquad (3\text{-}4\text{-}11)$$

where h is given by Eq.(3-4-6).

We solve the partial differential equation (3-4-1) for an inhomogeneous medium by use of the finite element method (FEM). The basic concept of FEM is reviewed briefly here. Let a partial differential equation with an unknown variable u be written as:

$$R(u;y,z) = 0 \qquad (3\text{-}4\text{-}12)$$

Any approximate solution, v, of Eq.(3-4-12) will generally give non zero residual; $R(v;y,z) \neq 0$. Assume that the residual is integrated over the entire region under investigation, and that the resulting integral takes null for a set of approximate solutions. In FEM, the approximate solution is determined so that the weighted integrals of the approximate value of Eq.(3-4-12), is null over the entire region:

$$R = \int_s \delta v \cdot R(v;y,z)\, dS = 0 \qquad (3\text{-}4\text{-}13)$$

where weight function δv is the variation of v, which is called here the test function. For numerical evaluation of Eq.(3-4-13), the whole space is divided into E elements with 'finite' areas. In this study, triangular elements are applied. By use of the finite element approximation, total residual can be written by summation of residual of each elements:

$$\sum_{e=1}^{E} \int_{se} \delta v_e \cdot R(v_e;y,z)\, dS = 0 \qquad (3\text{-}4\text{-}14)$$

where, $\int_{se} dS$ denotes the areal integral in the e'th element (Fig.3.8). In the present problem of Eq.(3-4-1), this may be written:

$$\sum_{e=1}^{E} \int_{se} \delta v_e \left[\frac{\partial}{\partial y} h \frac{\partial v_e}{\partial y} + \frac{\partial}{\partial z} h \frac{\partial v_e}{\partial z} + \lambda \cdot v_e\right] dS = 0 \qquad (3\text{-}4\text{-}15)$$

By performing partial integrals, we obtain so-called Galerkin equation as follows:

$$\sum_{e=1}^{E} \int_{se} [\, h \frac{\partial v_e}{\partial y} \cdot \frac{\partial \delta v_e}{\partial y} + h \frac{\partial v_e}{\partial z} \cdot \frac{\partial \delta v_e}{\partial z} + \lambda v_e \,] \, dS -$$

$$\sum_{e=1}^{E} \int_{ce} [\, h \cdot \frac{\partial v_e}{\partial n} \cdot \delta v_e \,] \, dl = 0 \qquad (3\text{-}4\text{-}16)$$

where $\int_{ce} dl$ and $\partial / \partial n$ denote the line integral along the boundary of e'th element and the differentiation normal to the boundary, respectively.

In this study, triangular element with a linear interporation function is applied. Fig.3.8 illustrates the situation with respect to the e'th element. The approximate solution in the e'th element, v_e, is explicitly written by the product of the interporation function and the potential at the nodes of each element, which should be determined by FEM:

$$v_e = {}^{T}\{ \phi_e(y,z) \} \cdot \{ v_e \} \qquad (3\text{-}4\text{-}17)$$

where T denotes the transpose. In Eq.(3-4-17), vector quantities can be written as follows:

$${}^{T}\{\phi_e(y,z)\} = [\phi_{i.e}(y,z), \phi_{j.e}(y,z), \phi_{k.e}(y,z)] \qquad (3\text{-}4\text{-}18)$$

and

$$\{ v_e \} = {}^{T}[v_{i.e}, v_{j.e}, v_{k.e}] \qquad (3\text{-}4\text{-}19)$$

For the e'th element shown in Fig.3.8, the interporation function at i'th node takes the form:

$$\phi_{i.e}(y,z) = (a_i + b_i \cdot x + c_i \cdot y)/2\Delta_e \qquad (3\text{-}4\text{-}20)$$

where Δ_e is the area of the e'th triangle and,

$$a_i = y_j \cdot z_k - y_k \cdot z_j$$

$$b_i = z_j - z_k \qquad (3\text{-}4\text{-}21).$$

$$c_i = y_k - y_j$$

The interporation functions at j'th and k'th nodes can similarly be evaluated by a combination of the coordinate of each node.

In Galerkin's algorithm, the same interporation function given by Eq.(3-4-20) is used for the test function, δv_e, in Eq.(3-4-16). Since the coordinate of each node is given, Eq.(3-4-16) can be reduced to a simple linear equation with an unknown vector v. Finally, the approximate solution of the induction equation can be obtained by solving a simple matrix equation

$$A(\omega, \sigma, r)\ v = b \qquad (3\text{-}4\text{-}22)$$

where A is a matrix determined from the frequency, ω, the conductivity of each element, σ, and the coordinate of each node, r, while b denotes a vector describing boundary conditions.

3.4.2 Boundary conditions

The approximate value of the electromagnetic potential, u, can be obtained at each node by solving the matrix equation under appropriate boundary conditions. Fig.3.9 describes the boundary conditions applied in the present study. The origin of the electromagnetic disturbances are considered to exist in the ionosphere or the magnetosphere. So we assume, as the source boundary condition, that the electromagnetic potential is unity at the top of the whole region, i.e.,

$$u(y,z) = 1 \qquad \text{at } z = z_{top} \qquad (3\text{-}4\text{-}22)$$

In other word, we investigate the electromagnetic response from an inhomogeneous earth by applying uniform source field variation. The height of the top boundary should be taken sufficiently high so that the internal field generated by electromagnetic induction is negligible at the boundary. For the side boundaries, at $y=y_w$ and $y=y_e$, the natural boundary condition is adopted, i.e.

$$\frac{\partial u(y,z)}{\partial n} = 0 \qquad \text{at } y = y_w \text{ and } y = y_e \qquad (3\text{-}4\text{-}23)$$

This means that the field variation obtained by spatial derivative of the potential has only the horizontal component. This condition is somewhat artificial. Therefore, these side boundaries also should be set up far away from the region under investigation.

The electromagnetic potential is assumed to be null at the bottom boundary, $z=z_{bot}$:

$$u(y,z) = 0 \qquad \text{at } z = z_{bot} \qquad (3\text{-}4\text{-}24)$$

This condition indicates that the perfect conductor exists below the bottom boundary. If the boundary is sufficiently deep, this condition seems reasonable, because the conductivity increases by several orders of magnitude at the depth of 400-600km as revealed by the spherical harmonic analysis (e.g. Banks, 1969; see Chapter 1).

Conditions given by Eqs.(3-4-22), (3-4-23) and (3-4-24) are applied both for E- and H-polarization modelings. As for the H-polarization case, following boundary condition is additionally required:

$$\frac{\partial\, u(y,z)}{\partial\, t} = 0 \qquad \text{at } z = z_{sur} \qquad (3\text{-}4\text{-}25)$$

where $\partial / \partial t$ denotes the tangential differentiation. This condition means that the normal component of the electric field should be zero at the earth's surface because the air can be regarded as a perfect insulator.

Once the electromagnetic potential at each node is calculated, the other field variables can be derived by taking spatial derivatives given in Eqs.(3-4-8)-(3-4-11). Since the linear interporation function is used here, these field variables are uniform in each element. This situation requires that the size of each element should be small enough to represent the complex feature of the electromagnetic responses in such a case that a large contrast is expected between the subterranean conductivity inhomogeneities.

3.4.3 A scheme for automatic mesh division

The advantage of using FEM for the numerical modeling lies in its applicability for the problem with arbitrary shaped boundary. Particularly, use of triangular elements enables us to simulate a structure with a fairly complicated feature. For example, in case of the interpretation of the result of seafloor measurements, we have to make a mesh network to model a complex shaped bathymetry; gradually deepening continental shelf, steep cliffs around trench etc.. Since the conductivity contrast is very large between the sea water and the land, the shape of model bathymetry should be as smooth as possible.

However, it takes much more time to make the mesh network than that to make numerical calculation on computer, if the mesh division is left to manual work. Therefore, in the present study, a practical scheme was developed for dividing triangular elements automatically. The scheme consists of three steps as follows:

1) The entire region is first divided into rectangular mesh, where y- and z-coordinate of each node are given as input data (Fig.3.10). Rows are divided into closer spacings around the earth's surface. At the same time, columns are divided so as to provide a sufficient spatial resolution in the region under investigation. Letting the numbers of rows and columns be n_y and n_z, respectively, the total number of nodes

becomes $n_y \cdot n_z$, and the number of rectangles becomes $(n_y-1)\cdot(n_z-1)$.

2) Each rectangle is divided into two triangles by a diagonal line. Two different ways are considered for the division as shown in Fig.3.11(a). The choice of the separation is given manually. Four modes can be considered for the division of a row (Fig.3.11(b)). Thus, the total number of triangular elements becomes $2\cdot(n_y-1)\cdot(n_z-1)$.

3) Global numbering is made for each node and element, i.e. nodes and elements are numbered sequentially in the entire region. The nodes of each element are also numbered locally. The local number of a node should correspond one to one to its global number.

4) Then, the entire region is divided into large polygonal blocks, so that the electrical conductivity in each block is constant. Data for each inhomogeneity consists of the number of corners, the coordinates of each corner and the code which indicates the conductivity in the block.

5) Mesh configuration is modified so that each side of the polygonal blocks of inhomogeneities coincides with a side of any triangular elements. Fig.3.12 describes schematically how the adjustment is made for each side. Then, codes are assigned to the corresponding elements to the conductivity inhomogeneities.

By use of this scheme, the time for the division of mesh network is much reduced. The adjustment described by Fig.3.12 enables us to represent a fairly complicated structure. Fig.3.13 is an example of the mesh network representing a cross section across central Japan. It is obvious that the shape of the subducting Philippine Sea Plate beneath the Japan Arc is well represented by a smooth line. In particular, sea floor topography should be as smooth as possible in the induction modeling because the effect of sea water is quite significant in the geomagnetic induction. Without the adjustment scheme, the slope is described by steps, which may cause erroneous results in the electromagnetic induction on the sea floor.

Mesh networks of two different scales were made in this study. One has 30 rows and 36 columns, or 1080 nodes and 2030 elements; the other has 42 rows and 78 columns, or 3276 nodes and 6314 elements. The former was used for the calculation of simple artificial models given in Section 3.6. The latter was used for the interpretation of the actual data, which will be seen in Chapters 6 and 7. The computer storage required for the calculation by use of these networks were 1.6 MB and 4.8 MB for the forward evaluation, and 3.8 MB and 10MB for the inverse calculation which will be explained in the next section.

3.5 Two-dimensional inverse problem

In this section, a mathematical formulation is presented for the direct inversion of the observed magnetovariational and magnetotelluric data. In the electromagnetic induction problem in an inhomogeneous medium, the rule of superposition does not hold, because electromagnetic fields perturbed by different inhomogeneities couple with each other. This situation often makes it very difficult to explain the observed inductive responses by a model calculation. Therefore, an approach by a direct inversion is desirable in order to obtain an unambiguous electrical structure. Since the situation is thus inevitably non-linear, generalized non-linear inversion technique should be applied to solve this problem.

If observable quantities can be calculated theoretically for an applied set of model parameters, and if the Jacobian matrix, the matrix of the partial derivatives of the theoretical equation with respect to each parameter, is obtained, optimum parameters can be determined iteratively as has been reviewed by Tarantola and Valette (1982). First, in this section, the expression of the partial derivatives of electromagnetic responses from inhomogeneous conductivities are put forward for two-dimensional conductivity structure by using FEM, and the possibility of the direct inversion of two-dimensional conductivity structures is discussed later. Similar approach has been done by Ku (1976) by use of a network method for the inversion of two-dimensional magnetotelluric data. Jupp and Vozoff (1977) has made a good progress using a finite difference method, although their algorithm is based on the linearization of the problem and their formulation is restricted to the magnetotelluric method. Weidelt (1975) presented a two-dimensional inversion for magnetovariational data using the integral equation method, in which undulation of the perfectly conductive layer or the conductivity distribution in an inhomogeneous thin sheet conductors was determined. In this study, more general formulation has been given and some improvements are achieved as compared with the previous works.

3.5.1 Parameters in the inverse problem

We consider a physical system which is described by a finite set of parameter $X = \{X_1, X_2, \cdots X_m\}$, which consists of two types of quantities as shown below.

$$X = \begin{bmatrix} X_1 \\ \vdots \\ X_m \end{bmatrix} = \begin{bmatrix} D_1 \\ \vdots \\ D_r \\ P_1 \\ \vdots \\ P_s \end{bmatrix} = \begin{bmatrix} D \\ \\ P \end{bmatrix} \qquad (3\text{-}5\text{-}1)$$

$$m = r + s$$

where vector D is usually called data which is directly observable, while vector P is called the parameter. In geophysical terms, D corresponds to observational data, and P to the physical properties of the Earth's material. More generally, D and P are functions of data and physical properties, respectively. P may include positions of inhomogeneities in the medium. However, we assume here that the position is fixed and only the physical properties vary for the sake of the simplicity.

Let any particular value of the parameter set be denoted by $x = \{x_1, x_2, \cdots x_m\}$, and physical description of them be expressed in a functional form:

$$f(x) = 0 \qquad (3\text{-}5\text{-}2)$$

When the parameter X takes partitioned form of Eq.(3-5-1), Eq.(3-5-2) can be replaced by a set of theoretical equations:

$$d = g(p) \tag{3-5-3}$$

Here we attempt to determine the parameter p from the observed data d in the least squares sense. In general, a priori information on the parameter set is required for the least squares process. We assume that all a priori information takes the form of a vector of expected values x_o and a covariance matrix C_o. Here, they are also assumed to have partitioned forms:

$$x_o = \begin{bmatrix} d_o \\ p_o \end{bmatrix}, \quad C_o = \begin{bmatrix} C_{d_o d_o} & C_{d_o p_o} \\ C_{p_o d_o} & C_{p_o p_o} \end{bmatrix} \tag{3-5-4}$$

Setting up these situations, the iteration formula can be written as follows (see Appendix A):

$$\begin{aligned} p_{k+1} = {} & p_k + ({}^{T}G_k \cdot C_{d_o d_o}{}^{-1} \cdot G_k + C_{p_o p_o}{}^{-1})^{-1} \cdot \\ & \{ {}^{T}G_k \cdot C_{d_o d_o}{}^{-1} \cdot [d_o - g(p_k)] - C_{p_o p_o}{}^{-1} \cdot [p_k - p_o] \} \end{aligned} \tag{3-5-5}$$

where the suffix k indicates the k'th sequence of the iteration process. G_k is the matrix of the partial derivatives of the theoretical equation g:

$$G_{ij.k} = \partial g_i / \partial p_{j.k} \tag{3-5-6}$$

In order to apply the present algorithm to the geomagnetic induction problem, we must first determine the exact expressions for d and p. As shown in Appendix A, Eq.(3-5-5) depends entirely on the assumption that the distributions of both **d** and **p** take Gaussian forms. Therefore, we have to search for such expressions as not to conflict to the assumption; in other word, we have to determine the reasonable scaling of data and parameter. On the other hand, the expressions should be as simple as possible. If they have complicated functional forms, numerical evaluation of Eqs.(3-5-5) and (3-5-6) will be fairly difficult.

As for the observable data, two different kind of response functions are generally used in the induction study; i.e. the geomagnetic transfer function and the magnetotelluric impedance. These two response functions have been analyzed separately in most of the previous works. The transfer function is known to be sensitive to the lateral heterogeneity of the conductivity, and therefore most of the induction studies in Japan have been made on the spatial and period dependences of the transfer function (e.g. Rikitake,1969; Honkura, 1975). On the other hand, the magnetotelluric impedance has been used for the determination of one-dimensional conductivity distribution as has been shown in Sections 3.2 and 3.3. Of course, impedance is also be affected by lateral heterogeneities of the conductivity distribution. However, as will be shown by numerical experiments later, impedance is more sensitive to the conductivity just below the observation site. Since these responses have different sensitivity to the same structure, the usage of both quantities provides much information and the higher resolution of the parameters.

Thus, the vector d, in the present case, will be expressed by two vectors:

$$d = \begin{bmatrix} d_T \\ d_Z \end{bmatrix} \qquad (3\text{-}5\text{-}7)$$

where d_T and d_Z are the vectors corresponding to the transfer function and the impedance, respectively. Here again, we should note that d_T and d_Z can be generally the functions of the transfer function and the impedance.

We apply a logarithmic scaling to the impedance as

$$d_Z = \log(Z) \qquad (3\text{-}5\text{-}8)$$

where Z is the vector composed of observed impedances for various frequencies from various observation sites. Bentley (1973) demonstrated the normal distribution of the logarithm of apparent resistivity. There is another reason why we take a logarithm of the impedance. The observation error of the impedance depends on the absolute value of the impedance; if the impedance is large, the error will be large in proportion to its absolute value. This implies that the distribution is logarithmically Gaussian.

On the other hand, the transfer function is considered to take a Gaussian distribution itself. The observational error does not depend on its absolute value. So we take as:

$$d_T = T \qquad (3\text{-}5\text{-}9)$$

where T is a vector composed of the transfer functions. We should note that d_Z and d_T are both complex quantities, since the impedance and the transfer function are complex quantities.

Thus, in the present problem, the vector of data can be written in a partitioned form as given by Eq.(3-5-7):

$$\mathbf{d} = \begin{bmatrix} \mathbf{d}_T \\ \mathbf{d}_Z \end{bmatrix}$$

The geomagnetic transfer function is the ratio of the vertical magnetic field to the horizontal field, while the impedance is the ratio of the electric to the magnetic field. Taking the above expression for a given set of data, the theoretical equation for $\mathbf{d}_T$ takes a different form from that for $\mathbf{d}_Z$. In other word, the theoretical equation (3-5-3) should also be written in a partitioned form as

$$\mathbf{g}(\mathbf{p}) = \begin{bmatrix} \mathbf{g}_T(\mathbf{p}) \\ \mathbf{g}_Z(\mathbf{p}) \end{bmatrix} \qquad (3\text{-}5\text{-}10)$$

Jupp and Vozoff (1977) took resistivity of the medium for the parameter p. In this study, however, log(σ) was taken for p:

$$\mathbf{p} = \log(\sigma) \qquad (3\text{-}5\text{-}11)$$

where σ is the vector of inhomogeneous conductivities. In the simplest case, i.e. the homogeneous model, the impedance is given by Eq.(3-2-10):

$$Z = (i\omega\mu/\sigma)^{1/2} \qquad (3\text{-}5\text{-}12)$$

In order not to conflict the precondition of Gaussian distribution for both p and d, we have to apply logarithmic form for the expression of the parameter p, too. The validity of this expression can be simply demonstrated as follows. Taking logarithms of both sides of Eq.(3-5-12), we obtain:

$$\log Z = \{ \log(i\omega\mu) - \log(\sigma) \} / 2 \qquad (3\text{-}5\text{-}13)$$

or by use of the above expression,

$$d_Z = \{ \log(i\omega\mu) - p \} / 2 \qquad (3\text{-}5\text{-}14)$$

Eq.(3-5-14) means that, if the distribution of d_Z is a Gaussian form, p also takes Gaussian distribution. This expression is reasonable because the conductivity varies by orders of magnitude with the variation of other physical properties or physical states. For example, the conductivity of rocks varies by several orders against a slight change in the temperature as shown in Fig.2.1. Another reason why we adopted logarithmic form for p is that, otherwise, the partial derivative depends on the absolute values of the parameters. Then, if we take the conductivity as the parameter, the resulting partial derivative will be quite different from what is obtained by letting resistivity as the parameter. This seems queer, because the physics should be the same independent of whether the equation is written in terms of conductivity or resistivity. Jupp and Vozoff (1977) adopted logarithm of the apparent resistivity and the phase for d, while the resistivity of the medium was taken for p. If their expressions are applied, the distributions of d and p will be inevitably different. This means that the expressions of the parameters conflict to the assumption.

3.5.2 Matrix of partial derivatives

Assume we are going to determine the conductivity structure by a direct inversion from a set of observed electromagnetic responses. The observation is usually carried out at a number of sites and responses were calculated for several frequencies. Now we have to obtain an exact expression to evaluate the Jacobian matrix G_K for sets of data **d** and parameter **p** defined in the previous section.

The structure is assumed to be two dimensional, and to be composed of s conductive bodies with unknown conductivities (Fig.3.14). The vector of the parameters, **p**, can be written as (the suffix k indicating the iteration process is omitted here for simplicity):

$$\begin{aligned} \mathbf{p} &= \{ p_1, p_2, \cdots p_s \} \\ p_j &= \log \sigma_j \qquad (j=1,2,\cdots s) \end{aligned} \qquad (3\text{-}5\text{-}14)$$

where σ_j is the conductivity of the j'th inhomogeneity. For a given set of **p**, the electromagnetic responses,T and Z, can be calculated numerically at each position corresponding to each observation site, for each frequency.

By applying FEM, the electromagnetic potential can be expressed as the solution of a matrix equation as shown in section 3.4. We can rewrite Eq.(3-4-22) as

$$A\,u \quad = b \qquad\qquad (3\text{-}5\text{-}15)$$

where A is the so-called element matrix which is the function of the coordinates of each node and the model parameters. Vector **b** is a vector determined from boundary conditions. Note that the vector of the approximate solution of the induction equation is denoted by **u**, instead of v in Eq.(3-4-22). Differentiating both sides of Eq.(3-5-15) by the parameter of the j'th body, p_j, we obtain:

$$\frac{\partial A}{\partial p_j}\cdot u \;+\; A\cdot\frac{\partial u}{\partial p_j} \;=\; \frac{\partial b}{\partial p_j} \;=\; 0 \qquad\qquad (3\text{-}5\text{-}16)$$

Since the matrix A is a linear function of the conductivity (see, for example, Eq.(3-4-16), its partial derivative can be obtained in a straight forward manner. The electromagnetic potential u is the solution of Eq.(3-5-15), which we can evaluate at each node beforehand by FEM. Thus, the first term of the left-hand side of Eq.(3-5-16) being a known vector, this equation gives another matrix equation by which we can obtain the partial derivative of the electromagnetic potential. This can be written as:

$$A\cdot\frac{\partial u}{\partial p_j} \quad = \quad c \qquad\qquad (3\text{-}5\text{-}17)$$

where $c = -\partial A/\partial p_j \cdot u$. The vector c can be regarded as the source field generated by a perturbation of the j'th conductivity. It is obvious that, if the i'th node of the finite element model is outside of the j'th inhomogeneity, the i'th component of c is null.

Let us consider the physical meaning of Eq.(3-5-17). The partial derivative $\partial u/\partial p_j$ can be regarded as the perturbation field by a small deviation of j'th conductivity. Since the characteristic matrix, A, is the same as that of Eq.(3-5-15), the perturbation field also follows the induction equation. The source of the perturbation field, c, takes non-zero value at each node consisting j'th element of the model. The perturbation field generated by this source propagates in the earth following the same induction equation as controls the electromagnetic potential u. Thus, we can obtain the partial derivative of the electromagnetic potential by solving the matrix equation similar to that for the potential itself.

From the partial derivative of the electromagnetic potential, we can evaluate those of the other field variables. As shown in the previous section, x-component of the electric field is the potential in E-polarization case and y- and z-components of the magnetic field can be obtained by performing spatial differentiation of the potential. In H-polarization case, y- and z-components of the electric field are the spatial derivatives of x-component of the magnetic field. Here we denote y- and z-components of the secondary field variable by v_y and v_z, respectively.

Following Eqs.(3-4-8)-(3-4-11), we can write the partial derivatives of v_y and v_z with respect to p_j as:

$$\frac{\partial v_y}{\partial p_j} = -\{ h \cdot \frac{\partial}{\partial z} [\frac{\partial u}{\partial p_j}] + \frac{\partial h}{\partial p_j} \cdot \frac{\partial u}{\partial z} \} \qquad (3\text{-}5\text{-}18)$$

$$\frac{\partial v_z}{\partial p_j} = \{ h \cdot \frac{\partial}{\partial y} [\frac{\partial u}{\partial p_j}] + \frac{\partial h}{\partial p_j} \cdot \frac{\partial u}{\partial y} \} \qquad (3\text{-}5\text{-}19)$$

where h is the same quantity as that in Eq.(3-4-3) or in Eq.(3-4-6). Note that the order of differentiation is exchanged in above equations. Since the conductivity is uniform in each element, this exchange is certainly possible. The transfer function and the impedance can be derived at each data points as:

$$T_q = v_{z.q} \;/\; v_{y.q} \qquad (3\text{-}5\text{-}20)$$

$$Z_t = u_{x.t} \;/\; v_{y.t} \qquad (3\text{-}5\text{-}21)$$

for E-polarization case. For H-polarization case, the impedance is given by:

$$Z_l = v_{y.l} \;/\; u_{x.l} \qquad (3\text{-}5\text{-}22)$$

where the suffices q, t and l correspond to each frequencies at each observation sites where the transfer function and the impedance were obtained. By differentiating equations (3-5-20), (3-5-21) and (3-5-22) by p_j, we can obtain the expressions for the partial derivatives of the theoretical response functions:

$$\frac{\partial d_{T.q}}{\partial p_j} = \frac{\partial T_q}{\partial p_j} = \frac{\dfrac{\partial v_{z.q}}{\partial p_j} v_{y.q} - v_{z.q} \dfrac{\partial v_{y.q}}{\partial p_j}}{v_{y.q}^2} \qquad (3\text{-}5\text{-}23)$$

$$\frac{\partial d_{Z.t}}{\partial p_j} = \frac{\partial \log(Z_t)}{\partial p_j} = \frac{\dfrac{\partial u_{x.t}}{\partial p_j} v_{y.t} - u_{x.t} \dfrac{\partial v_{y.t}}{\partial p_j}}{Z_t \cdot v_{y.t}^2} \qquad (3\text{-}5\text{-}24)$$

for E-polarization case, and,

$$\frac{\partial d_{z,i}}{\partial p_j} = \frac{\partial \log(Z_i)}{\partial p_j} = \frac{\dfrac{\partial v_{y,i}}{\partial p_j} u_{x,i} - v_{y,i} \dfrac{\partial u_{x,i}}{\partial p_j}}{Z_i \cdot u_{x,i}^2} \qquad (3\text{-}5\text{-}25)$$

for H-polarization case.

The Jacobian matrix of Eq.(3-5-6) can be obtained by assembling these partial derivatives. Then, we can execute the direct inversion by use of the iterative formula of Eq.(3-5-5).

3.5.3 Remarks on actual usage of the inversion method

The covariance matrices of the a priori information, $C_{d_o d_o}$ and $C_{p_o p_o}$, take the following form in actual case:

$$C_{d_o d_o} = {}^{T}s_d \cdot I \qquad (3\text{-}5\text{-}26)$$

$$s_{i,d} = r_{i,d}^2 \qquad (3\text{-}5\text{-}27)$$

$$C_{p_o p_o} = {}^{T}s_p \cdot I \qquad (3\text{-}5\text{-}28)$$

$$s_{j,p} = r_{j,p}^2 \qquad (3\text{-}5\text{-}29)$$

where I is the identity matrix. $r_{i,d}$ and $r_{j,p}$ are the observation errors in the i'th data and the ambiguity in estimation of the j'th parameter, respectively.

Since the data vector for impedance, d_z, takes the logarithmic form as shown in Eq.(3-5-10), the observation error in Eq.(3-5-27) should be the relative error in estimation of the impedance. The observation error works as a weight of each observed data in the iterative process Eq.(3-5-5); i.e. data with smaller error will make larger contribution in the feed back system.

The covariance $C_{d_o d_o}$ works as a weight function for tangent linear projection in Eq.(3-5-5). The evaluation of the covariance matrix $C_{p_o p_o}$ is a little more complicated, because we guess the starting model of the conductivity structure by taking into account not only electromagnetic, but also other geophysical and geological evidences. Nevertheless, its evaluation has a significant effect on the iterative process of Eq.(3-5-5). The term $-C_{p_o p_o}{}^{-1}\cdot(p_K-p_o)$ in Eq.(3-5-5) will stabilize the solution, as shown schematically in Fig.3.15. Consider an extreme case where $r_{j,p}{}^2\rightarrow\infty$ for all j. This means that the a priori constraints on parameters are infinitely weak. In this extreme limit, Eq.(3-5-5) will be written as

$$p_{K+1} = p_K + ({}^TG_K\cdot C_{d_o d_o}{}^{-1}\cdot G_K)^{-1} \cdot {}^TG_K\cdot C_{d_o d_o}{}^{-1}\cdot\{d_o-g(p_K)\} \qquad (3\text{-}5\text{-}30)$$

which coincides with the formulation of the classical non-linear least squares problem by linearization (Tarantola and Valette,1982). This implies that, if the nonlinearity of the problem is sufficiently weak, the iterative process will be stable independent of the a priori constraints on the parameters and give the exact solution. For the present problem of the electromagnetic induction, however, the nonlinearity is usually so strong that the stability of the iterative process is highly dependent on the a priori constraints. Therefore, we have to be careful in the estimation of $C_{p_o p_o}$.

The a posteriori covariance matrix in the least squares can be given as:

$$C_{pp} = ({}^{T}G \cdot C_{dodo}{}^{-1} \cdot G + C_{popo}{}^{-1})^{-1} \qquad (3\text{-}5\text{-}31)$$

Since this definition is valid only for linear cases, the covariance matrix of Eq.(3-5-31) would not be of great interest. If the non-linearity is strong, a posteriori errors will be far from Gaussian. However, we can recognize some information in the a posteriori covariance. The first term in the right-hand side of Eq.(3-5-31) describes the propagation of error from d-space to p-space. If a parameter is purely unresolved, the propagated error would be infinitely large. In general,

$$(C_{pp})_{jj} \leqq (C_{popo})_{jj} \qquad (3\text{-}5\text{-}32)$$

equality holds only for an unresolved parameter. Thus the ratio of a posteriori to a priori variance will work as an indicator of confidence. The larger the ratio means that the more definitely the parameter is determined. More details about the reliability of the solution, evaluation of a priori covariance, etc. will be discussed in the following section. Examples of numerical experiment will also be presented by using simple models.

The formulation of the iterative process has been made in a general form: i.e. using both E- and H-polarization cases together. However, we limited only E-polarization response functions for data in actual application of the present method. This is because of two reasons as followings.

(1) In actual case, each polarization may reflect different induction effect within the earth. The real structure has generally a three-dimensional nature. We can determine an equivalent structure at a two-dimensional approximation. Moreover, subsurface conductivity may, in

some case, have intrinsic anisotropy as has been discussed in the seismic velocity structure.

(2) The element matrices for the two polarization cases are different with each other because they are constructed under different boundary conditions. This means that the usage of the two polarization cases requires twice as much computer storage as that for single polarization case.

The essence of the present formulation lies not in the usage of the two polarization, but in the combination of the transfer function and the impedance in the direct inversion. This can be achieved if we use E-polarization response functions. In the following section, performance of the present scheme will be presented by some numerical experiments using simple models.

3.6 Numerical experiments on the direct inversion method

Before the actual application of the two-dimensional inversion method presented in the previous sections, several numerical experiments have been made by using simple conductivity models. It will be helpful for actual interpretation to see the spatial and period dependences of the partial derivatives of the electromagnetic responses, from a simple conductivity inhomogeneity. In the numerical experiments, we examine the stability of the inversion process of Eq.(3-5-5). It is particularly important to get information about the optimum range of the covariance for a priori value of the parameter, C_{popo}, in order to stabilize the iterative process.

3.6.1 Data preparation

Electromagnetic responses were calculated for the configuration as illustrated in Fig.3.16, which consists of 2 inhomogeneities A and B and the host medium C. Numerical calculations were made according to the applied conductivity values to the inhomogeneities as shown in Table 3.1, for the period of 15 and 120 minutes for each model. The finite element network given in Table 3.2 is adopted for each numerical calculation.

Model I is the simplest, which consists of one buried inhomogeneity, whose conductivity is 10^{-1} S/m, with a rectangular cross section in a homogeneous host medium with conductivity 10^{-3} S/m. The effects of ocean on geomagnetic induction are simulated by model II.

In model III, the electromagnetic coupling will be of interest between the ocean and the buried inhomogeneity. The conductivity of sea water is taken as 4 S/m.

Theoretical responses from model I on the earth's surface are given in Figs.3.17(a) and (b). Since the model structure is completely symmetric, the resulting responses show symmetric features within errors in numerical evaluation. The apparent resistivity, either for E-polarization (ρ_a-E) or for H-polarization (ρ_a-H), takes minimum just above the conductive body. On the other hand, the amplitude of transfer function has two maxima above the side edges of the body. In general, ρ_a-H reveals a clear contrast between the subterranean inhomogeneities, while ρ_a-E gives an averaged conductivity in a volume corresponding to the skin depth. The anti-symmetric distribution of the phase of the transfer function indicates that the induction vector points to the direction of the conductive inhomogeneity on both sides of it, which is a well-known character of the induction vector. The distribution of the response functions tends to have the longer spatial wavelength for the longer period of electromagnetic field variation. This character of spatial distribution may work as a key to reveal the depth of the unknown conductive inhomogeneity.

Figs.3.18(a) and (b) give the distributions of theoretical responses from model III. The theoretical evaluations were made on seafloor-land profile. Due to the highly conductive sea water, the response shows quite anomalous feature particularly around the continental shelf. The E-polarization apparent resistivity (ρ_a-E) does not take minimum just above the conductive body, but some maximum on the shelf. This is considered to be caused by the concentration of the induced electric current in the sea water. On the other hand, the H-polarization apparent resistivity (ρ_a-H) shows a large contrast between land and seafloor: i.e. ρ_a-H on land is more than 2 order of magnitude resistive compared with that on seafloor. This variation occurs abruptly at the coast. In the H-polarization case, a charge separation will occur on the interface of the inhomogeneity, which causes the discontinuous variation in ρ_a-H around the shore line. The current concentration creates a large vertical component of the magnetic field variation not only on the seafloor but also on the coastal area inland. Transfer function is in-phase (between -90 and 90 degrees) on the right-hand side of the position of the current concentration and out-of-phase on the left-hand side. These features indicate that the induction vector points to the position of highly conductive region where a concentration of induced current occurs. Hence, the induction vector in the coastal area points to the ocean. This phenomenon is called the geomagnetic coast effect on which many investigations have been made (e.g. Parkinson 1951; Rikitake 1972). Most of the geomagnetic coast effects can be, at a first order approximation, attributed to the induction effect by the highly conductive sea water. However, electromagnetic field variation has definite information on the deeper structure. Figs.3.19(a) and (b) give theoretical responses from model Ⅱ, i.e. uniform earth model except ocean. The response functions in Figs.3.18(a) and (b), particularly on seafloor, differ from those of model Ⅱ in the absence of the subterranean conductive body (Figs.3.19(a) and (b)). These discrepancies are undoubtedly due to the existence of the conductive body beneath the seafloor. As clearly seen in these results, the induction effect from an inhomogeneous structure can't be obtained by simple superposition of response from each inhomogeneity. For example, the response of model

III can never be expected by adding the responses from models I and II. Since the situation is thus complicated, the electrical structure beneath seafloor is sometimes difficult to determine even with seafloor data (Fischer and Weaver 1986).

In the electromagnetic induction studies, most of the interest is focused on the determination of the deep electrical conductivity structure in the earth. Next we check the direct inversion scheme against the conductivity models I and III. We prepare synthetic data sets for its purpose. Fig 3.20 shows the distribution of the data point where observational data is synthesized. These are possible configurations in actual array studies. As previously stated, we perform the direct inversion only for E-polarization case. Data sites denoted by triangles correspond to those of magnetovariational observations where only the geomagnetic transfer functions are obtained, while those denoted by diamonds to those of magnetotelluric observations where the impedances, as well as the transfer functions, are obtained. Both theoretical data were synthesized from the result of the theoretical calculations by adding scatters of ± 10 % random error as well as observational errors of also ± 10 % random error.

Synthesized data sets for the model I are given in Tables 3.3(a) and (b) along the earth's surface. In case of the model III, we make preparations of synthetic data along two traverses: i.e. traverses along seafloor-land and along sea surface-land. The formers are given in Tables 3.4(a) and (b), and the latters in Tables 3.5(a) and (b). Complex data to be evaluated in the iterative process in Eq.(3-5-5) can be directly derived from the real quantities in these tables, i.e. the complex transfer function, T, is given by

$$T = \mathrm{Amp}(T)\cdot\exp[i\phi_T], \qquad (3\text{-}6\text{-}1)$$

where Amp(T) denotes the amplitude of the complex transfer function T, and ϕ_T the argument of T. The complex impedance, Z, will be written as

$$Z = [\rho_a \omega \mu]^{1/2}\cdot\exp[i\phi_Z], \qquad (3\text{-}6\text{-}2)$$

where ρ_a denotes the apparent resistivity, and ϕ_Z the phase difference between the electric and the magnetic fields.

The observation errors in the tables are used in construction of the a priori covariance of data, $C_{d_0 d_0}$, following Eqs.(3-5-26) and (3-5-27).

3.6.2 Inversion of the conductivity of a buried inhomogeneity

Here we carry out the direct inversion for the synthetic data sets from models I and III, in such a case that we know perfectly the shape of the buried inhomogeneity. Model setups are denoted by T1 and T2 in Table 3.6, respectively. In T1, we determine the conductivity of the inhomogeneity buried in a homogeneous half space by use of data from land sites, while we treat an inhomogeneity beneath the sea in T2 with data set from seafloor sites as well as land sites.

There are many difficulties in the inversion of induction problem. One of them may lie in the fact that we can not expect a 'standard structure' appropriate for an initial model, p_0. Therefore, applied initial model may happen to be apart from the optimum one by orders of magnitude. In other word, the iterative process should be stable for an initial model several orders of magnitude apart from the true one. The stability check was made by T1, the simplest model, against the initial values up to 2 orders of magnitude more and less conductive than the true conductivity. Results of the direct inversion for T1 are tabulated in Table 3.7. As shown in the table, each iterative process converged to the conductivity value sufficiently close to the true one. Although the iteration of 6 cycles was made to get each result, it is found that at most 4 cycles are enough for sufficient convergence as shown in Fig.3.21. Fig.3.22 shows how improved the parameter is by the iteration, by comparing the observed ρ_a-E with the theoretical one from the initial conductivity of 1×10^{-3} S/m (above) and the final conductivity (below). The initial model is the perfectly homogeneous one, and therefore, the calculated apparent resistivity is constant everywhere in spite of the large variation in the observations. After 6 cycles of iteration, however, the model is so much improved that the final model well explains the observation. χ^2 of the impedance has reduced by more than two orders of magnitude as shown in Table 3.7. Fig.3.23 gives the same comparison for the transfer function. In the initial homogeneous model, the amplitude of the transfer function is null anywhere(above) since no vertical component of the magnetic field is produced, while the final model gives a good agreement between the observation and the calculation(below). χ^2 of the transfer function has also reduced by nearly three orders of magnitude by the iteration (Table 3.7).

In case the initial value apart from the true one by one order of magnitude,i.e. 1 S/m and 1×10^{-2} S/m, the process is considered to be quite stable since convergence has been achieved for a priori covariance, $C_{p_0p_0}$, as large as 8. This means that the nonlinearity is weak for this case, according to the discussion in section 3.5.3. On the other hand, the cases of initial values with more and less conductive by two orders have not converged until $C_{p_0p_0}$ as small as 5 x 10^{-2} and 1 x10^{-1} have been applied, respectively. In these cases, the nonlinearity of the process becomes so severe that the next point in each iteration step given by Eq.(3-5-5) is sometimes quite far from the solution. Thus, large constraints on the initial parameters are required in order to stabilize the process.

Figs.3.24(a) and (b) give the distributions of the partial derivatives of d_Z and d_T with respect to the parameter, p_1 = log[σ_1], when the conductivity of the inhomogeneity σ_1 is taken as 10^{-2} S/m. The partial derivative at each observation site gives the information on the sensitivity for the structure. At a site with a large partial derivative, we can expect a significant change in the response functions for a slight change in the conductivity of a given structure. This means that the site is sensitive to the conductivity of the structure. On the other hand, when the partial derivative at a site is quite small against the conductivity of a given structure, the site is called quite insensitive to the structure, because the response function will be almost the same for any values of the conductivity. As clearly seen on these figures, the absolute value of $\partial d_Z/\partial p_1$ becomes maximum just above the inhomogeneity, while that of $\partial d_T/\partial p_1$ has two maxima corresponding to the side edges of the inhomogeneity. These figures clearly show that the impedance obtained at a site is the most sensitive to the conductivity of the inhomogeneity just below the site, while the transfer function is sensitive to the conductivity contrast, or lateral heterogeneity, in the subsurface structure.

The amplitude of the partial derivative at each observation point indicates how largely the observed data is fed back to the next iteration of the parameter in Eq.(3-5-5). If the observations were made without errors, the iterative process will always converge (Tarantola and Valette 1982). Otherwise, convergence depends on both the partial derivatives and the initial covariance. If the derivatives are quite small everywhere and if the initial covariance is small, then the next points never move away from the initial point, because the iterative process is perfectly controlled by the set of initial parameters. On the other hand, if the initial covariance is very large, the process will become unstable because each next point of the parameter assigned by tangent linear projection at each observation point will have large scatter due to the observation errors. Thus, the partial derivative and the a priori covariance are both important information on the stability and the reliability of the inversion process. Discussion will be held later again.

In case of the existence of the sea, the nonlinearity becomes somewhat larger. Table 3.8 gives the results of the direct inversion for T2: i.e. the same inhomogeneity lies below the seafloor. Numerical evaluations were made for the initial values with one order of magnitude more and less conductive than the true conductivity ($1\text{x}10^{-1}$ S/m). In either case, the iteration has converged stably to the value sufficiently close to the true one after 6 cycles. χ^2's, both for the impedance and the transfer function, have been reduced by more than two orders of magnitude by the iteration (Table 3.8), i.e. the same level as in the previous result. However, the initial covariances in Table 3.8 are found to be about one order of magnitude smaller than those for the same initial parameters in the previous example (Table 3.7). This difference indicates that the electromagnetic coupling between the highly conductive sea water and the buried inhomogeneity below enhances the nonlinearity of the problem.

Fig.3.25(a) gives the distribution of the partial derivative of the impedance along the seafloor-land traverse. Similar to the case of homogeneous host medium (model T1), the absolute value of $\partial d_Z/\partial dp_1$ has maximum above the inhomogeneity. But the distribution is not symmetric. The derivative tends to remain large in the offshore side compared to the inland side. This indicates that the seafloor measurement is more sensitive to the inhomogeneity beneath sea than the land measurement. The derivative of the transfer function, $\partial d_T/\partial p_1$, (Fig.3.25(b)) has quite different behavior from one for model T1. It has only one maximum on the deepening slope. The position, where the derivative is maximum, moves offshore for longer period, and does not coincide with the position where the transfer function becomes maximum (Cf. Fig.3.18(a) and (b)). Thus, we can not always guess the most sensitive position for an unknown structure only by referring the distribution of the amplitude of the expected response functions. Anyway, the derivatives in models T1 and T2 has large amplitude enough to provide sufficient amount of feed back in the iterative process Eq.(3-5-5), and thus stable nature of the iteration process can be expected.

3.6.3 Direct inversion with unknown block configurations

The previous results have shown some examples of the application of the present method, in the simplest case where the shape of the inhomogeneity with an unknown conductivity is perfectly known. In actual applications, we can obtain the information on the shape of the boundary with reference to not only electromagnetic but also other geophysical, geological and geochemical investigations. If such information is not sufficient to get complete description of the subsurface structure, however, we have to carry out the inversion with unknown block configurations. Here we check such a case by numerical experiments with the same data sets as those in the previous section.

When the shape of the inhomogeneity of model I is not given, one of the possible configuration may be presented by Fig.3.26 (above) with 4 blocks denoted by numbers from 1 to 4, whose conductivities are unknown. If the inhomogeneity exists below ocean, i.e. model III, configuration of the array will be given by Fig.3.26(below). We consider three cases here, i.e. models T3 with homogeneous host medium, and T4 and T5 with ocean, with observations along seafloor-land and sea surface-land traverses, respectively.

In model T3, the initial conductivity of 1×10^{-2} S/m, which is one order of magnitude higher than the true value, has been adopted to both blocks No.1 and 4. On the other hand, 1×10^{-2} and 1 S/m have been applied for the initial conductivities of the blocks No.2 and 3 whose true conductivities are both 1×10^{-1} S/m. Table 3.9 gives the results of the two cases for model T3. Here again sufficient convergence has been obtained by six cycles of iteration for each case. χ^2's of the impedance and the transfer function for the final model are by more than two orders of magnitude smaller than those for the initial model in either case. Therefore, these final models can be considered to explain the observation to similar extent to those of model T1. The conductivities of the conductive blocks, No.2 and 3, are estimated considerably close to the true values. However, those of the resistive blocks, No.1 and 4, are apart from the true values by factor of about five for each, in spite of the stable behavior of each parameter in the iteration process (Fig.3.27). The relatively small values of the initial to final covariance ratio, C_{popo}/C_{pp} less than 2, indicate that the present method has weaker resolving power for the resistive structure. This seems a quite reasonable result, for the more conductive structure will have the stronger induction effect. Thus, the initial to final covariance ratio reveals the information on the resolution of each unknown.

Figs.3.28(a) and (b) show the distribution of the partial derivatives of the impedance and the transfer function with respect to the conductivity of block No.1 (shaded area), while Figs.3.29(a) and (b) give those with respect to the conductivity of block No.2, in case the same initial conductivity 1 S/m is assigned to blocks 2 and 3. Figs.3.30(a), (b) and Figs.3.31(a), (b) are the same plot in case of the initial conductivity of 10^{-2} S/m for all blocks. The derivatives with respect to the blocks no.3 and 4 are not presented here because their distributions are easily obtained from these figures because of the perfect symmetricity of the model.

In a linear problem, the partial derivative with respect to p_1 should be the same as that to p_2 regardless of the assigned conductivity or the surrounding structure. However, as shown in these figures, the derivative with respect to an inhomogeneity depends not only on the surrounding conductivity structure, but also on the conductivity of itself. Hence, different distribution of conductivity results in different distribution of the partial derivatives, even if the block configurations are completely the same, particularly when the conductivity contrast is large as shown Figs.3.28(a) and 30(a).

When the structure with an unknown block configuration lies below ocean, the problem becomes much more difficult because of the inductive coupling between the sea water and the conductive structure. Table 3.10 gives the result of the inversion for model T4 with observations along seafloor-land traverse. Here, we show only one example with the initial conductivity of 10^{-2} S/m for each block No.1-4. The iterative process has converged after as many as 16 cycles of iteration. Rather complicated behavior of each parameter during the iteration (Fig.3.32) suggests that the process affects strong non-linear effects. The final conductivity of each block, however, is as close to the true value as that in the model T3. Having similar values of initial to final covariance ratio to those in Table 3.9 indicates that the block conductivities have been resolved to similar extent to that in model T3 without ocean.

The inversion could not be stabilized unless we applied the initial covariances of the parameter of submarine blocks, No.1 and 2, to be half of those below the shallower sea, No.3 and 4. This indicates the non-linear effect is more severe beneath the deeper ocean, in determination of the parameter. Figs.3.33(a), (b), (c) and (d) give the distributions of the partial derivatives of impedance, while Figs.3.34(a),(b), (c) and (d) those of transfer function, with respect to the conductivities of the blocks No.1, 2, 3 and 4, respectively. In this case, the distributions of the derivatives with respect to p_1 and

p_2 are not symmetric to those to p_4 and p_3, respectively, as was the case in the previous example. However, each derivative having the similar amplitude indicates that the synthetic observations have similar resolving power against each block. Hence, with the seafloor data, the parameters of the blocks beneath ocean can be successfully determined.

On the other hand, determination of the same conductivity structure with data sites along sea surface-land profile becomes sometimes quite difficult. Table 3.11 gives the result of direct inversion of the same situation as given in Table 3.10 without seafloor data but with sea surface data (T5). As shown in the table, the conductivities of the blocks No.1 and 2 have scarcely been improved by 6 cycles of iteration, for their final values are almost the same as their initial ones. The weaker resolution is also indicated by the values of $C_{p_0p_0}/C_{pp}$ nearly equal to unity, which is about one order of magnitude smaller than those of blocks No.3 and 4. The corresponding partial derivatives are shown in Figs.3.35(a), (b), (c) and (d), and Figs.3.36(a), (b), (c) and (d) with respect to the conductivities of blocks No.1, 2, 3 and 4, respectively. The derivatives have similar amplitude against the blocks no.3 and 4 to those in the previous example. However, those against the blocks no.1 and 2 are about one order of magnitude smaller even for the maximum value. The small value of the partial derivative means the small amount of the feed buck in the iterative process. Therefore, the conductivities of these two blocks have been determined unsuccessfully, although they behaved quite stably in the iteration (Fig.3.37). The maximum values of the derivatives are less than 10^{-2} both for impedance and transfer function, while they exceed 10^{-2} in the above examples. Thus, one of the requirements for the reliable convergence may be stated as having the partial derivative exceeding 10^{-2}.

Above result clearly shows the importance of the seafloor data in determining the conductivity structure below ocean. Observation on the sea surface, though actually not practical, is not sufficient for the purpose, because partial derivative is much attenuated on the surface through the conductive sea water. Ocean with 4 km depth will provides difference of one order of magnitude in the amplitude of partial derivative between the bottom and the surface as shown in Fig.3.38.

30 data points have been used in the above experiments: i.e. impedances at 5 sites and transfer functions at 10 sites, for the periods 15 and 120 min. On the other hand, the number of blocks able to be determined by the present method seems to be at most 4 or so, because the experiment on the model T4 with 8 blocks was found to be unstable for the initial model one order of magnitude apart from the true one. This maximum number may seem too few compared with the total number of data. However, the maximum number can be considered as proper one for the number of blocks, by taking into account the following facts:

1) Data at one period obtained at a site does not provide information completely independent on data at other periods. As previously explained, electromagnetic response function contains information on the subsurface structure as a sort of volumetric average. The longer the period is, the larger the volume of averaging becomes, i.e. each response gets information on the deeper and wider structure.

2) Nearby site provides similar response functions to each other and, therefore, not independent. This is also because of the same reason as

before: i.e. the response function is derived from a sort of average in a volume.

3) Each data has not a unity weight in the iterative process given by Eq.(3-5-5). The weight of each data point is defined as a reciprocal of the squared standard error following Eqs.(3-5-26) and (3-5-27). Thus, sum up of the contributions from all data points in the iteration does not equal to the number of points, but far less than that. Besides, each data has, as well as the observational error due to instrumental and stochastic origins, bias error or scatter in the estimated value. The present method will give an optimum model, which explain the observations, by the least squares.

4) The partial derivative is the solution of the matrix equation given by Eq.(3-5-17). As previously stated, the matrix equation represents a induction equation with a source term vector $c=-\partial A/\partial p_j \cdot u$, where A denotes the characteristic matrix of the induction equation and u the solution vector of the induction equation with an external uniform source. Considering the nature of the induction equation, the amplitude of the solution $\partial u/\partial p_j$ will depend on both the volume and the depth of the unknown block;i.e. the amplitude of the derivative will be enlarged with increasing volume of the block at the same depth; it will be reduced with increasing depth of the block with the same volume. Hence, the present method can not be applied to such a small block division that creates derivatives with amplitude less than 10^{-2}.

3.6.3 Summary of the numerical experiments

Several numerical experiments have thus clarified some characteristics of the present inversion method. Some criteria relating to the reliability of the solution have also been established, which will be summarized as follows:

1) It is shown numerically that the impedance gives information on the conductivity of the structure just below the observation site, while the transfer function provides high sensitivity to the lateral heterogeneity of the structure.

2) The relation between the degree of freedom of the model and the stability of the inversion has been established. Letting the number of unknown conductivities S and the minimum number of data M, the critical ratio can be empirically given as

$$M / S \sim 8 \qquad (3\text{-}6\text{-}3)$$

3) The maximum amplitude of the partial derivative is found to work as an important key on the convergence and the reliability of the solution. The initial to final covariance ratio has also information on the reliability. The amplitude of the partial derivatives both of impedance and transfer function should be greater than about 10^{-2} for reliable solution. Solutions, with the covariance ratio less than about 1.5 should be regarded as unreliable ones even if the convergence seems apparently stable.

4) The present method is found to provide the higher resolving power for the more conductive structure. This seems a proper result because the larger induction effect is generally expected from the higher con-

ductive structure.

5) The numerical experiment has definitely revealed the importance of the seafloor data in determining the structure below ocean. Resolution will be much reduced if the inversion is performed even with data on the surface of ocean.

6) Perturbation field is sometimes enhanced on the continental shelf and slope, and the enhancement brings large amplitudes of partial derivatives in these area. The model experiments indicates that the electromagnetic measurements on and around the continental shelf area are of particular importance in the inversion of structure beneath the ocean-continent transition zones.

7) The a priori covariance C_{popo} is applied rather empirically in the present method. At first, each diagonal element $C_{popo}(i,i)$ is equally given by

$$C_{popo}(i,i) = C_o \cdot 2^{-(S-1)} \qquad (3\text{-}6\text{-}4)$$

where S is the number of blocks with unknown conductivity. C_o takes the value between 1 and 10, depending upon the complexity of the 'host medium' and the error level in the observational data. In the extreme case with data set without error, C_o may be as large as infinite to converge the process, which is called the purely overdetermined problem. If the host medium contains a highly conductive layer near the surface, such as the ocean, appropriate value of C_o will be about 1. If large scatter is recognized in data, smaller value should be applied to C_o. Then, for the applied initial model, a few steps of iteration are carried out. If the expected value of a parameter seems too stable, its initial covariance is doubled. When a parameter varies by orders in each iteration step, value given by Eq.(3-6-4) is replaced by its half. For moderately changing parameters, several factors in each step, no action is taken. This procedure is repeated until a set of optimum value of C_{pop0}'s is obtained. After making sure of the stability of each parameter, total inversion of Eq.(3-5-5) is performed. Convergence of the process is confirmed by referring the variation of each parameter, as well as the residual χ^2's of both impedance and transfer function between observed and calculated values. The iterative process is terminated when few change is recognized in either each parameter or each χ^2.

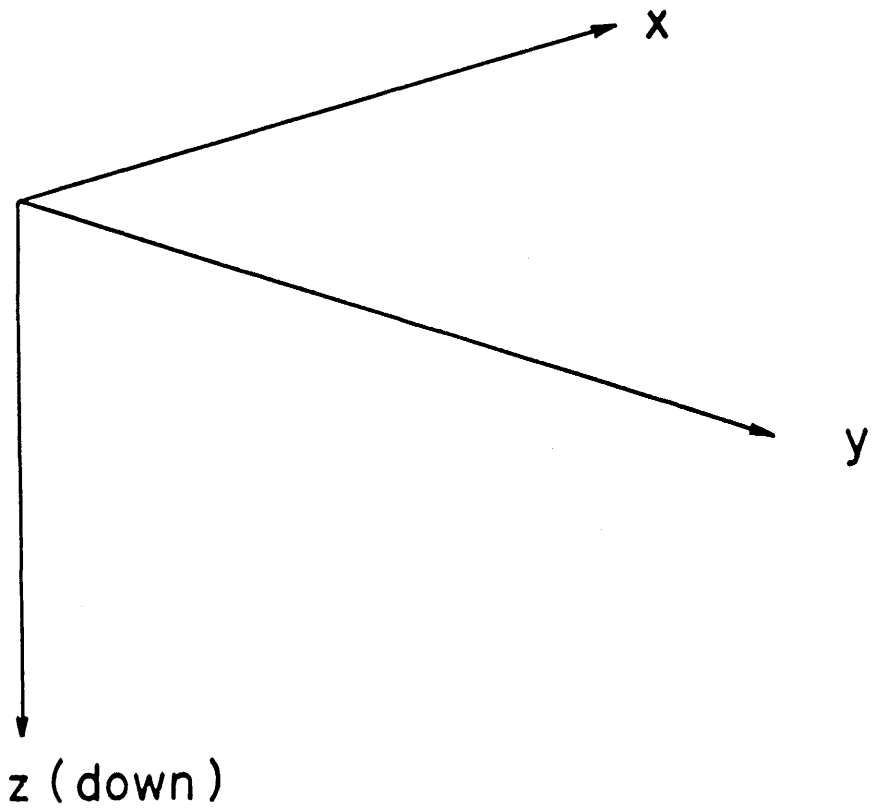

Fig.3.1 Coordinate system used in this study. In two-dimensional case, x, y and z axis are taken to be parallel to the trend of the structure, perpendicular to it and downward, respectively.

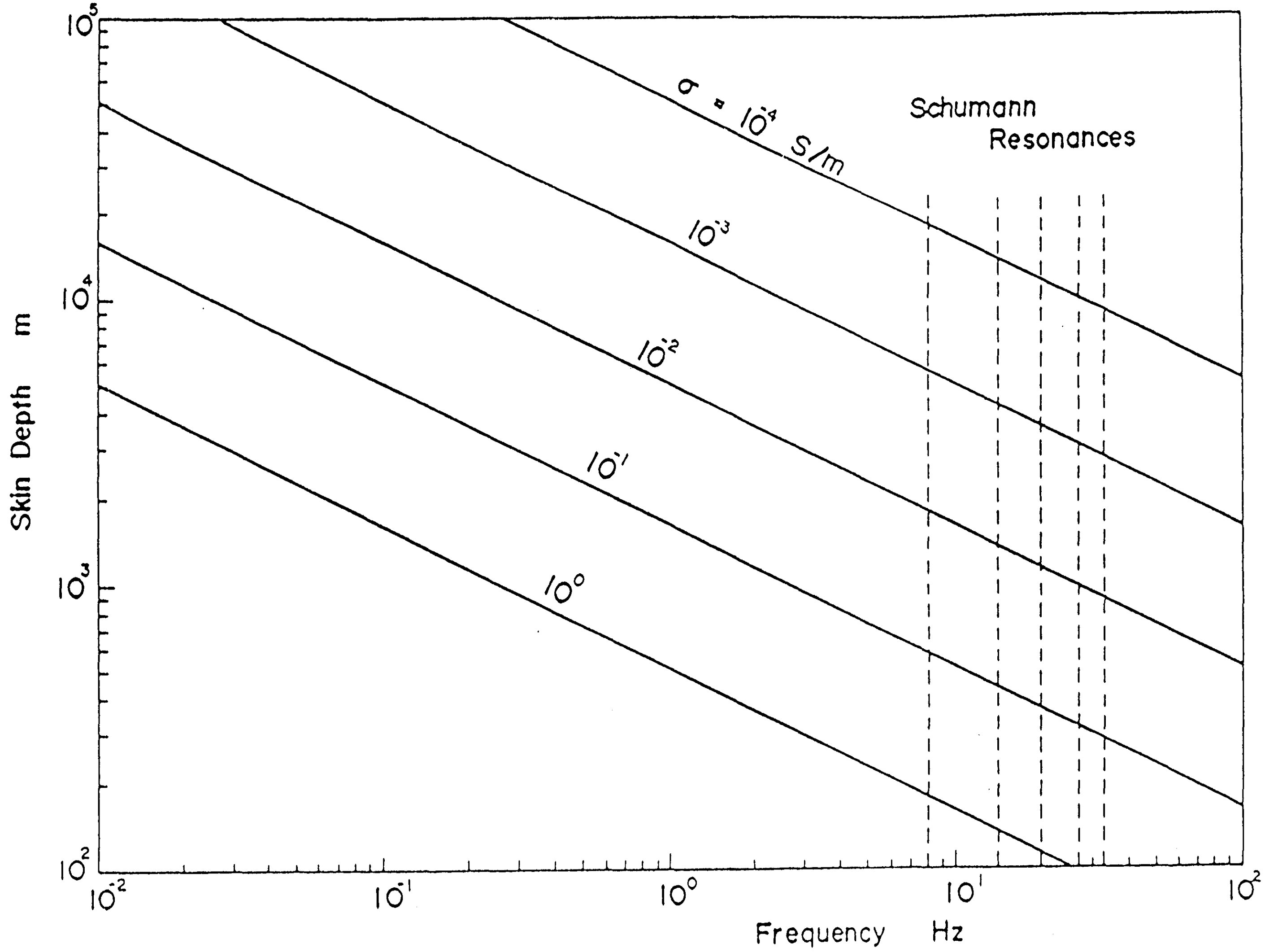

Fig.3.2 Relation between the skin depth and frequency for various conductivities. Dashed lines indicate the Schumann resonance frequencies.

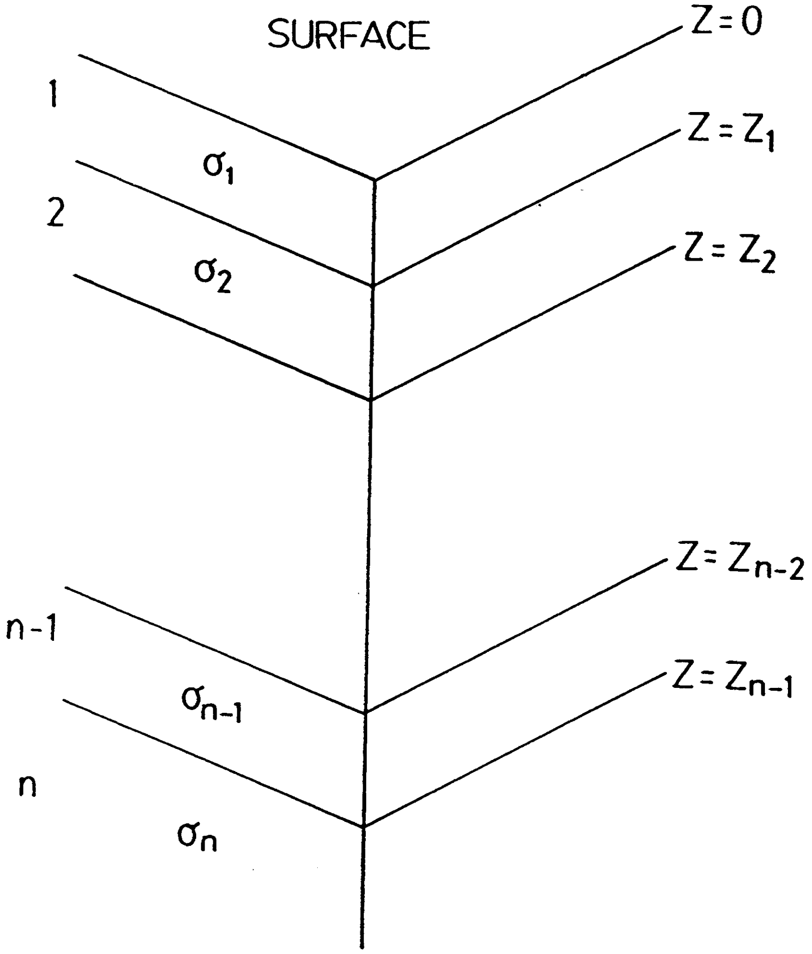

Fig.3.3 Horizontally stratified earth model.

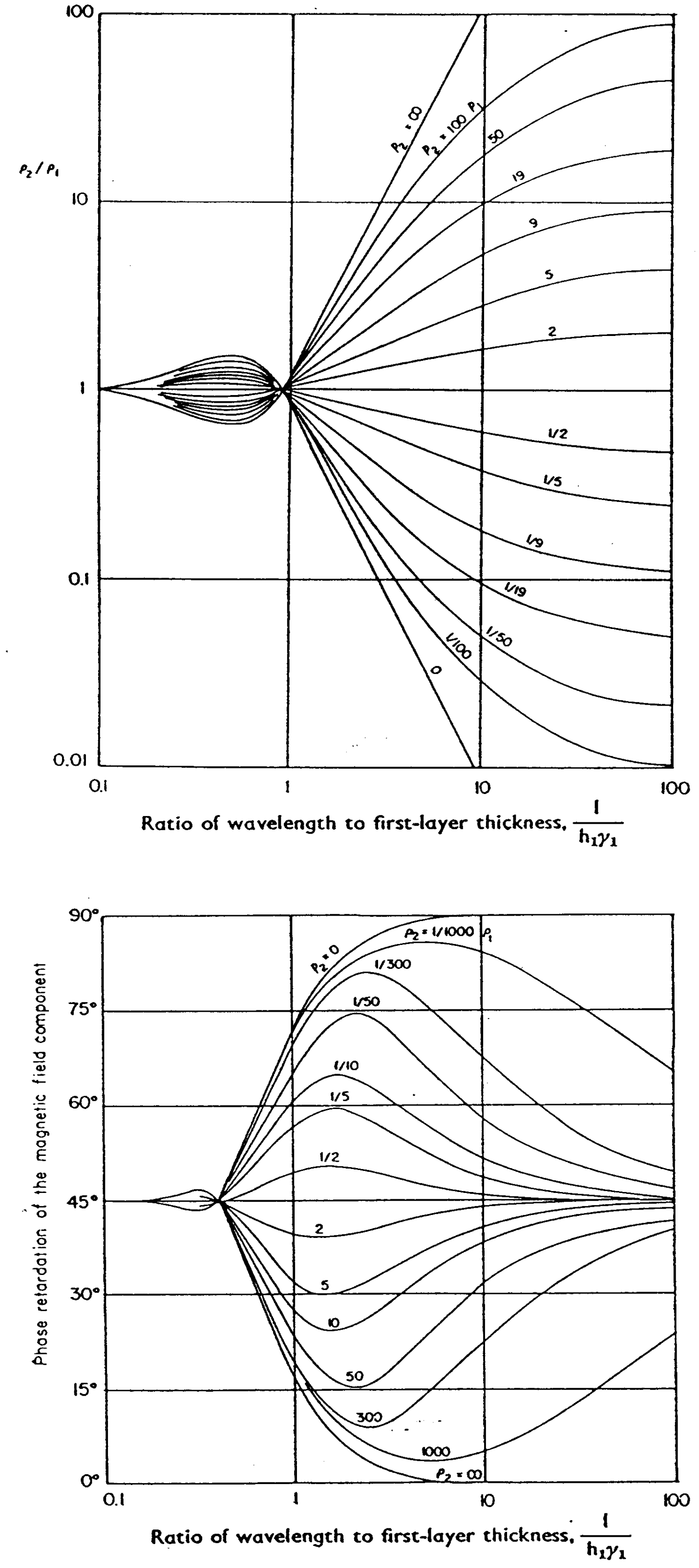

Fig.3.4 Theoretical magnetotelluric sounding curves for two layered earth model (after Keller and Frischknecht, 1966). The apparent resistivity (above) and phase (below) are plotted against the ratio of wavelength to first layer thickness for various resistivity contrast.

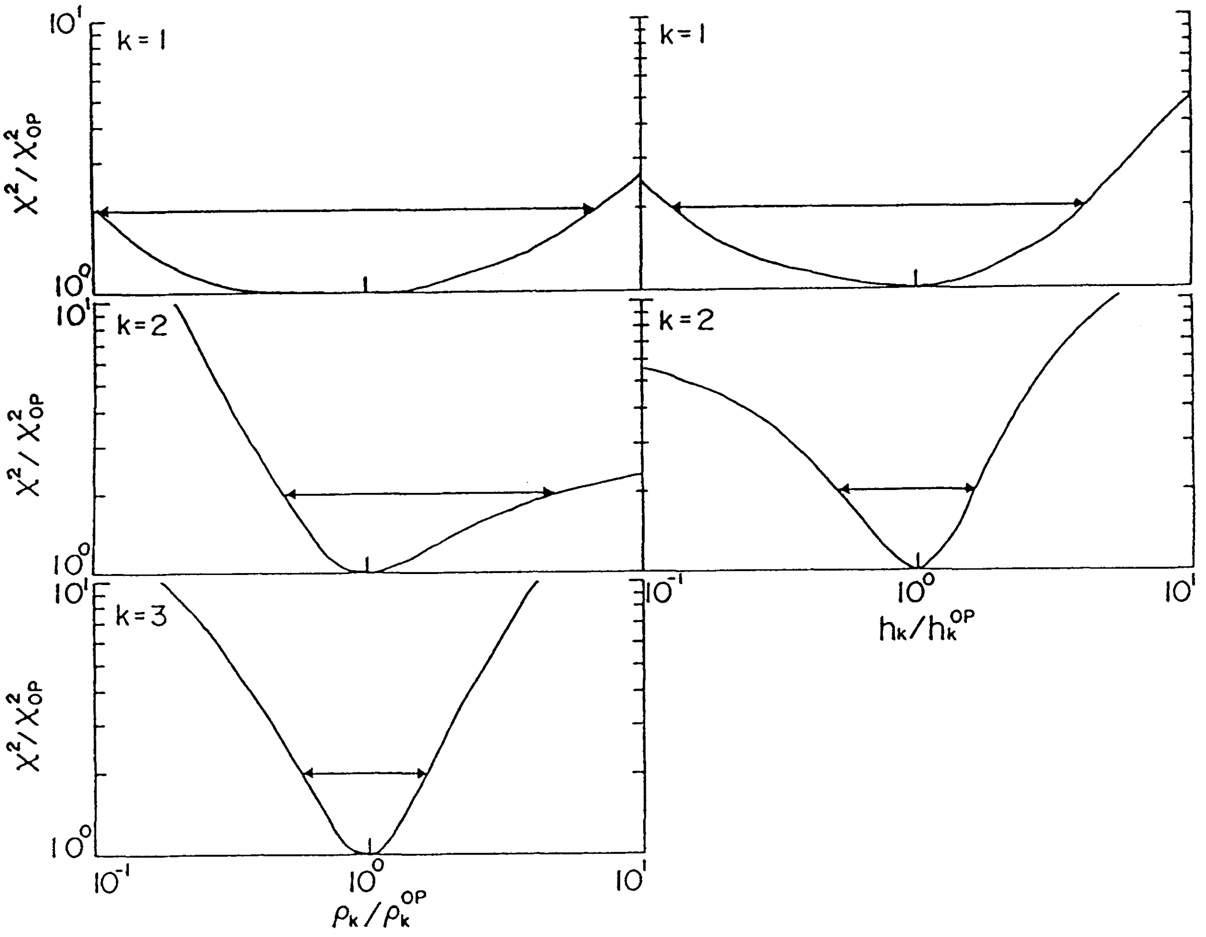

Fig.3.5 χ^2-ρ_i (left) and χ^2-h_i (right) cross sections. Half width of each curve gives the measure of the confidence interval of each parameter.

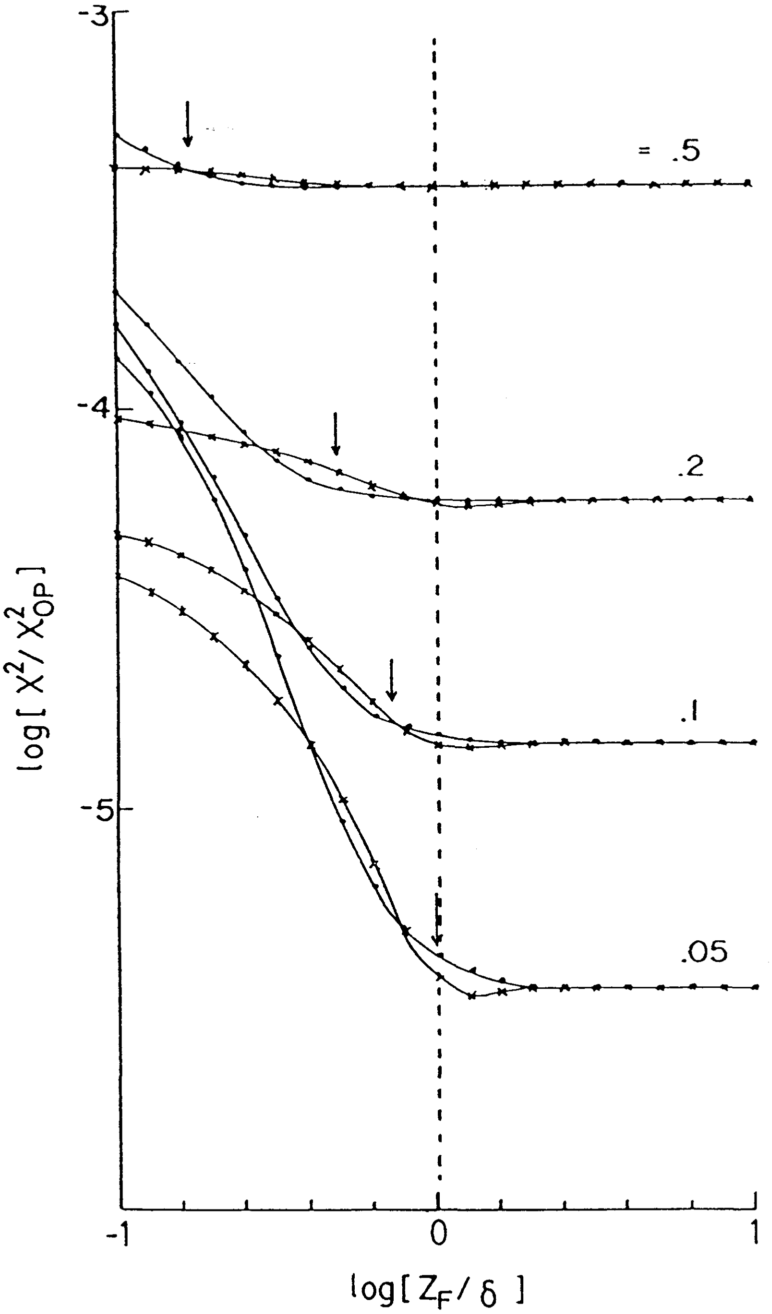

Fig.3.6 Relations between χ^2 and the depth of the fictitious boundary, for four levels of scatter. Arrow indicates the estimated maximum sounding depth for each case. See text for details.

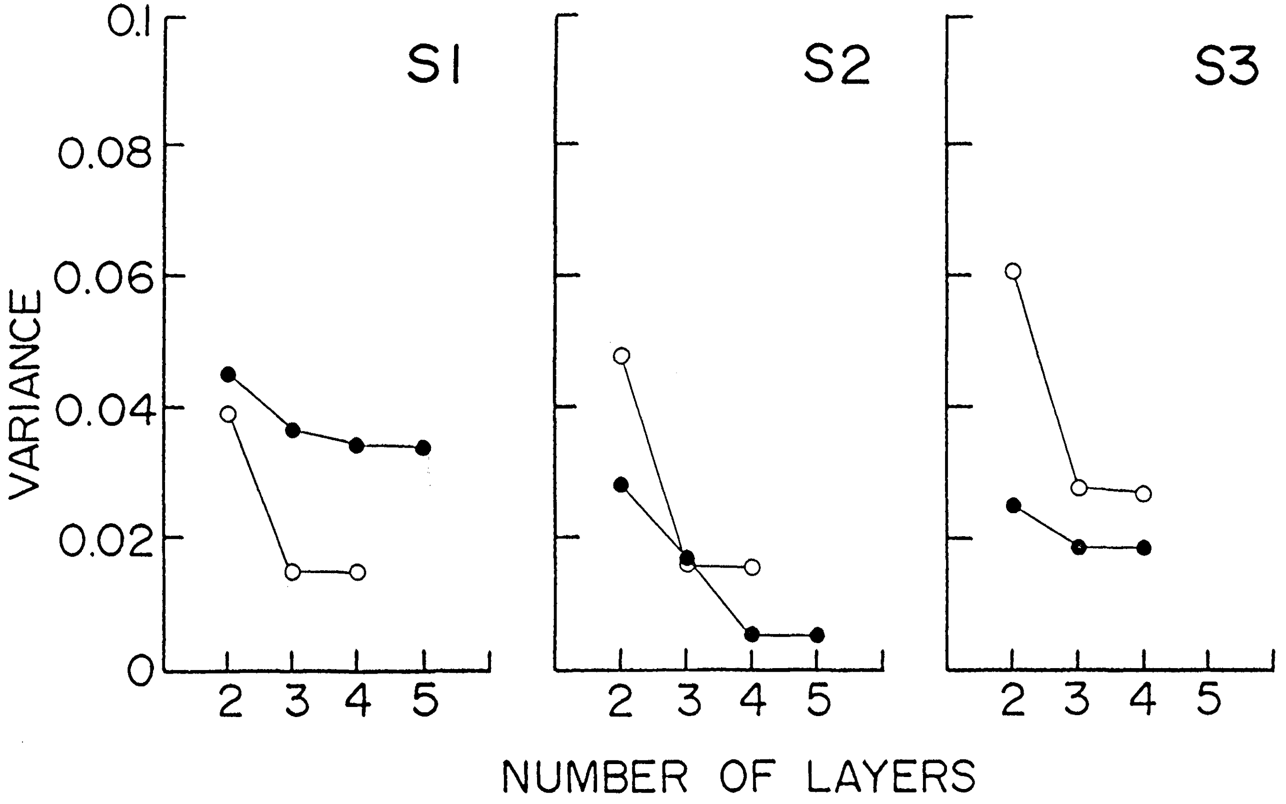

Fig.3.7 Behavior of variance (χ^2) with increasing number of layers. Closed and open circles correspond to the off-diagonal elements of impedance tensor, Z_{xy} and Z_{yx}, respectively.

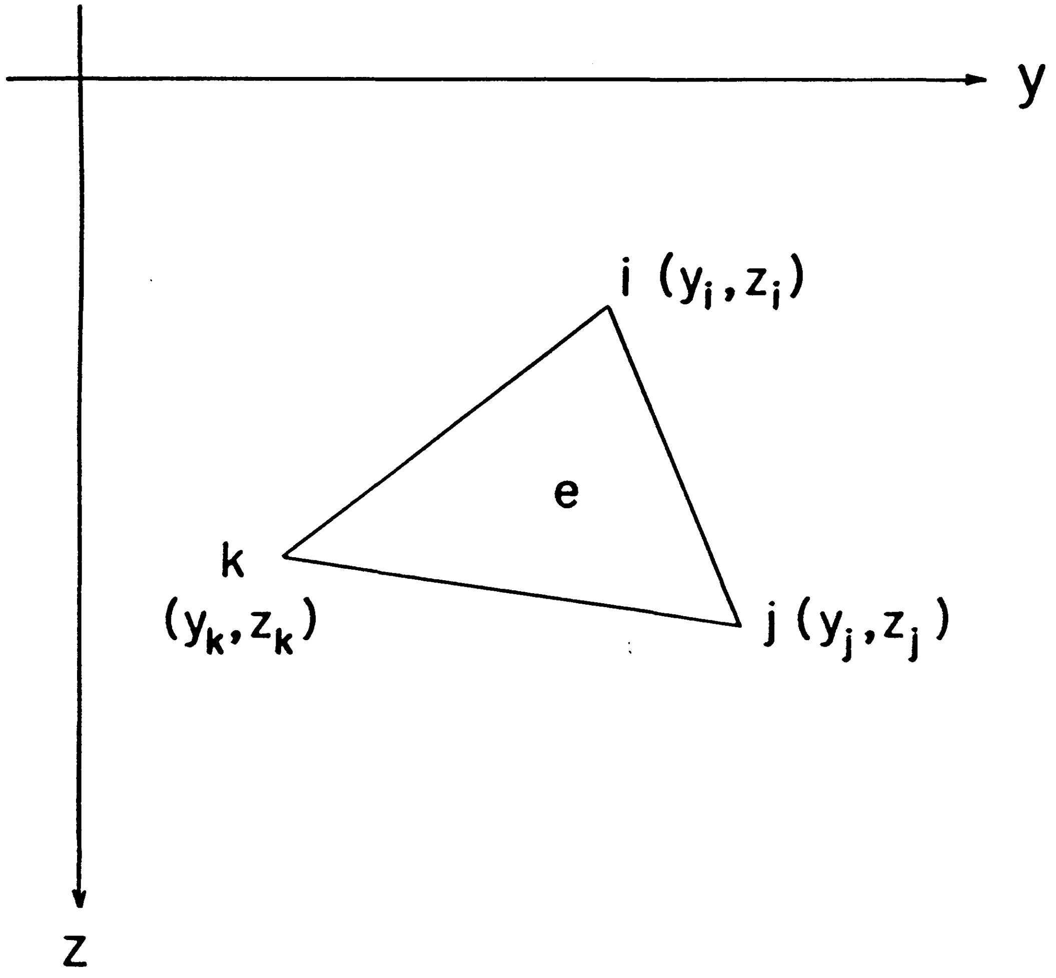

Fig.3.8 The e'th element of the finite element network.

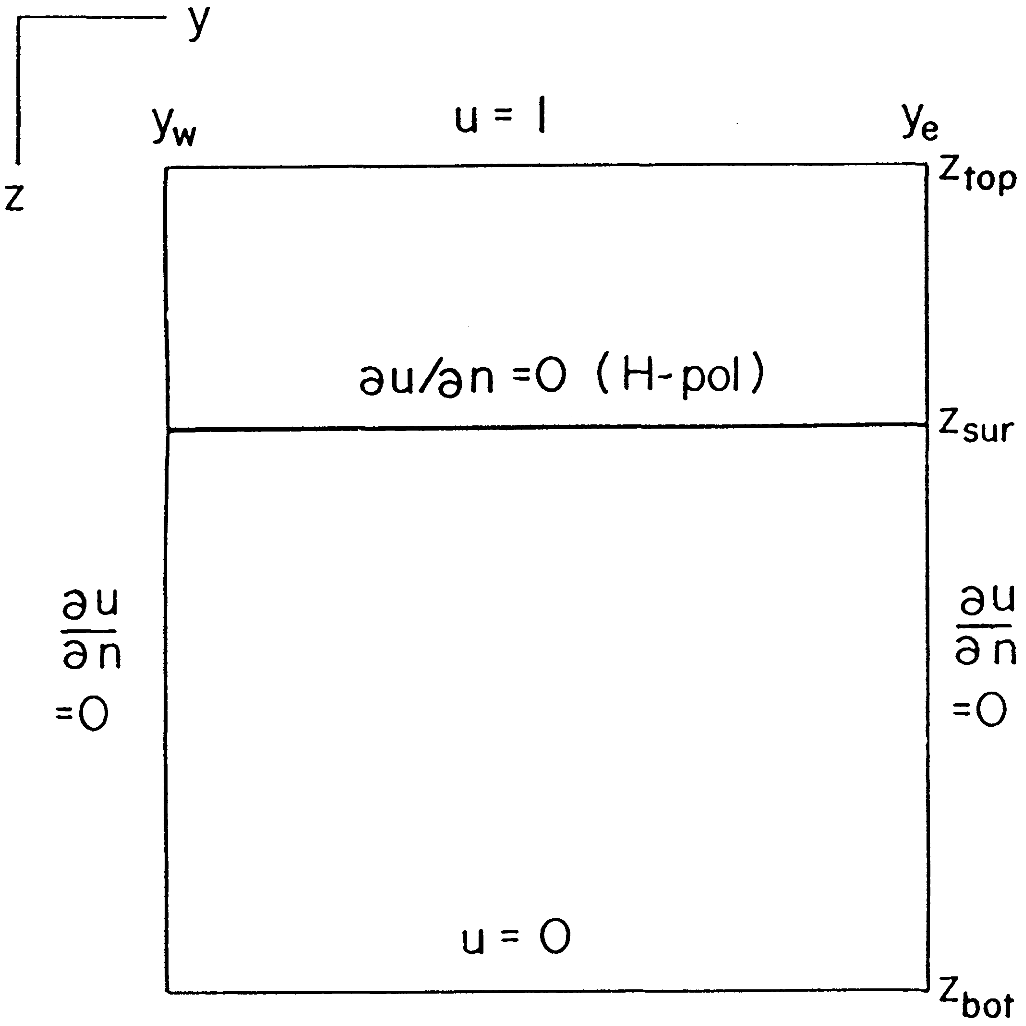

Fig.3.9 Setup of boundary conditions for two-dimensional modeling. Conditions on top, both sides and bottom are applied for both E-and H-polarization cases. Condition on the earth's surface is used only for H-polarization case.

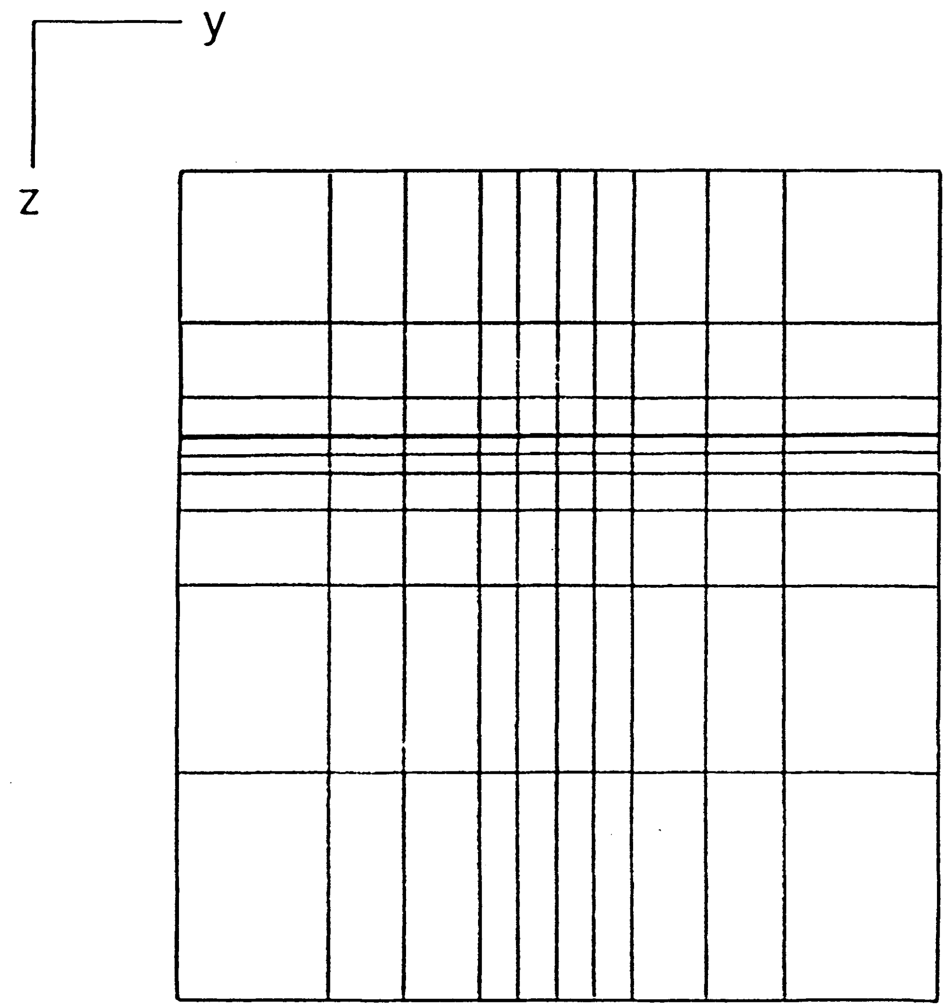

Fig.3.10 The initial step of the mesh division. Entire space is divided into 10 rows and 11 columns.

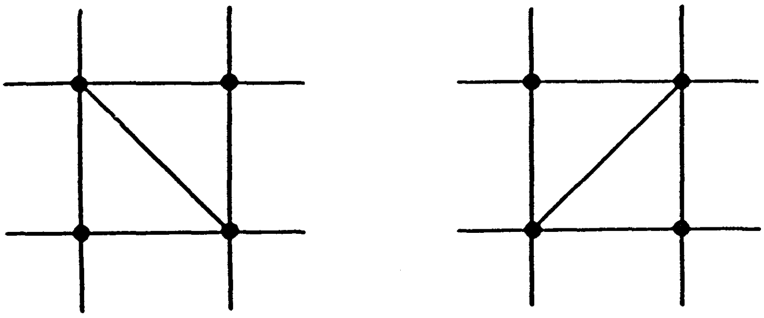

Fig.3.11(a) Two ways for separation of a rectangle into two triangles by a diagonal line.

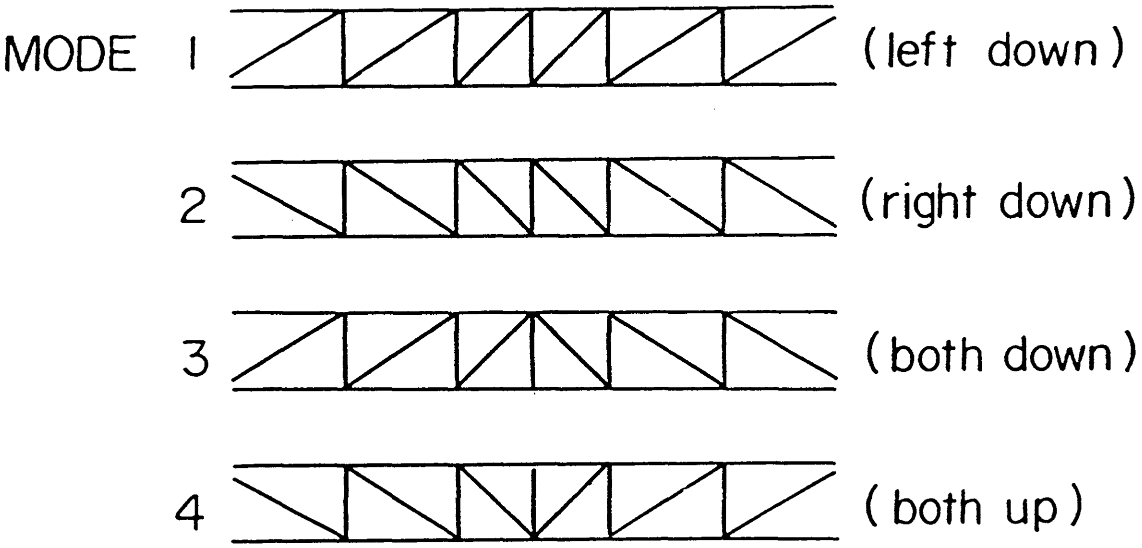

Fig.3.11(b) Four modes for separation of rectangles in a row.

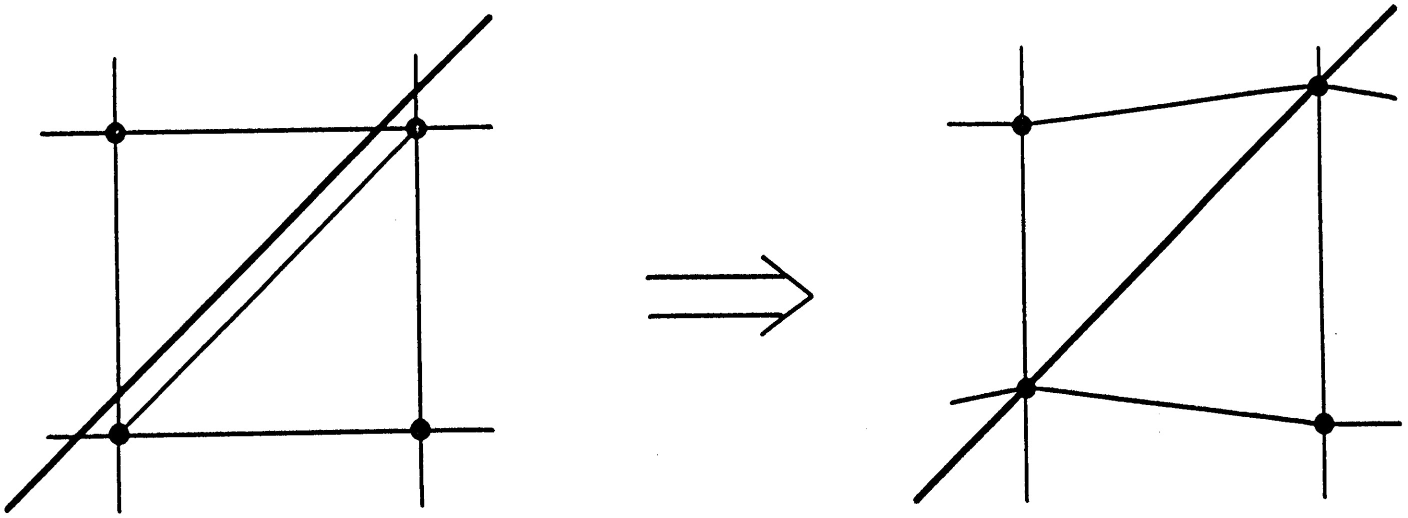

Fig.3.12 Adjustment of nodes onto the block boundary of an inhomogeneity. Thin and thick lines denote the boundary lines between the elements and the blocked structure. When any nodes are not on the boundary (left), the nearest nodes are shifted on to the block boundary (right).

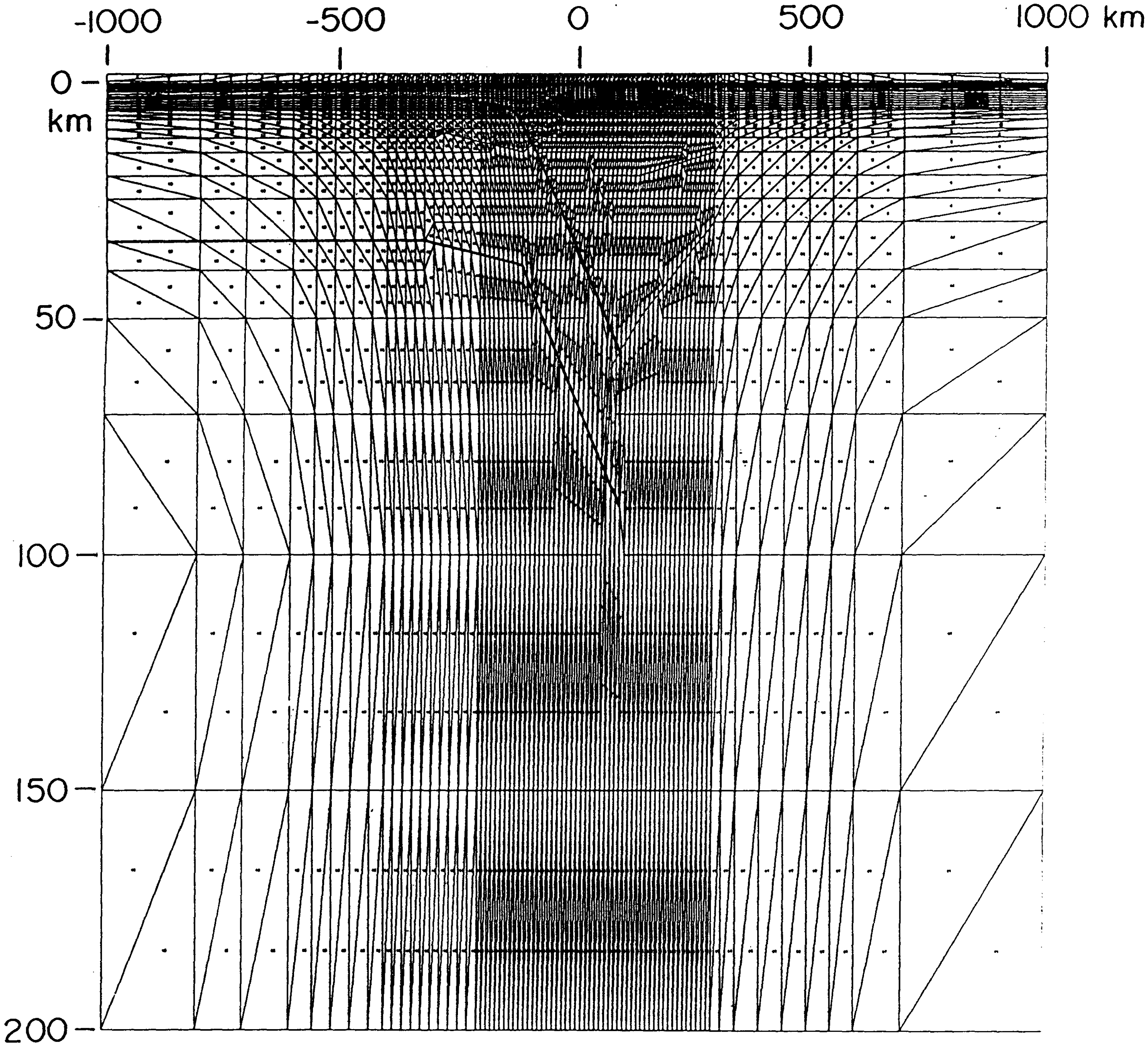

Fig.3.13 A mesh network for the cross section of central Japan. Note that the subducting Philippine Sea Plate (thick line) is represented by smooth line.

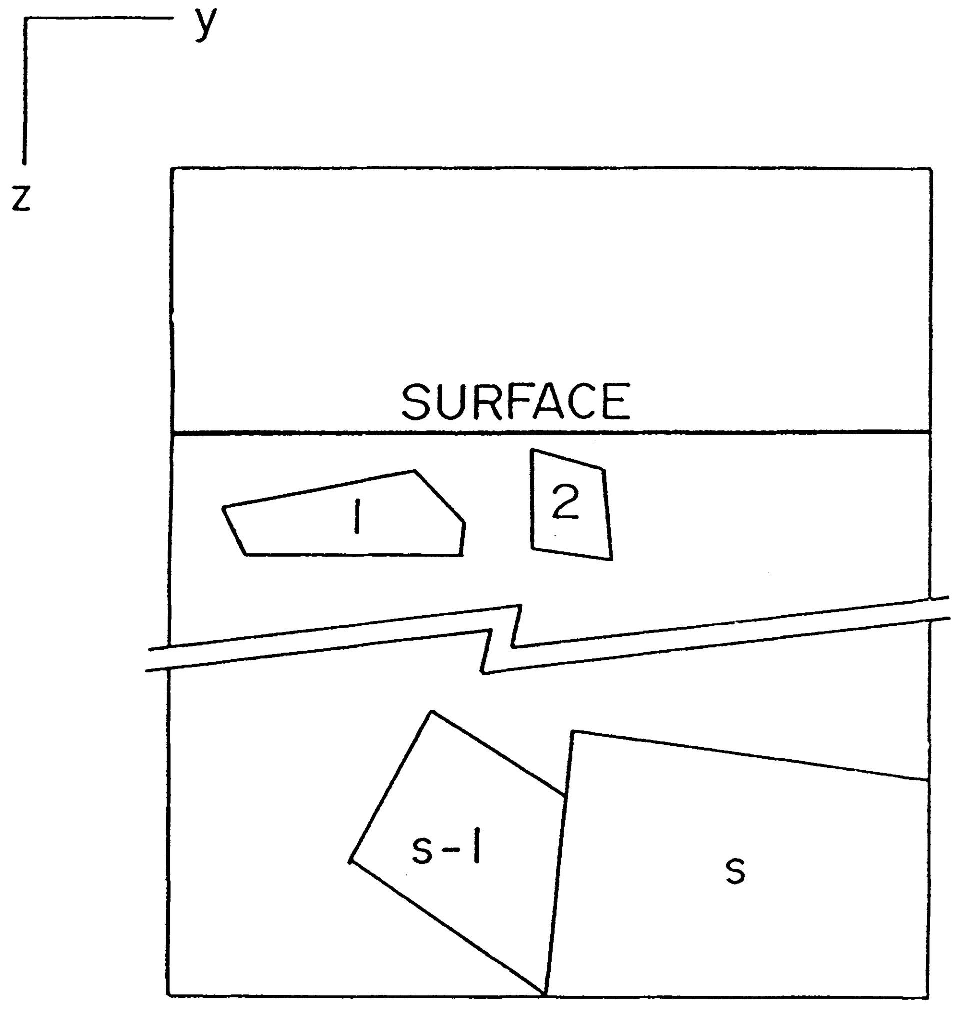

Fig.3.14 A schematic cross section of a conductivity model for the two dimensional inverse problem. Inhomogeneities with unknown conductivity are numbered from 1 to s.

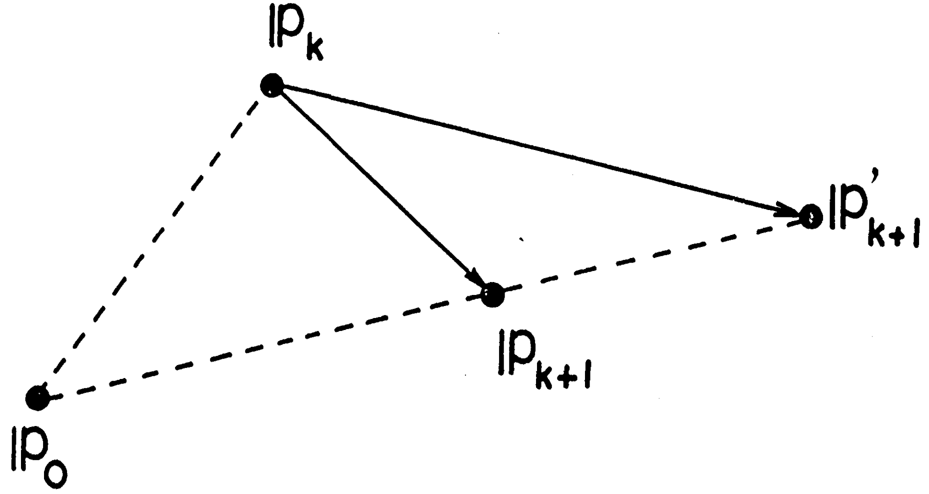

Fig.3.15 A schematic diagram showing the k'th cycle of the iteration process. p_k is the current point of the parameter set. p_{k+1}' is the next point when the term of a priori constraints, $-C_{p_0p_0}(p_k-p_0)$, is neglected in Eq.(3-5-5). The next point in the present algorithm, p_{k+1} is always closer to the initial point, p_0, than p_{k+1}'.

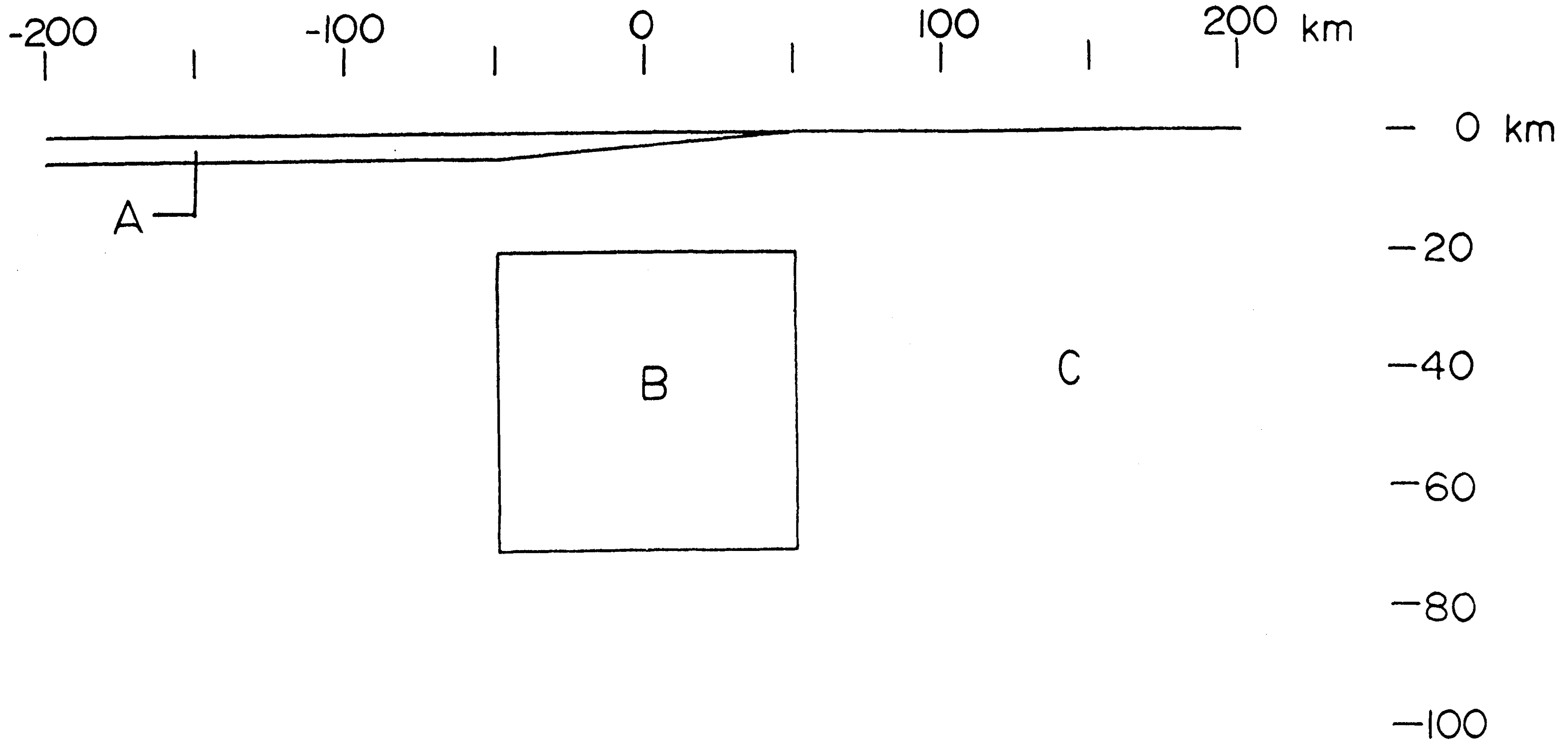

Fig.3.16 A model configuration for the numerical experiment.

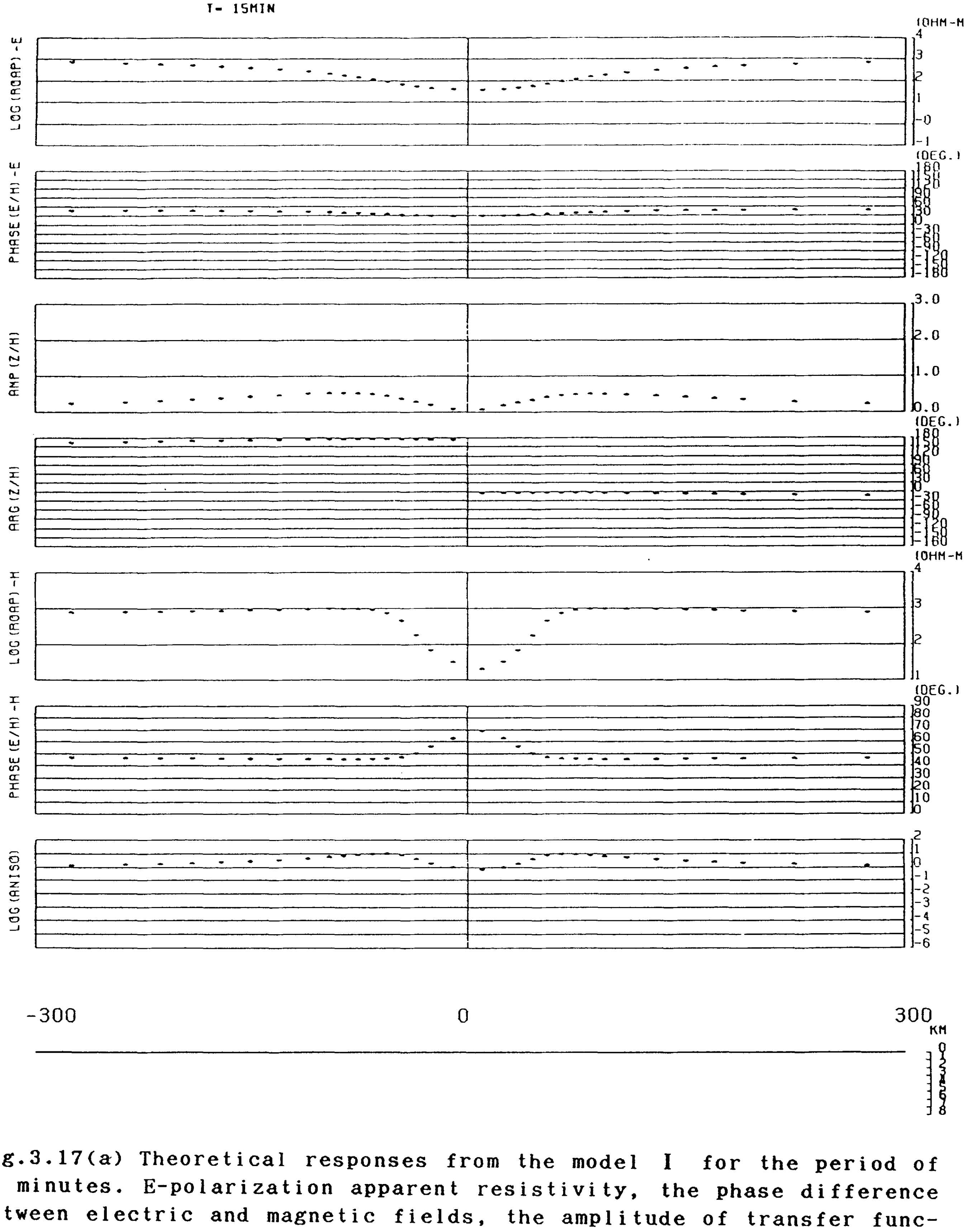

Fig.3.17(a) Theoretical responses from the model I for the period of 15 minutes. E-polarization apparent resistivity, the phase difference between electric and magnetic fields, the amplitude of transfer function, its phase, H-polarization apparent resistivity, the phase difference, and the ratio of E- to H-polarization apparent resistivity are plotted from above to below. Data points situate on a flat surface as shown at the bottom.

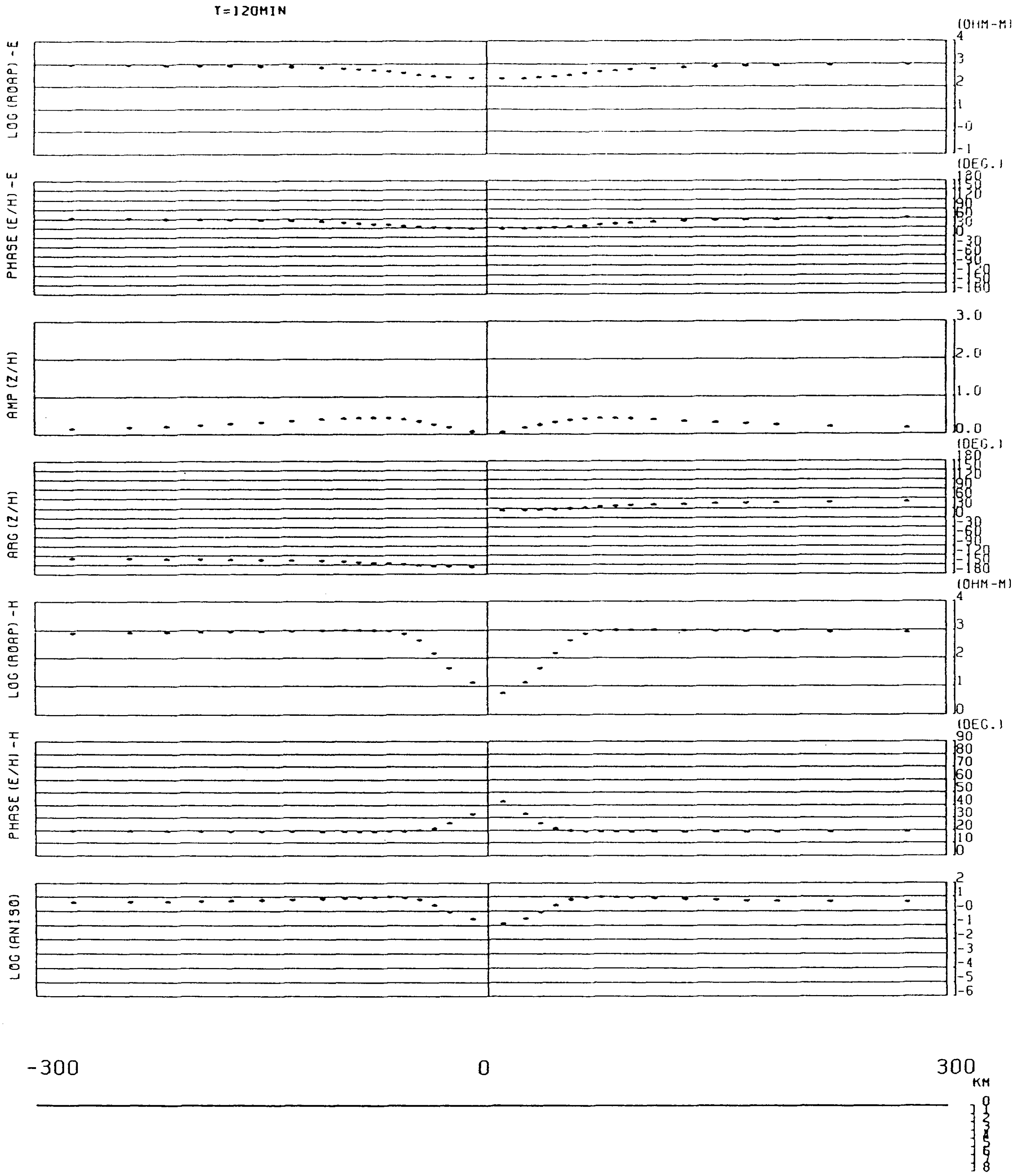

Fig.3.17(b) Theoretical responses from the model I for the period of 120 minutes.

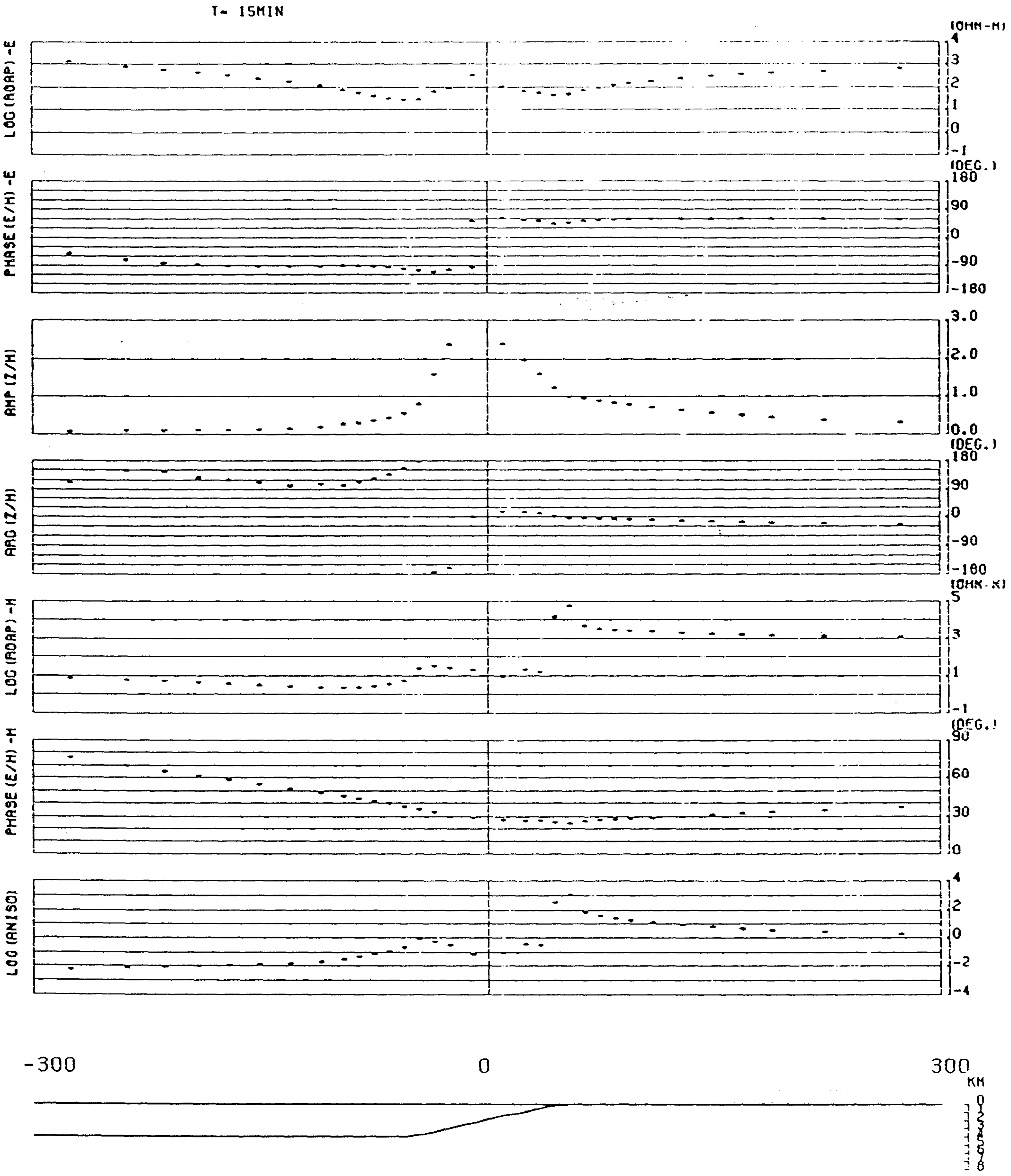

Fig.3.18(a) Theoretical responses from the model Ⅲ for the period of 15 minutes. Data points situate on the seafloor and the earth's surface.

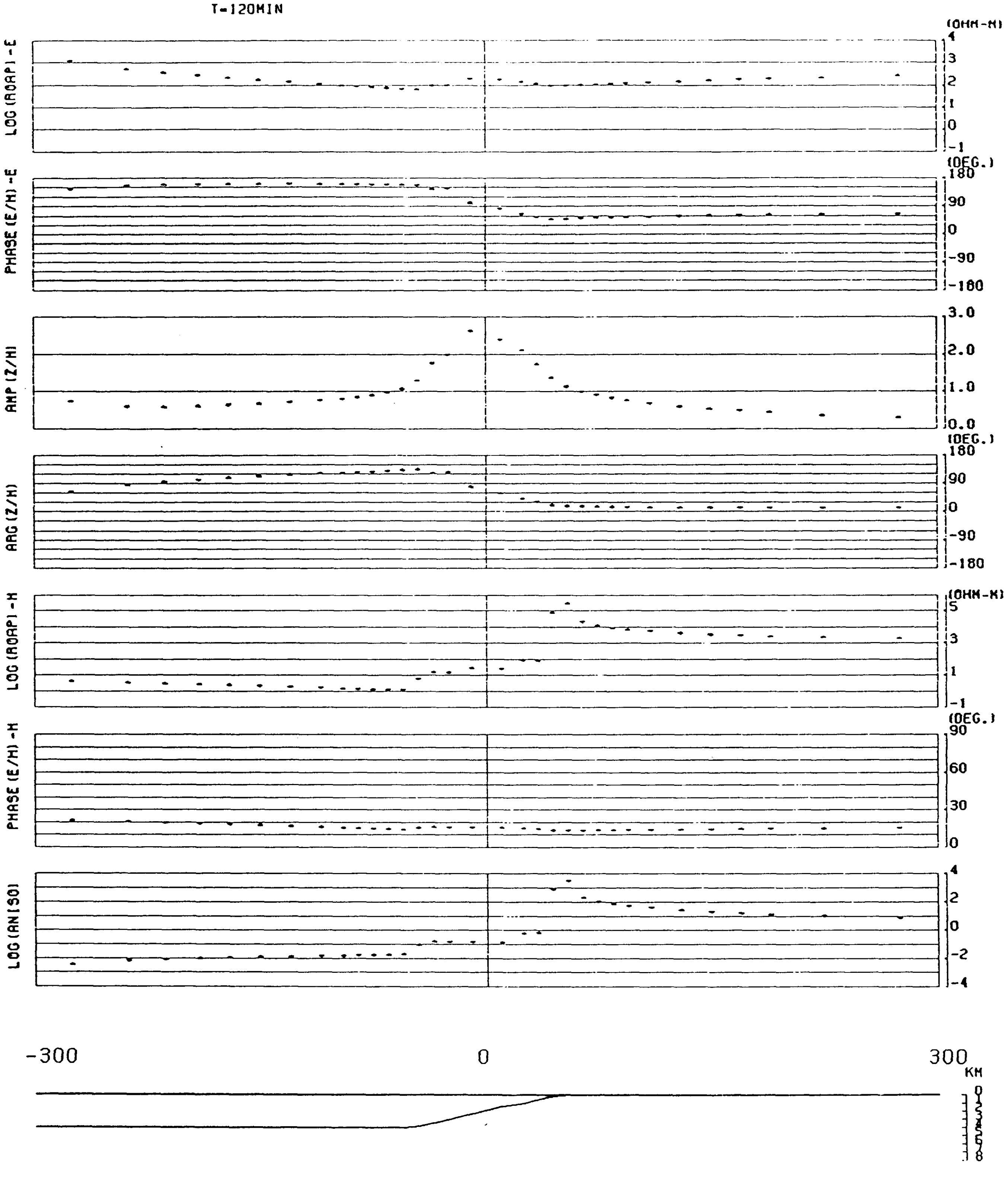

Fig.3.18(b) Theoretical responses from the model III for the period of 120 minutes.

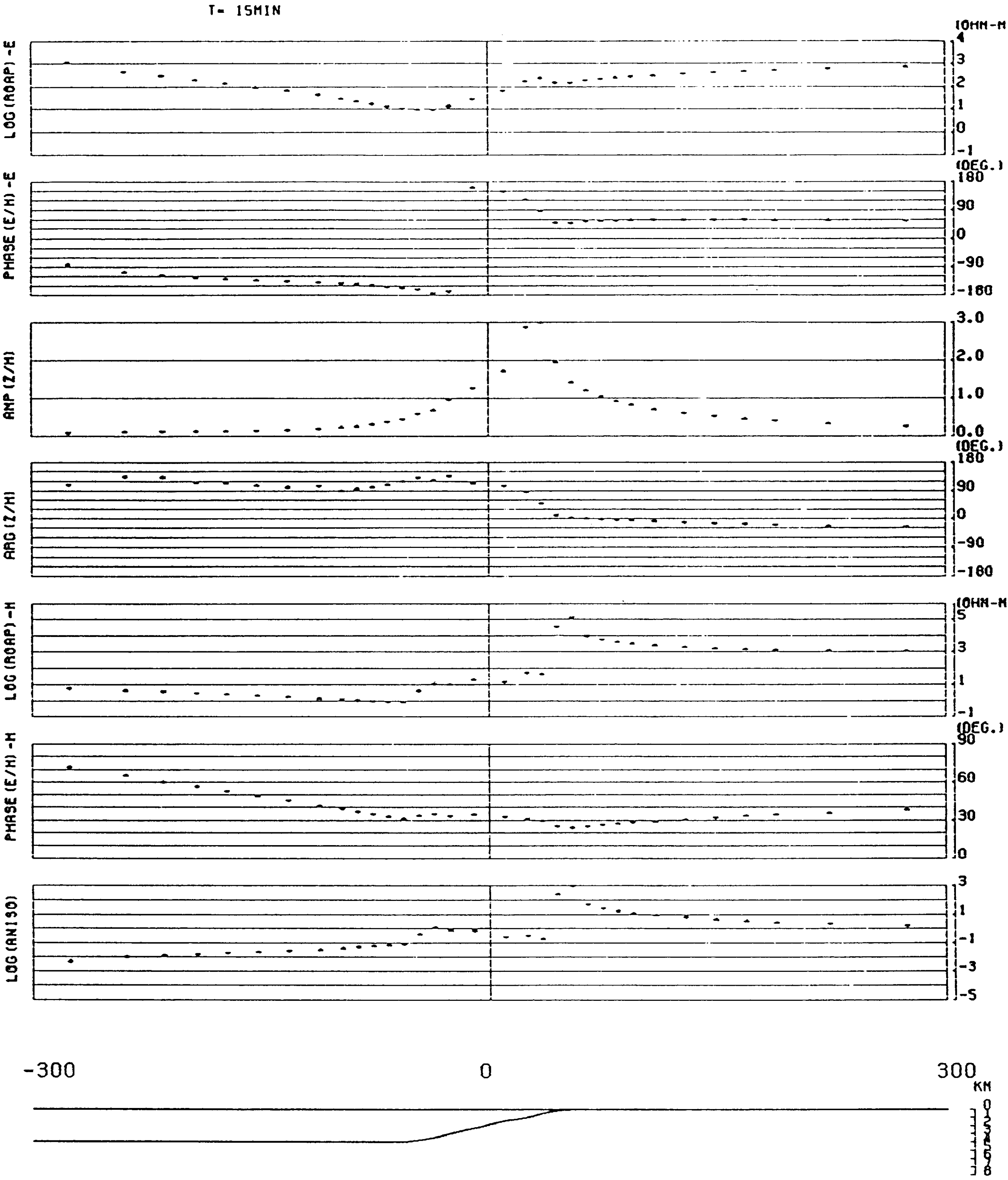

Fig.3.19(a) Theoretical responses from the model II for the period of 15 min.

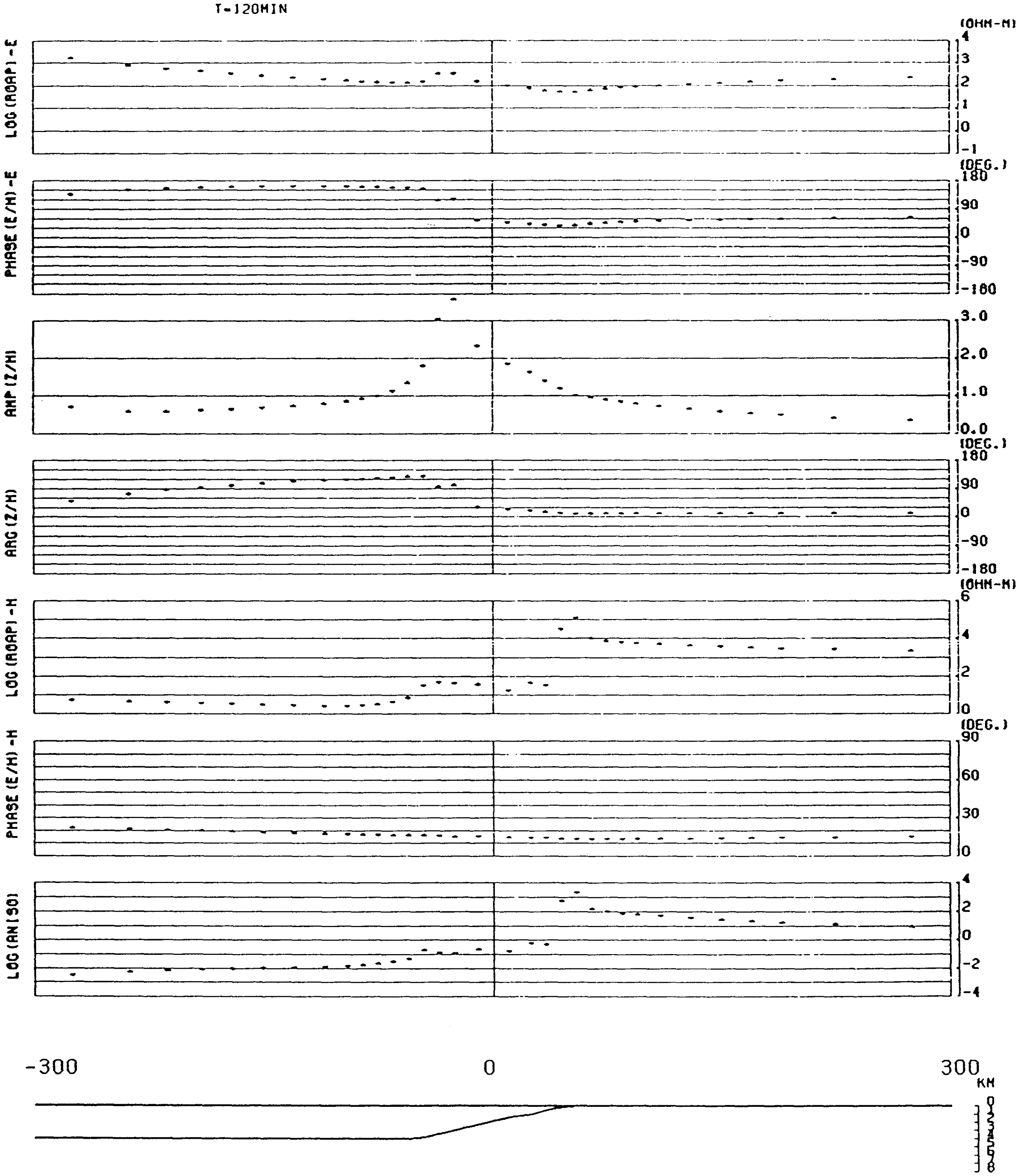

Fig.3.19(b) Theoretical responses from the model II for the period of 120 min.

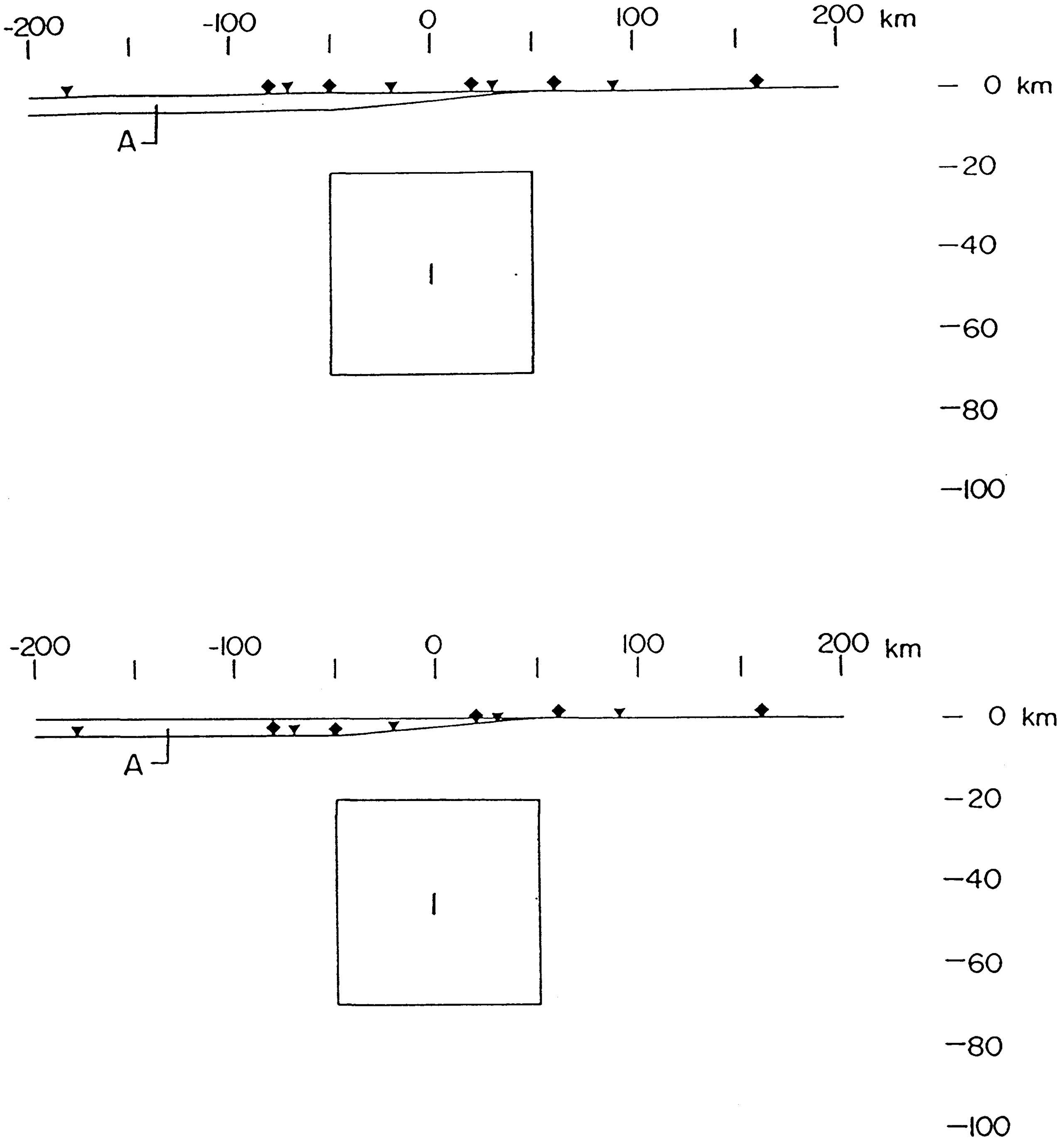

Fig.3.20 Distribution of synthetic data sites along the earth's surface (above) and seafloor-land traverse (below). Triangles denote magnetovariational (MV) sites where only transfer functions are calculated. Diamonds correspond to magnetotelluric (MT) sites where and impedances, together with transfer functions, are calculated.

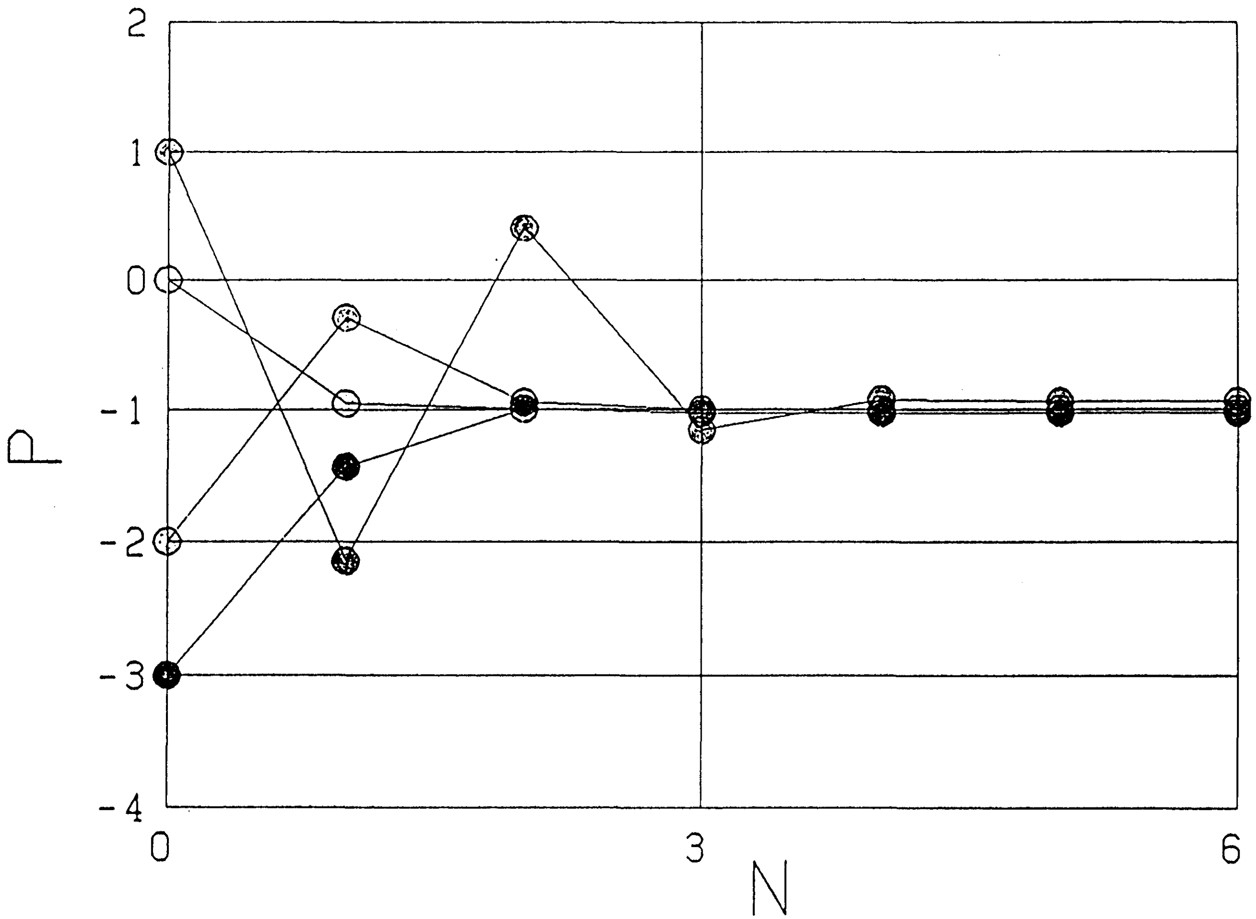

Fig.3.21 Result of the direct inversion for the model T1. Variations of the parameter, $p_1 = \log[\sigma_1]$, are plotted against iteration cycle, N, for 4 different initial values 10 S/m, 1 S/m, 10^{-2} S/m and 10^{-3} S/m.

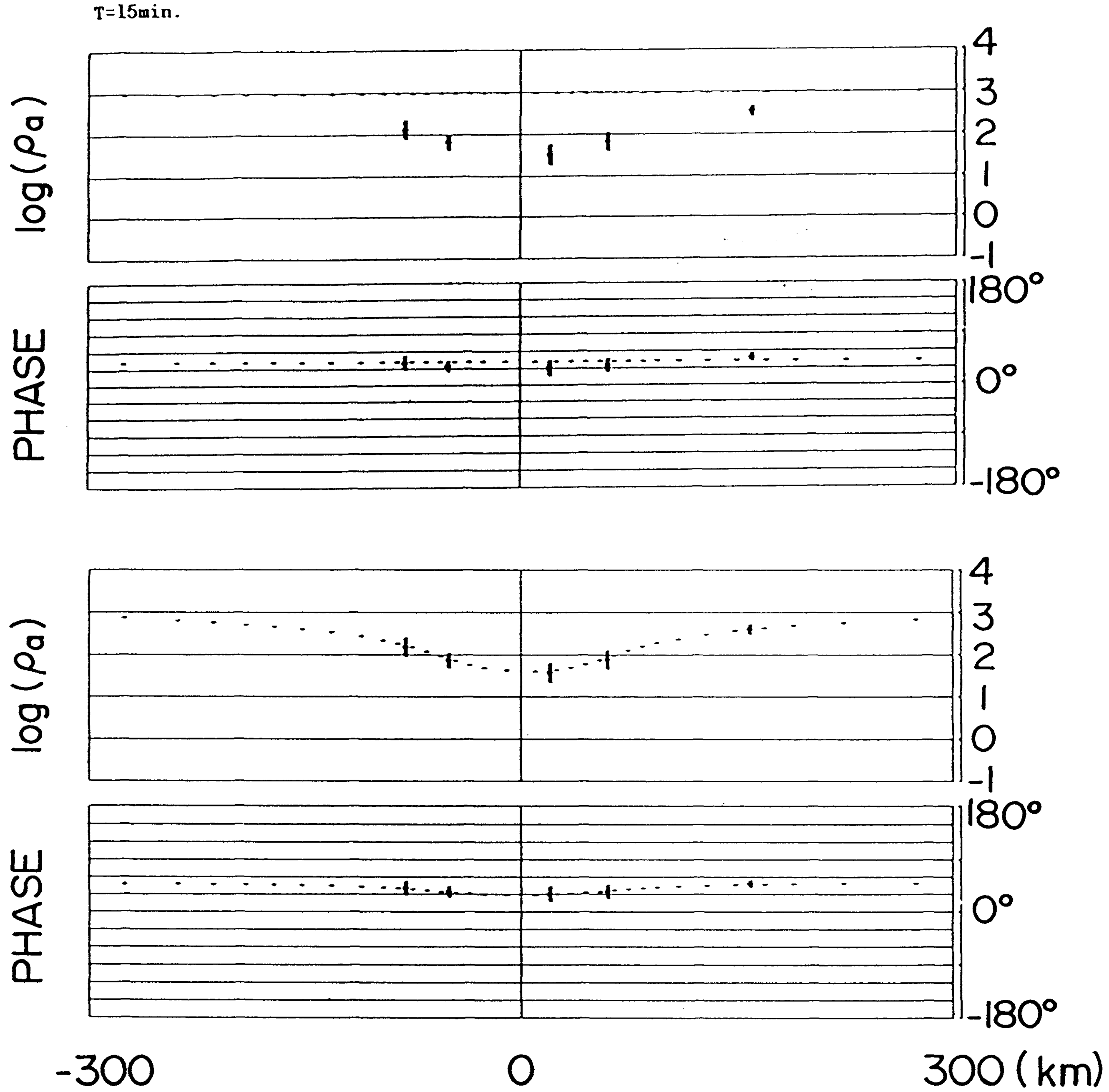

Fig.3.22 Comparison of apparent resistivity and phase of the synthetic data (bars) and of calculated values (dots) from initial (above) and final (below) models of T1. Initial conductivity of 10^{-3} produces constant apparent resistivity everywhere, while the theoretical responses almost coincide with the observations within their error bars after 6 cycles of iteration.

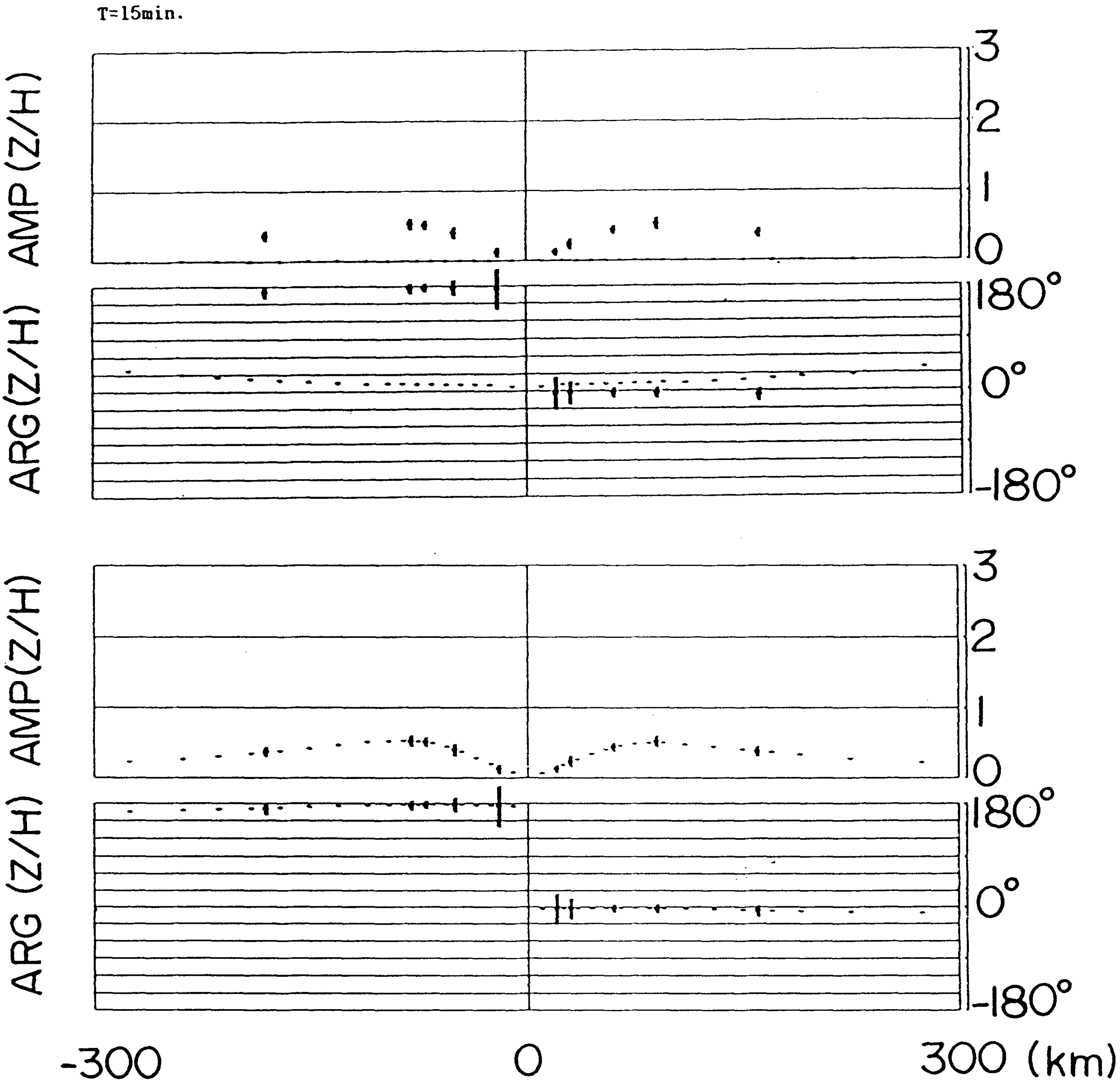

Fig.3.23 Similar comparison of transfer function and phase to Fig. 3.22. The initial conductivity, which produces null transfer function everywhere (above), has been highly improved by the iteration so as to explain the data (below)

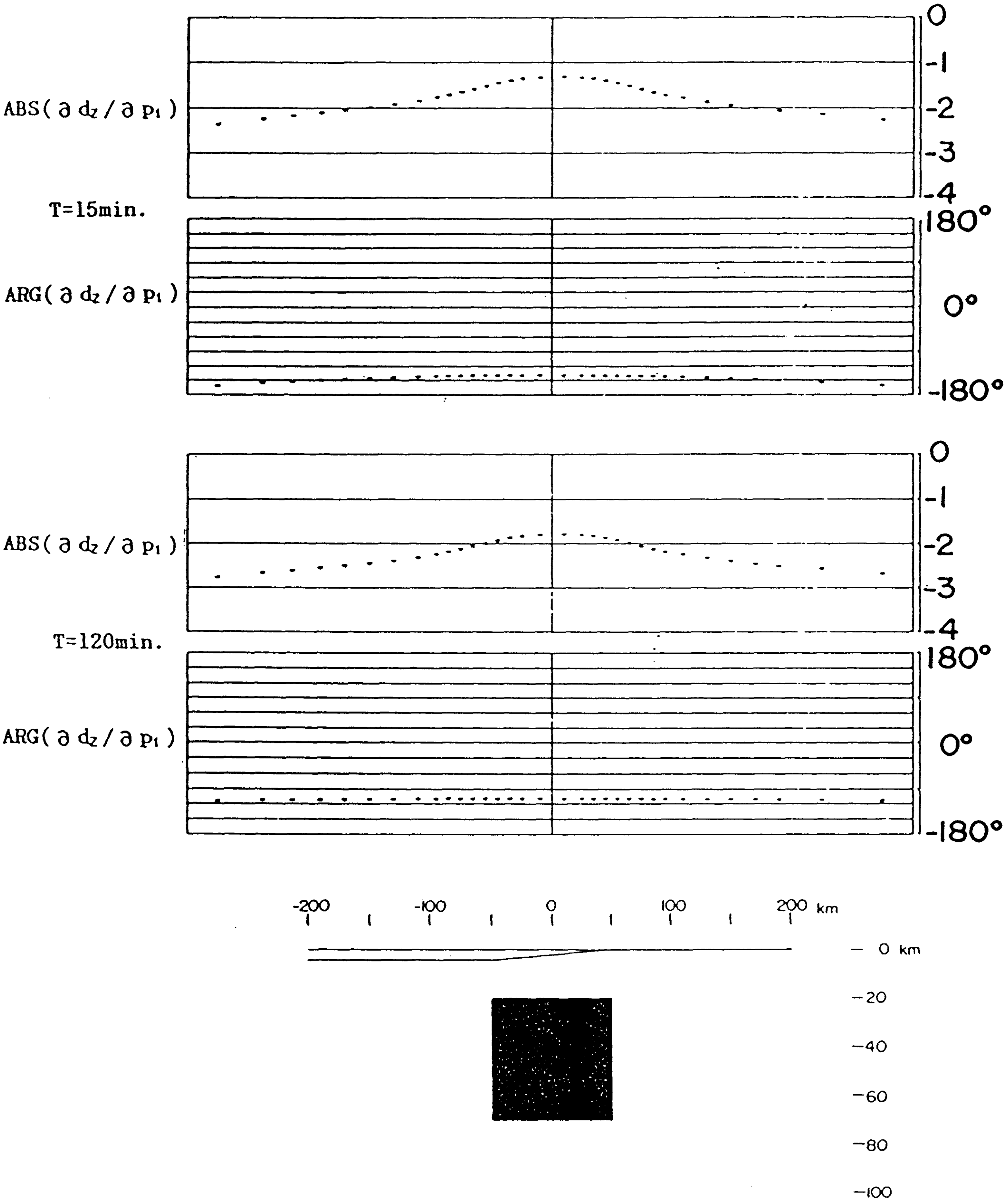

Fig.3.24(a) Distribution of the absolute value and the argument of the partial derivative of the impedance with respect to the inhomogeneity no.1 (shaded area), $\partial d_z/\partial p_1$, for the model T1, for the periods of 15 (above) and 120 minutes (below), respectively, on the earth's surface. The conductivity of the inhomogeneity no.1, σ_1, is taken as 10^{-2} S/m.

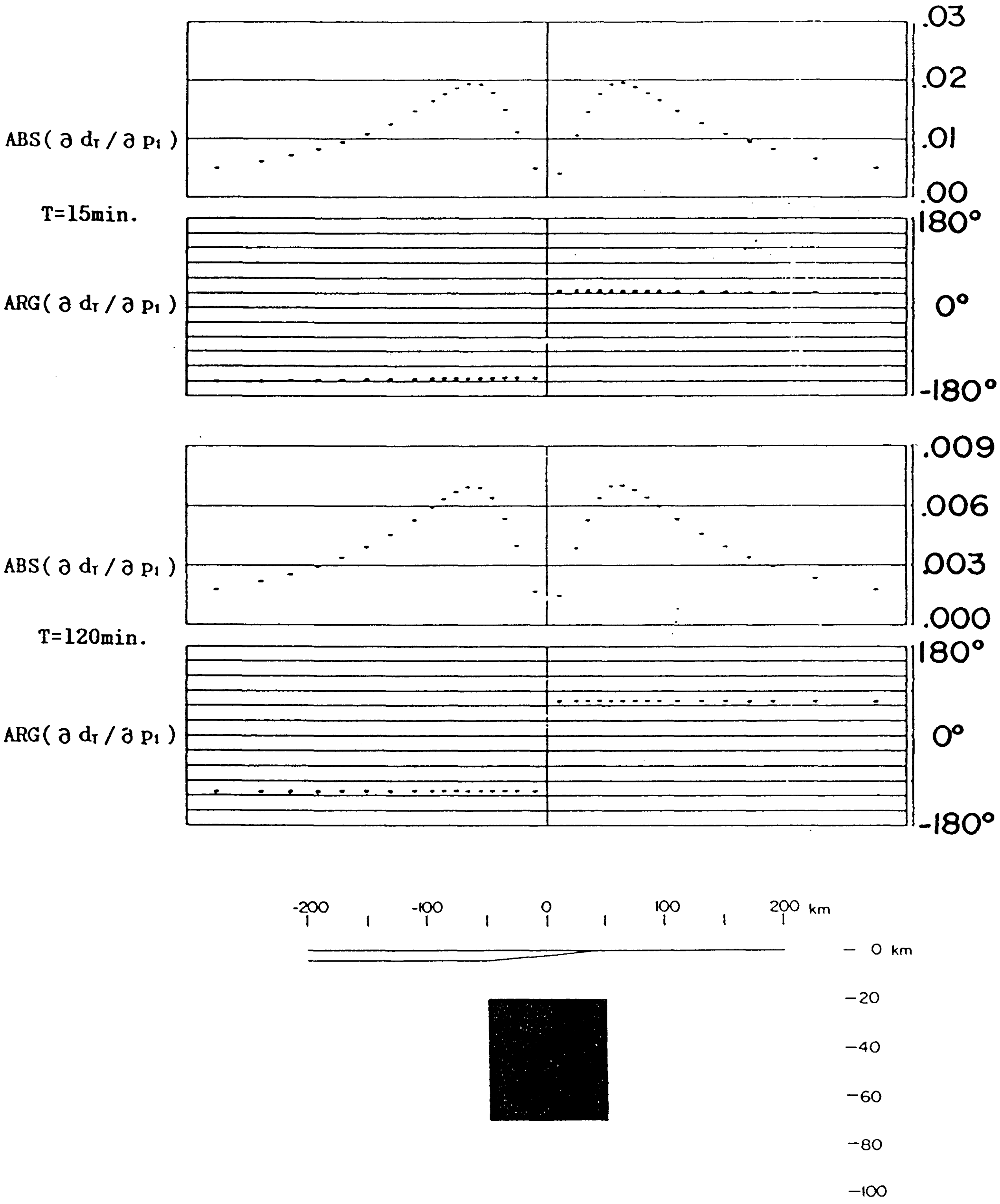

Fig.3.24(b) Distribution of the partial derivative of the transfer function, $\partial d_T/\partial p_1$, for the model T1 with initial conductivity of 10^{-2} S/m.

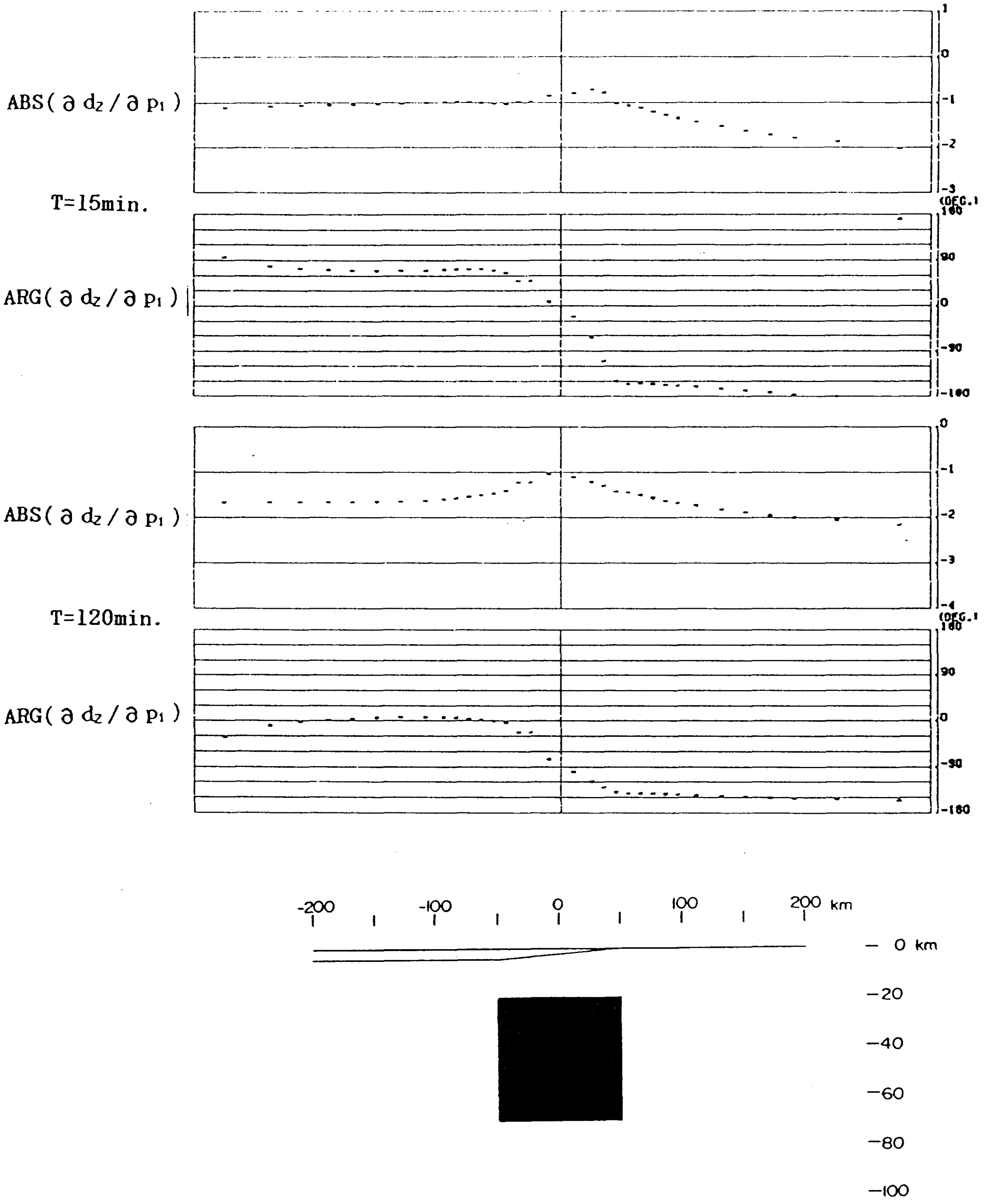

Fig.3.25(a) Distribution of the partial derivative, $\partial d_z/\partial p_1$, for the model T2 along seafloor-land traverse with initial conductivity of 10^{-2} S/m.

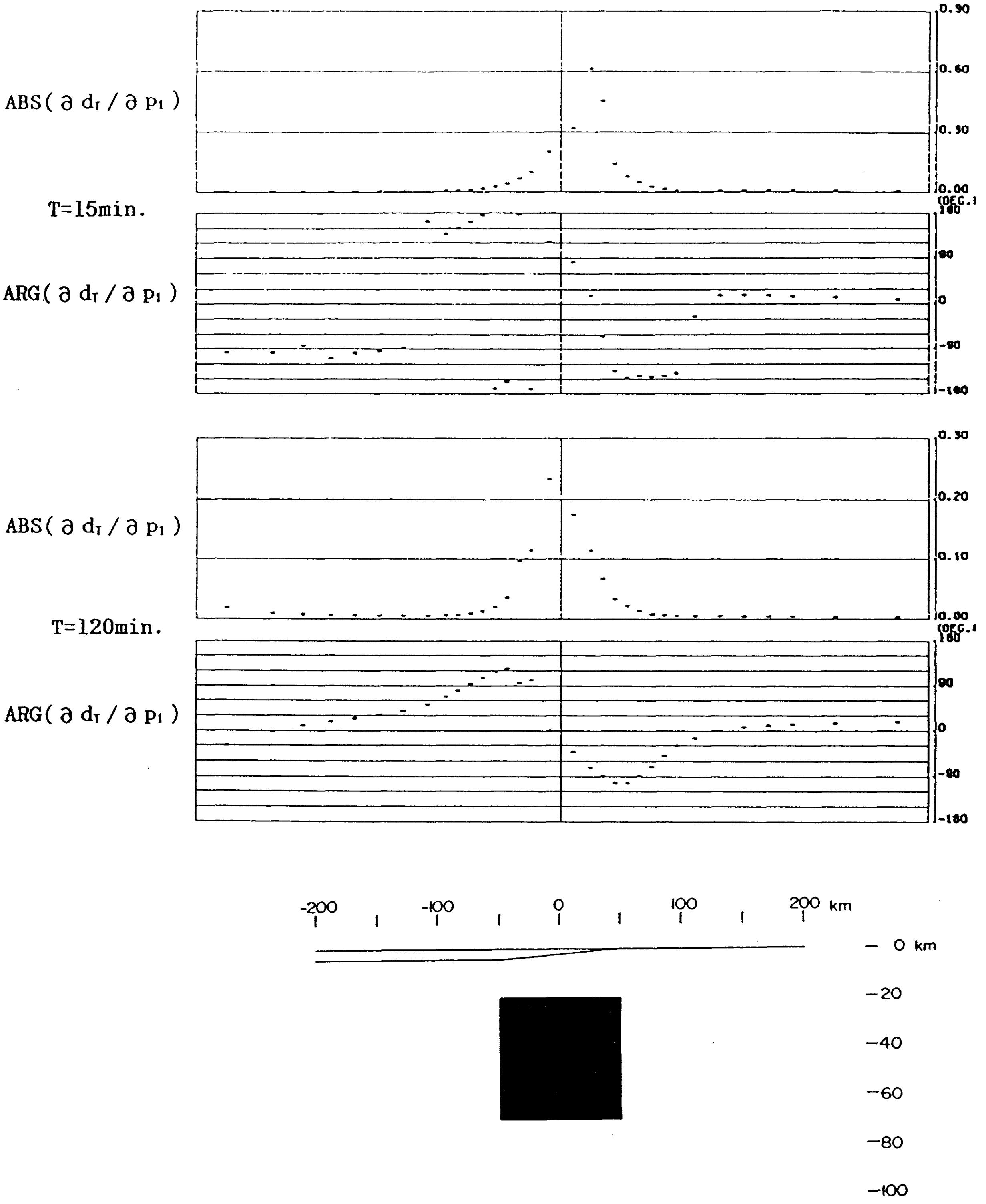

Fig.3.25(b) Distribution of the partial derivative, $\partial d_T/\partial' p_1$, for the model T2 with initial conductivity of 10^{-2} S/m.

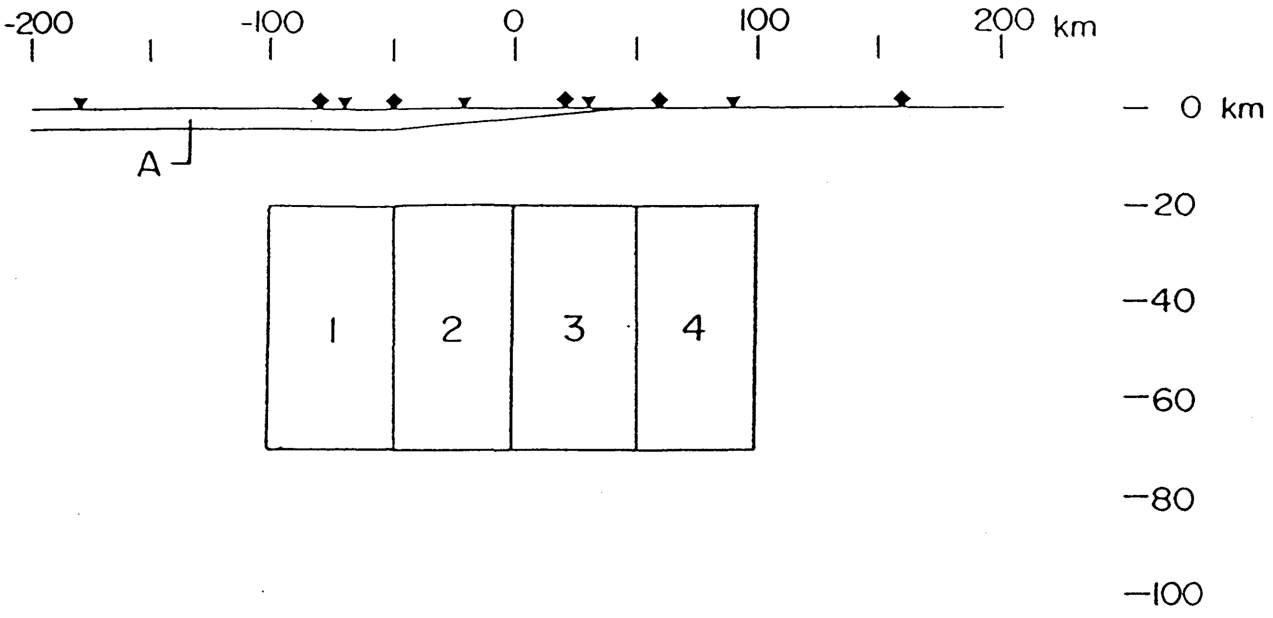

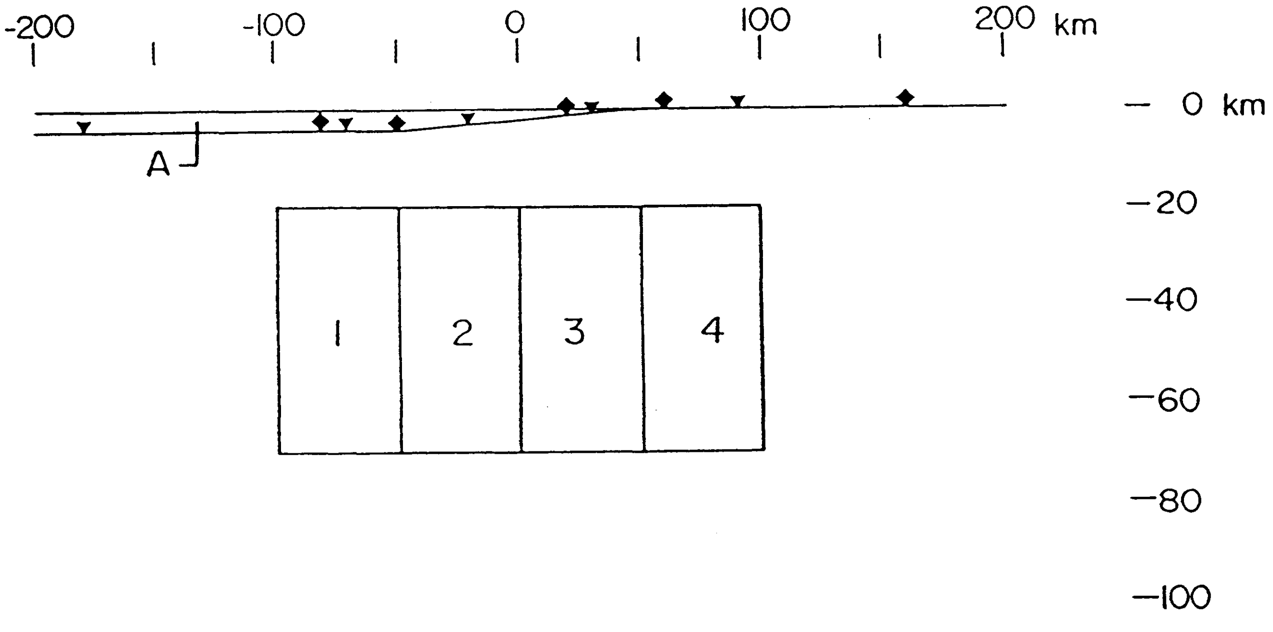

Fig.3.26 Model configurations of 4 block divisions with observation sites on the earth's surface or along sea surface-land traverse (above) and along seafloor-land traverse (below). MV and MT sites are denoted by triangles and diamonds, respectively.

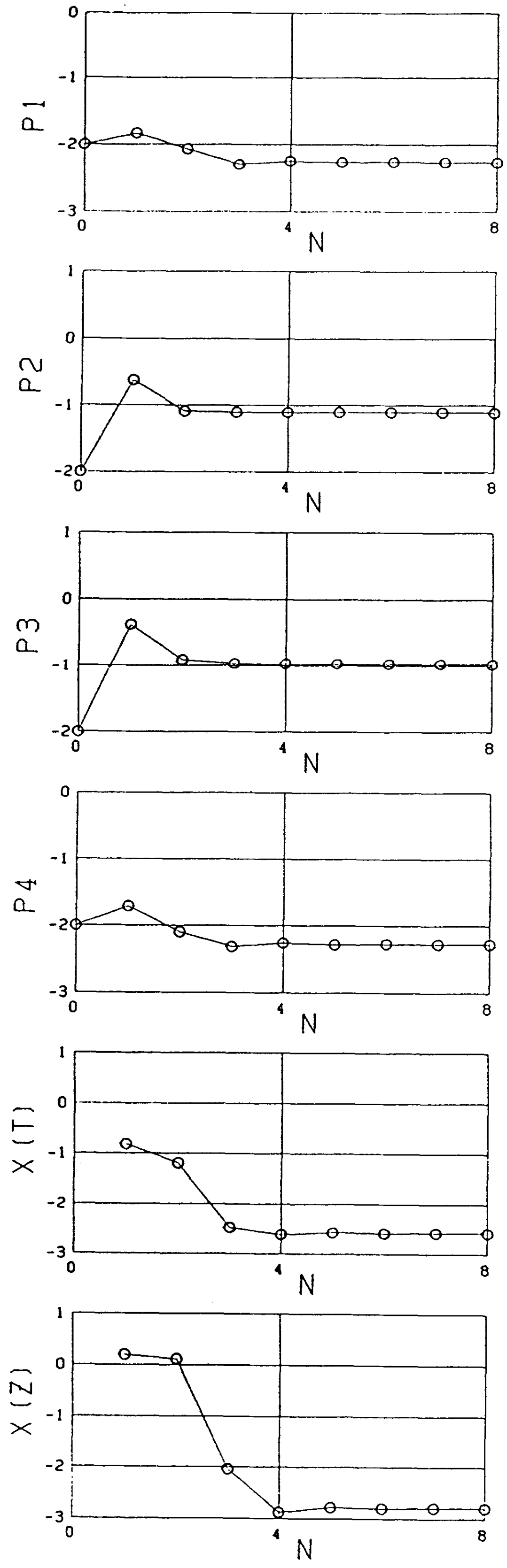

Fig.3.27 Result of the direct inversion for the model T3 with initial conductivities of 10^{-2} S/m for each inhomogeneity. The variations of parameters, p_1, p_2, p_3 and p_4, χ^2 of impedance, and χ^2 of transfer function are plotted against the iteration cycle, N.

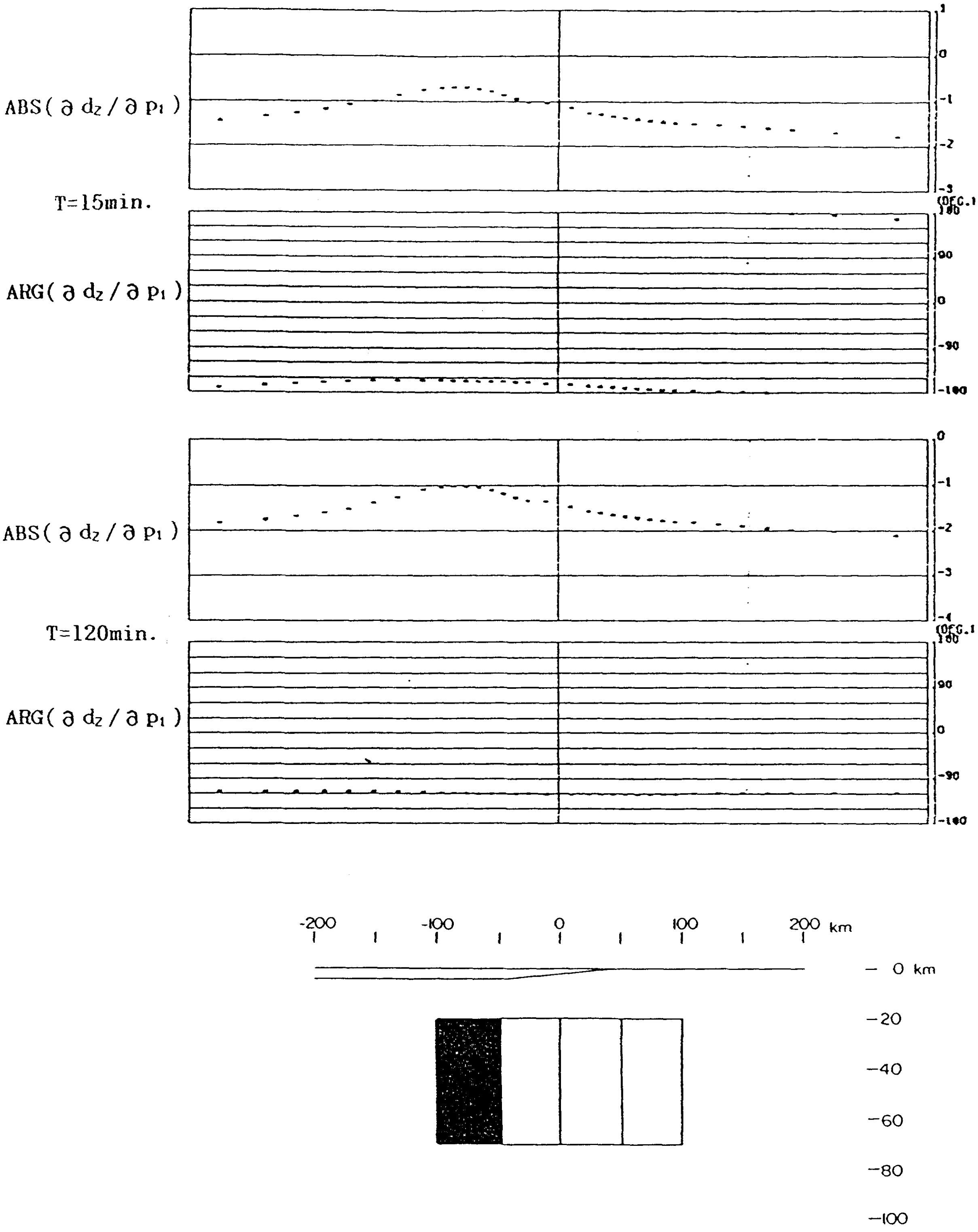

Fig.3.28(a) Distribution of the partial derivative, $\partial d_z/\partial p_1$, for the model T3, when the initial conductivity is taken as 10^{-2} S/m for the blocks no.1 and 4, and as 1 S/m for no.2 and 3, respectively.

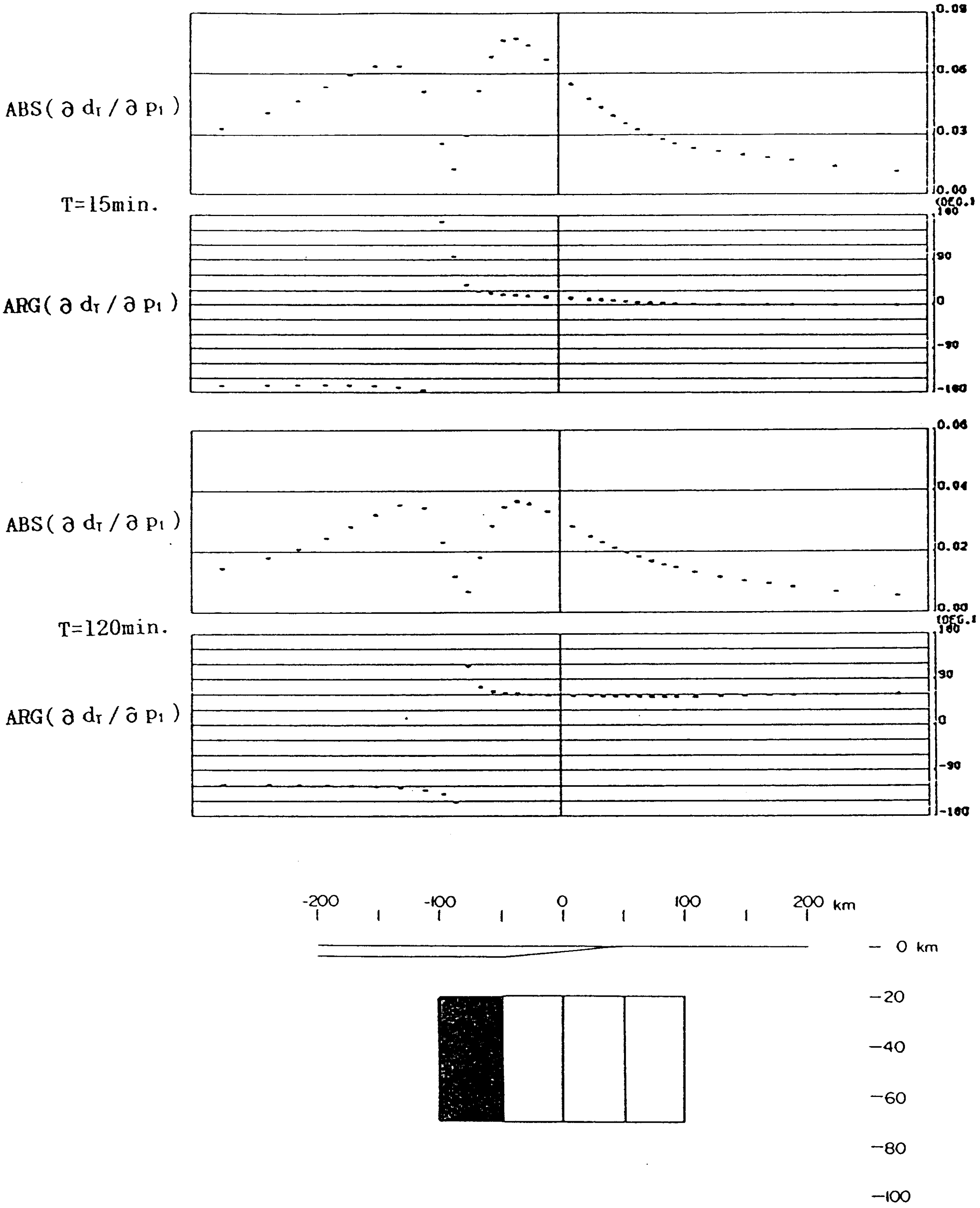

Fig.3.28(b) Distribution of the partial derivative, $\partial d_T/\partial p_1$, for the same condition as (a).

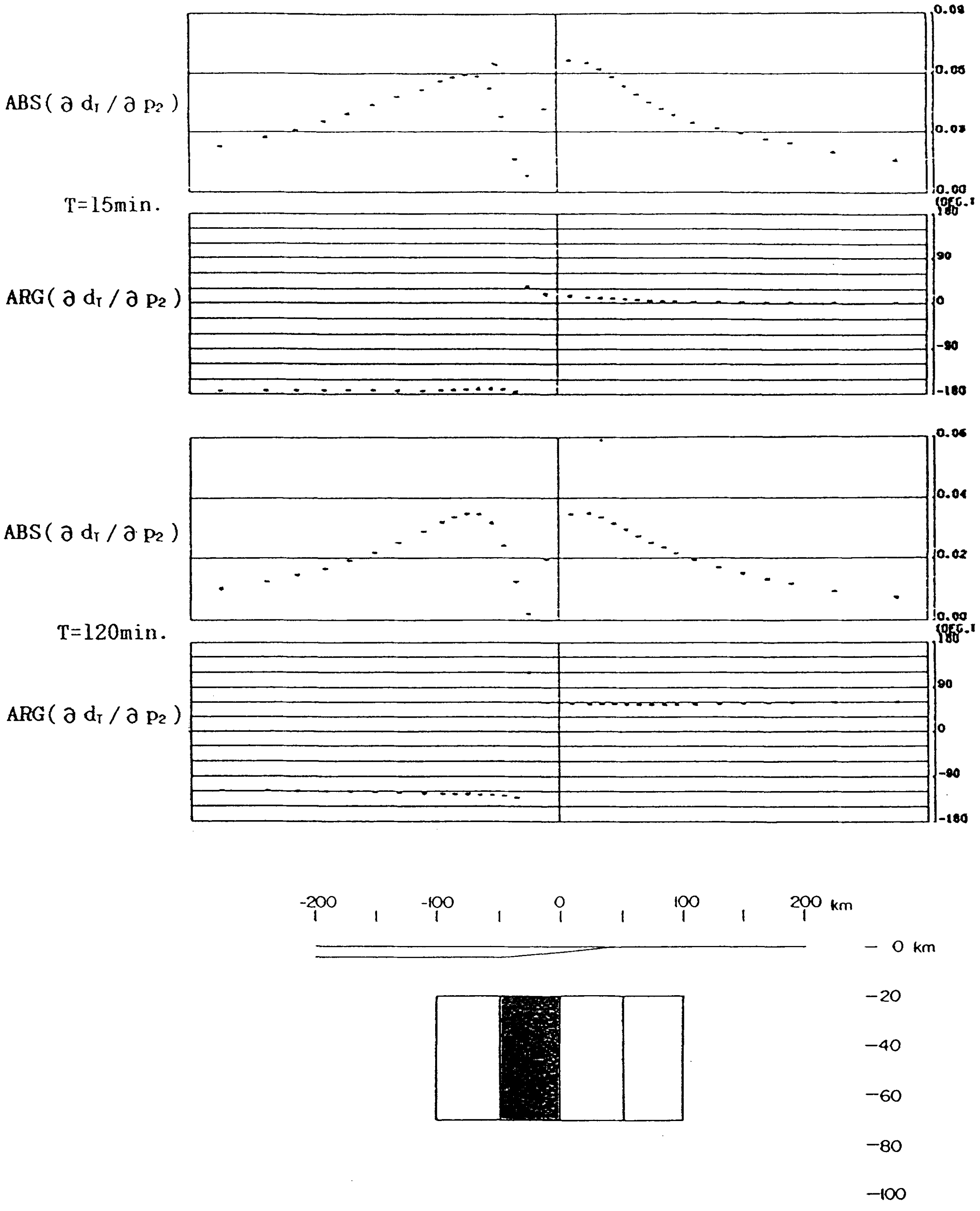

Fig.3.29(b) Distribution of the partial derivative, $\partial d_T/\partial p_2$, for the same condition as (a).

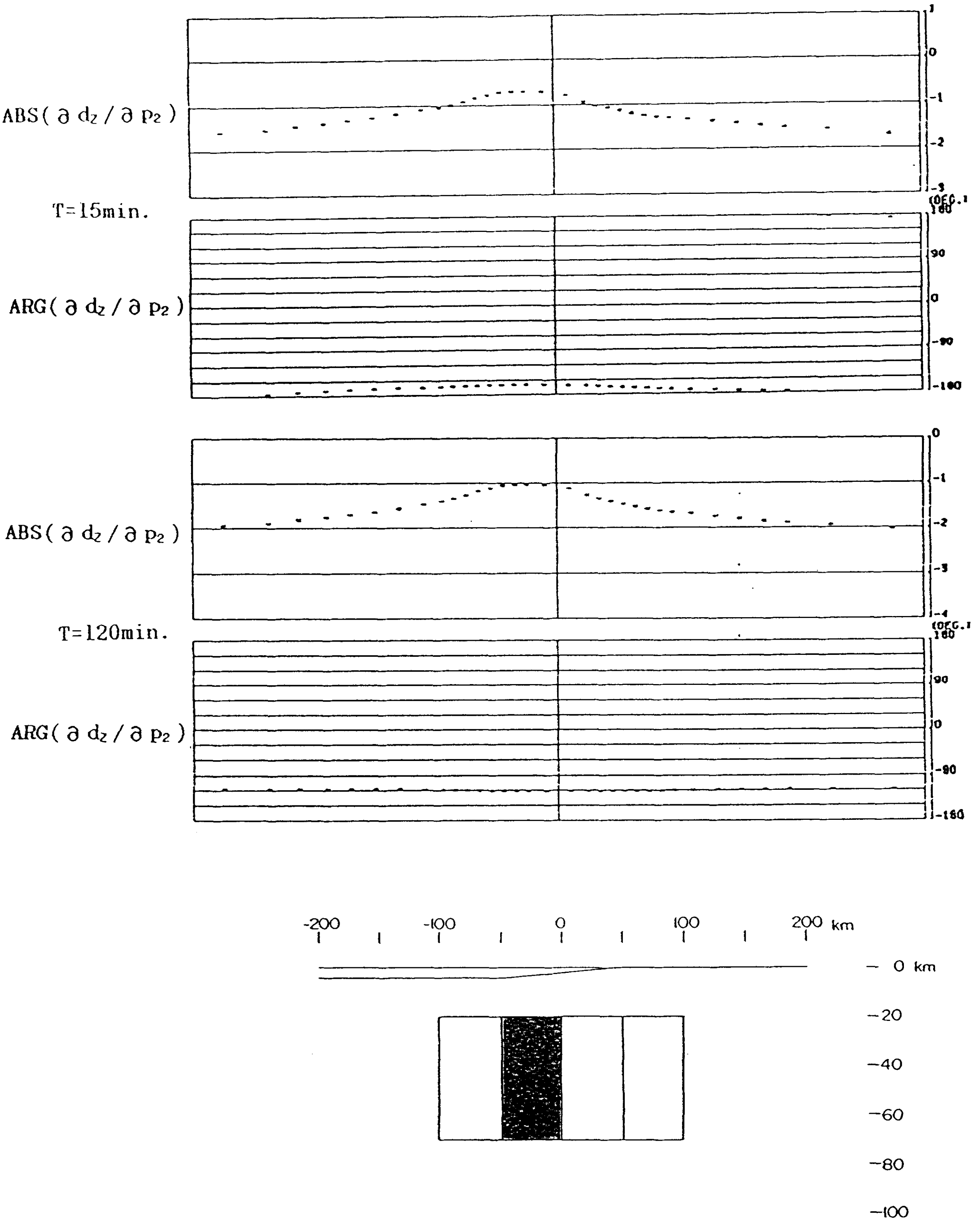

Fig.3.29(a) Distribution of the partial derivative, $\partial d_z/\partial p_z$, for the same condition as Fig.28.

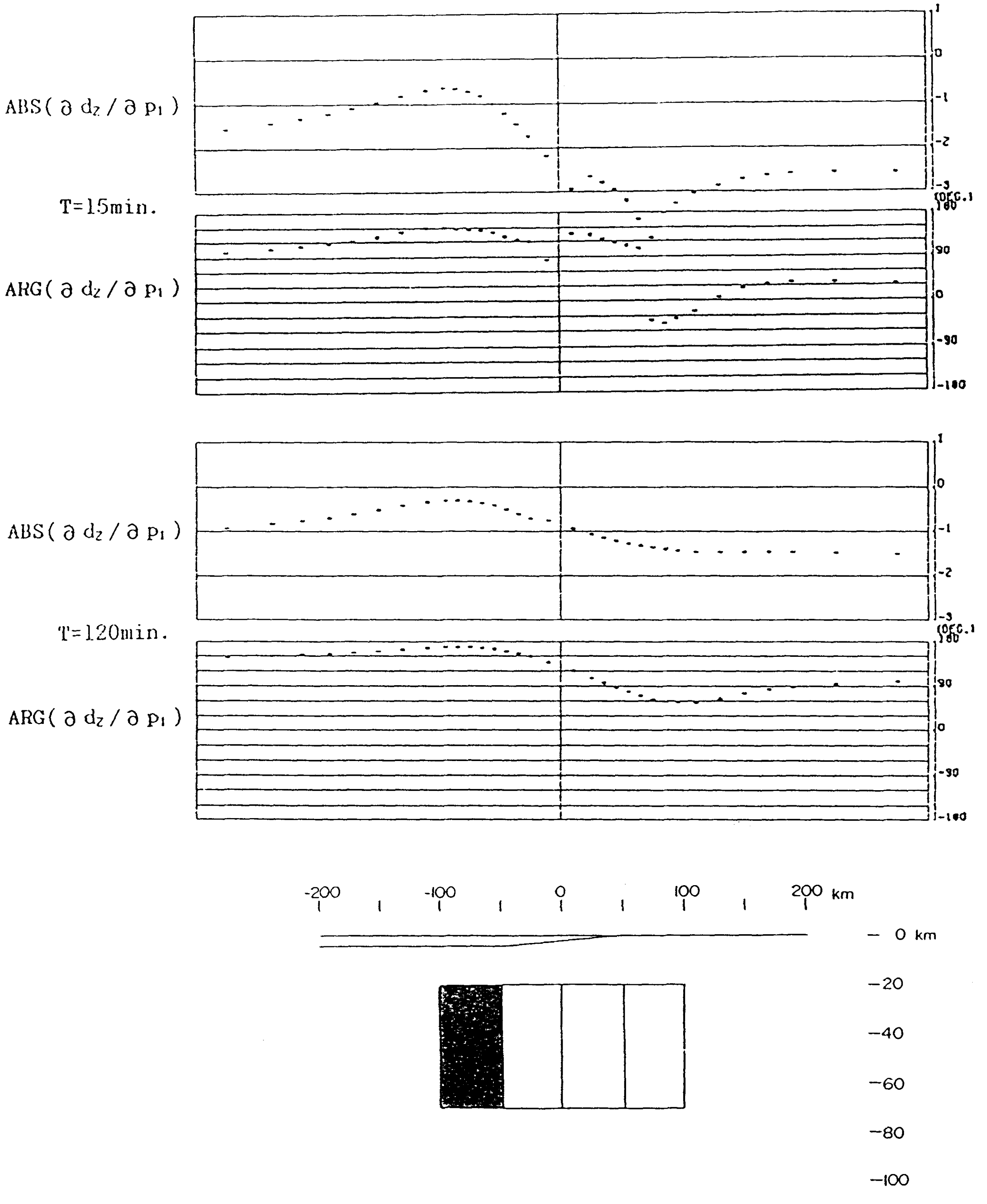

Fig.3.30(a) Distribution of the partial derivative, $\partial d_z/\partial p_1$, for the model T3, when the initial conductivity is taken as 10^{-2} S/m for each block.

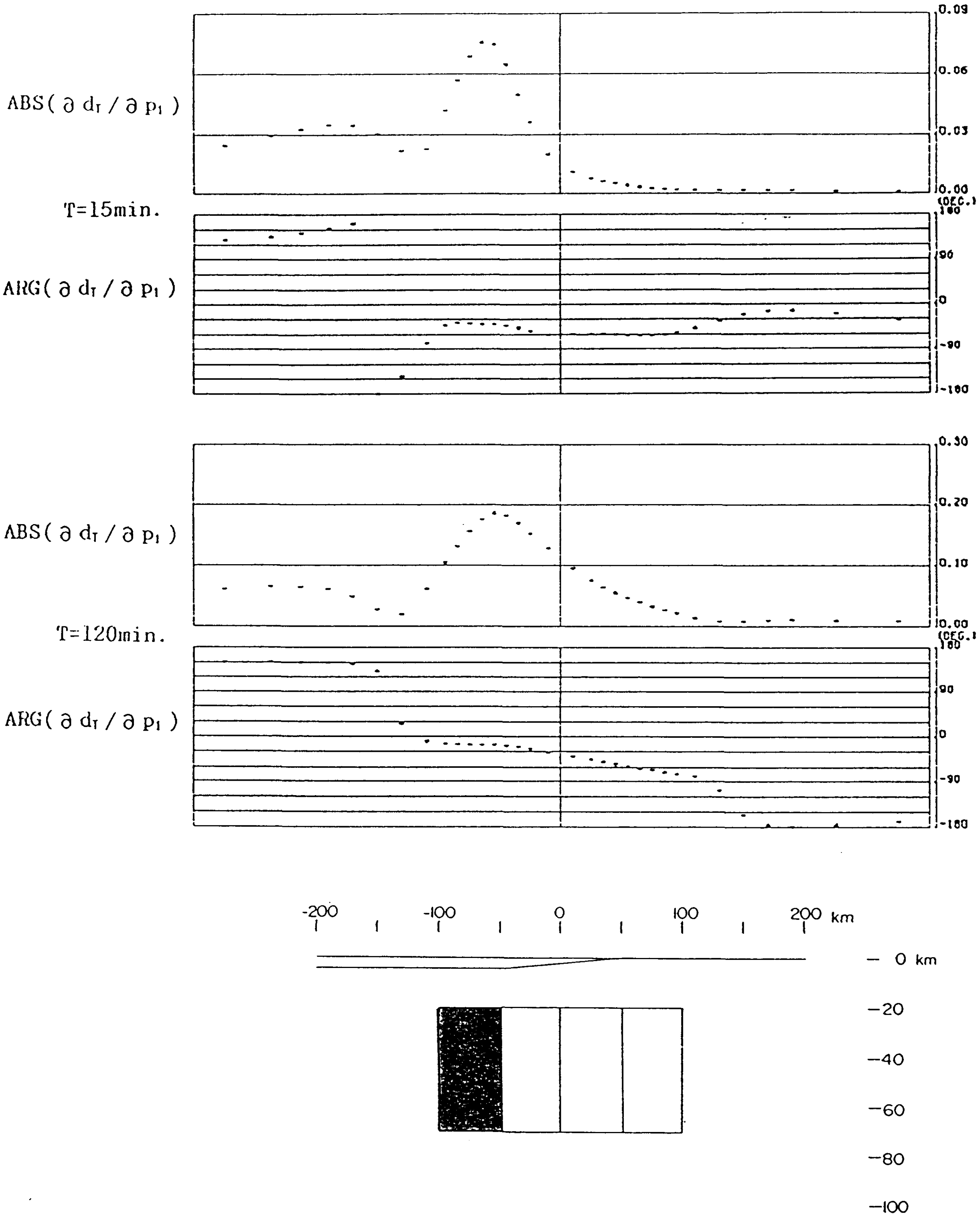

Fig.3.30(b) Distribution of the partial derivative, $\partial d_T/\partial p_1$, for the same condition as (a).

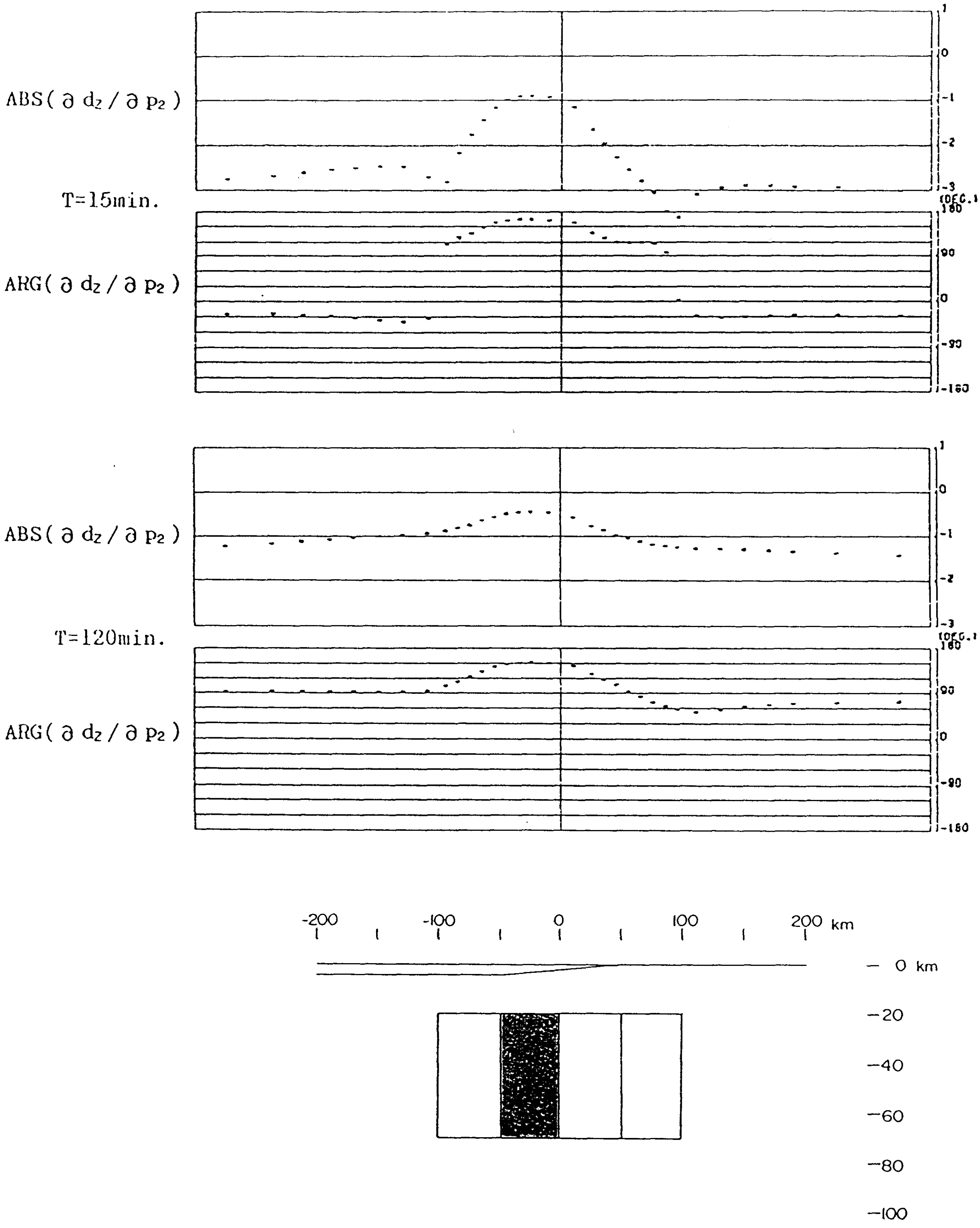

Fig.3.31(a) Distribution of the partial derivative, $\partial d_z/\partial p_2$, for the same condition as Figs.30(a) and (b).

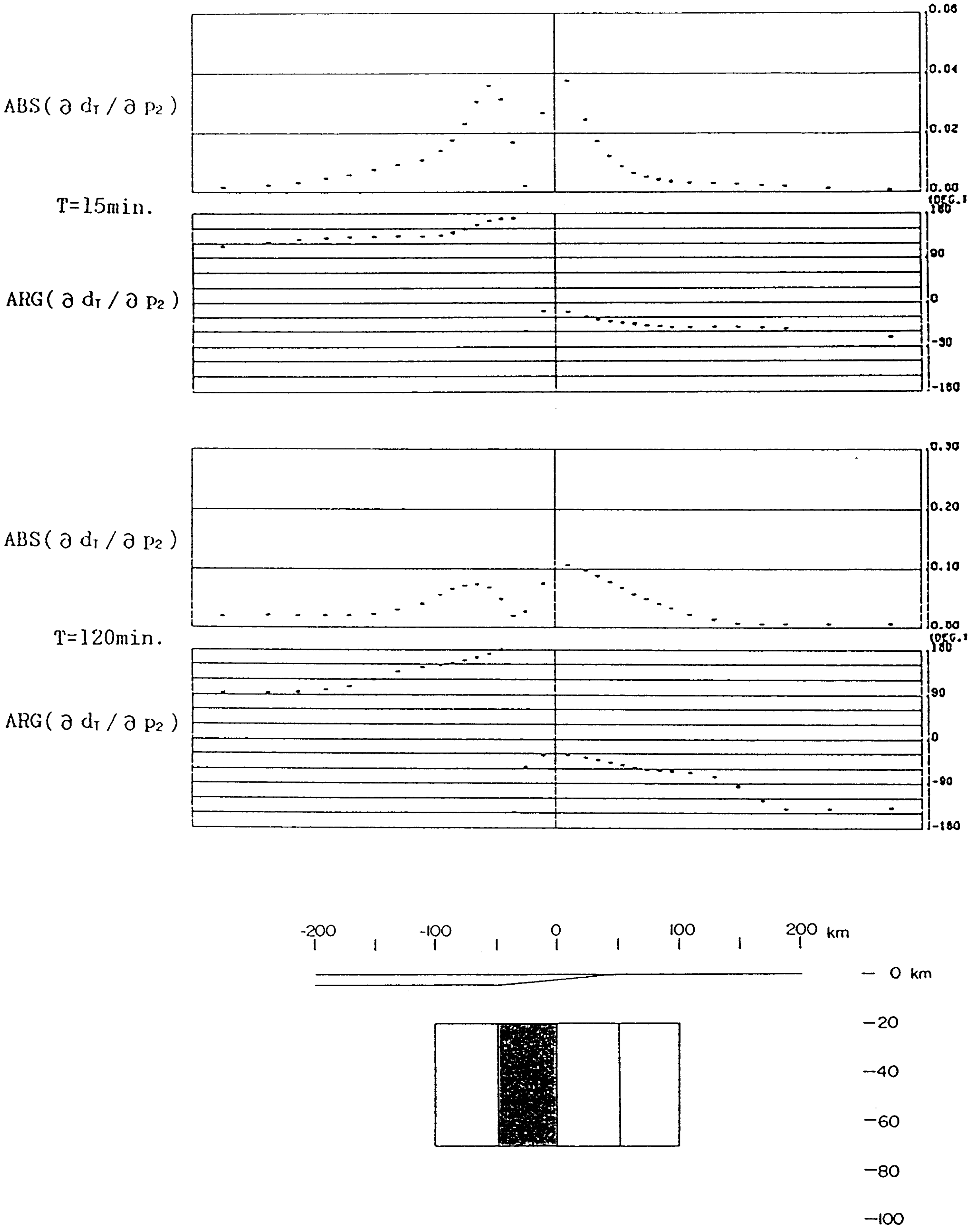

Fig.3.31(b) Distribution of the partial derivative, $\partial d_T / \partial p_2$, for the same condition as (a).

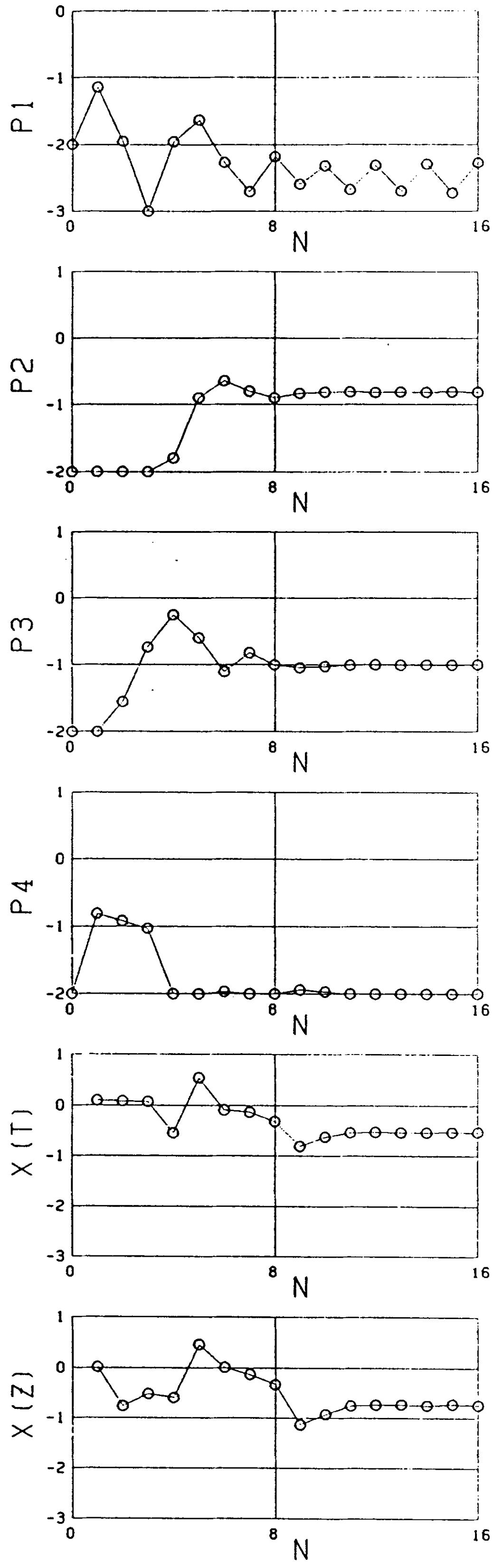

Fig.3.32 Result of the direct inversion for the model T4 with initial conductivities of 10-2 S/m for each inhomogeneity. The variations of parameters, p_1, p_2, p_3 and p_4, χ^2 of impedance, and χ^2 of transfer function are plotted against the iteration cycle, N.

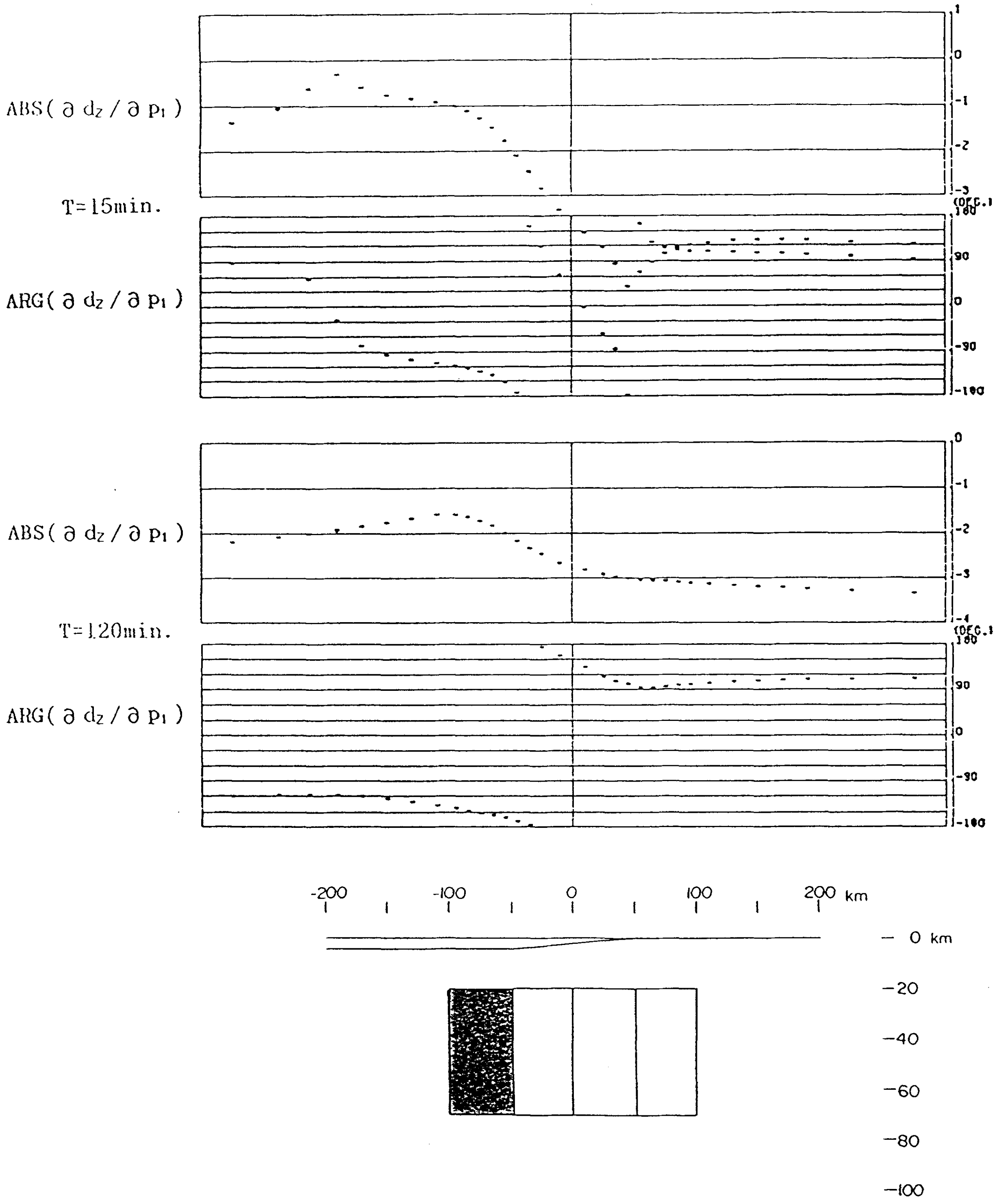

Fig.3.33(a) Distribution of the partial derivative, $\partial d_z/\partial p_1$, for the model T4, when the initial conductivity is taken as 10^{-2} S/m for each block.

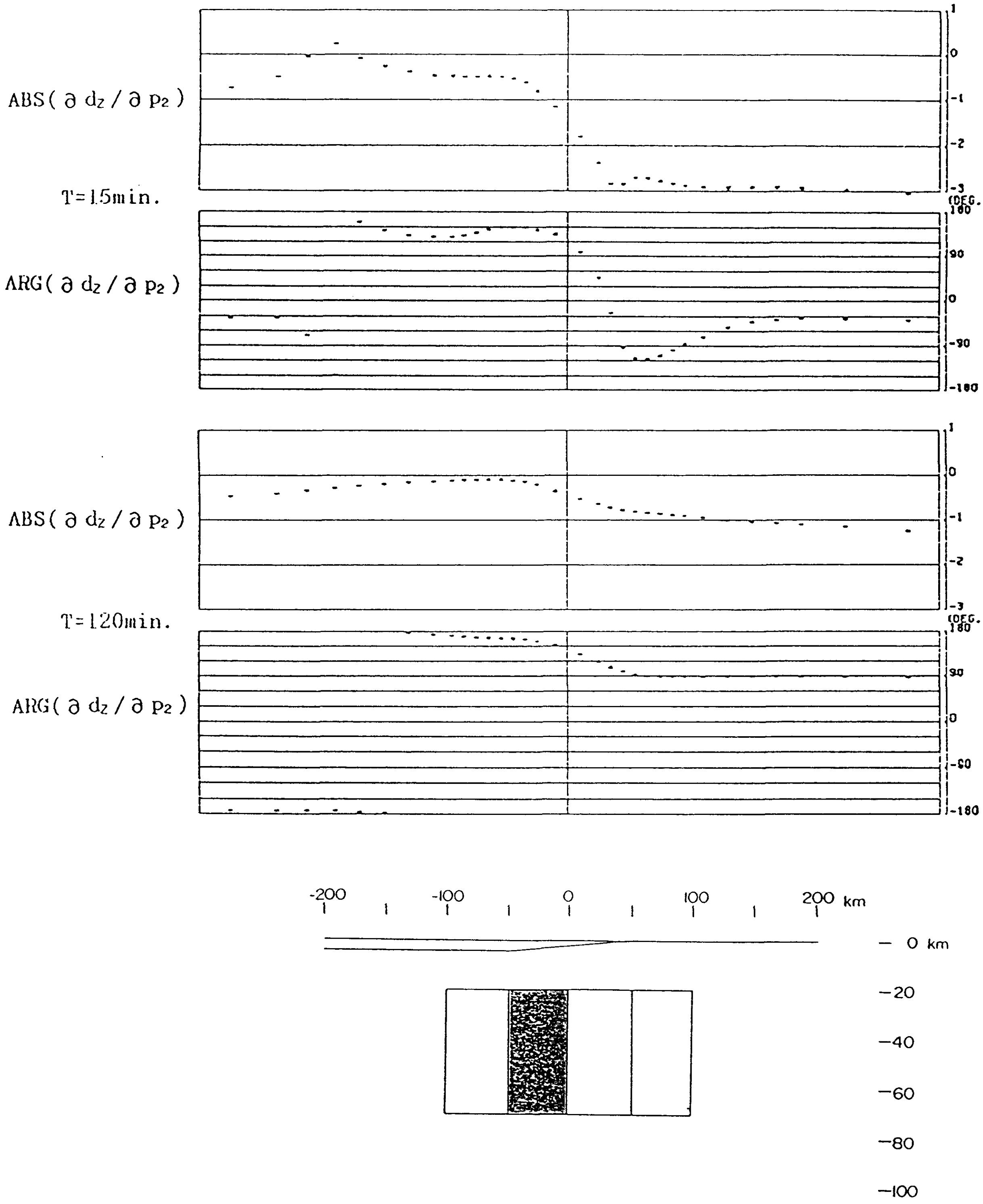

Fig.3.33(b) Distribution of the partial derivative, $\partial d_z/\partial p_2$, for the same condition as (a).

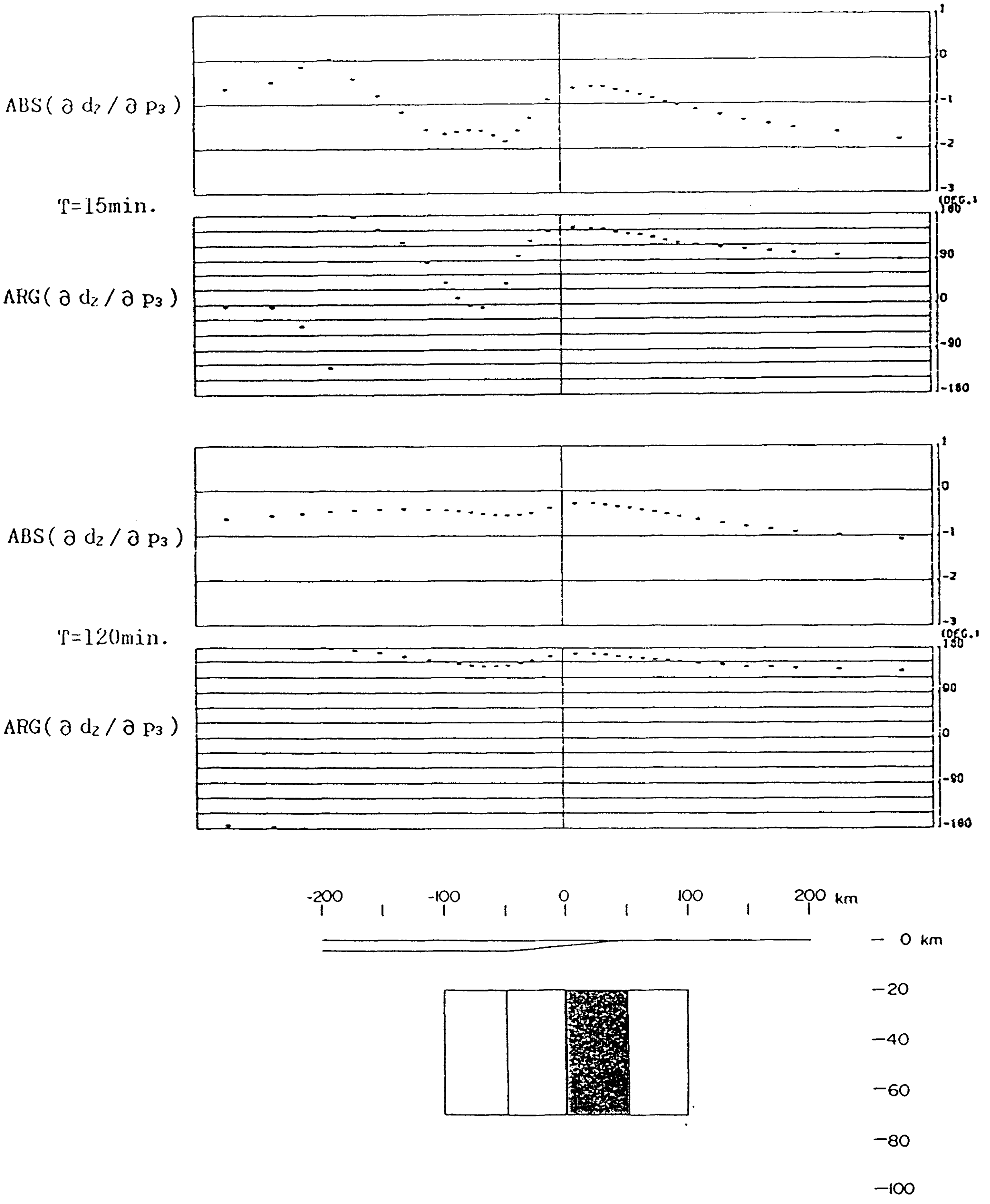

Fig.3.33(c) Distribution of the partial derivative, $\partial d_z/\partial p_3$, for the same condition as (a).

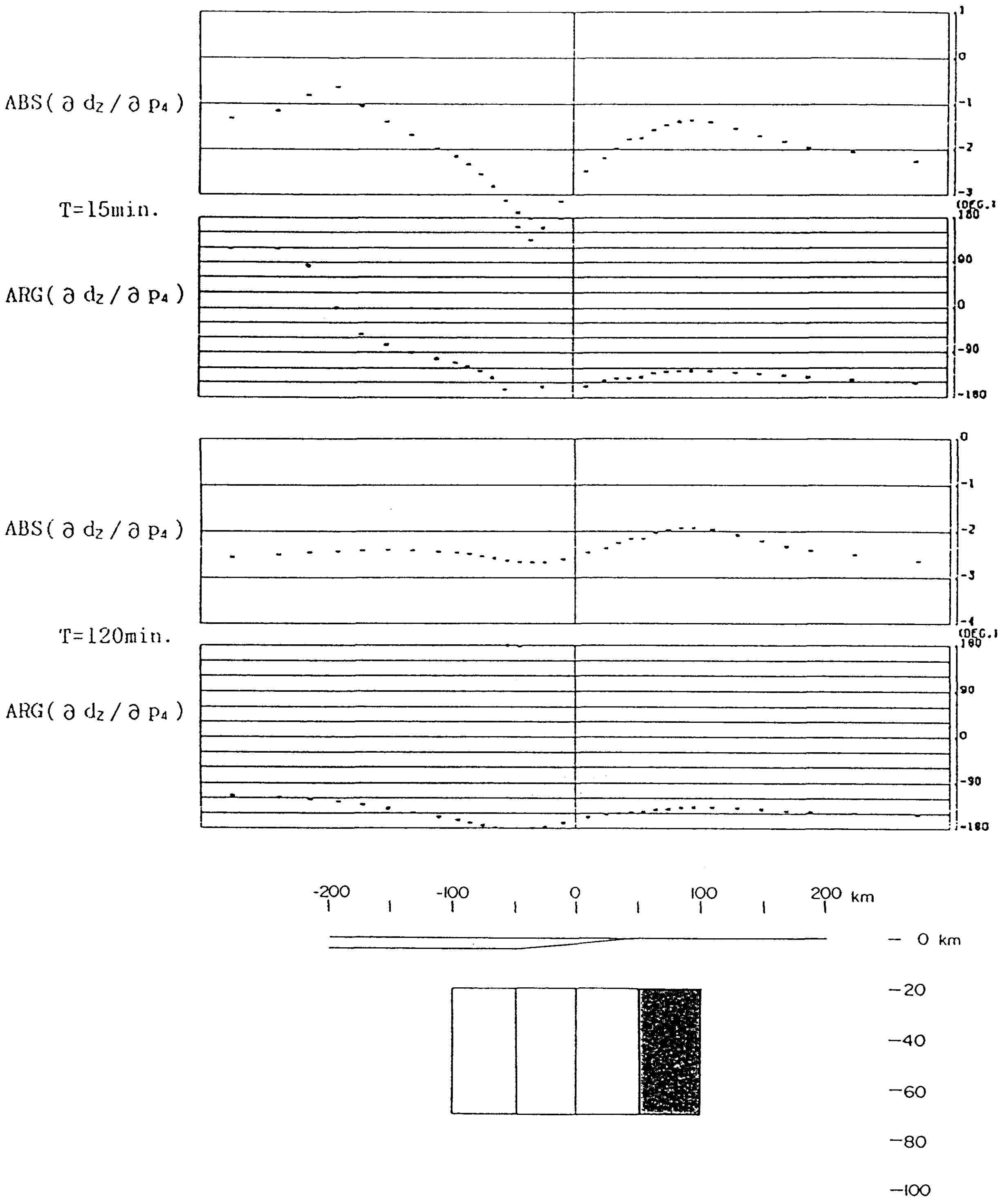

Fig.3.33(d) Distribution of the partial derivative, $\partial d_z/\partial p_4$, for the same condition as (a).

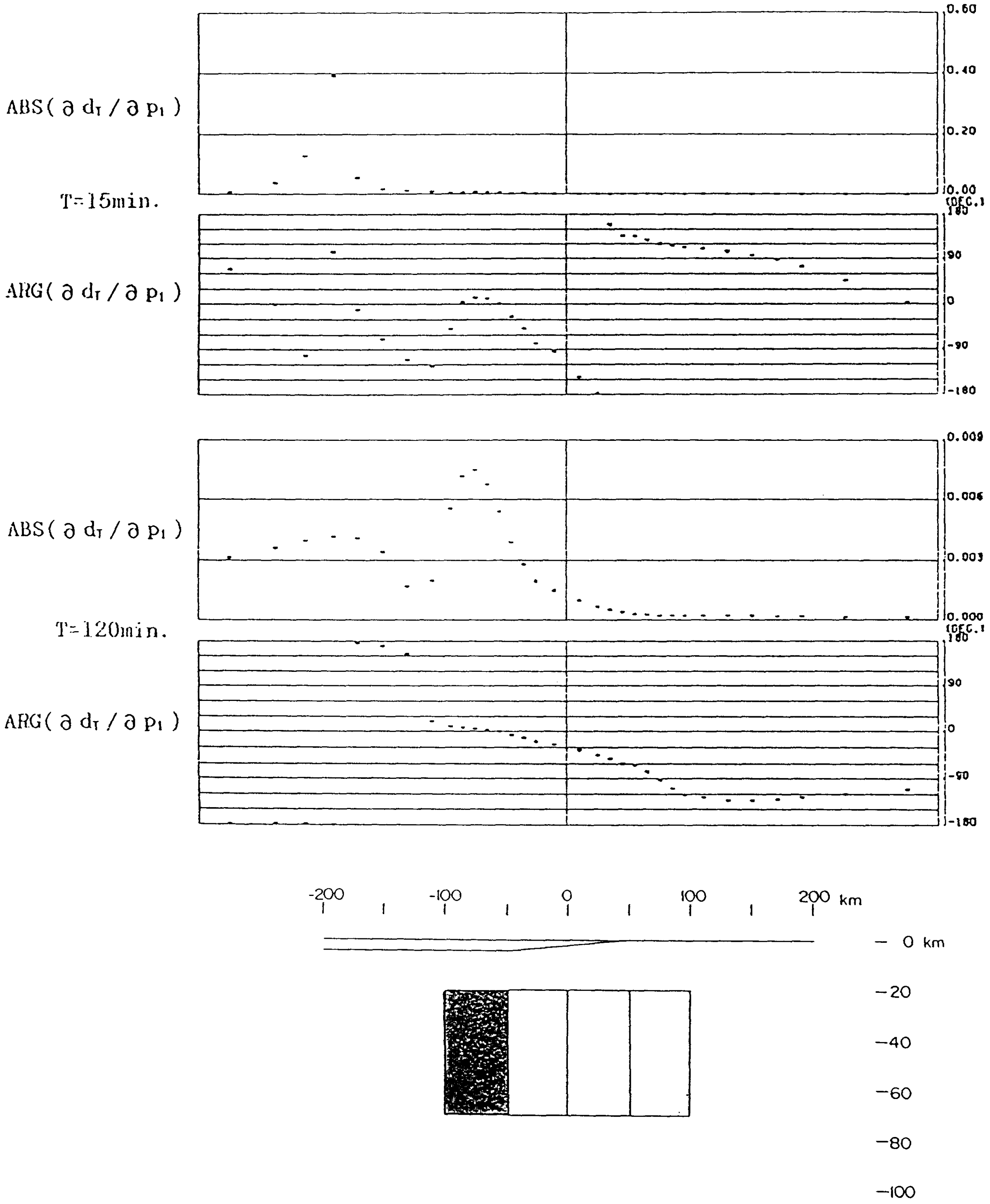

Fig.3.34(a) Distribution of the partial derivative, $\partial d_T/\partial p_1$, for the same condition as Figs.3.33(a)-(d).

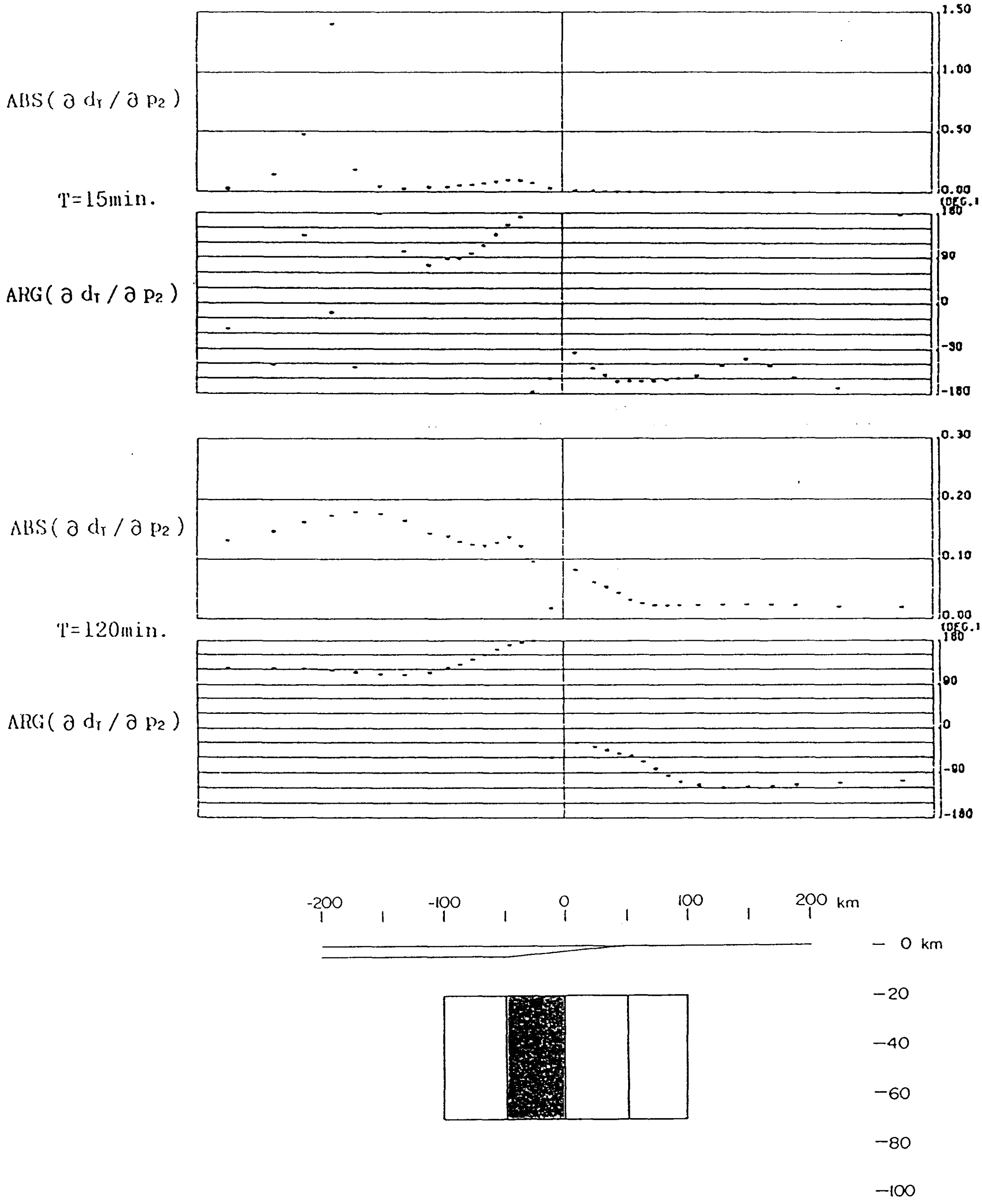

Fig.3.34(b) Distribution of the partial derivative, $\partial d_T / \partial p_2$, for the same condition as (a).

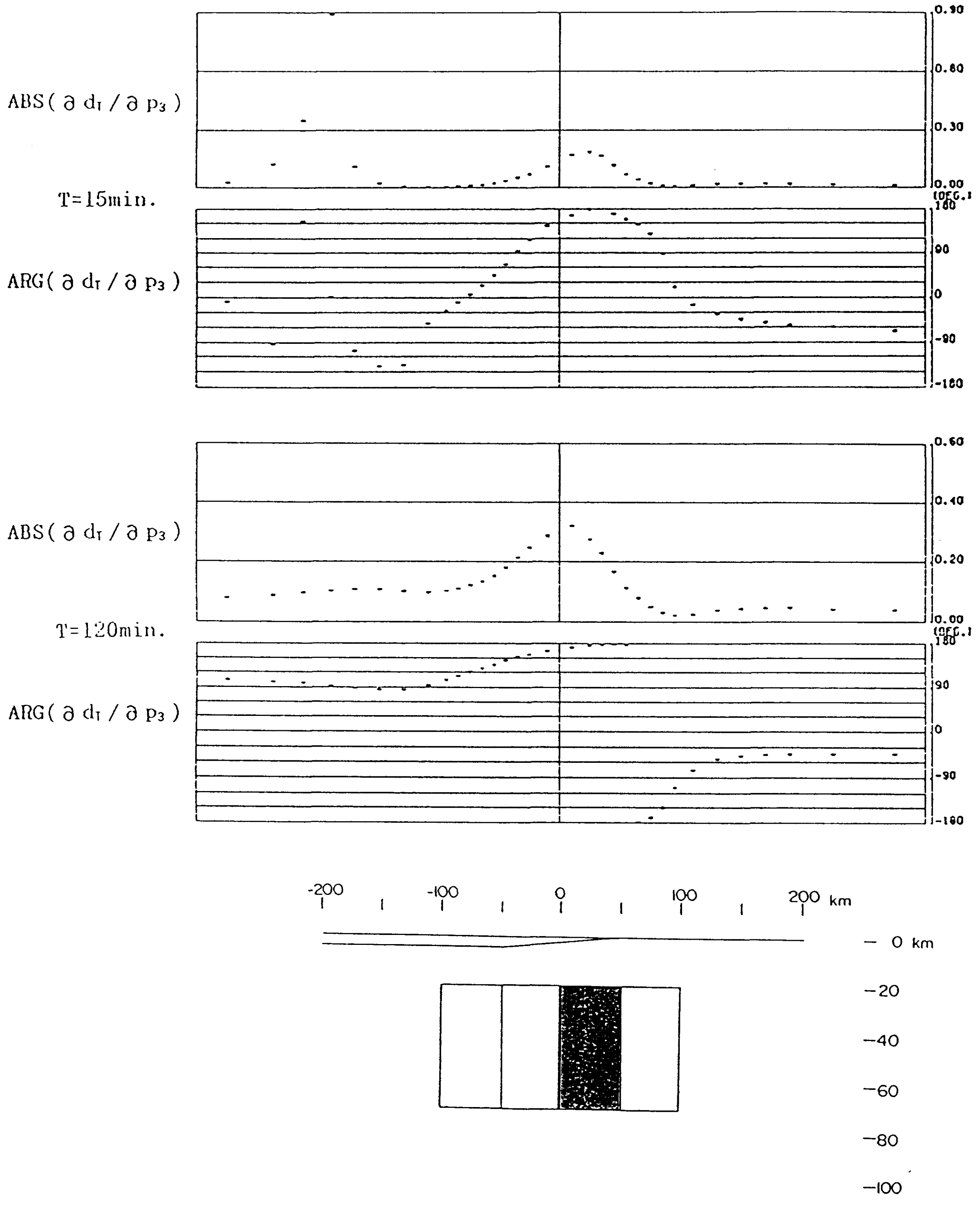

Fig.3.34(c) Distribution of the partial derivative, $\partial d_T/\partial p_3$, for the same condition as (a).

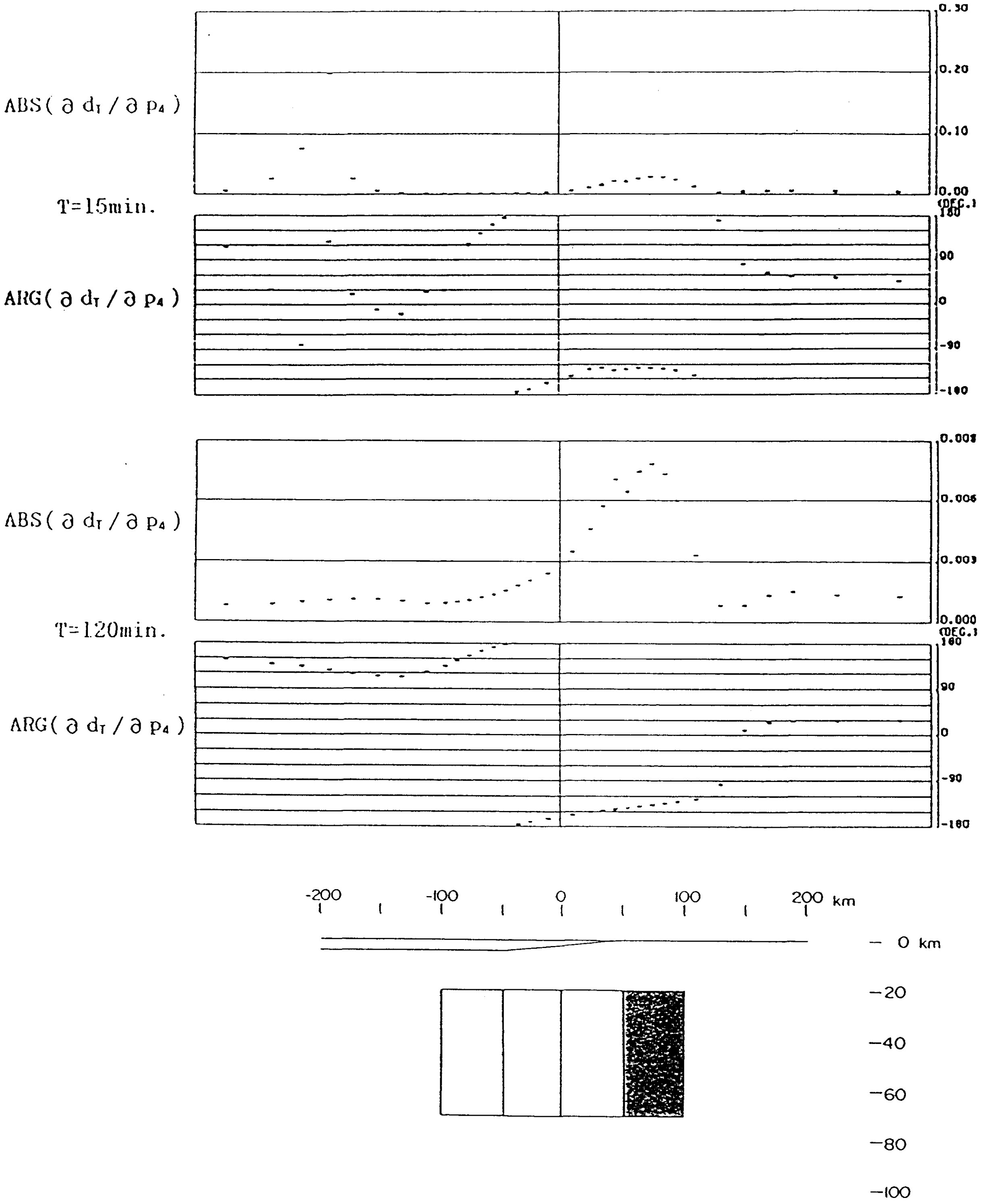

Fig.3.34(d) Distribution of the partial derivative, $\partial d_T/\partial p_4$, for the same condition as (a).

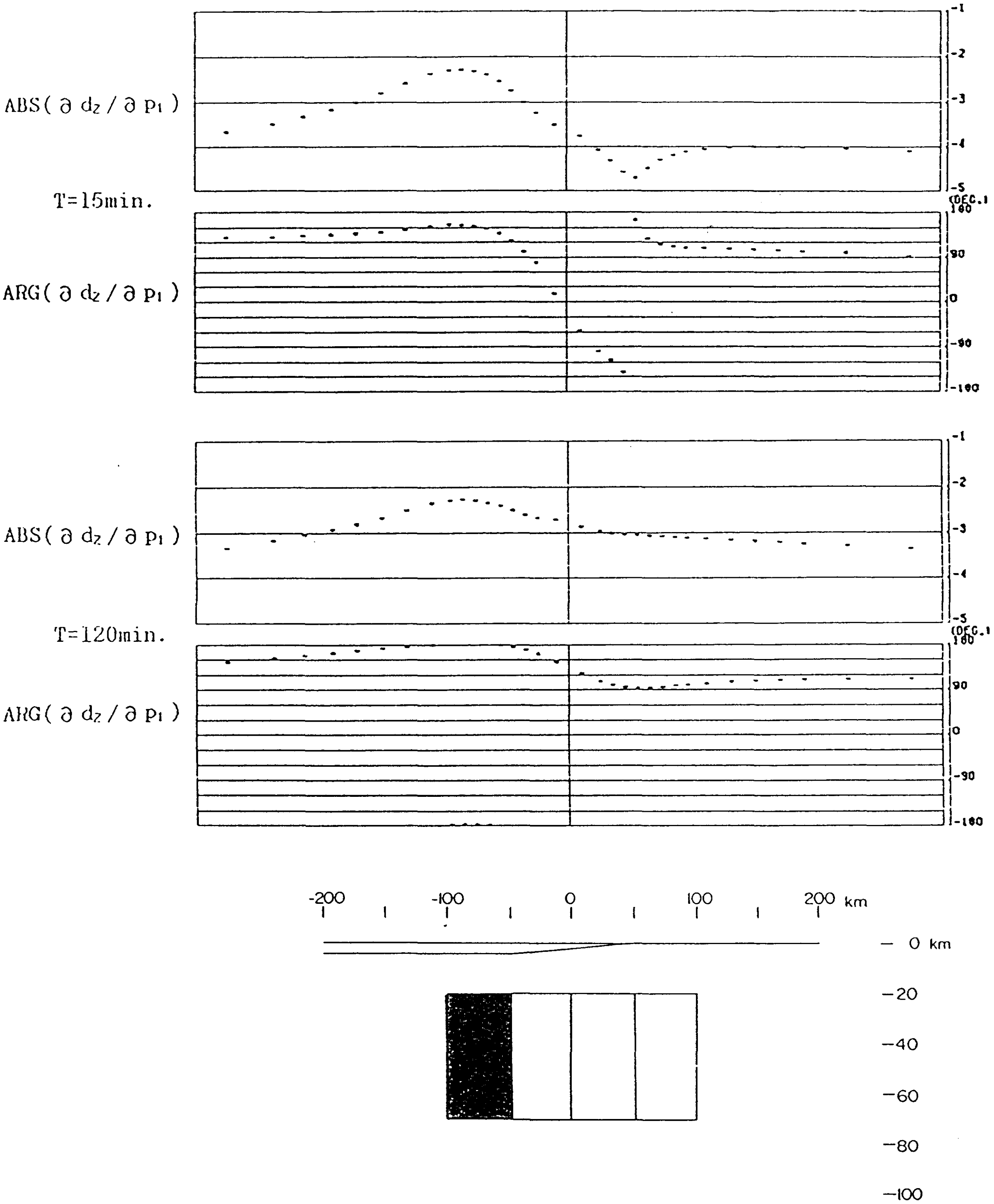

Fig.3.35(a) Distribution of the partial derivative, $\partial d_z/\partial p_1$, for the model T5, when the initial conductivity is taken as 10^{-2} S/m for each block.

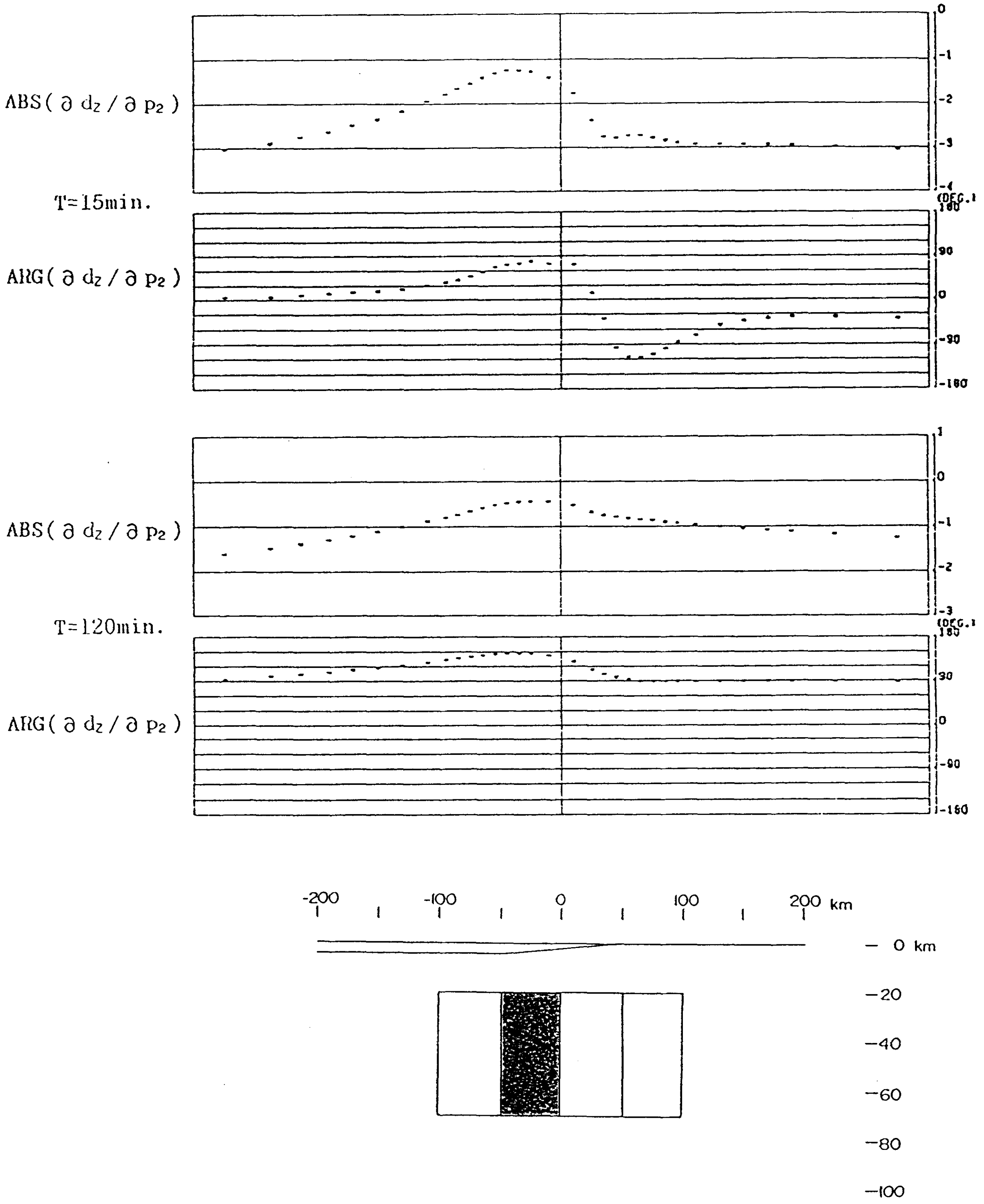

Fig.3.35(b) Distribution of the partial derivative, $\partial d_z/\partial p_z$, for the same condition as (a).

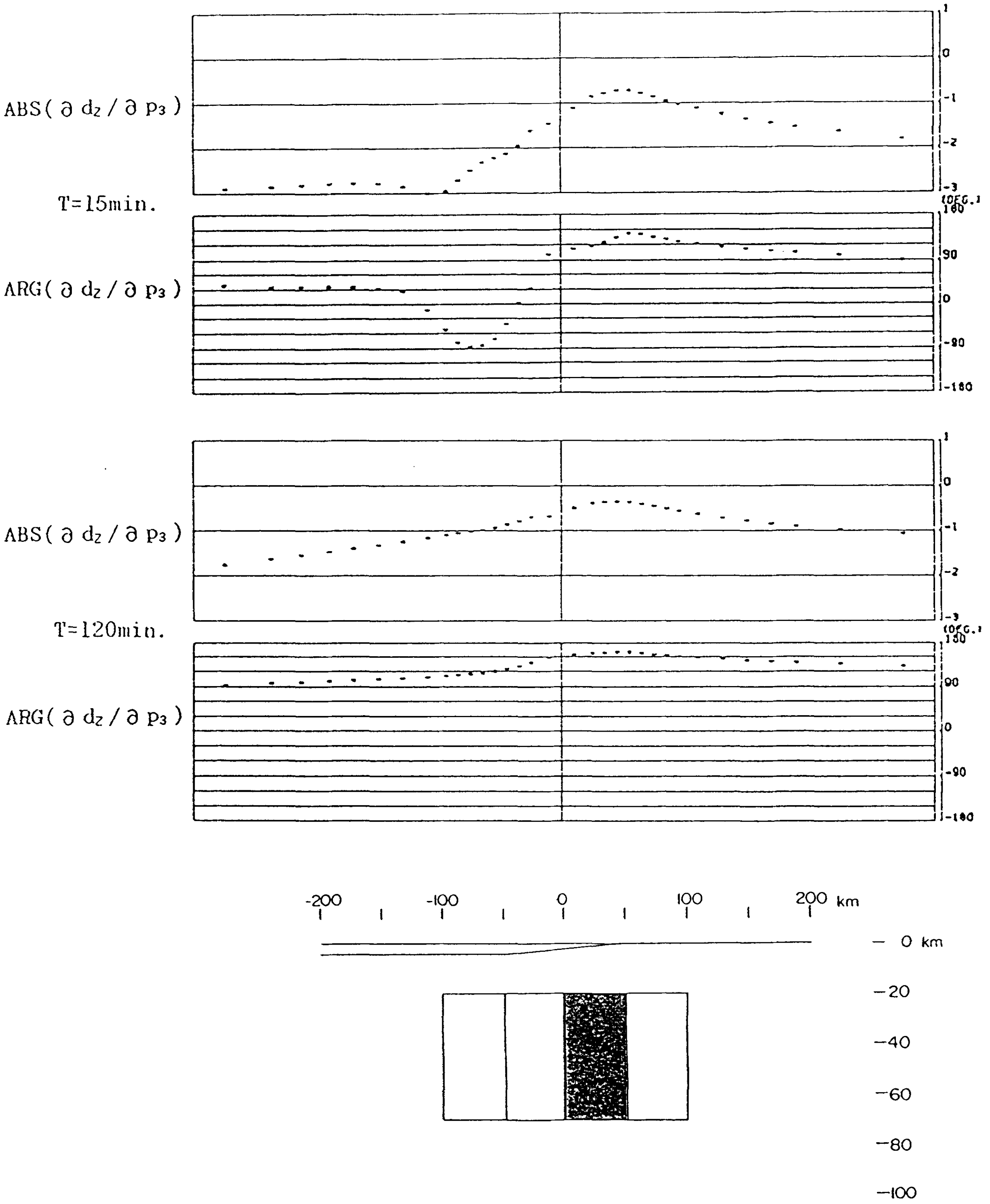

Fig.3.35(c) Distribution of the partial derivative, $\partial d_z/\partial p_3$, for the same condition as (a).

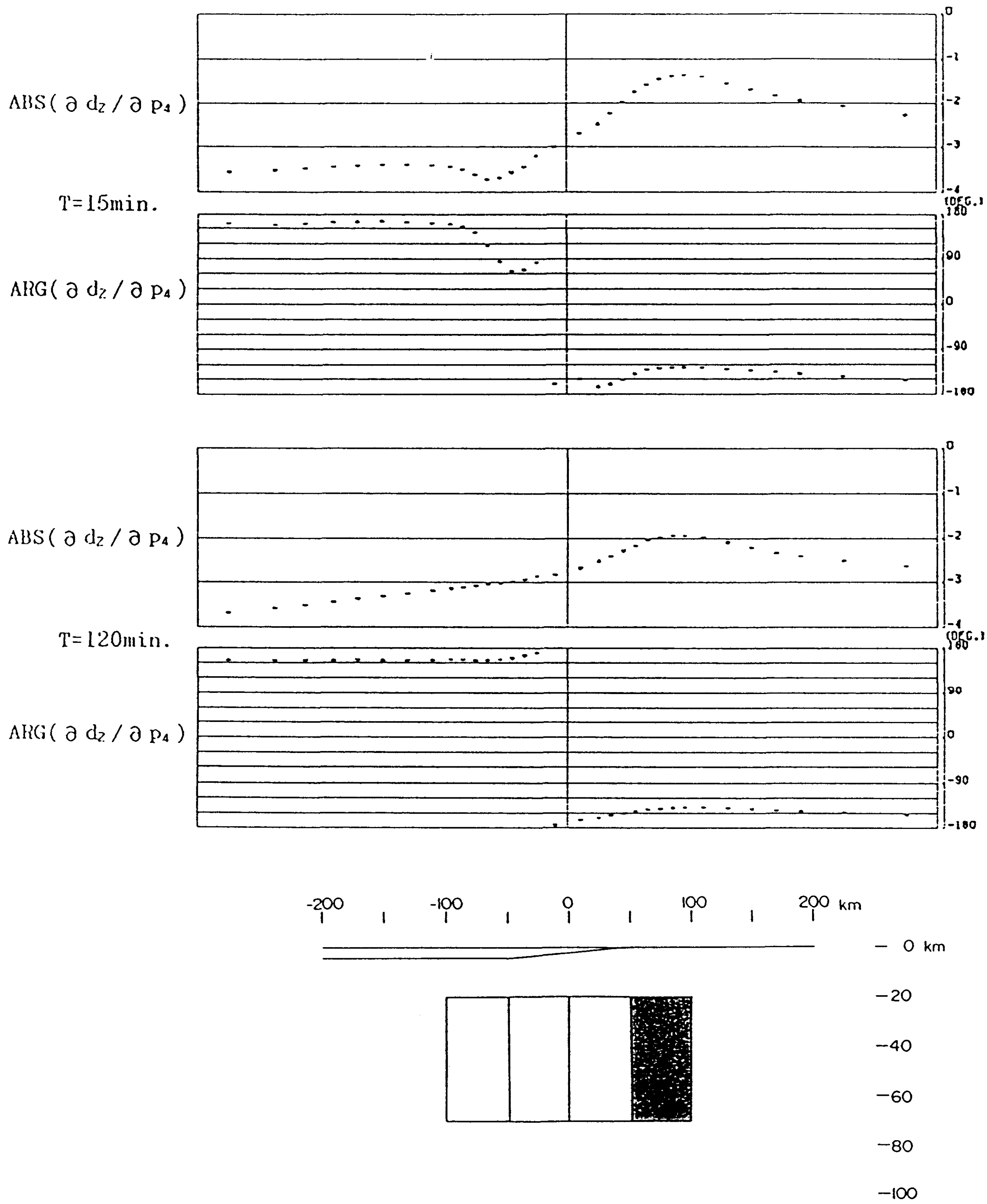

Fig.3.35(d) Distribution of the partial derivative, $\partial d_z/\partial p_4$, for the same condition as (a).

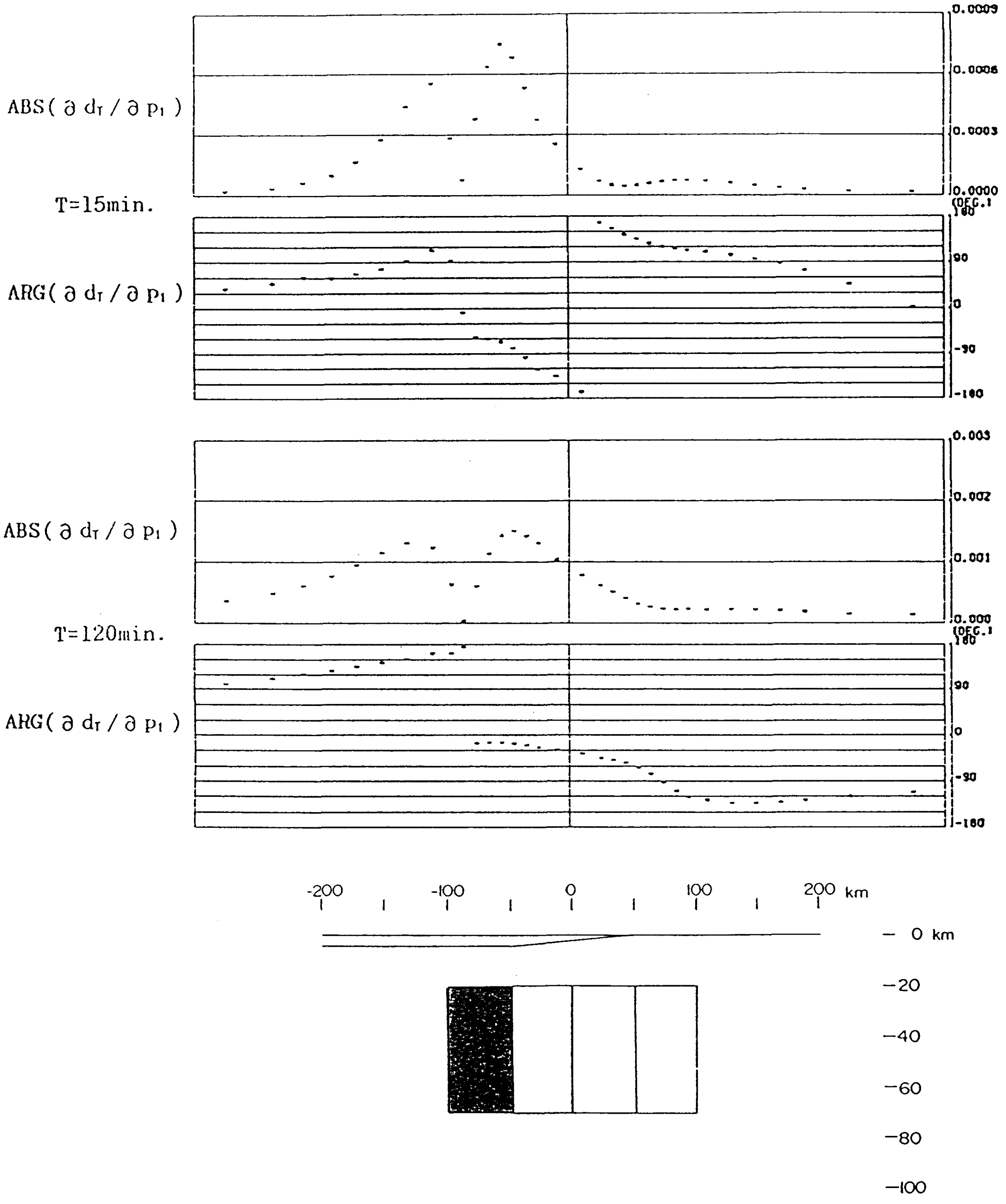

Fig.3.36(a) Distribution of the partial derivative, $\partial d_T/\partial p_1$, for the same condition as Figs.35(a)-(d).

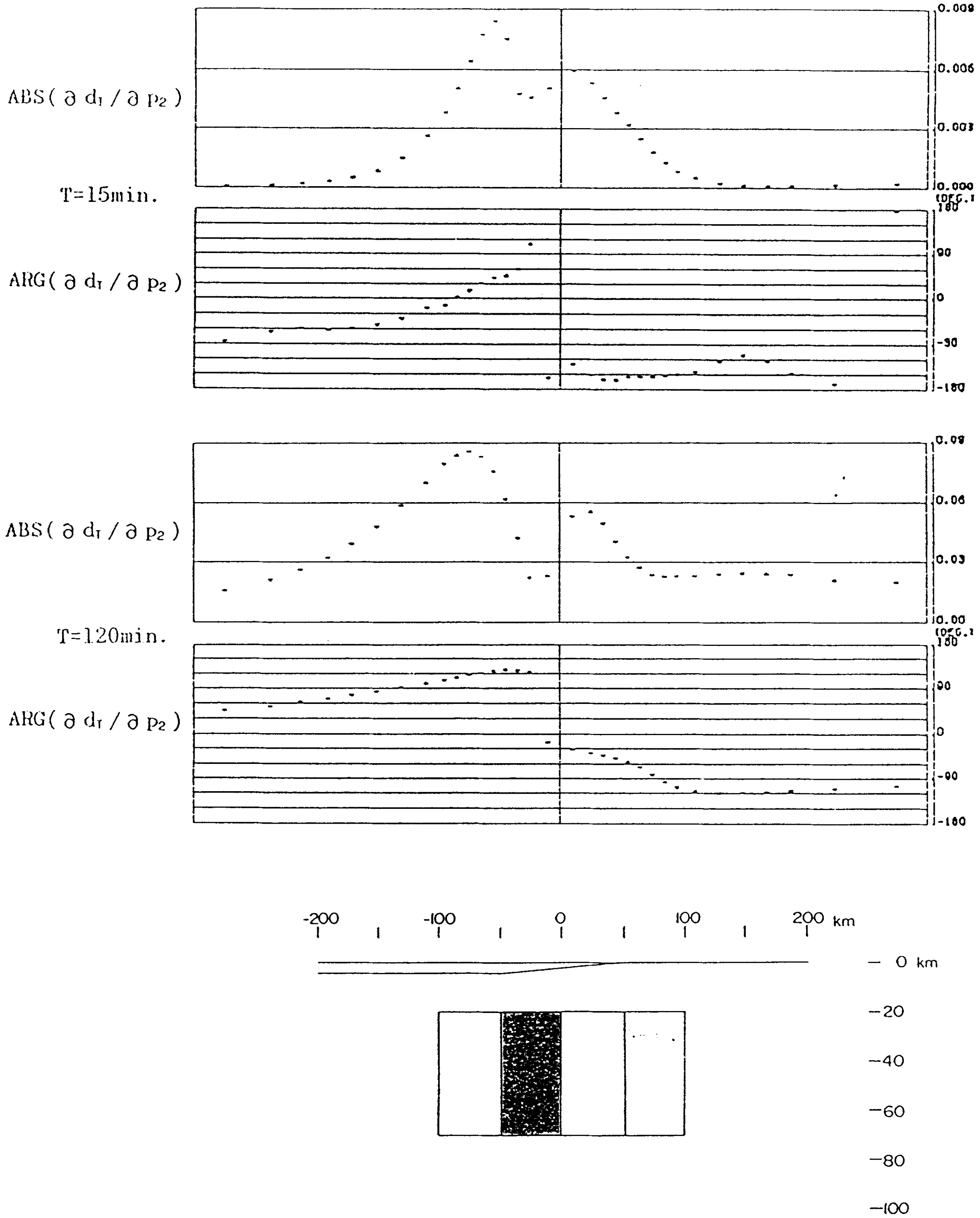

Fig.3.36(b) Distribution of the partial derivative, $\partial d_T/\partial p_2$, for the same condition as (a).

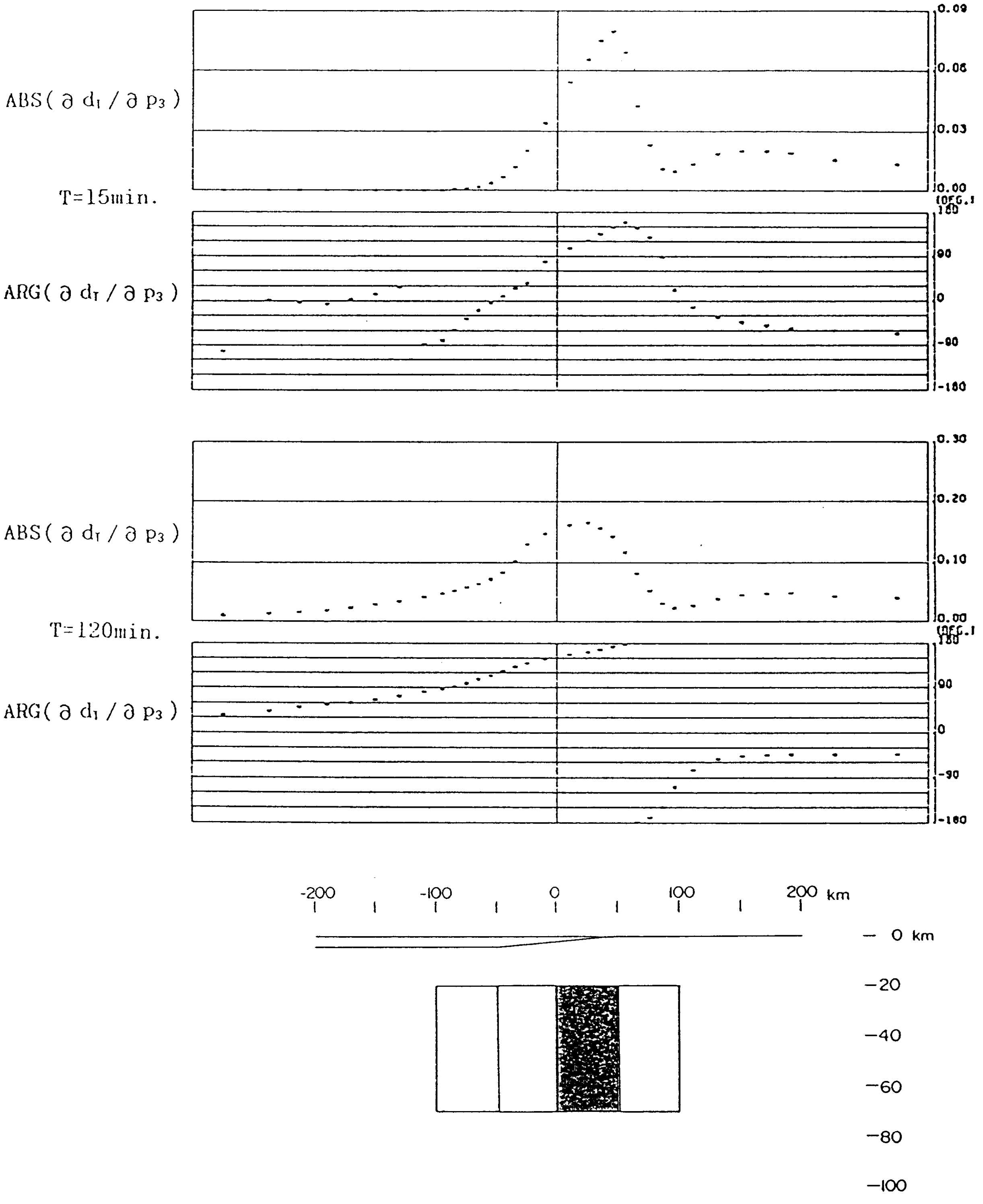

Fig.3.36(c) Distribution of the partial derivative, $\partial d_T/\partial p_3$, for the same condition as (a).

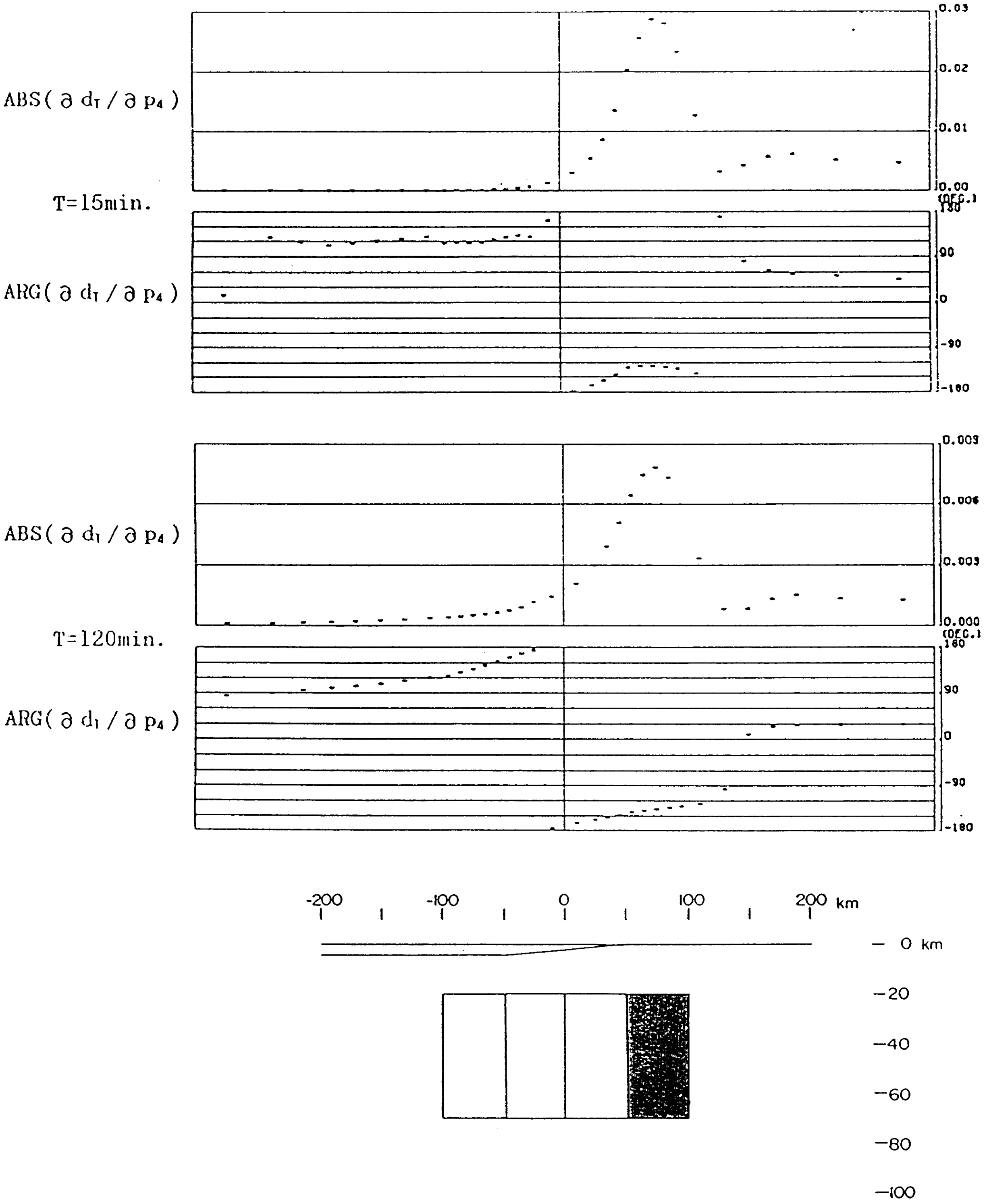

Fig.3.36(d) Distribution of the partial derivative, $\partial d_T / \partial p_4$, for the same condition as (a).

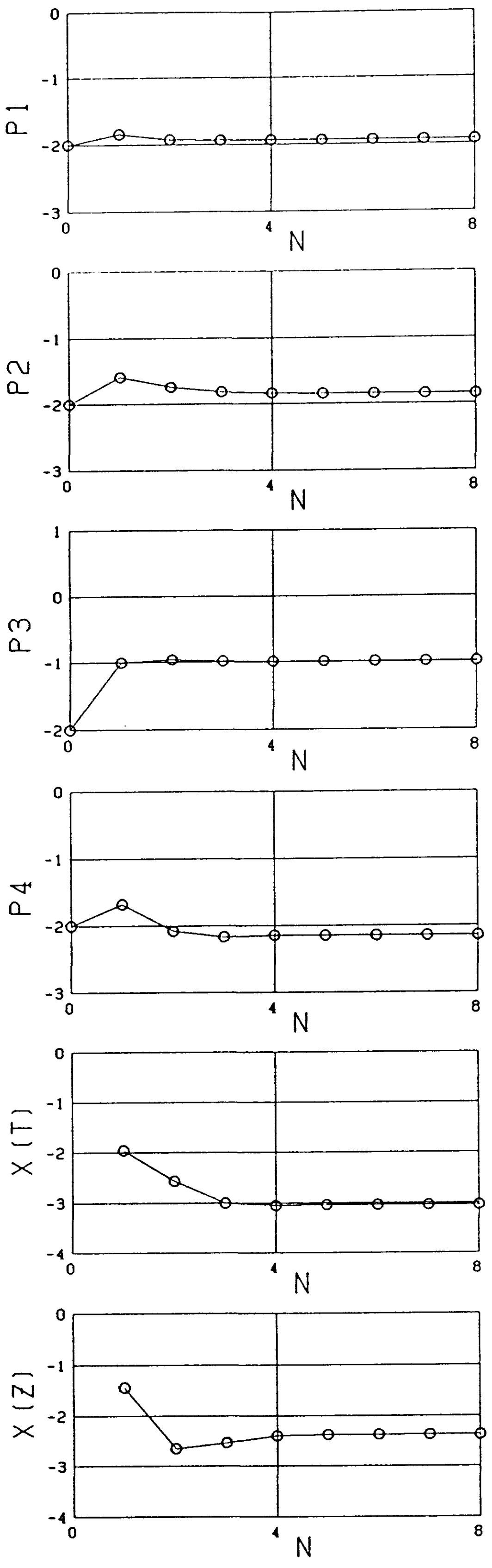

Fig.3.37 Result of the direct inversion for the model T5. The variations of parameters, p_1, p_2, p_3 and p_4, χ^2 of impedance, and χ^2 of transfer function are plotted against the iteration cycle, N.

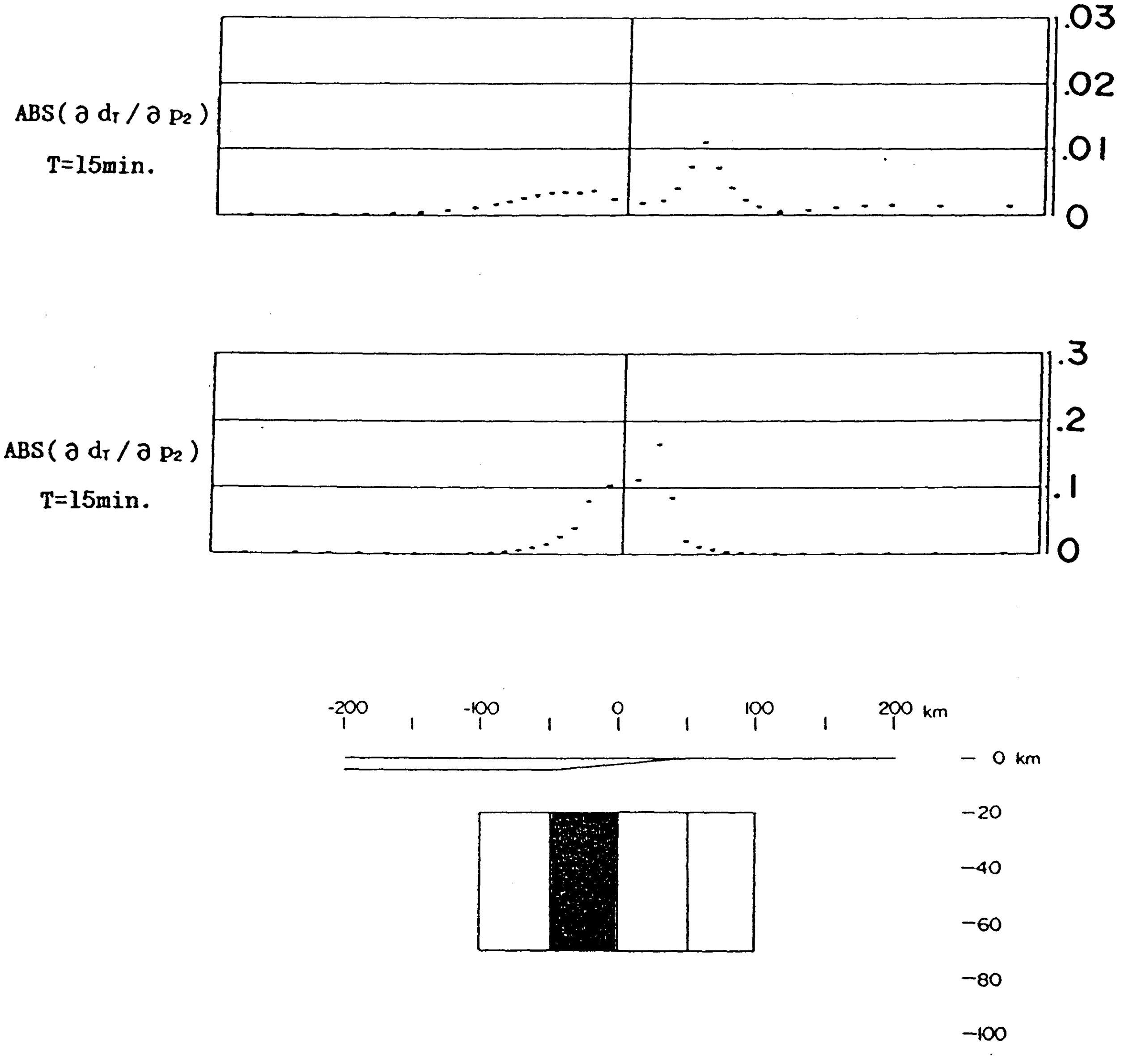

Fig.3.38 Comparison of the amplitude of the partial derivative, $\partial d_T / \partial p_2$, on sea-surface (above) and on seafloor (below).

Table 3.1 Conductivity models for the calculations of typical responses. Conductivity is given in S/m.

Model	σ_A	σ_B	σ_C
I	1×10^{-3}	1×10^{-1}	1×10^{-3}
II	4×10^{0}	1×10^{-3}	1×10^{-3}
III	4×10^{0}	1×10^{-1}	1×10^{-3}

Table 3.2 Finite element network for the numerical experiments on a simple models I , II and III .

Number of nodes	1080
Number of elements	2030
Upper boundary	-150 km
Lower boundary	1500 km
Side boundary (left)	-800 km
Side boundary (right)	800 km
size of element matrix	38 x 1080

Table 3.3(a) Synthesized data for numerical experiment of the direct inversion for the model T1,T3 and T6 (Traverse on land) for the period of 15 min. Amp(T), ϕ T and ε T denote respectively amplitude, phase and obsevation error of the transfer function. ρ a, ϕ Z and ε Z denote the apparent resistivity, phase of the impedance and observation error in ρ a, respectively.

Y(km)	Z(km)	Amp(T)	ϕ_T(deg)	ε_T	ρ_a($\Omega\cdot$m)	ϕ_z(deg)	ε_z
-180	0	0.365	170.0	0.072			
-80	0	0.530	176.0	0.085	133.0	40.0	30.0
-70	0	0.515	177.0	0.078			
-50	0	0.400	177.0	0.091	65.0	34.0	12.0
-20	0	0.122	174.0	0.072			
20	0	0.125	-4.0	0.064	33.0	30.0	8.0
30	0	0.233	-3.5	0.081			
60	0	0.438	-3.1	0.078	67.0	35.0	15.0
90	0	0.527	-4.0	0.085			
160	0	0.385	-7.5	0.075	350.0	48.0	45.0

Table 3.3(b) Synthesized data for numerical experiment of the direct inversion for the model T1 and T3 (Traverse on land) for the period of 120 min.

Y(km)	Z(km)	Amp(T)	ϕ_T(deg)	ε_T	ρ_a($\Omega\cdot$m)	ϕ_z(deg)	ε_z
-180	0	0.260	-132.0	0.055			
-80	0	0.445	-140.0	0.077	450.0	44.0	84.0
-70	0	0.443	-144.0	0.064			
-50	0	0.365	-148.0	0.078	310.0	35.0	75.0
-20	0	0.133	-155.0	0.068			
20	0	0.115	24.0	0.056	190.0	28.0	30.0
30	0	0.205	24.5	0.079			
60	0	0.387	30.0	0.094	294.0	36.0	77.0
90	0	0.420	38.0	0.088			
160	0	0.294	44.0	0.062	630.0	55.0	95.0

Table 3.4(a) Synthesized data for numerical experiment of the direct inversion for the model T2 and T4 (Traverse on sea floor-land) for the period of 15 min.

Y(km)	Z(km)	Amp(T)	ϕ_T(deg)	ε_T	ρ_a($\Omega \cdot$m)	ϕ_Z(deg)	ε_Z
-180	4.0	0.084	119.0	0.070			
-80	4.0	0.327	117.0	0.080	45.0	-92.5	8.2
-70	4.0	0.397	129.0	0.072			
-50	4.0	0.676	-178.3	0.111	26.2	-105.0	6.8
-20	2.8	3.330	-86.0	0.342			
20	1.2	2.160	16.7	0.261	80.0	59.0	11.2
30	0.8	1.770	13.8	0.181			
60	0	0.970	-3.3	0.110	58.0	48.2	15.0
90	0	0.822	-6.8	0.088			
160	0	0.536	-14.5	0.074	325.0	61.7	45.0

Table 3.4(b) Synthesized data for numerical experiment of the direct inversion for the model T2 and T4 (Traverse on sea floor - land) for the period of 120 min.

Y(km)	Z(km)	Amp(T)	ϕ_T(deg)	ε_T	ρ_a($\Omega \cdot$m)	ϕ_Z(deg)	ε_Z
-180	4.0	0.626	103.8	0.055			
-80	4.0	0.959	122.9	0.087	161.0	161.0	24.0
-70	4.0	1.075	125.0	0.122			
-50	4.0	1.590	129.8	0.178	156.0	156.0	27.0
-20	2.8	3.122	72.5	0.366			
20	1.2	1.751	23.1	0.188	91.0	44.0	16.0
30	0.8	1.520	19.2	0.143			
60	0	0.994	12.0	0.094	62.2	41.3	13.2
90	0	0.829	13.0	0.088			
160	0	0.561	13.3	0.062	145.0	57.6	29.5

Table 3.5(a) Synthesized data for numerical experiment of the direct inversion for the model T5 (Traverse on seafloor-land) for the period of 15 min.

Y(km)	Z(km)	Amp(T)	ϕ_T(deg)	ε_T	ρ_a(Ω·m)	ϕ_Z(deg)	ε_Z
-180	0	0.0025	-164.2	0.040			
-80	0	0.0301	-159.2	0.081	0.44	4.0	0.13
-70	0	0.0433	-145.2	0.070			
-50	0	0.0987	-103.5	0.091	0.52	0.0	0.18
-20	0	0.2566	-58.3	0.120			
20	0	0.508	-27.4	0.160	4.18	16.7	1.21
30	0	0.639	-20.0	0.180			
60	0	0.970	-3.3	0.112	58.3	49.1	19.2
90	0	0.822	-6.8	0.088			
160	0	0.536	-14.0	0.075	325.0	61.7	45.0

Table 3.5(b) Synthesized data for numerical experiment of the direct inversion for the model T5 (Traverse on seafloor-land) for the period of 120 min.

Y(km)	Z(km)	Amp(T)	ϕ_T(deg)	ε_T	ρ_a(Ω·m)	ϕ_Z(deg)	ε_Z
-180	0	0.066	-62.5	0.056			
-80	0	0.176	-35.6	0.087	5.21	4.7	2.33
-70	0	0.202	-31.2	0.122			
-50	0	0.286	-17.3	0.108	5.43	6.2	2.47
-20	0	0.499	-11.8	0.126			
20	0	0.774	-2.2	0.128	17.3	19.7	7.31
30	0	0.860	2.0	0.143			
60	0	0.994	12.0	0.095	62.2	41.3	13.2
90	0	0.829	13.0	0.088			
160	0	0.561	13.3	0.065	145.0	57.6	29.5

Table 3.6 Setup of models for numerical experiments on th direct inversion scheme.

model	host medium	inhomogeneity A	unknowns
T1	1×10^{-3}(S/m)	1×10^{-3}(S/m)	1
T2	1×10^{-3}(S/m)	4×10^{0} (S/m)	1
T3	1×10^{-3}(S/m)	1×10^{-3}(S/m)	4
T4	1×10^{-3}(S/m)	4×10^{0} (S/m)	4
T5	1×10^{-3}(S/m)	4×10^{0} (S/m)	4

Table 3.7 Results of direct inversion for the model T1.

No.	Initial(S/m)	C_{popo}	Final(S/m)	C_{pp}	True(S/m)	C_{popo}/C_{pp}
1	1×10^{1}	5×10^{-2}	1.162×10^{-1}	1.5×10^{-3}	1×10^{-1}	3.3×10^{2}

Iteration cycles	6
Initial $\chi^2(d_Z)$	7.082×10^{0}
Final $\chi^2(d_Z)$	1.520×10^{-2}
Initial $\chi^2(d_T)$	2.097×10^{-1}
Final $\chi^2(d_T)$	2.163×10^{-3}

No.	Initial(S/m)	C_{popo}	Final(S/m)	C_{pp}	True(S/m)	C_{popo}/C_{pp}
1	1×10^{0}	8×10^{0}	1.013×10^{-1}	2.8×10^{-2}	1×10^{-1}	2.9×10^{2}

Iteration cycles	6
Initial $\chi^2(d_Z)$	3.550×10^{0}
Final $\chi^2(d_Z)$	7.017×10^{-4}
Initial $\chi^2(d_T)$	1.528×10^{-1}
Final $\chi^2(d_T)$	5.192×10^{-4}

No.	Initial(S/m)	C_{popo}	Final(S/m)	C_{pp}	True(S/m)	C_{popo}/C_{pp}
1	1×10^{-2}	8×10^{0}	9.983×10^{-2}	5.3×10^{-2}	1×10^{-1}	1.5×10^{2}

Iteration cycles	6
Initial $\chi^2(d_Z)$	1.991×10^{0}
Final $\chi^2(d_Z)$	7.053×10^{-4}
Initial $\chi^2(d_T)$	1.676×10^{-1}
Final $\chi^2(d_T)$	5.143×10^{-4}

No.	Initial(S/m)	C_{popo}	Final(S/m)	C_{pp}	True(S/m)	C_{popo}/C_{pp}
1	1×10^{-3}	1×10^{-1}	9.463×10^{-2}	1.6×10^{-3}	1×10^{-1}	6.3×10^{2}

Iteration cycles	6
Initial $\chi^2(d_Z)$	2.822×10^{0}
Final $\chi^2(d_Z)$	5.021×10^{-3}
Initial $\chi^2(d_T)$	2.502×10^{-1}
Final $\chi^2(d_T)$	5.231×10^{-4}

Table 3.8 Results of direct inversion for the model T2.

No.	Initial(S/m)	C_{popo}	Final(S/m)	C_{pp}	True(S/m)	C_{popo}/C_{pp}
1	$1x10^{0}$	$1x10^{0}$	$1.024x10^{-1}$	$7.8x10^{-2}$	$1x10^{-1}$	$1.3x10^{1}$

Iteration cycles	8
Initial $\chi^{2}(d_Z)$	$3.629 x 10^{0}$
Final $\chi^{2}(d_Z)$	$5.928 x 10^{-3}$
Initial $\chi^{2}(d_T)$	$1.915 x 10^{0}$
Final $\chi^{2}(d_T)$	$3.424 x 10^{-2}$

No.	Initial(S/m)	C_{popo}	Final(S/m)	C_{pp}	True(S/m)	C_{popo}/C_{pp}
1	$1x10^{-2}$	$1x10^{0}$	$9.112x10^{-2}$	$9.3x10^{-2}$	$1x10^{-1}$	$1.1x10^{1}$

Iteration cycles	8
Initial $\chi^{2}(d_Z)$	$2.996 x 10^{0}$
Final $\chi^{2}(d_Z)$	$5.491 x 10^{-3}$
Initial $\chi^{2}(d_T)$	$1.634 x 10^{0}$
Final $\chi^{2}(d_T)$	$3.242 x 10^{-2}$

Table 3.9 Results of direct inversion for the model T3.

No.	Initial(S/m)	C_{popo}	Final(S/m)	C_{pp}	True(S/m)	C_{popo}/C_{pp}
1	$1x10^{-2}$	$1x10^{0}$	$4.744x10^{-3}$	$4.7x10^{-1}$	$1x10^{-3}$	$2.1x10^{0}$
2	$1x10^{0}$	$1x10^{0}$	$8.102x10^{-2}$	$.5x10^{-2}$	$1x10^{-1}$	$4.0x10^{1}$
3	$1x10^{0}$	$1x10^{0}$	$1.076x10^{-1}$	$2.5x10^{-2}$	$1x10^{-1}$	$4.0x10^{1}$
4	$1x10^{-2}$	$1x10^{0}$	$5.042x10^{-3}$	$.2x10^{-1}$	$1x10^{-3}$	$8.3x10^{0}$

Iteration cycles	6
Initial $\chi^2(d_Z)$	1.611×10^{0}
Final $\chi^2(d_Z)$	4.274×10^{-3}
Initial $\chi^2(d_T)$	1.659×10^{-1}
Final $\chi^2(d_T)$	3.172×10^{-3}

No.	Initial(S/m)	C_{popo}	Final(S/m)	C_{pp}	True(S/m)	C_{popo}/C_{pp}
1	$1x10^{-2}$	$1x10^{0}$	$4.744x10^{-3}$	$3.6x10^{-1}$	$1x10^{-3}$	$2.8x10^{0}$
2	$1x10^{-2}$	$1x10^{0}$	$8.102x10^{-2}$	$2.1x10^{-2}$	$1x10^{-1}$	$4.8x10^{1}$
3	$1x10^{-2}$	$1x10^{0}$	$1.076x10^{-1}$	$1.0x10^{-2}$	$1x10^{-1}$	$1.0x10^{2}$
4	$1x10^{-2}$	$1x10^{0}$	$5.042x10^{-3}$	$7.3x10^{-1}$	$1x10^{-3}$	$1.4x10^{0}$

Iteration cycles	6
Initial $\chi^2(d_Z)$	1.557×10^{0}
Final $\chi^2(d_Z)$	1.666×10^{-3}
Initial $\chi^2(d_T)$	1.519×10^{-1}
Final $\chi^2(d_T)$	3.242×10^{-3}

Table 3.10 Result of direct inversion for the model T4.

No.	Initial(S/m)	C_{popo}	Final(S/m)	C_{pp}	True(S/m)	C_{popo}/C_{pp}
1	1×10^{-2}	5×10^{-1}	5.242×10^{-3}	2.2×10^{-1}	1×10^{-3}	2.3×10^{0}
2	1×10^{-2}	5×10^{-1}	1.527×10^{-2}	2.6×10^{-2}	1×10^{-1}	1.9×10^{1}
3	1×10^{-2}	1×10^{0}	9.961×10^{-1}	3.7×10^{-2}	1×10^{-1}	2.7×10^{1}
4	1×10^{-2}	1×10^{0}	8.994×10^{-3}	7.2×10^{-1}	1×10^{-3}	1.4×10^{0}

Iteration cycles	16
Initial $\chi^2(d_Z)$	1.031×10^{0}
Final $\chi^2(d_Z)$	1.796×10^{-1}
Initial $\chi^2(d_T)$	1.253×10^{0}
Final $\chi^2(d_T)$	2.972×10^{-1}

Table 3.11 Result of direct inversion for the model T5.

No.	Initial(S/m)	C_{popo}	Final(S/m)	C_{pp}	True(S/m)	C_{popo}/C_{pp}
1	1×10^{-2}	5×10^{-1}	1.155×10^{-2}	4.9×10^{-1}	1×10^{-3}	1.02×10^{0}
2	1×10^{-2}	5×10^{-1}	1.419×10^{-2}	4.8×10^{-1}	1×10^{-1}	1.04×10^{0}
3	1×10^{-2}	1×10^{0}	1.029×10^{-1}	4.2×10^{-2}	1×10^{-1}	2.3×10^{1}
4	1×10^{-2}	1×10^{0}	7.141×10^{-3}	6.5×10^{-1}	1×10^{-3}	1.53×10^{0}

Iteration cycles	6
Initial $\chi^2(d_Z)$	3.597×10^{-2}
Final $\chi^2(d_Z)$	4.262×10^{-3}
Initial $\chi^2(d_T)$	1.096×10^{-2}
Final $\chi^2(d_T)$	9.119×10^{-3}

4. VLF·ELF Magnetotelluric Measurements

The aim of this study lies in determination of deep (lower crust and upper mantle depth) geoelectric structure of the earth. However, this does not mean that information on the shallower structure is unnecessary. The near-surface structure of the earth is considerably complex. It is known that the surface geology sometimes causes significant geomagnetic and geoelectric variation anomalies (e.g. Porath and Dziewonski, 1971) even at fairly long periods.

Since the field penetration depth, or the skin depth of the electromagnetic variation increases with the period of the variation, higher frequencies (shorter periods) are preferred to determine the structure at shallower depth. An artificial electromagnetic wave at VLF range and natural electromagnetic phenomenon at ELF range can be used for this purpose. The former is the signal for communication use with 17.4 kHz frequency which is always transmitted from the radio station at Yosami, Aichi Prefecture, Japan. The latter is the electromagnetic resonance in the cavity bounded by the earth and the ionosphere, which is known as the Schumann Resonance (Schumann, 1953).

Since these are signals at relatively high frequencies, the measurement is a little different from the ordinary geomagnetic observation. Field techniques and methods of data processing will be shown in this chapter.

4.1 VLF magnetotelluric measurement

VLF magnetotelluric (MT) method was first developed for the purpose of sounding the thickness of the permafrost. Since then, because of its easiness in measurements, it has been applied to many fields of geophysical exploration; mineral exploration, geothermal exploration, etc.. Sometimes this technique has been used for volcanological researches (Zablocki, 1978; Utada, et al., 1984) or research of the structure of active faults (e.g. Yukutake, 1985).

There are eight VLF stations in the world transmitting VLF signals. Among these signals, 17.4 kHz from Yosami(NDT), Aichi Prefecture is always detectable in Japan except in the period of the maintenance of transmission apparatus. The signal of 20.2 kHz from Northwest Cape(NWC), Australia can also be detected sometimes, but the signal is much weaker than 17.4 kHz signal. Therefore we mostly use the 17.4 kHz signal from Yosami.

The skin depth of 17.4 kHz signal in a homogeneous medium is estimated as, from Eq.(3-2-5), about 12 m and 120 m assuming the resistivity of the medium to be 10 Ω·m and 1 kΩ·m, respectively. These sounding depth seem to be sufficient to measure the conductivities of the surface sedimentary layer, outcrop of basement rocks and other geological structures.

A VLF measuring apparatus EM16-EM16R of Geonics Corporation, Canada, was used for VLF MT measurements. Fig.4.1 shows the conceptual block diagram of VLF MT measurement by use of the apparatus. The magnetic field of the VLF wave is detected by loop antenna. The electric field is measured by use of a pair of stainless electrodes grounded 5m apart. Both fields are once amplified and sharply filtered, and then the phase of the electric field signal is shifted by the phase shifter. If the electric field signal is adjusted to be in-phase to the magnetic field signal, one can make the final output to be null by varying the gain of the electric field amplifier. The impedance, which is the ratio of the magnetic to the electric field intensity, can be obtained since the gain of the amplifier, electrode spacing and the sensitivity of the antenna are known. By using EM16-EM16R apparatus, the apparent resistivity and the phase difference can be directly read on a scale without any conversion. The measurement can be done easily and highly efficiently; it takes a few minutes for one measurement.

Usually the VLF MT measurements are conducted together with the ELF MT measurements (Section 4.2). Several VLF measurements are done at one ELF MT site and the average is used as the representing value of the site.

The purpose of the VLF measurement is to determine the conductivity at the shallowest depth. Since the field penetration depth of VLF signal is very shallow, there is a possibility of daily or seasonal variation in the VLF apparent resistivity due to, for example, effects of temperature or precipitation. If these effects cause a significant variation, the measured value can not be used as a characteristic value or the time independent response function to determine the subterranean structure.

Another apparatus was newly developed for the purpose of a continuous recording of VLF data (Utada and Yukutake, 1983). This apparatus enables us an automatic recording of the data, including the intensities of electric and magnetic fields, the apparent resistivity and the phase, in the cassette magnetic tape in every minutes. By use of the new apparatus, the presences of the daily and the seasonal variations were examined.

A typical record of 1 day's duration is given in Fig.4.2, which was obtained at Fujinomiya(FJM), Shizuoka Prefecture. The measurement began in March, 1984, and is still carrying on. A typical daily variations are recognized both in the electric and magnetic field intensities. Generally, the level of the field intensity is high and fluctuates at night, but is low and rather stable in daytime. These variations is supposed to be due to the ionospheric effect. Since the D-layer of the ionosphere disappears at night, the level of sky wave increases compared with that in the daytime. This is the principal cause of the high level and the fluctuations at night. Though the fluctuations looks random in both field intensities, they are almost in parallel. Therefore, these features can be subscribed to the change in the wave propagation condition of ionospheric origin. The largest variation is seen at dawn and dusk. This feature also implies that the variation is due to ionospheric effect. Anyway, there is a variation of about 20 Ω·m in the apparent resistivity. This variation corresponds to only about 2 % of the measured value of about 1000 Ω·m, so that we can reasonably regard the daily variation in the apparent resistivity as negligible. The daily variation in the phase difference can also be regarded as insignificant, since the amplitude amounts to no more than 2 degrees or so.

Fig.4.3 is a plot of daily means of the apparent resistivity and the phase measured at FJM. The apparent resistivity decreases in summer, during June to August.This apparent annual variation is amounting to 300 Ω·m. The variation in the phase difference is about 5 degrees. Since the decrease in the apparent resistivity begins in June, precipitation is the most probable cause of this variation.

Such continuous observation of VLF MT has not been conducted elsewhere, so it is quite uncertain that the annual variation as shown in Fig.4.3 is a general feature of the VLF MT measurement. In general, the conductivity of the earth's surface varies by orders of magnitude from place to place. Therefore this annual variation of up to 30% in apparent resistivity can not exert an significant influence on the determination of the earth's structure, particularly in case of the investigation of large scale structure. In this study, we use the VLF MT results as time invariant responses of the shallow subsurface structure.

4.2 ELF magnetotelluric measurement

The Schumann resonance (Schumann, 1953), an electromagnetic cavity resonance in a space between the earth and the ionosphere, lies at the lowest part of extremely low frequency (ELF) range. Since it is activated by lightning flashes which occur all over the world, this resonance field is always detectable as is shown schematically in Fig.4.4. Moreover, its spectral characteristics are very typical and have been well studied; the resonance frequencies are 8, 14, and 20 Hz for three fundamental modes, and their Q-factor (reciprocal of the damping coefficient) is about 3-6 (Balser and Wagner 1960; Ogawa and Tanaka 1970; Handa 1971). The skin depth at the frequency of the fundamental mode will be about 2 km when the resistivity of the medium is 1 kΩ·m.

Above mentioned natures imply that the Schumann resonance is a good source field for induction methods to study earth's conductivity structure at shallow depths. In Japan, there are many sources of the artificial electromagnetic noise in ELF range such as electric railways, power lines and telephone lines, and therefore measurement is usually restricted to the frequency up to its third fundamental mode, 20 Hz. Recently, many MT measurements in this frequency range have been carried out for investigation of active faults (e.g. Handa and Sumitomo,1984) and volcanoes (e.g. Utada, et al.,1984) in Japan, and the method is called the ELF-MT method. Since the measurement of vertical component of magnetic field is difficult and time consuming for ELF range, the MT analysis is common by means of measurement of horizontal electric and magnetic fields.

The magnetic field data were measured by orthogonally oriented induction coils with parmalloy cores whose effective cross sections are both about 3 x 10^{3} m^{2}. The frequency characteristic of sensitivity of the sensor is given in Fig.4.5. The output voltage from the sensor is amplified and filtered by a so-called ELF amplifier whose block diagram is shown in Fig.4.6. This instrument can achieve maximum gain of 100 dB in total: 35 dB first, 65 dB after filtered. Notch filters (f_o =50/60,100/120Hz) are used in order to reject the noises from commercial power lines. We use low pass filter of third order Butterworth type (f_c =32Hz) for eliminating the artificial noises at higher frequencies , whose levels in Japan are so high as to often exceed the signal levels of the Schumann resonance fields.

The electric field signals are detected by using graphite or brass electrodes grounded 30-50 m apart in N-S and E-W direction. Amplifiers and filters have the same characteristics as those of magnetic fields except the total gain is 90 dB in this case. A co-axial cable is used for electric field measurement. The shield is attached to the ground point of the electric circuit, which is very effective to eliminate the electrostatic noises in the record.

An analogue data recorder is used for recording the signals in cassette magnetic tape. At one site, measurements is carried for 5 to 10 minutes duration, which is sufficient for reliable estimation of the impedance tensor, unless the noise level is comparable or exceeds the signal level. The reliability of the impedance estimates will be discussed in the last section. Analogue records are digitized with sampling frequency of 200 Hz, or sampling interval of 5 msec, and each data set is stored in the 9 truck magnetic tape. The data set may contain noises and, at some portions, the signal level may be too low to detect spectral peaks of the Schumann resonance. In the next section, a simple and effective method will be shown for the estimation of the surface impedance at ELF range.

4.3 Processing of ELF magnetotelluric data

The Magnetotelluric impedance Z is defined by the linear equation (e.g. Hermance 1973):

$$E(f) = Z(f)\ H(f) \qquad (4\text{-}3\text{-}1)$$

where E(f) and H(f) are Fourier transforms at a frequency f of observed horizontal electric and magnetic field vectors, respectively, and Z(f) is 2x2 tensor called the impedance tensor.

Instead of measuring the magnetic field variations , however, their time derivative were measured in ELF MT method by using induction coils. Therefore impedances were calculated on the basis of following equation , which is obtained by rewriting Eq.(4-3-1), with the replace of the time derivative by $-i\omega$:

$$E(f) = -Z(f)H(f)/i\omega \qquad (4\text{-}3\text{-}2),$$

where dot denotes the time derivative. The impedance estimates can be obtained for observed time series in the least square sense by calculating four independent estimates E(f) and H(f), applying spectral analysis technique (e.g. Vozoff, 1972).

As has been mentioned in the previous section, data set from one observation site has time duration of 5 to 10 minutes with a sampling interval of 5 msec. First, observed time series are divided into 10 to 18 subsets, each of which has 5120 data points (25.6 sec in length). From each data subsets, band averaged power and cross spectra of electromagnetic fields are calculated by conventional F.F.T. scheme. Here, we take the degree of freedom for spectral smoothing as 40, resulting the frequency resolution to be 0.78 Hz. As investigated by many workers previously referred, the Q factors of the Schumann resonance fields take values between 3 and 6, so that the band width of the spectral peak is between 2.7 and 1.6 Hz for the fundamental mode of 8Hz. Even if the Q factor takes the lowest value, frequency resolution applied here is sufficiently high to estimate unbiased spectra of the Schumann resonance phenomena.

If the nature of observed magnetotelluric fields were considered to be of stationary and random process, tensor impedance estimates should be, within their standard errors of means, time invariant responses depending only on the resistivity distribution of the earth's interior. This is not true, as will be discussed in the next section. A stacking method is adopted to obtain final impedance estimates for each data set.

Eq.(4-3-1) is an equation of linear system with input H(f) and output E(f), whose transfer function is Z(f). The standard error of the impedance for this linear system can be written as (Bendat and Piersol,1976):

$$r_{ij}^2 = \frac{4}{(2N-4)} \cdot F(N,4,\alpha) \cdot \frac{(1-\mathrm{coh}^2(E_i))}{(1-\mathrm{coh}^2(xy))^{1/2}} \cdot \frac{P(E_i)}{P(H_j)} \qquad (4\text{-}3\text{-}3)$$

$$(i = x,y \ , \ j = x,y)$$

where $coh^2(E_i)$ and $coh^2(xy)$ are multiple coherency between i'th component of the electric field and the horizontal magnetic fields, and the coherency between orthogonal magnetic field components, respectively; N is the degree of freedom of spectral analysis; $F(N,4,\alpha)$ is α percent point of F-distribution; $P(E_i)$ and $P(H_j)$ are power spectra of i'th and j'th components of electric and magnetic field, respectively.

Final estimate is taken as an ensemble average of all the data subsets with the averaging weight as follows:

$$Z_{ij}(f) = 1/W \sum_k w_K Z_{ij}^{(K)}(f) \qquad (4\text{-}3\text{-}4),$$

where,

$$W = \sum_k w_K \qquad (4\text{-}3\text{-}5)$$

and we take,

$$w_K = 0 \qquad (4\text{-}3\text{-}6)$$

in case without peak at resonance frequency, otherwise,

$$w_K = 1/r^{(K)}{}_{ij}{}^2 \qquad (4\text{-}3\text{-}7)$$

where $r^{(K)}{}_{ij}$ is the standard error of the impedance estimate from k'th data subset given by Eq.(4-3-2). The definition of the weight function given in Eqs.(4-3-6) means that the impedance of a data subset, whose spectrum has no peaks at the Schumann resonance frequencies, should be excluded first from averaging. Usually we can detect steep spectral peaks at the resonance frequencies as shown in Fig.4.7. Non-existence of the peak implies that the data contains high level noise, or the thunder storm activity in the world was remarkably low at the recording instance. Both are thought to cause instability of the least squares method of impedance estimation.

This averaging effect on final impedance estimates is that the larger the standard error of estimated value is, the smaller the weight on resulting average becomes. Since the standard error is written as Eq.(4-3-3), estimates with large values of the coherency between electric and magnetic fields have large weights, while those with high coherencies between two horizontal magnetic fields have small weight.

4.4 Reliability of the impedance tensor estimates at ELF range

Since the duration of measurement is less than 10 minutes for the ELF-MT method, we cannot use the impedance in order to determine the earth's resistivity structure, if the source field nature of the schumann resonance varies with time, and therefore, the impedance estimate is time dependent. In this section, we examine the reliability and the stability of the impedance estimates based on observational results.

First, we examine the existence of local time dependence in the magnetotelluric response functions. The ELF data were used for the purpose, which were observed on Nov.17-18, 1981, at Yatsugatake geomagnetic observatory, Earthquake Research Institute.

The first measurement was performed at 11h30m, Nov.17,1981 with 10 minutes' duration. After that, measurements had been repeated once every one hour with a duration of 4 minutes and a half until 16h00m of the next day. The whole measurements were performed automatically controlled by timer system.

Fig.4.8 shows the normal run magnetogram with electric field record observed at the observatory during the two days of the ELF measurement. The solid triangle above the magnetogram denotes each period of ELF measurement. As is seen on the record, the noise level in the electric field is highly elevated at night, in fact, more than 60 dB higher than that in the daytime. This noise has, of course, no relations to geomagnetic activities, and, unfortunately enough, seems to exist within very wide frequency range including ELF band. Because of this noise contamination, we were obliged to analyze the data collected only in daytime (between 8 and 16 o'clock). Unused portions are denoted by open triangles in Fig.4.8. A typical record of the Schumann resonance fields is given in Fig.4.9, while Figs.4.10 shows the same record after band-pass filtered.

Fig.4.11 shows the power spectra calculated at 8, 14 and 20 Hz from 18 data subsets from the first measurement. It is obvious that there is a significant variation in the electromagnetic field intensity for the Schumann resonance frequencies. The variation in the source field intensity may cause an error in the estimate of the impedance. Usually, the coherency between electric and magnetic fields is used for an indicator to decide how reliably the impedance is obtained (Vozoff ,1972). In spite of each data subsets having coherency of almost same value (between .85 and .92), except the noise contain-ing 10'th subset, and therefore all the estimates can be acceptable in usual means (e.g. Vozoff, 1972), the impedance varies from one to the other subset as shown in Fig.4.12.

This implies that the ELF data can not be regarded as perfectly stationary random time series. Therefore, the stacking method put forward in the previous section is considered to be effective. Fig.4.13 presents efficiency of the stacking method. Here, open circle denotes the impedance estimate from each data subset, with each radius being proportional to the standard error. It is clearly seen that the final estimates (hatched circles) situate in the middle of reliable ensembles (small circles) and far from those with large errors (large circles). By using this method, a standard error of less than 10 % is usually attained if noise level is not extremely high.

From all data sets except those at night, tensor impedances were calculated. Figs. 4.14 and 4.15 show the behaviors of the amplitudes and the phase deferences of off-diagonal elements of the complex impedance against the local time for three fundamental modes of the Schumann resonance. Error bar is taken to be one standard error of mean; i.e. 67 % confidence interval.

Amplitudes are generally stable and few of them seem to vary beyond the confidence intervals. Seeing in detail of the variations, a data point with a large standard error tends to move downward from the mean value. For example, values of Zxy at 13h00m of Nov.18 have large error bars and go downward for all the three frequencies, while those of Zyx are well estimated and stable. This can be regarded as the bias error (Goubau et al. 1978; Gamble et al., 1979) due to noise in Y-component of magnetic field record.

Next, we check the local time dependence of other impedance related parameters; i.e. direction of the principal axis, minimum to maximum impedance ratio and skew. Tensor impedances were rotated into the principal axis (Swift, 1967). Again, direction of the principal axis which satisfies:

$$\left| Z_{xy} \right|^2 + \left| Z_{yx} \right|^2 = \text{max.} \qquad (4\text{-}4\text{-}1)$$

and ratio of maximum to minimum impedance are plotted against the local time in Figs. 4.16 and 4.17, respectively. The skewness parameter

$$\text{Skew} = [Z_{xx}+Z_{yy}]/[Z_{xy}-Z_{yx}] \qquad (4\text{-}4\text{-}2)$$

is a measure relating to the 2 or 3 dimensionality of subsurface structure. Fig.4.18, which is the same plot of skew as the previous ones, shows that the skew values vary crossing the dashed line which corresponds to the value of 0.2. The skew value of less than 0.2 usually implies one or two dimensionality of the structure. The behavior of the skew shown in Fig.4.18 may seem queer, because it is unlikely that the 2 dimensional structure changes to 3 dimensional one in such a short time. This is possibly due to the fact that the skew is a noise dependent estimate, but depends especially on noise contained in the diagonal elements of the impedance tensor. In other word, if there is common mode noise in the same components of electric and magnetic fields, then the estimates of diagonal elements are biased above the noise free level, resulting in the increase of the skew value. The direction of the principal axis of impedance tensor has a similar noise dependence. When common mode noise are high and calculated diagonal elements are large, the principal direction cannot be well determined. In this case, rotated maximum and minimum impedances are no longer reliable.

As a brief conclusion, following three results should be remarked here:

1) The amplitudes of off-diagonal elements of the impedance tensor can be estimated with sufficient reliabilities, with relative error of less than 10%. Off-diagonal elements are also satisfactory stable against the local time.

2) The error of the phase estimates of the off-diagonal elements is about 5 degrees. The phase is also a stable estimate against the local time.

3) The diagonal elements can be estimated less reliably and stably than the off-diagonal elements. This is possibly because the noise effects on the diagonal elements are much enhanced compared with those on the off-diagonal elements. The impedance related parameters, skew, direction of the principal axis and the maximum to minimum impedance ratio are also noise dependent. Therefore, skew of lager than .2 dose not always mean that the structure is three dimensional unless noise free condition is proved.

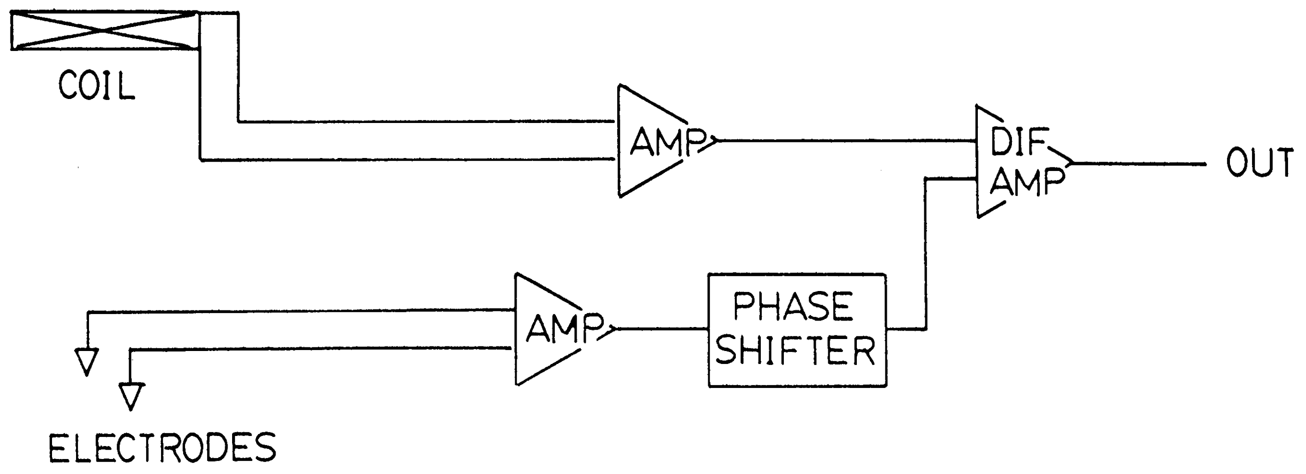

Fig.4.1 Block diagram of VLF MT measurement.

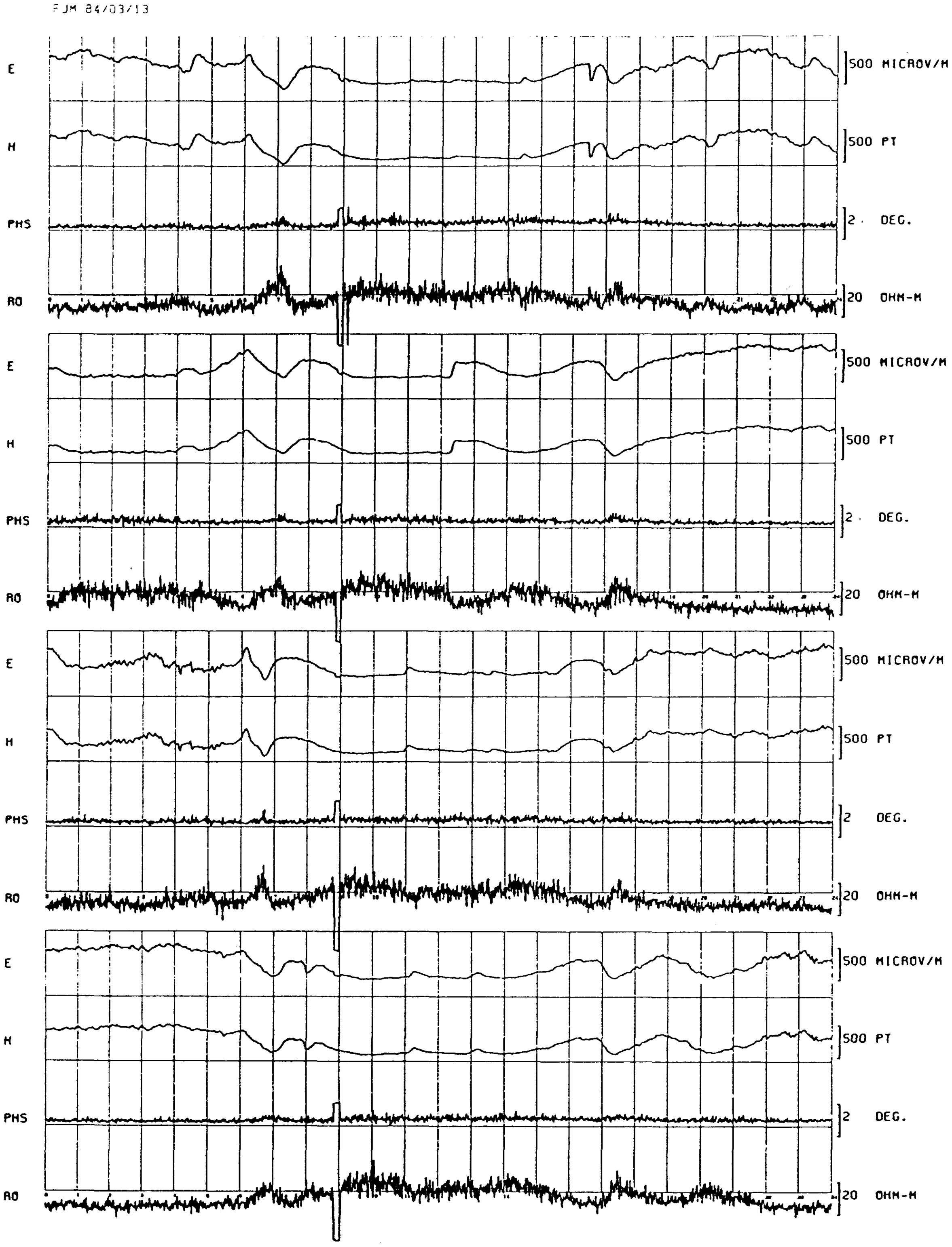

Fig.4.2 Daily variation of VLF signals and the magnetotelluric responses during Mar.13-16, 1983. Electric field intensity, magnetic field intensity, apparent resistivity and phase are illustrated. Scale is presented by bar on the right-hand side of each diagram.

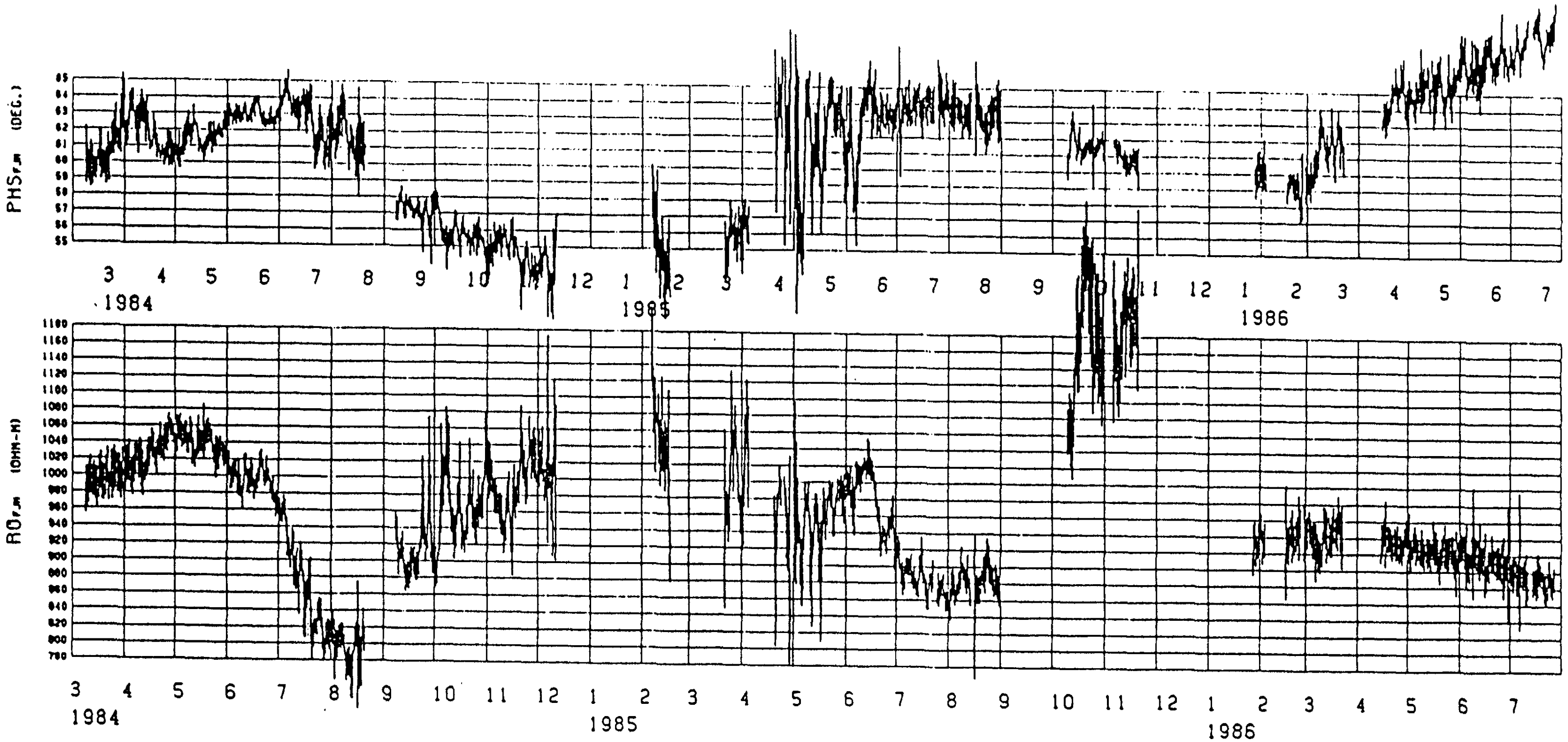

Fig.4.3 A result of continuous measurement of VLF MT at Fujinomiya(FJM) in Shizuoka Prefecture during Mar.,1984 and Jul.,1986. Note that the seasonal variation in the apparent resistivity amounts 30 % of its mean value in 1984 (below). Similar variation is detectable in the phase data (above).

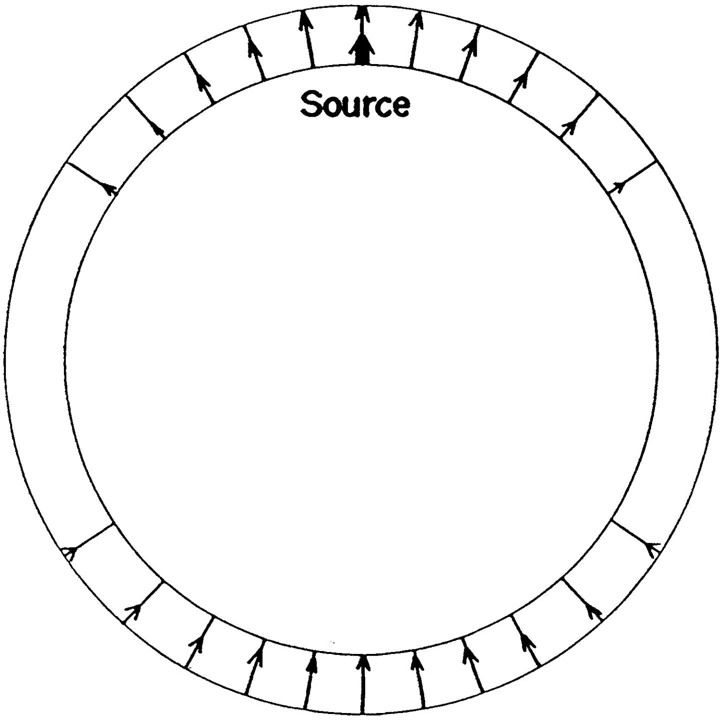

Fig.4.4 A sketch showing the propagation of the Schumann resonance field from the lightening flash (large arrow) in the cavity bounded by the earth and the ionosphere.

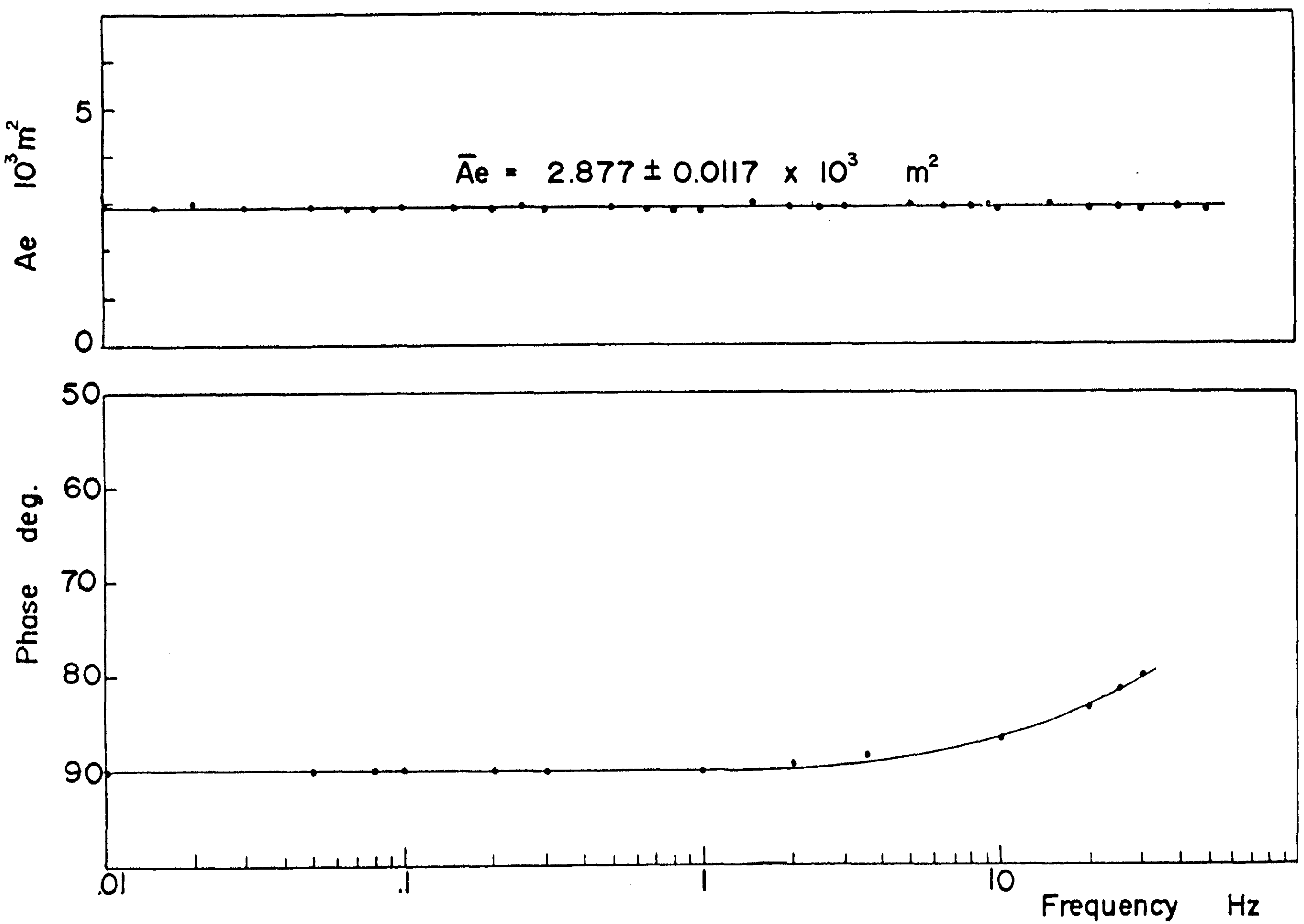

Fig.4.5 Frequency characteristics of the sensitivity (above) and the phase (below) of the induction coil used as the sensor of ELF MT measurement.

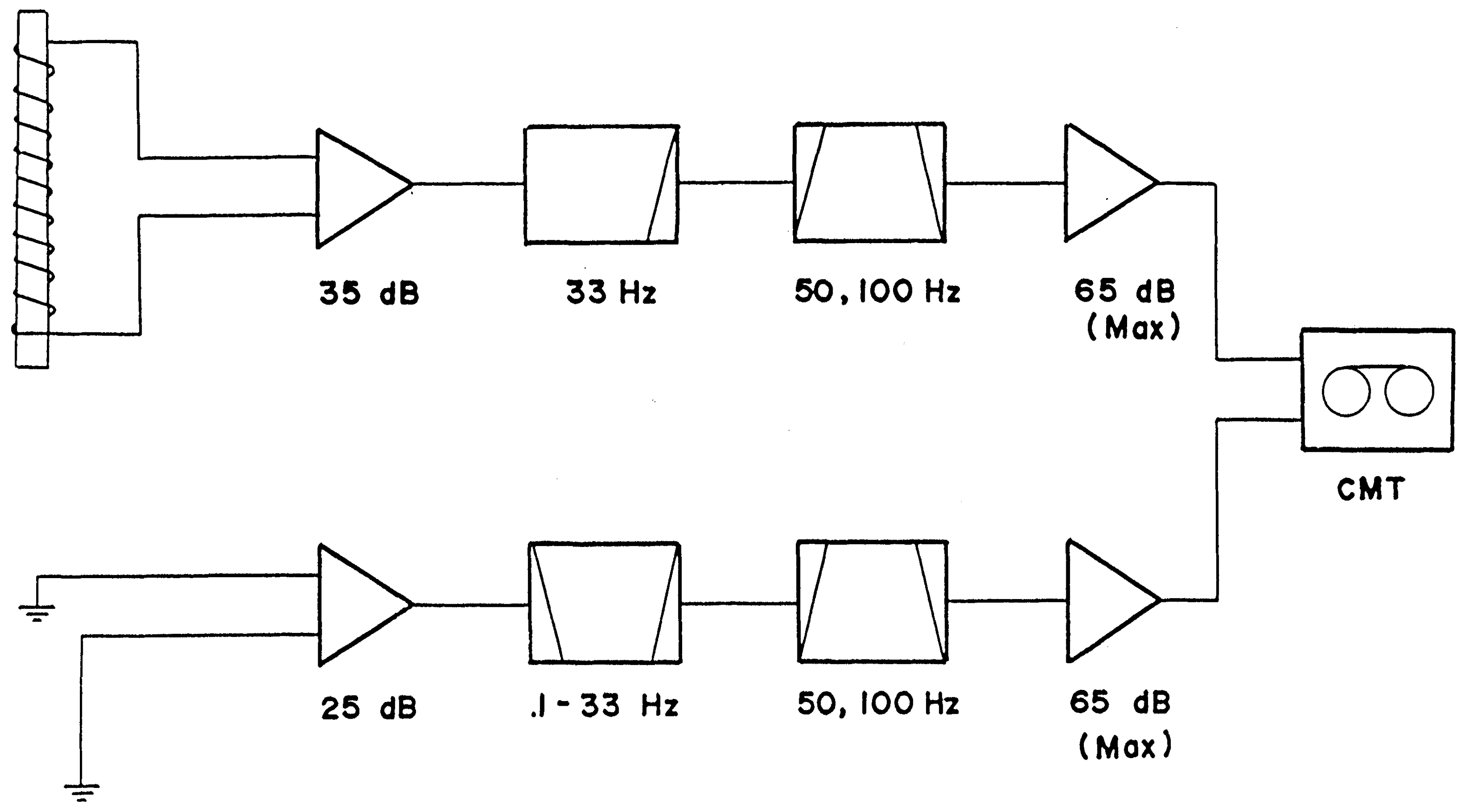

Fig.4.6 Block diagram of the measurement system of ELF MT.

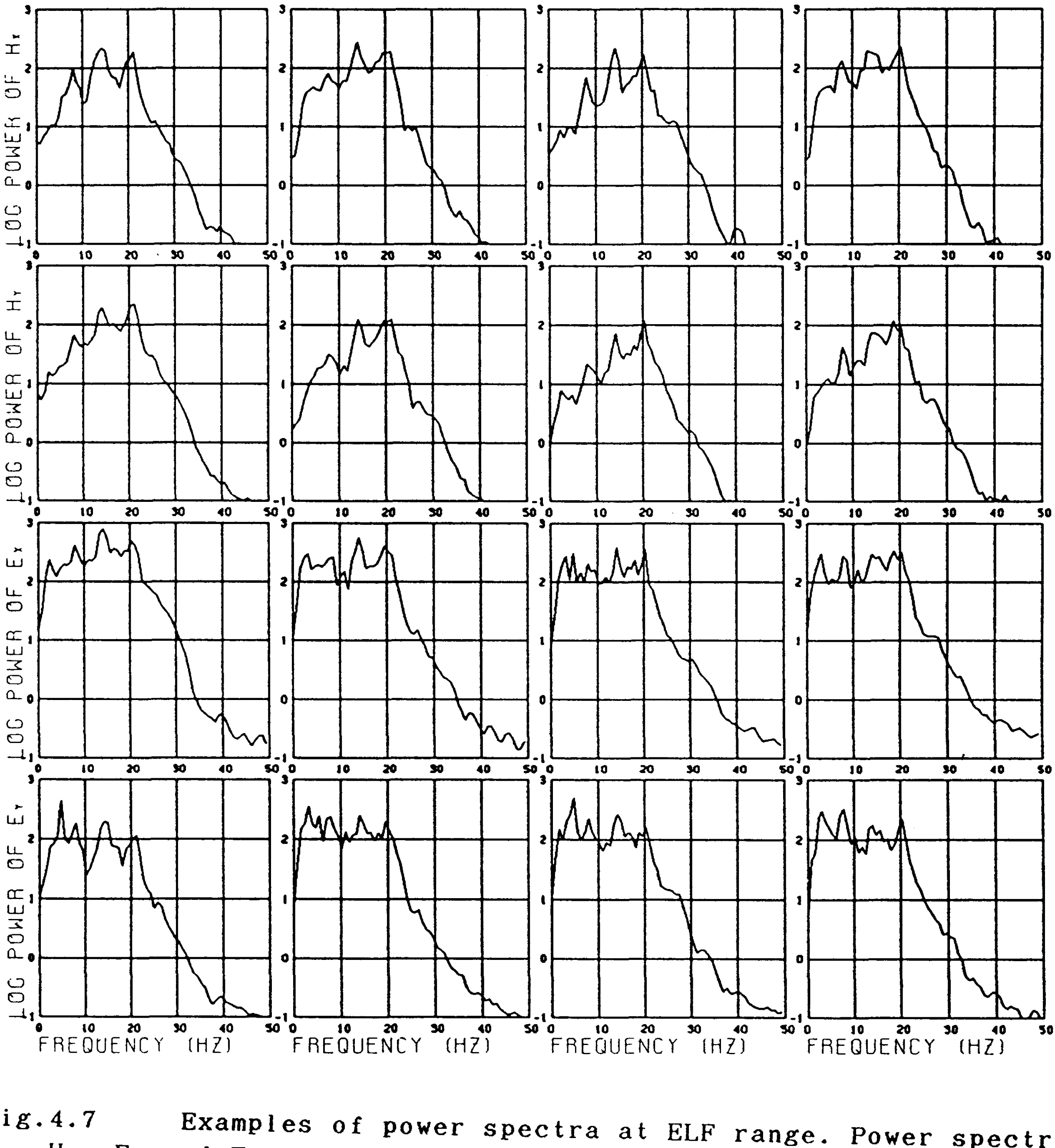

Fig.4.7 Examples of power spectra at ELF range. Power spectra of H_x, H_y, E_x and E_y calculated from 4 data subsets are plotted against frequency.

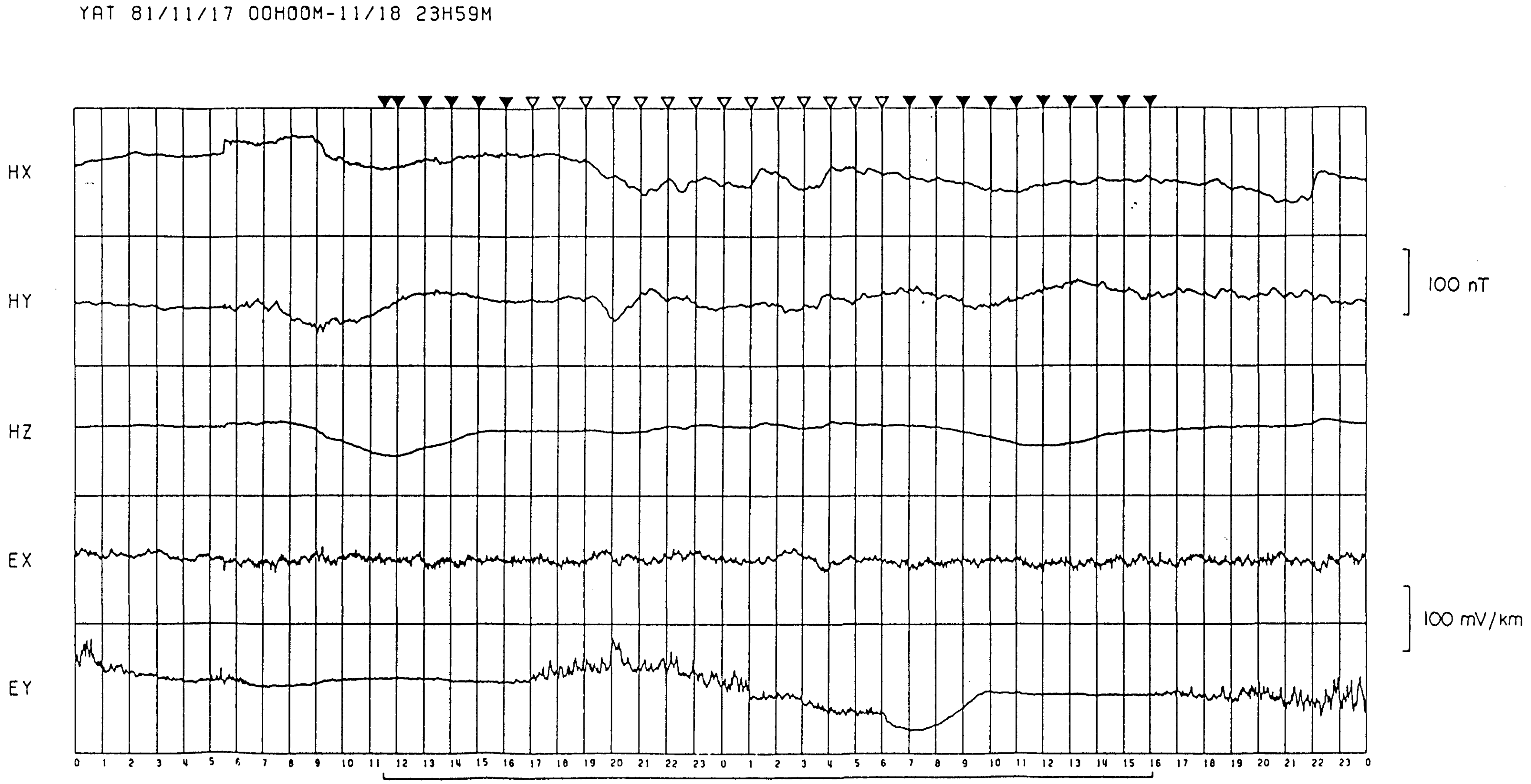

Fig.4.8 Normal run magnetogram at Yatsugatake Geomagnetic Observatory during the repeated measurements of ELF MT. Variations of electric field components are also given. Each ELF MT measurement is denoted by closed triangle above the diagram. Open triangles indicate the intervals of noise contamination in the electric field data.

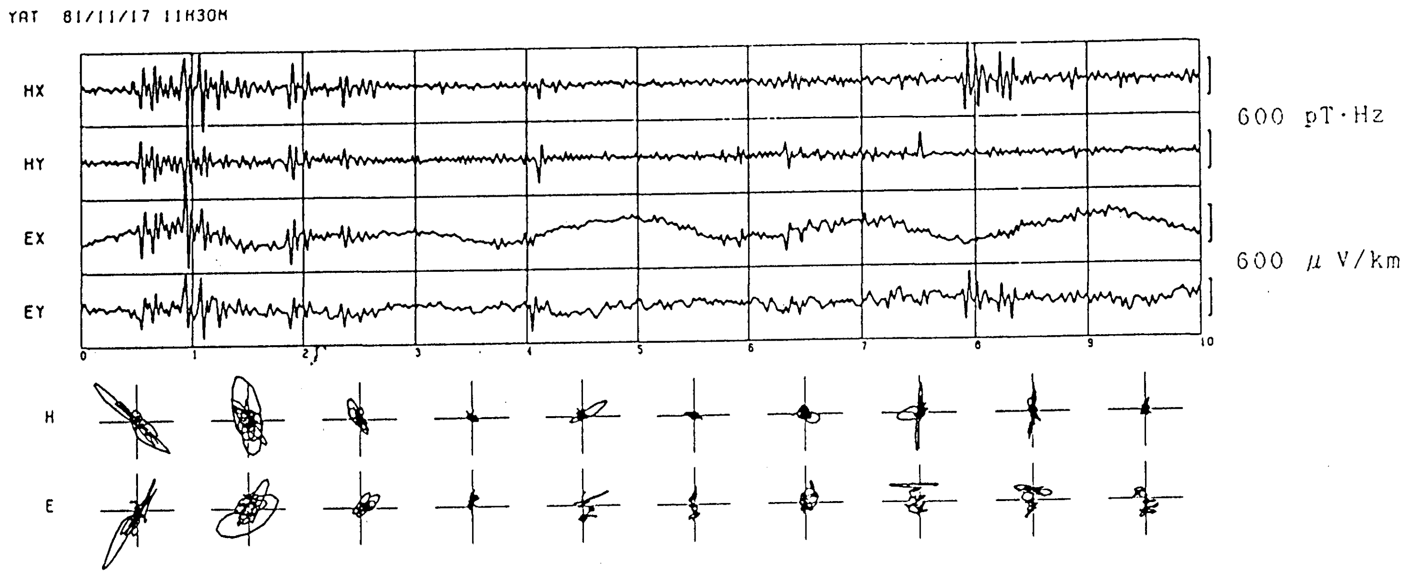

Fig.4.9 The Schumann resonance fields observed at Yatsugatake Geomagnetic Observatory. Wave orbit at each one second interval is illustrated below.

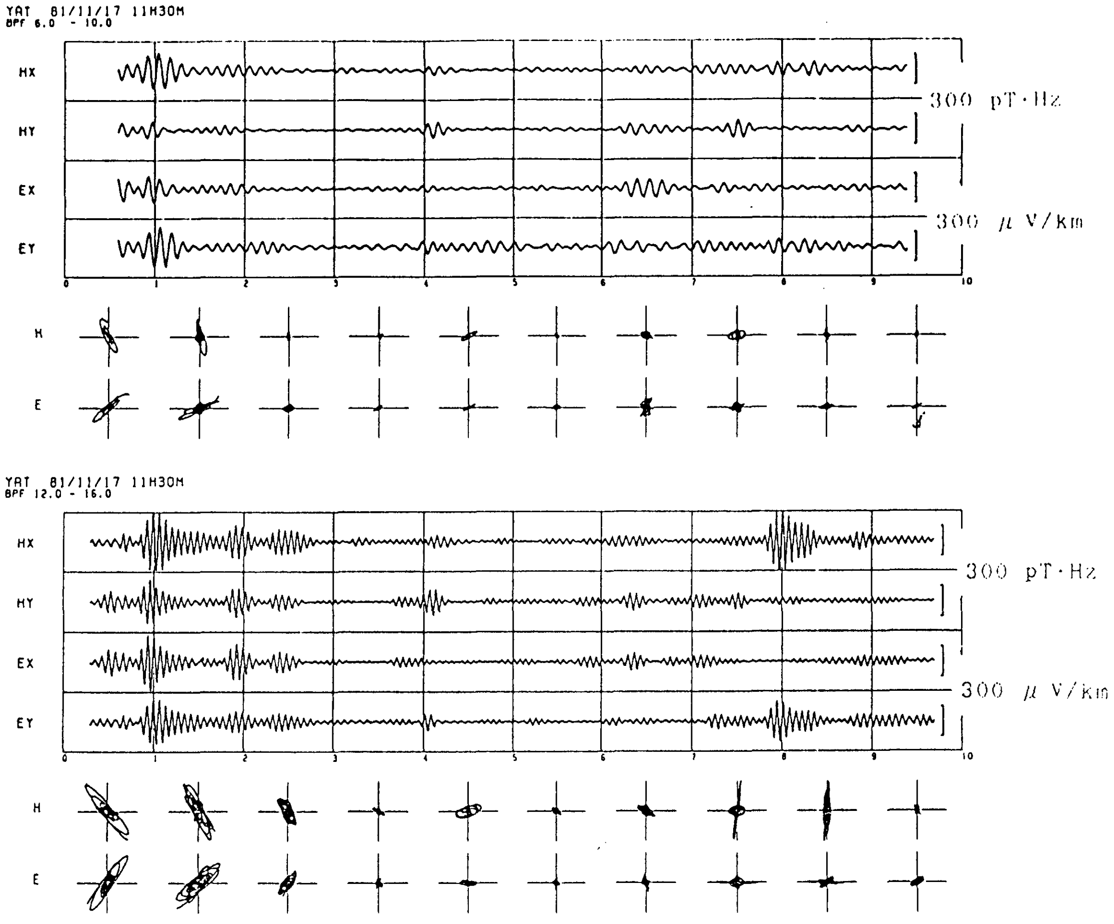

Fig.4.10 The same record as Fig.4.9 after band-pass filtered with center frequency at 8 Hz(above) and 14Hz(below).

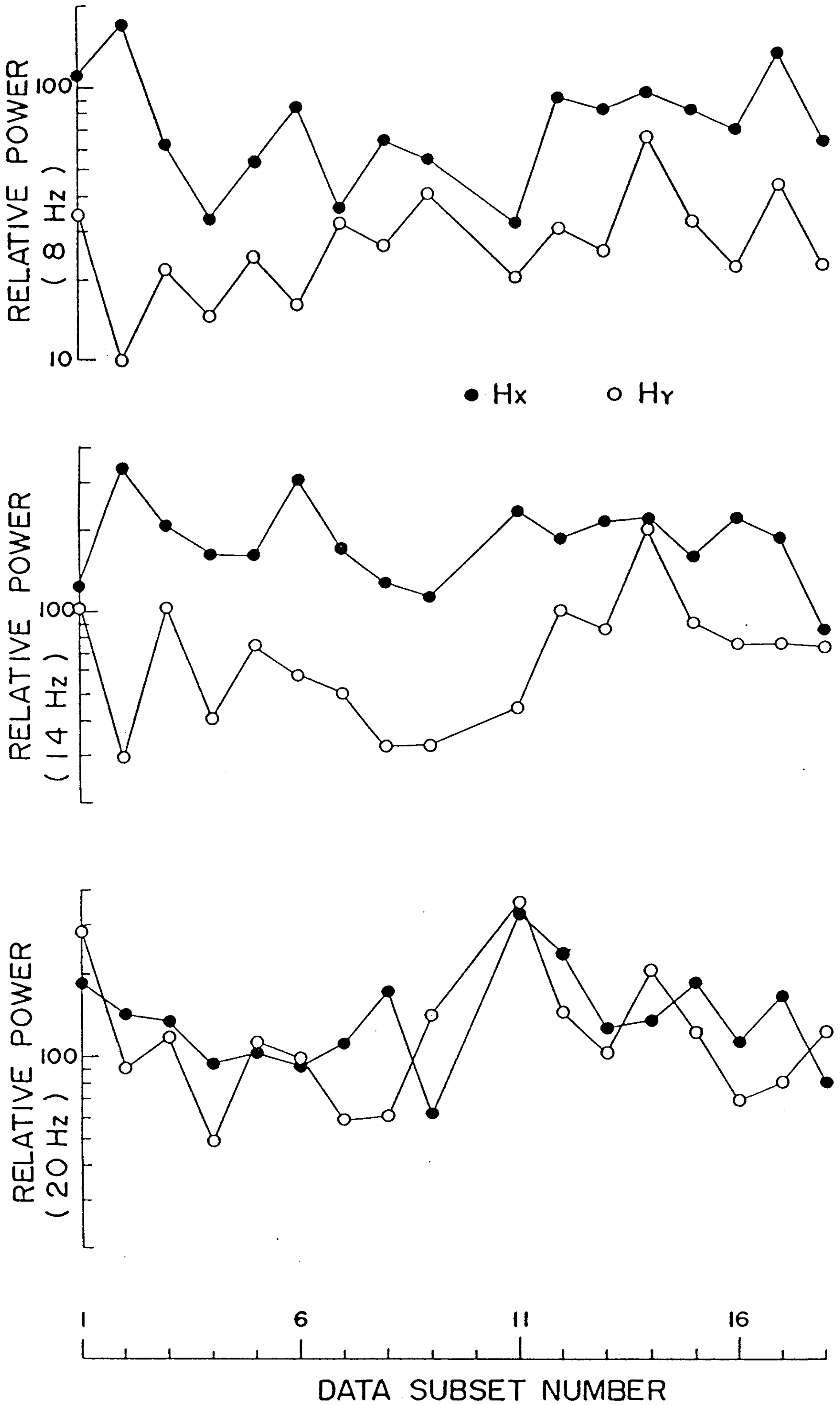

Fig.4.11 Power spectra of the northward (closed circles) and eastward components of ELF magnetic field variation for 18 data subsets.

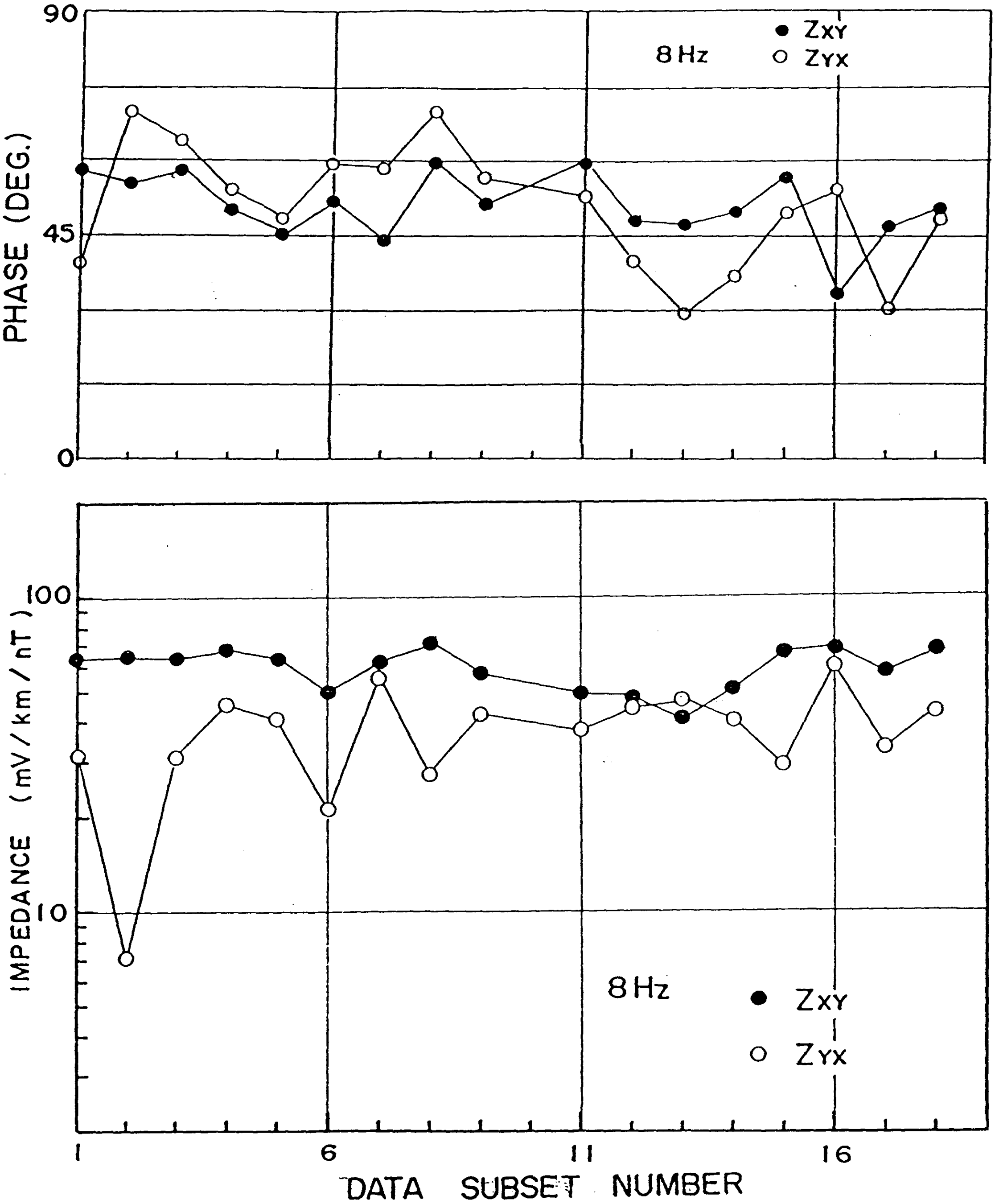

Fig.4.12 Variations in amplitude (below) and phase (above) of the magnetotelluric impedance Z_{xy} (closed circles) and Zyx (open circles) for 18 data subsets.

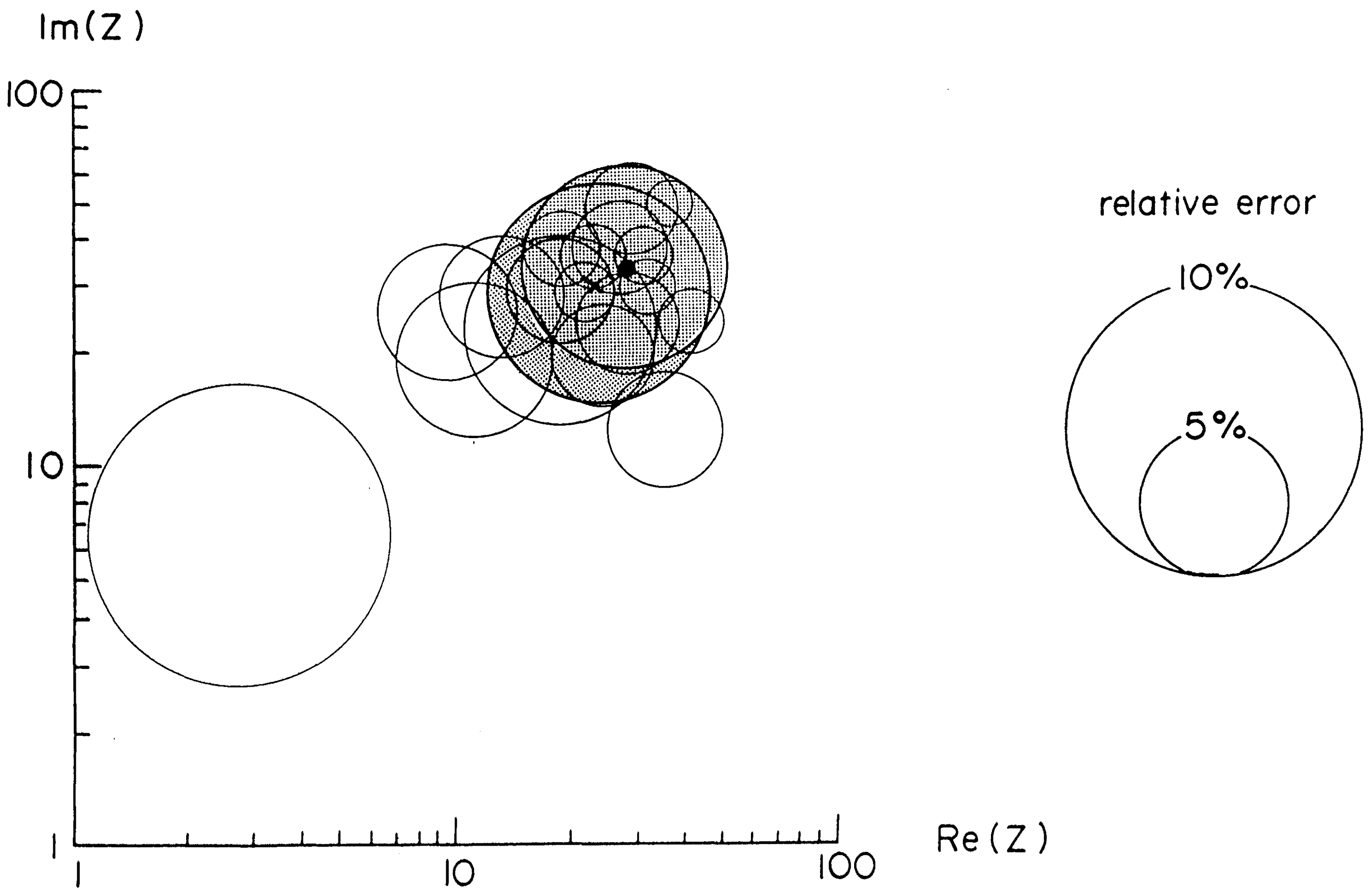

Fig.4.13 Visualized stacking process plotted in the complex plane. Each open circle denotes the range of error in impedance estimate that is the center of the circle, for each data subset. Cross and shaded circle denote the final impedance estimate and its confidence range, respectively.

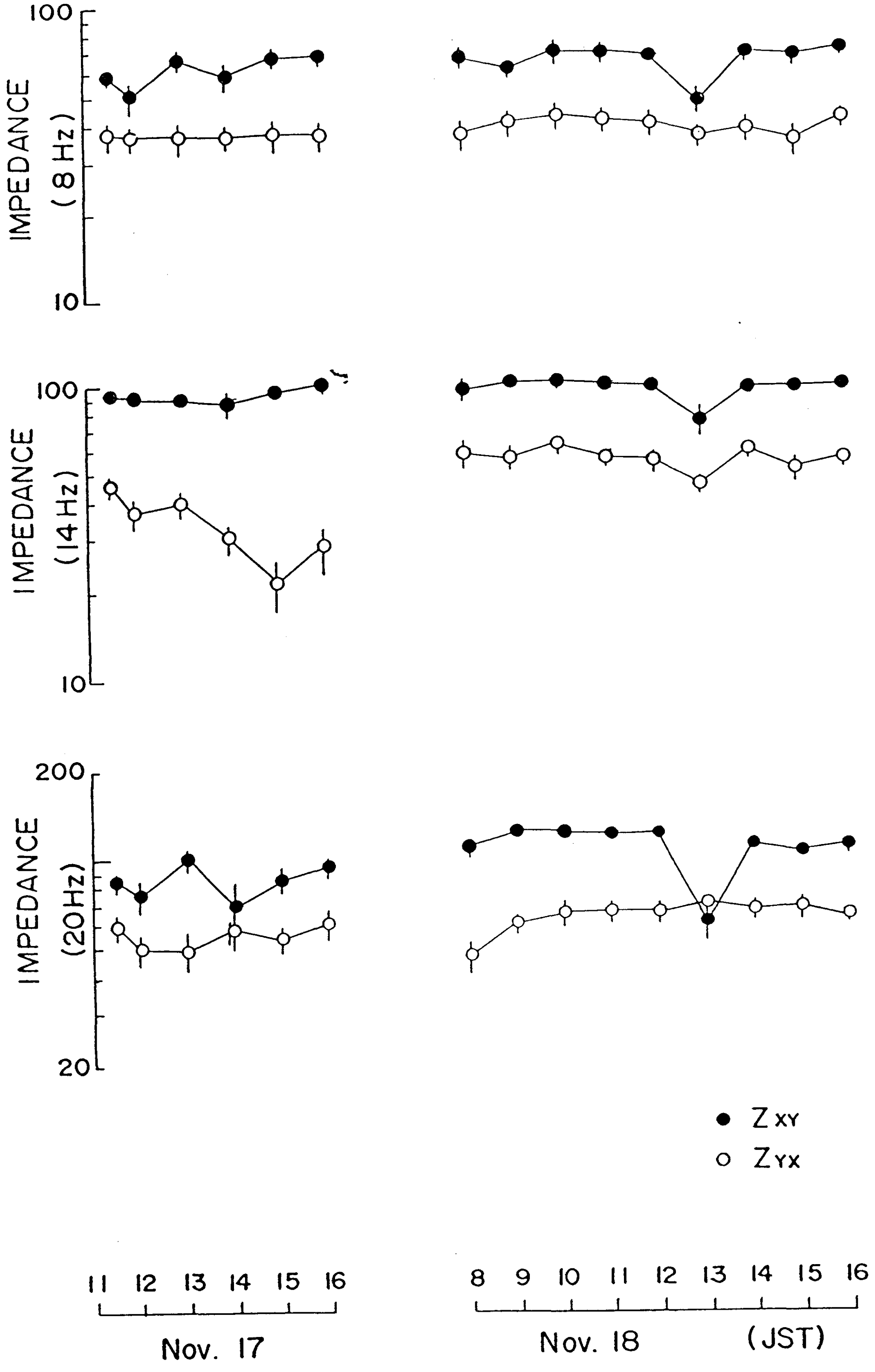

Fig.4.14 Local time dependence of the amplitudes of the off-diagonal elements of the impedance tensor for three fundamental modes of the Schumann resonance, 8, 14 and 20 Hz.

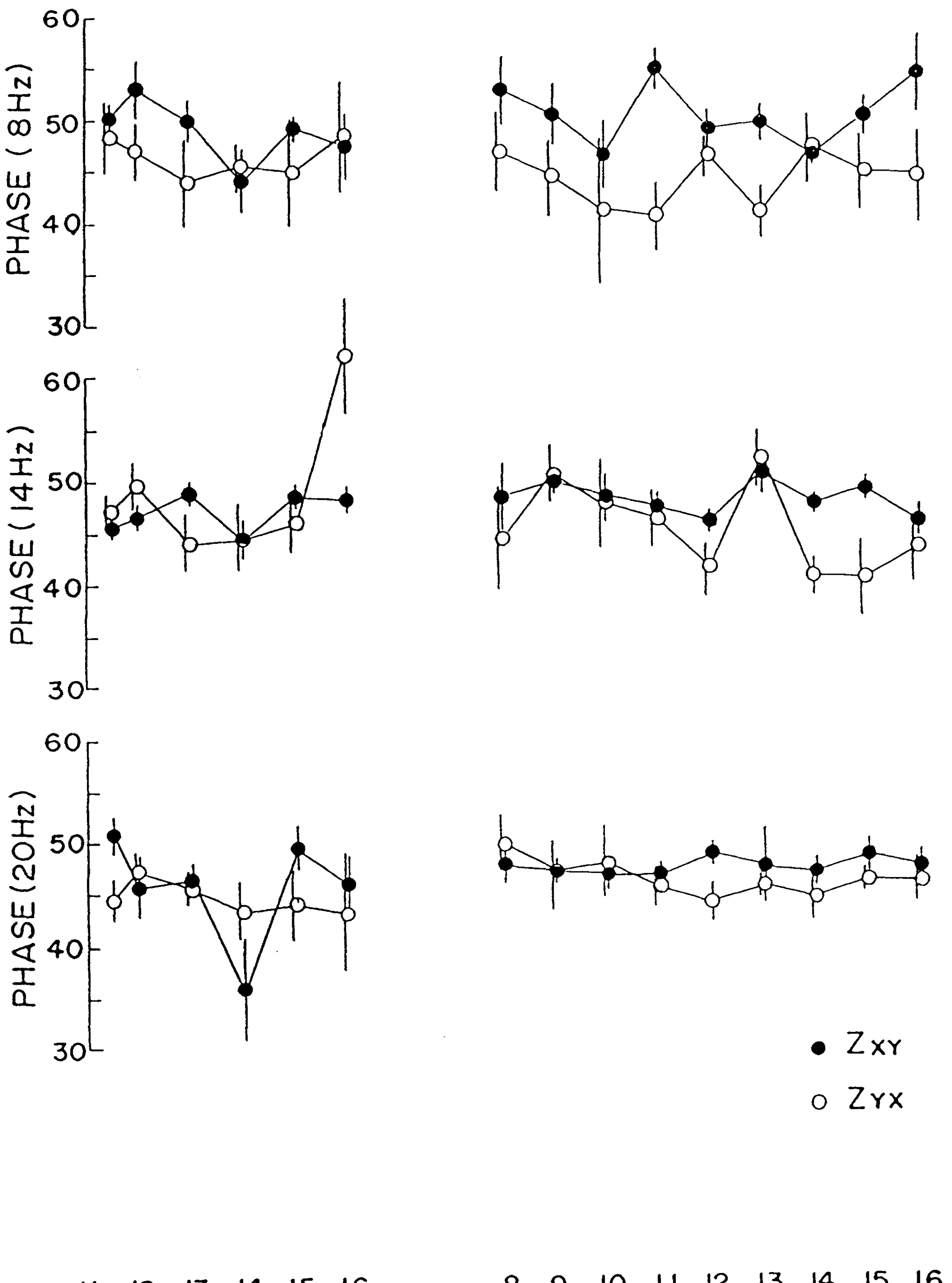

Fig.4.15 Local time dependence of the phases of the off-diagonal elements of the impedance tensor for three fundamental modes of the Schumann resonance.

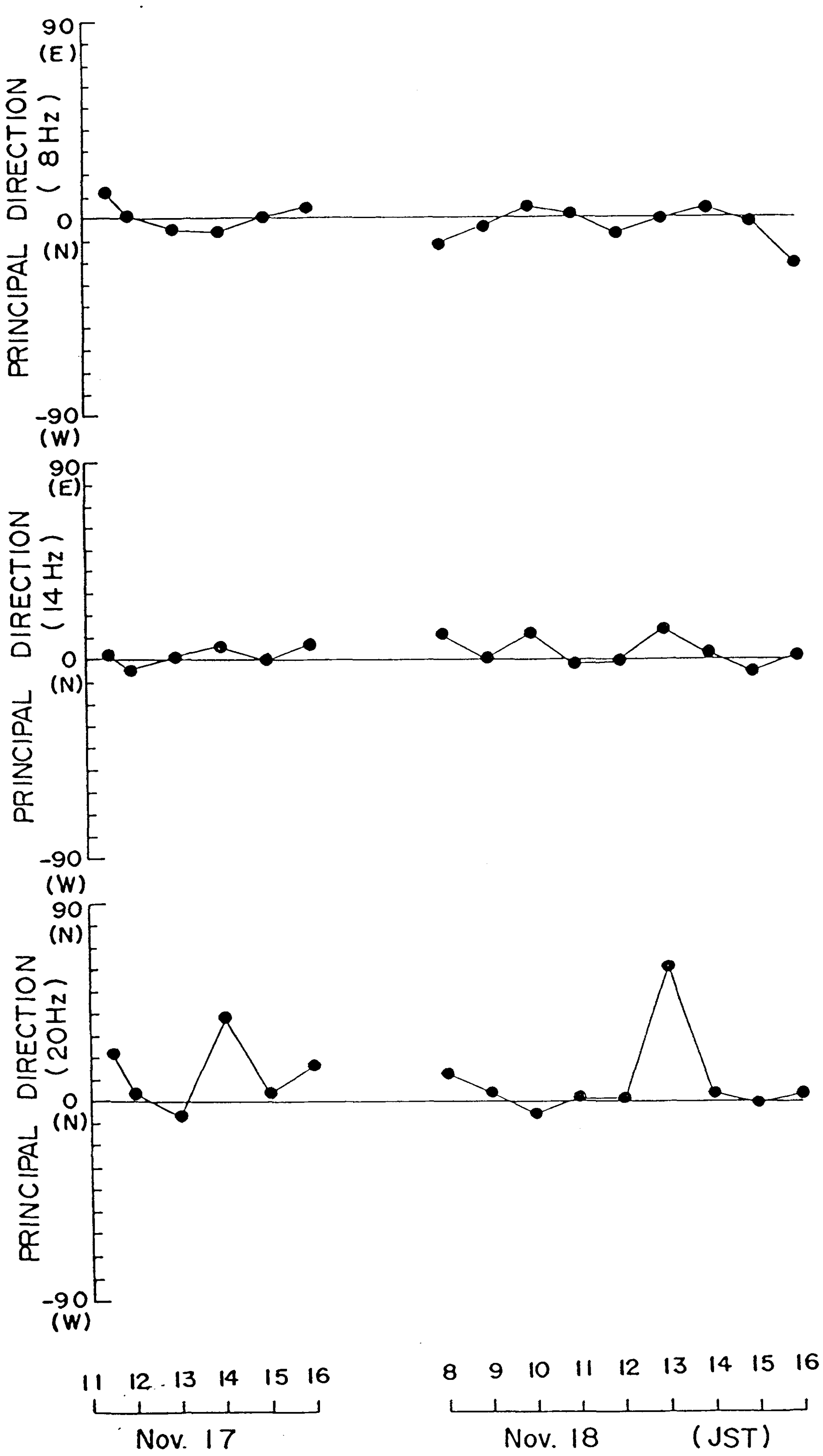

Fig.4.16 Local time dependence of the direction of the principal axis of the impedance tensor for three fundamental modes of the Schumann resonance.

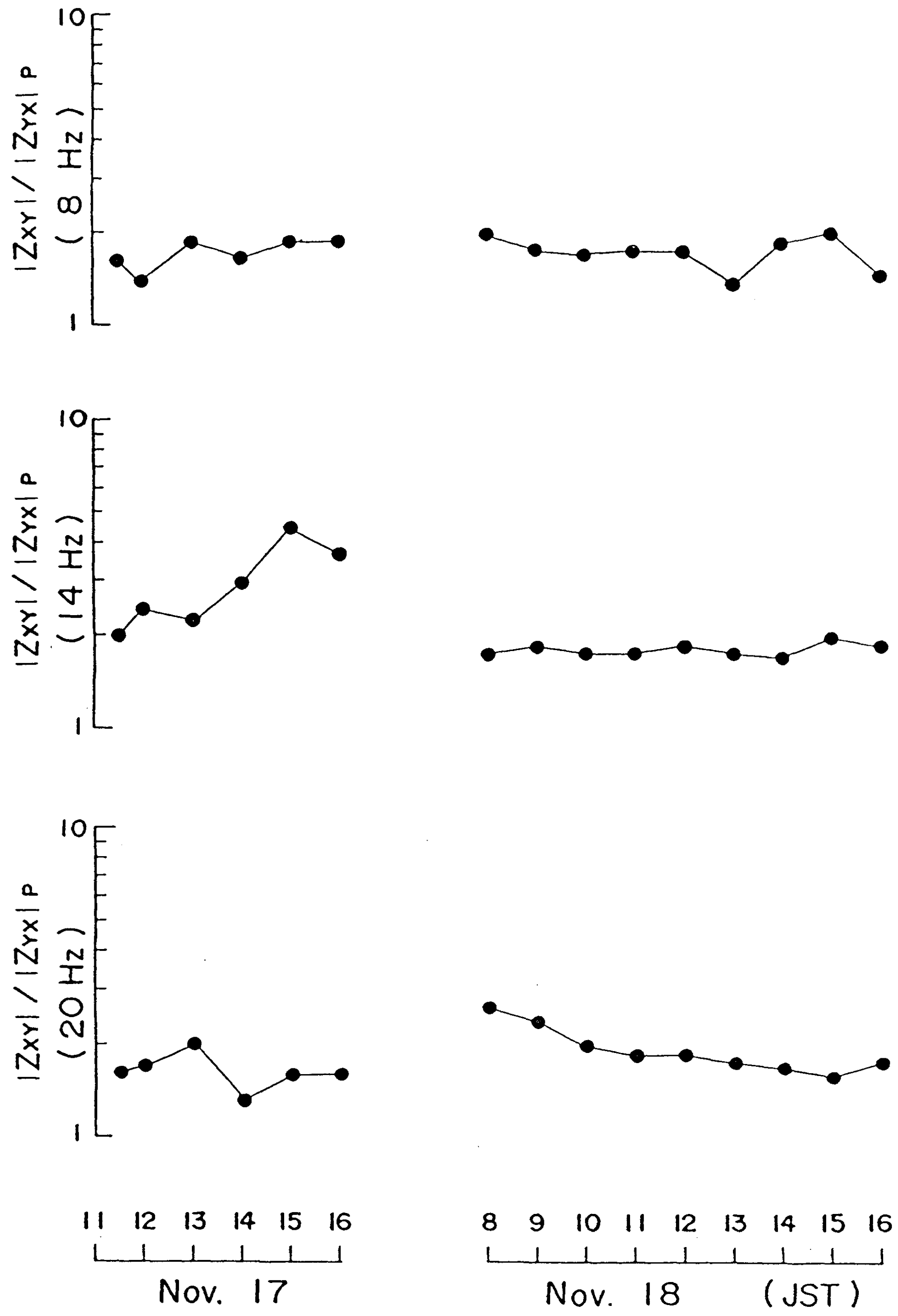

Fig.4.17 Local time dependence of maximum to minimum impedance ratio for three fundamental modes of the Schumann resonance.

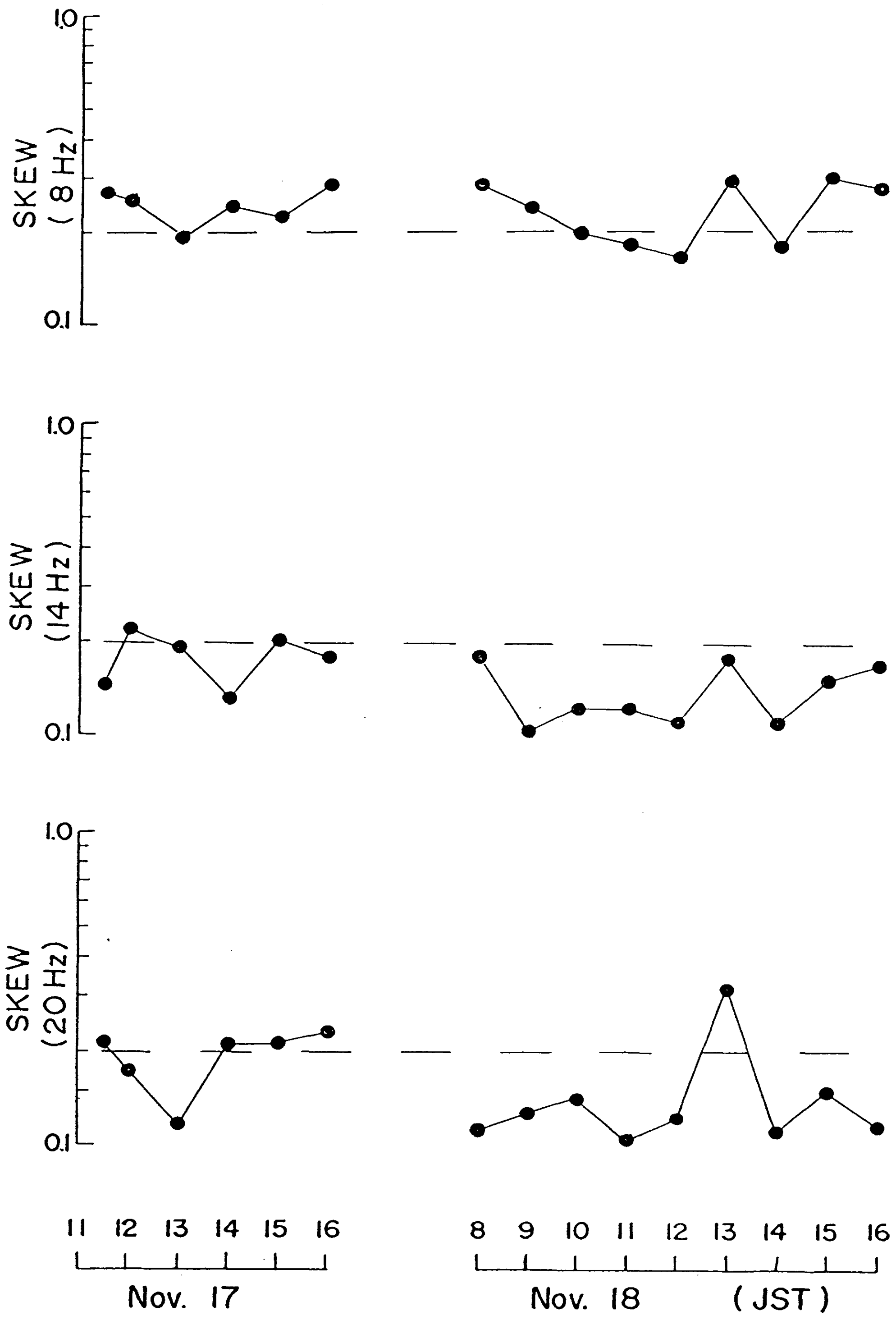

Fig.4.18 Local time dependence of Skew parameter for three fundamental modes of the Schumann resonance.

5. Measurement and Data Processing of the Electromagnetic Field Variations at ULF Range on Land

The ultra low frequency (ULF) range covers the lowest frequency band, lower than 1 Hz, of the electromagnetic waves. For the purpose of the electrical investigation of the earth's crust and the upper mantle, the frequency range between 10^{-1} and 10^{-4} Hz (10 second and several hours of period) is usually used. In the present study, the direct inversion method is applied by use of the electromagnetic responses at the lower band of ULF. Data at the higher frequency bands such as micropulsation band, ELF and VLF signals are used as supplementary information; i.e. giving the one-dimensional model or surface conductivity distribution.

The corresponding field penetration depth (skin depth) becomes as deep as several hundreds kilometers for the lower ULF in homogeneous earth with the conductivity 10^{-4} S/m as shown in Fig.5.1. By making use of the electromagnetic responses at this frequency band, we attempt to reveal the conductivity structure in the lower crust and the upper mantle.

Since the amplitude of the geomagnetic field variation at ULF range varies by several orders with frequency, observation was made by two different kinds of instruments. One covers the period range longer than several minutes, and the flux-gate magnetometer is used for the magnetic field measurement. The other apparatus covers shorter period band between several seconds and a few minutes, by use of induction coil as a magnetic field sensor. In this chapter, techniques of measurements at these period ranges will be given, as well as the method of data processing.

5.1 Measurement of electromagnetic field variations at ULF range

The electromagnetic fluctuations at ULF range are of magnetospheric or ionospheric origin. Typical values of magnetic field intensity are given in Fig.5.2 for the frequency ranges of most typical events. The sudden commencement of the geomagnetic storm (ssc) activates electromagnetic waves in a fairly wide range of frequency. One of the longest period variation has typical period of a few to several hundred minutes, accompanying the main phase of the geomagnetic storm. Geomagnetic bays observed at the substorm time have also durations of 30-60 minutes. At periods shorter than several minutes, geomagnetic micropulsations are widely observed not only for the investigation of the earth's interior but also for the ionospheric and magnetospheric studies. Three types of pulsations are given in Fig.5.2, i.e. Pc-5, Pc-3 and Pc-1. These are classified as continuous pulsations which are characterized by sinusoidal wave forms. Although Pc-1 covers the highest portion of the ULF range, it is quite difficult to measure particularly in Japan. This is because of the existence of 1 Hz stepwise noise through ground points of commercial telephone lines. Pc-3, whose period ranges between 20 and 40 seconds, is frequently observable at middle latitude like Japan. There is another type of micro pulsations called Pi's (pulsations irregular). Pi-2 is often observed accompanying the geomagnetic bays which appears at midnight to dawn. At the geomagnetic storm time, pulsations (Psc) appear with relatively large amplitude, not only in the prescribed period range, but also at each frequency corresponding to that of Pc's.

The storm time fluctuations has amplitude of several tens of nT in horizontal magnetic field variation. Magnetic field intensity of Pc-5 is 1-5 nT at middle latitudes. The amplitude of Pc-3 varies between 0.1 and 1 nT depending on the geomagnetic activity. Fig.5.3 presents an example of magnetogram at the geomagnetic storm time observed at Yatsugatake Geomagnetic Observatory. An example of Pc-3 micro pulsation is also given in Fig.5.4, which was observed at a temporal observation site Narugo(NRG), Miyagi Prefecture, Northeast Japan.

Since the amplitude of geomagnetic variation varies by several orders of magnitude in the ULF range, the whole range (i.e. 10^{-1}-10^{-4} Hz) is divided into two bands in usual. Measurement is made by use of a different instrument for each band. The lower band instrument covers the period range between several hours and a few minutes. The flux-gate magnetometer is used to measure the magnetic field variation for the lower band which has a linear sensitivity to the applied magnetic field intensity. The noise level of the flux-gate magnetometer lies at about 0.1 nT, as shown in Fig.5.2, which provides a sufficiently high signal to noise ratio throughout this frequency band. However, the signal level, at frequencies higher than 10^{-2} Hz, becomes comparable or even lower than that of the noise level of the flux-gate magnetometer. Therefore, we have to use other instrument, the induction magnetometer, to measure the magnetic field variations of higher frequencies.

The induction magnetometer consists of the sensor coil with a highly permeable metal core and the amplifier. This type of magnetometer is also used for ELF measurement as described in the previous chapter. The output voltage induced between both end of the sensor coil is suitably amplified, filtered and then recorded. The induced voltage, V_e, equals to the negative of the time change rate of the total magnetic flux crossing the coil, Φ_T: i.e. the well-known Faraday's theorem tells,

$$V_e = - \partial \Phi_T / \partial t \qquad (5\text{-}1\text{-}1).$$

Letting the effective area of the sensor coils as A_e, and the applied magnetic flux density parallel to the coil's axis as B, Eq.(5-1-1) is rewritten as:

$$V_e = - A_e \cdot \partial B / \partial t \qquad (5\text{-}1\text{-}2)$$

If we assume a sinusoidal variation with time term $\exp[-i\omega t]$, Eq.(5-1-2) gives the relation between the applied magnetic field and the output voltage at frequency f,

$$V_e(f) = i\omega \cdot A_e \cdot B(f) \qquad (5\text{-}1\text{-}3)$$

where $\omega = 2\pi f$. Thus, the induction magnetometer has a sensitivity proportional to the time change of the magnetic field. The sensor coil used in this study has the effective cross section of $2\text{x}10^4$ m^2 up to about 1 Hz (see Fig.5.5). The noise level of the amplifier of the induction magnetometer is as low as 0.1 μV, reduced to the input voltage. With Eq.(5-1-3), we have the frequency dependent noise level of the induction magnetometer, $B_n(f)$, as:

$$B_n(f) = 0.81 / f \text{ x } 10^{-3} \text{ (nT)} \qquad (5\text{-}1\text{-}4)$$

The noise level given by this equation is sufficiently lower than the signal level of the micropulsations throughout the range as shown in Fig.5.2.

The electric field variation is measured by use of a pair of electrodes and amplifier. Here, different sets of instrumentation are used for the corresponding frequency bands. Moreover, the measurement of the electric field variations requires more considerations because their amplitudes vary by several orders from place to place depending on the subsurface conductivity distribution. The relation of apparent resistivity and impedance, Eq.(3-2-11), gives the rough estimate of the electric field intensity, E, against the magnetic field variation, H, at a proper observation site

$$E = [\omega \mu \rho_a]^{1/2} \cdot H \qquad (5\text{-}1\text{-}5)$$

When the magnetic field variation of 1 nT is applied at the period of 30 seconds (i.e. Pc-3 pulsation), the expected intensity of electric field will become about 0.4 μV/m (mV/km) with an apparent resistivity of 10 $\Omega \cdot$m. If the observation site situates in the rather resistive area with an apparent resistivity of 1000 $\Omega \cdot$m, 4 μV/m of the electric field will be induced. For the variation of 30 minutes period, on the other hand, corresponding electric field variations have the intensity of about 1.6 μV/m and 16 μV/m, for the specific values of the apparent resistivity 10 and 1000 $\Omega \cdot$m, respectively. Thus, the gain of the amplifier and spacing of the electrodes should be selected properly for corresponding frequency band, by taking into account the subsurface conductivity distribution. Result of VLF and ELF Magnetotelluric measurements often works as a reference of the rough estimate of the apparent resistivity.

Lead bar or lead-lead chloride (Pb-$PbCl_2$) electrodes are used for the electric field measurements at ULF range. The latter is one of the chemical equilibrium electrodes, which provides a electrochemical equilibrium at the interface between the surface of the electrode and soil, and therefore a long time stability can be expected. Though the former is not a chemically balanced electrodes, it is often used for its easiness to handle and relatively high stability.

For the measurement of each component of electric field, a pair of electrodes are buried about 1 m deep with a spacing of about 100 m. Each electrode is connected to the amplifier by shielded co-axial cable. An Instrumentation amplifier of parallel input is used as an receiving amplifier (Fig.5.6). The input voltage between the electrode pair is suitably filtered and amplified after D.C. component of the voltage is compensated if necessary. The shield of the co-axial cable have to be connected to the ground of the circuit. This is found to be effective to eliminate the induced voltage between the both ends of the cable (electrostatic shield).

The filter is indispensable for an electric field amplifier at ULF range, because the level of the electric field of ELF range usually exceeds that of ULF range. Moreover, in order to reject the artificial noises at 1 Hz from telephone lines and 50 or 60 Hz from power lines, a suitable set of filter is required for a precise measurement. The filter system for the higher band of ULF (pulsations) consists of three parts:i.e. a band pass filter between 300 and 10 seconds and notch filters at 1 and 50 or 60 Hz. The lower band instrument has also three filters such as a low pass filter with a cut-off period of 3 minutes and two notch filters. These filter systems are necessary particularly when the digital recordings are made, in order to eliminate the so-called aliasing effect.

Electric and magnetic field data, 5 components in all, is digitally recorded in a cassette magnetic tape or solid state memories with 12 bits resolution. In some data acquisition system, differences from the previously measured value are recorded with 8 bits resolution in order to save the data storage. Sampling interval is 1 second for the higher frequency band and is 1 minute for the lower band. By use of cassette tape, 15 days and half a day of recording are possible for the lower and higher bands, respectively.

Occurrence of the geomagnetic storm is closely related to the solar activity with a typical period of 27 days. Therefore, lower band observation should be carried out for at least one month, which requires tape change at least once a field operation. The solid state memory, EP-ROM, enables us a fairly long time recording. This recording system is used only for flux-gate magnetometers at present, both for land use and ocean bottom magnetometer (OBM), by which a continuous measurement as long as one and a half months is possible with sampling interval of 1 minute by battery operation.

5.2 Data processing

In this study, two kinds of response functions are used in order to investigate the conductivity structure of the earth. One is the geomagnetic transfer functions, A and B, which relate the vertical component, H_z, to the horizontal components, H_x and H_y, of geomagnetic field variation in the frequency domain as:

$$H_z(f) = A(f)\cdot H_x(f) + B(f)\cdot H_y(f) \qquad (5\text{-}2\text{-}1)$$

This equation describes that the vertical component variation is proportional to the north component and/or the east component. In other word, the geomagnetic field variation is restricted within a plane whose normal vector is determined by A(f) and B(f), which is well-known as Rikitake-Yokoyama Plane (Rikitake and Yokoyama 1953). The other is the impedance tensor as is already shown in the previous chapter. The impedance describes the relationship between the electric and the horizontal magnetic field variations as given by Eq.(4-3-1). Here, the linear relationship is rewritten explicitly with the components of the electromagnetic field as:

$$\begin{aligned} E_x(f) &= Z_{xx}(f)\cdot H_x(f) + Z_{xy}(f)\cdot H_y(f) \\ E_y(f) &= Z_{yx}(f)\cdot H_x(f) + Z_{yy}(f)\cdot H_y(f) \end{aligned} \qquad (5\text{-}2\text{-}2)$$

When the magnetic field is measured by use of the induction magnetometer, each component can be replaced by its time derivative like Eq.(4-3-2).

Eqs.(5-2-1) and (5-2-2) are of the same type of linear formula. Therefore, we are going to express these relationship in a general form hereafter as following which describes a relationship between two inputs I_1 and I_2 and an output O of a linear system with response functions R_1 and R_2:

$$O(f) = R_1(f)\cdot I_1(f) + R_2(f)\cdot I_2(f) \qquad (5\text{-}2\text{-}3)$$

In the actual observation, a set of data from k'th subset, $[O_K(f), I_{1K}(f), I_{2K}(f)]$, does not completely satisfy the relation Eq.(5-2-3), but yield some error or discrepancy, $\delta_K(f)$:

$$\delta_K(f) = O_K(f) - [R_1(f)\cdot I_{1K}(f) + R_2(f)\cdot I_{2K}(f)] \qquad (5\text{-}2\text{-}4)$$

If this unfitness can be assumed as random for each data subset, we can determine the set of response functions $[R_1(f), R_2(f)]$ by means of the least squares under the condition of

$$\sum_k \delta_K(f)^2 = \text{min.} \qquad (5\text{-}2\text{-}5)$$

Then, the response function can be obtained with sets of observations as follows:

$$R_1(f) = \frac{\langle I_2\cdot{}^{*}I_2\rangle\cdot\langle O\cdot{}^{*}I_1\rangle - \langle I_2\cdot{}^{*}I_1\rangle\cdot\langle O\cdot{}^{*}I_2\rangle}{\langle I_1\cdot{}^{*}I_1\rangle\cdot\langle I_2\cdot{}^{*}I_2\rangle - \langle I_1\cdot{}^{*}I_2\rangle\cdot\langle I_2\cdot{}^{*}I_1\rangle} \qquad (5\text{-}2\text{-}6)$$

$$R_2(f) = \frac{\langle I_1\cdot{}^{*}I_1\rangle\cdot\langle O\cdot{}^{*}I_2\rangle - \langle I_1\cdot{}^{*}I_2\rangle\cdot\langle O\cdot{}^{*}I_1\rangle}{\langle I_1\cdot{}^{*}I_1\rangle\cdot\langle I_2\cdot{}^{*}I_2\rangle - \langle I_1\cdot{}^{*}I_2\rangle\cdot\langle I_2\cdot{}^{*}I_1\rangle} \qquad (5\text{-}2\text{-}6)$$

where <> denotes an ensemble mean such as

$$\langle I_1 \cdot {}^*I_2 \rangle = \frac{1}{N} \sum_{k=1}^{N} I_{1K}(f) \cdot {}^*I_{2K}(f) \qquad (5\text{-}2\text{-}7)$$

where * denotes a complex conjugate. Eq.(5-2-7) is equivalent to the definition of the cross spectrum estimate with time series of finite data length (e.g. Hino 1978). Hence, ensemble means in Eqs.(5-3-5) and (5-2-6) are often replaced by estimates of power and cross spectra (e.g. Everett and Hyndman 1977). The standard error in the estimate of $R_1(f)$, for example, can be given in a similar form to Eq.(4-3-3) following Bendat and Piersol (1976),

$$r_1(f)^2 = \frac{4}{2n-4} \cdot F(n,4,\alpha) \cdot \frac{(1-coh^2(O))}{(1-coh^2(12))} \cdot \frac{P(O)}{P(I_1)} \qquad (5\text{-}2\text{-}8)$$

where P(O) and $P(I_1)$ denote power spectra of O and I_1, respectively; $F(n,4,\alpha)$ gives α percent point of F-distribution with a degree of freedom n; $coh^2(O)$ and $coh^2(12)$ are the multiple coherency between O and $[I_1, I_2]$, and the coherency between I_1 and I_2, respectively.

The multiple coherency, $coh^2(O)$, can be obtained as:

$$coh^2(O) = 1 - P(\delta)/P(O) \qquad (5\text{-}2\text{-}9)$$

where $P(\delta)$ denotes the power spectrum of the unfitness for $\delta(f)$ given in Eq.(5-2-4). When the output, O(f), can be perfectly predicted by the linear relationship Eq.(5-2-4), $P(\delta)$ will be diminished and therefore the multiple coherency will become unity. If the relationship cannot be described well by the linear equation Eq.(5-2-4), on the other hand, the unfitness, δ (f), will have almost equal power to that of the output, O(f). In such a case, the multiple coherency becomes quite small.

The coherency between I_1 and I_2 is given by

$$\mathrm{coh}^2(12) = [P(12)]^2/\{P(I1)\cdot P(I2)\} \qquad (5\text{-}2\text{-}10)$$

where P(12) denotes the cross spectrum of I1(f) and I2(f). It is obvious that, when $I_1(f)$ is proportional to $I_2(f)$, the coherency becomes unity. We can see one of such examples in linearly or circularly polarized electromagnetic field variation. In this case, we can not determine the response functions together, because the each denominator in Eqs.(5-2-5) and (5-2-6) becomes null, by use of such data set with unity coherency. Eq.(5-2-8) tells a simple relations between the estimation error of the response function and the coherencies: error decreases with higher multiple coherency, $\mathrm{coh}^2(O)$, and with lower coherency, $\mathrm{coh}^2(12)$.

In actual data processing, we have to plot the whole record to select portions appropriate for the time series analysis. In order to obtain a reliable result, time series analysis requires a data set with a sufficient length. In usual, a record of the geomagnetic storm with several days of duration is selected for the analysis. Total number of the data points of a data set, M, and of each data subset, L, should satisfy the following condition for stable power and cross spectra (Bendat and Piersol,1974):

$$N = M/L \geqq 10 \qquad (5\text{-}2\text{-}11)$$

where N is the number of data subsets. Therefore, if we are going to determine the response function up to 120 minutes of period, data set with length of at least 1200 minutes is necessary to obtain a reliable estimates. Actual procedure is summarized as followings.

1) Select a data set of high geomagnetic activity. Missed data or obviously erroneous data, if any, are suitably interpolated.

2) Remove a trend by the least squares for each 5 component.

3) Apply a numerical band pass filter. Recursive filter of Butterworth type (Saito, 1978) is used twice:i.e. once forward and once backward. The shorter cut-off period is determined so as to be equal to the double of the nyquist period, while the longer cut-off is coincide with the length of each data subset.

4) Since filtering causes large scatters at the initial and last portions of data set, such portions are abandoned. Length of data to be abandoned, n_a, can be determined by corresponding length of filter coefficients, n_f, as:

$$n_a = 20\, n_f \qquad (5\text{-}2\text{-}12)$$

5) Each data subset is Fourier transformed by use of FFT method, and then smoothed power and cross spectra are estimated by ensemble averaging of Eq.(5-2-7).

6) Geomagnetic transfer functions and impedances, as well as their standard errors, are calculated by use of the equations presented above.

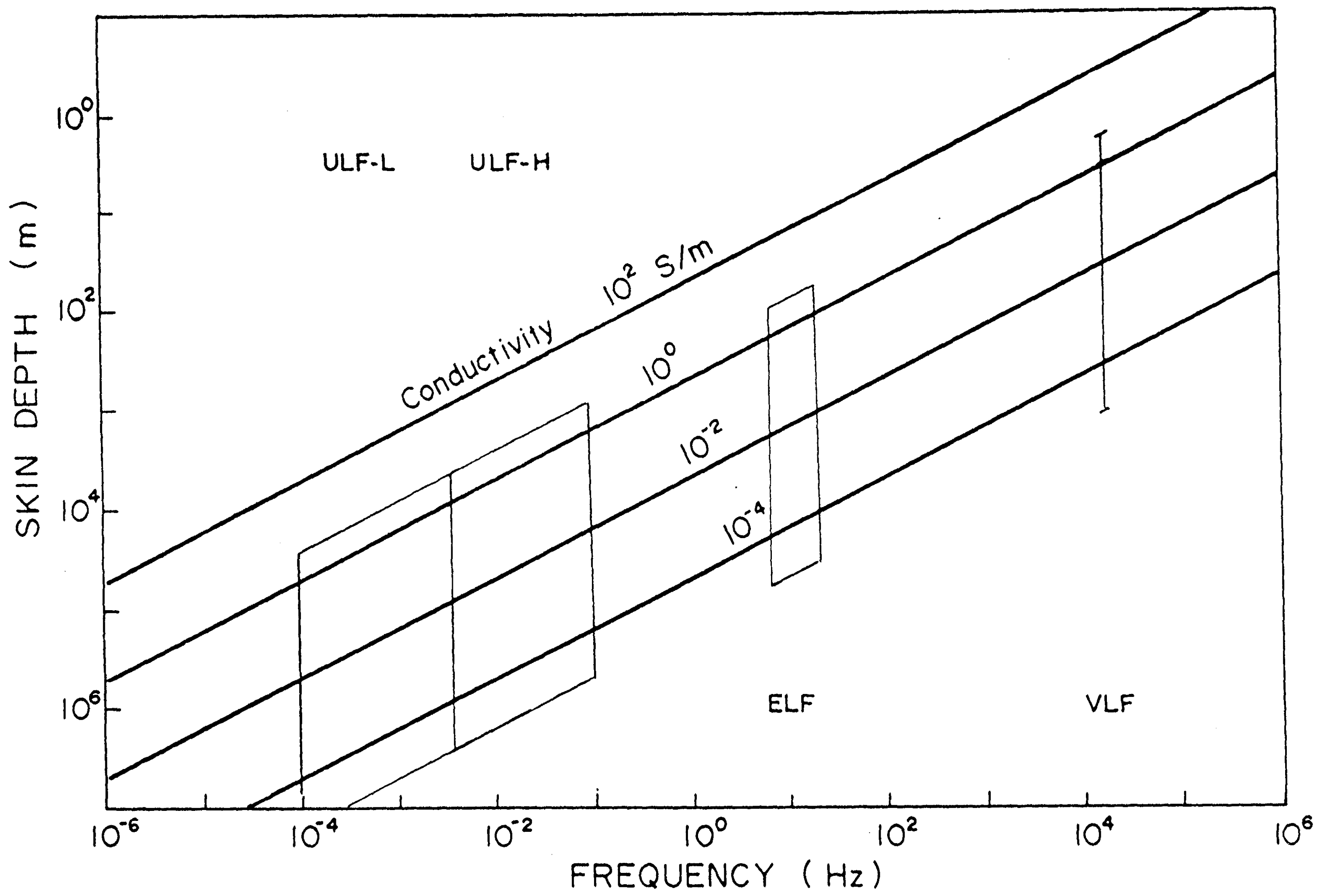

Fig.5.1 Skin depth as a function of frequency for various values of conductivity. Typical range of sounding depth is denoted by a square for each observation band used in this study.

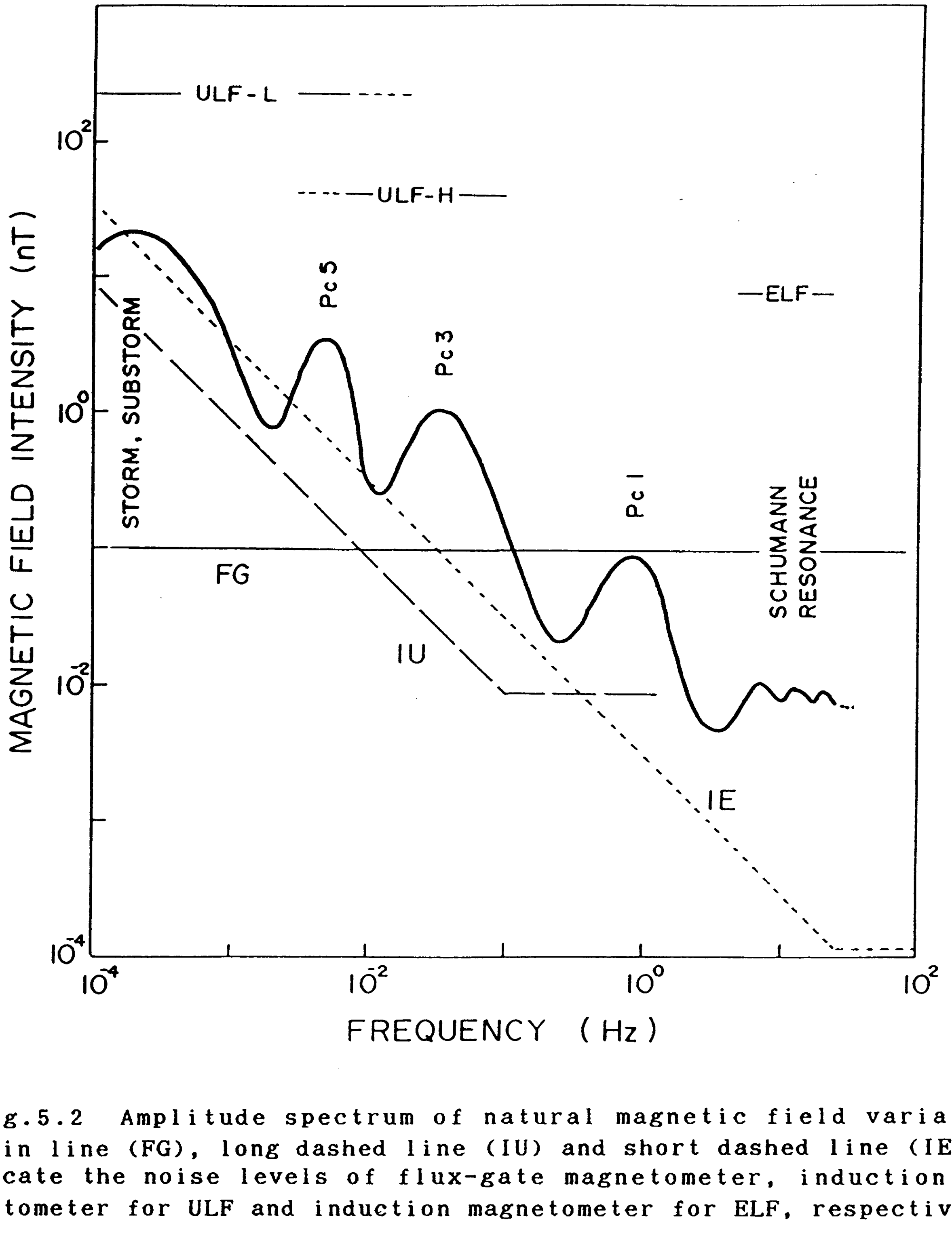

Fig.5.2 Amplitude spectrum of natural magnetic field variation. Thin line (FG), long dashed line (IU) and short dashed line (IE) indicate the noise levels of flux-gate magnetometer, induction magnetometer for ULF and induction magnetometer for ELF, respectively.

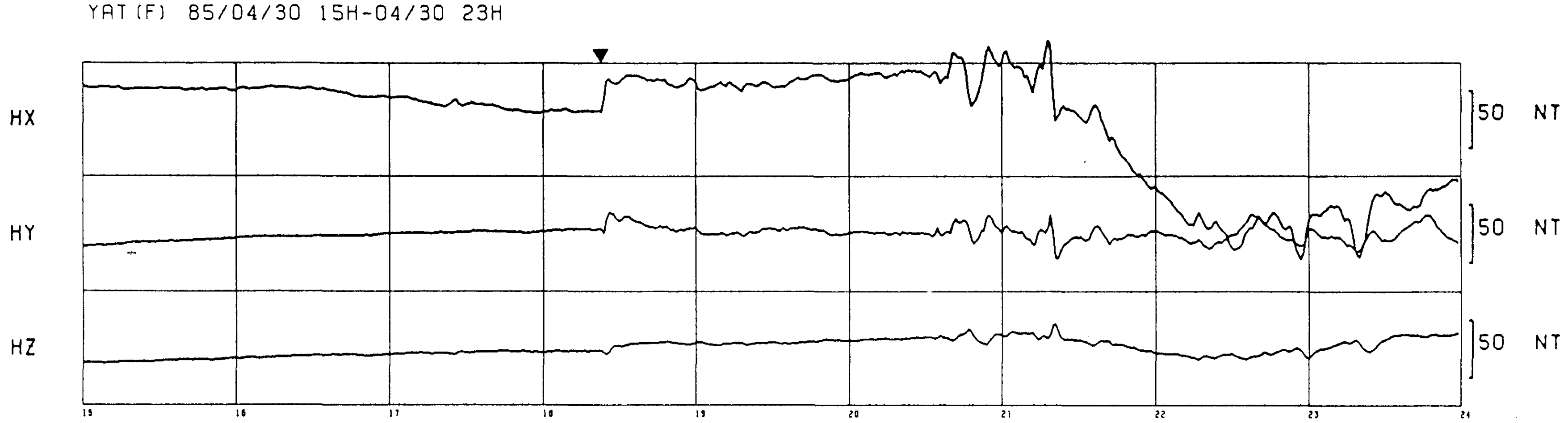

Fig.5.3 An example of geomagnetic storm observed on Apr.30, 1985 at Yatsugatake Geomagnetic Observatory. Triangle denotes the sudden commencement of geomagnetic storm (ssc).

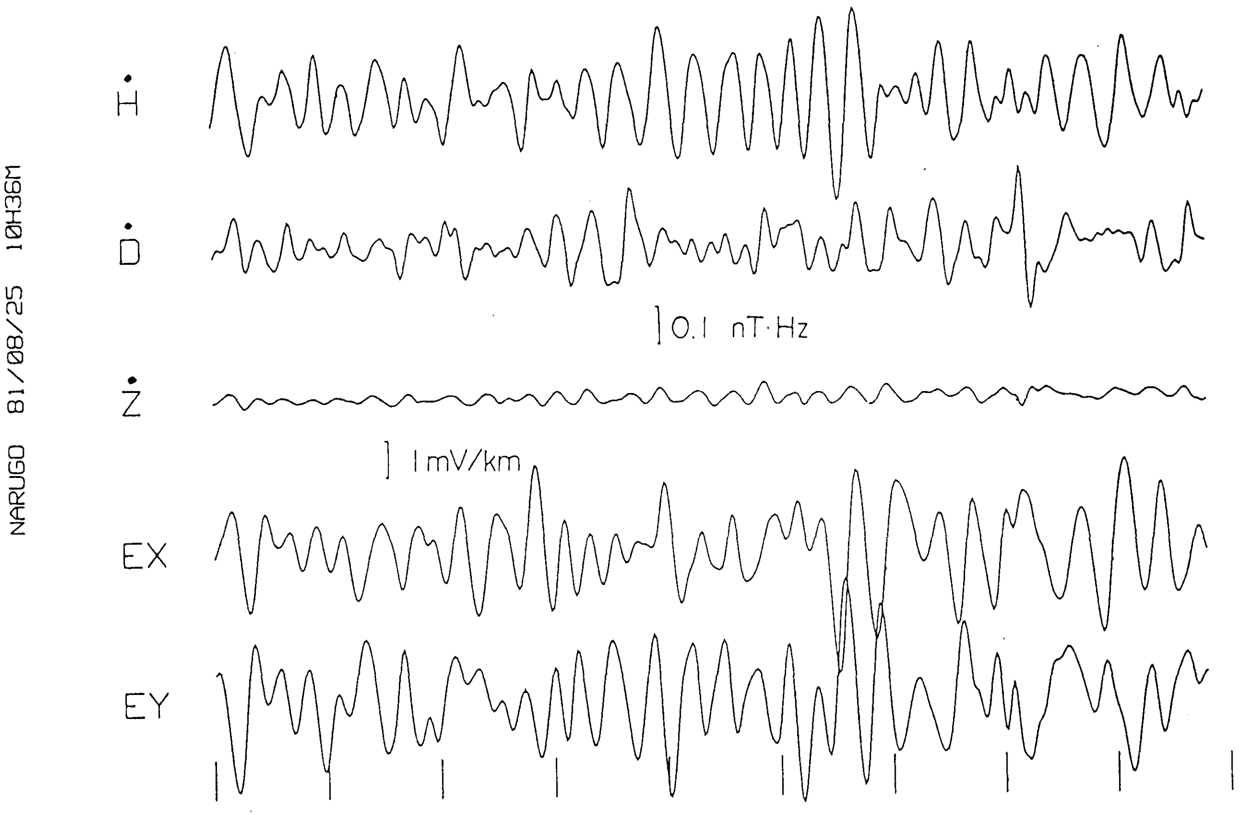

Fig.5.4 Pc-3 micropulsation observed on Aug.25, 1981 at Narugo in Miyagi Prefecture, northeast Japan. Three components of magnetic field and two components of electric field are shown.

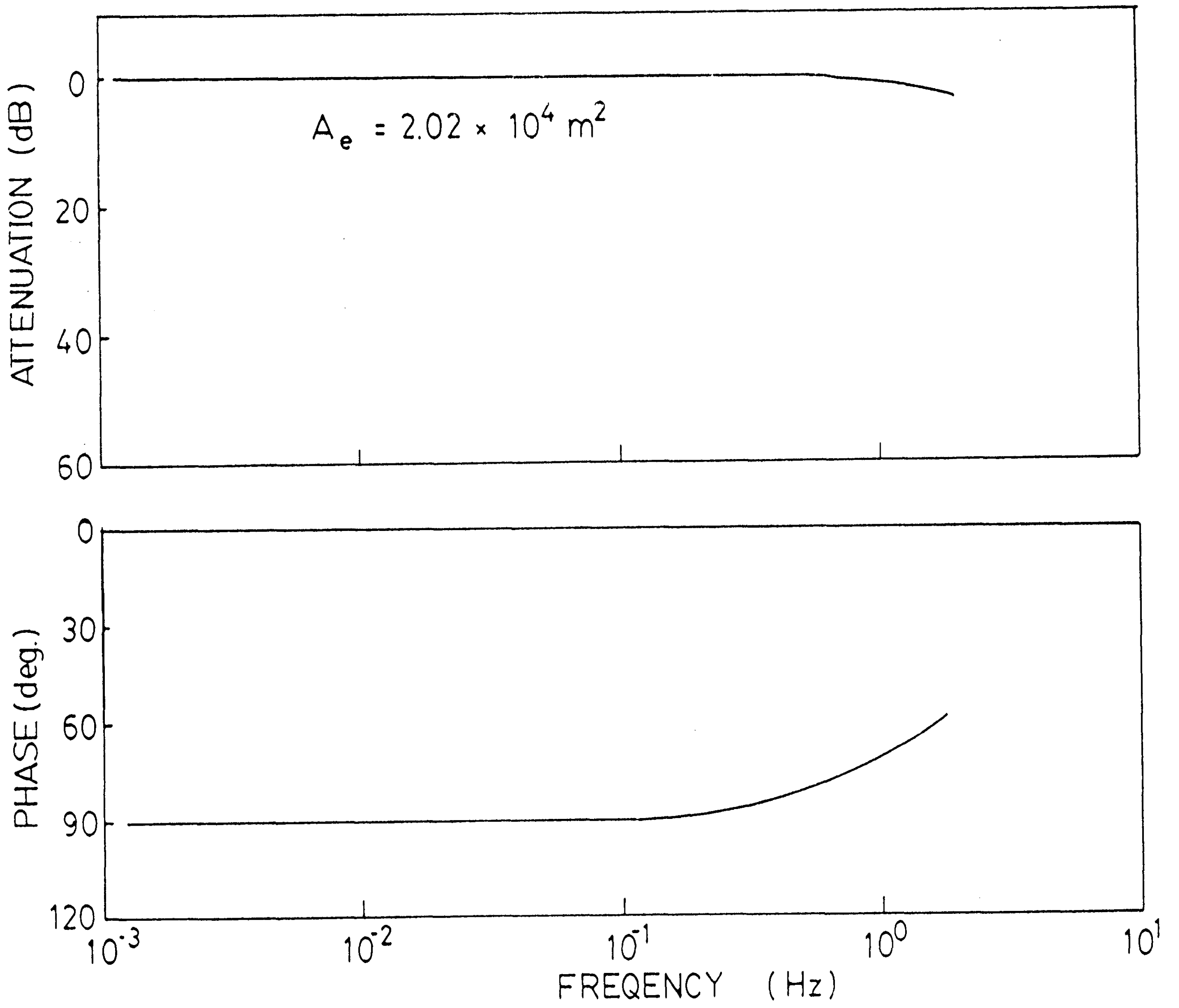

Fig.5.5 Frequency characteristics of the induction coil used for the measurement of geomagnetic field at the higher band of ULF range in this study.

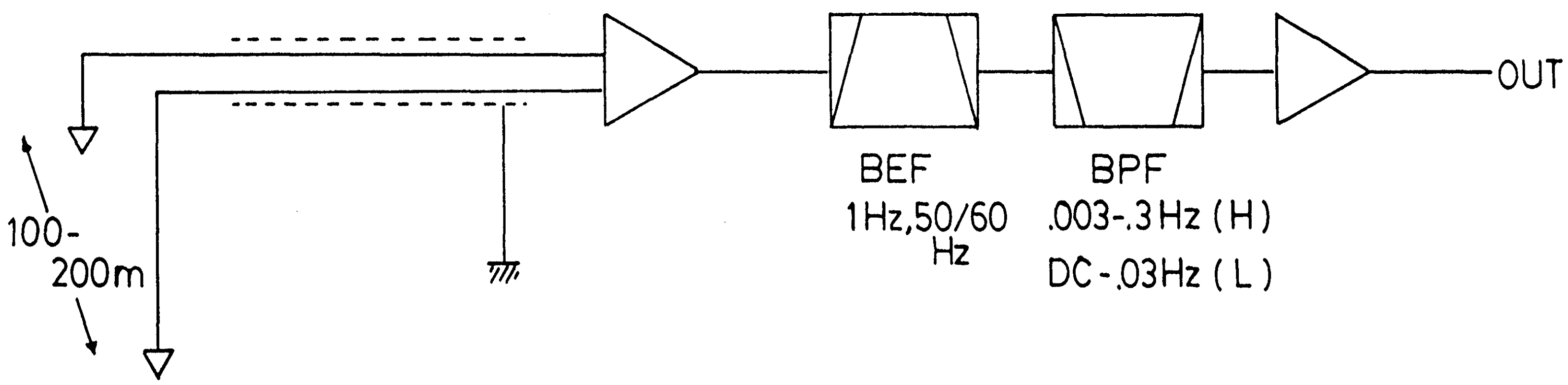

Fig.5.6 Block diagram of measurement system for electric field at ULF range.